Silesian University of Technology

Department of Chemistry

DOCTORAL THESIS

Development of PET imaging agents with potential applications in immunotherapy

Anna Kastelik-Hryniewiecka

Supervisor: **Prof. dr hab. inż. Nikodem Kuźnik**,
Silesian University of Technology, Gliwice, Poland

Supporting supervisor: **Dr inż. Paweł Jewuła,**
Central European Institute of Technology, Brno, Czechia

Supporting supervisor: **Prof. dr hab. n. med. Gabriela Kramer-Marek,**
Maria Sklodowska-Curie National Research Institute of Oncology, Gliwice branch,
Poland

Politechnika
Śląska

Gliwice, 2025

Acknowledgements

I would like to express my sincere gratitude to my supervisor **Professor Nikodem Kuźnik,** for introducing me to the world of science, stimulating discussions and guiding me in the right direction, and most of all for his infinite kindness and support.

Equally, I would like to thank my supporting supervisor **Professor Gabriela Kramer-Marek,** for her support in new, previously unexplored scientific disciplines, and for her constant motivation to develop and learn.

Many thanks to my supporting supervisor **dr inż. Paweł Jewuła,** for his valuable advice and comments, especially in organic syntheses part of this work.

I am extremely grateful to my team at **Radiopharmacy and Preclinical PET Imaging** of National Institute of Oncology! Working with you is pure pleasure, full of surprising challenges and a constant learning experience. I would especially like to thank **dr Marlena Golec** for her work on *in vivo* experiments and preclinical imaging; **mgr inż. Bartłomiej Gawełczyk**, and **mgr inż. Artur Tomasik**, for their support in relaxation studies on an MRI scanner; **mgr Alicja Szeliga** for help and support in cell culture lab. I have to also mention **Andrzej, Karolina, Agnieszka S., Agnieszka J.** for their support, encouragement and help throughout this whole adventure.

I would like to express my sincere gratitude to **Professor Agata Blacha-Grzechnik** for conducting structural analyses (XPS and Raman spectroscopy) and for her help in interpreting the data.

I would also like to thank **Professor Grzegorz Dzido** for the invaluable help in obtaining Zeta potential and dynamic light scattering measurements of the nanoparticles.

Sincere thanks to **Preclinical Molecular Imaging group** of Institute of Cancer Research in London, UK. Many thanks for the opportunity to undertake a highly enriching research internship, for your kindness and assistance. This internship was founded by **The Biologist Ltd** (travel fellowship grant).

The dissertation was prepared as part of the '**Implementation Doctorate IV'** programme, carried out in cooperation with National Research Institute of Oncology and Silesian University of Technology, financed by the Ministry of Education and Science.

The research presented in this dissertation (Aim II) was partially funded by the National Science Centre under grant PRELUDIUM 21 *Development of novel bimodal PET/MRI probes targeting PD-L1*

Abstract

The aim of this doctoral thesis was to design and evaluate bimodal PET/MRI probes to enhance precision imaging and support therapeutic decision-making, particularly in the context of immunotherapy. Two principal objectives were defined: firstly, to improve the stability of ^{89}Zr-based PET agents for immunoPET applications, and secondly, to develop bimodal probes suitable for combined PET/MRI imaging, reflecting the growing clinical interest in this hybrid modality.

The first objective involved the design of a novel chelator for 89Zr, based on deferoxamine (DFO) but modified with a bisphosphonate moiety to enhance complex stability. Two synthetic pathways were proposed and experimentally explored; however, the final target structure could not be obtained. The second objective focused on the functionalisation of commercially available superparamagnetic iron oxide nanoparticles (SPIONs), coated with dextran, to create bimodal probes. These were conjugated with the Atezolizumab (anti-PD-L1 monoclonal antibody), DFO, and ^{89}Zr.

The resulting probes were characterised in terms of their physicochemical properties and biological behaviour. Two radiolabelling methods were optimised and compared, alongside two-step bioconjugation protocol. Amount of antibody and chelator introduced into the SPION structure was confirmed with appropriately selected analytical methods. Structural confirmation was achieved via X-ray photoelectron spectroscopy (XPS), while size and surface charge were assessed using dynamic light scattering (DLS). Quantitative assays were developed to determine the degree of functionalisation. In vitro studies demonstrated target specificity, internalisation, and cytotoxicity, while relaxivity measurements at two magnetic field strengths revealed the influence of surface modifications on MRI contrast properties. In vivo PET/CT and MRI imaging of mice bearing PD-L1-positive tumour xenografts, followed by ex vivo biodistribution, showed rapid accumulation of the probes in the hepatobiliary system.

To enable the integration of nanoparticle-based probes into the portfolio of the Radiopharmacy and Preclinical PET Imaging Unit (ZRO), it was necessary to develop and implement synthetic and analytical protocols previously unused in the Unit. The methodologies established in this project lay the groundwork for future adaptation of similar compounds, varying in isotope or targeting vector and contribute to the expansion of radiopharmaceutical tools for personalised and theranostic applications.

Keywords: PET/MRI, radiopharmaceutical, contrast agent, bimodal probes, immunotherapy, oncological diagnostics, relaxivity

Streszczenie

Celem niniejszej pracy doktorskiej było zaprojektowanie i ocena bimodalnych sond PET/MRI w celu poprawy precyzji obrazowania i wsparcia procesu podejmowania decyzji terapeutycznych, szczególnie w kontekście immunoterapii. Określono dwa główne cele: po pierwsze, poprawę stabilności radiofarmaceutyków PET na bazie ^{89}Zr, a po drugie, opracowanie sond bimodalnych odpowiednich do łączonego obrazowania PET/MRI, odzwierciedlając rosnące zainteresowanie kliniczne tą hybrydową metodą.

Pierwszy cel obejmował zaprojektowanie nowego chelatora dla 89Zr, opartego na deferoksaminie (DFO), ale zmodyfikowanego grupą bisfosfonianową w celu zwiększenia stabilności kompleksu. Zaproponowano dwie ścieżki syntezy i zbadano je eksperymentalnie, jednak nie udało się uzyskać docelowej struktury. Drugi cel skupiał się na funkcjonalizacji dostępnych na rynku superparamagnetycznych nanocząstek tlenku żelaza (SPION) pokrytych dekstranem w celu stworzenia sond bimodalnych. Zostały one skoniugowane z Atezolizumabem (przeciwciałem monoklonalnym anty-PD-L1), DFO i ^{89}Zr.

Otrzymane sondy scharakteryzowano pod względem właściwości fizykochemicznych i zachowania biologicznego. Zoptymalizowano i porównano dwie metody znakowania radioaktywnego oraz dwuetapowy protokół biokonjugacji. Ilość przeciwciała i chelatora wprowadzonego do struktury SPION potwierdzono za pomocą odpowiednio dobranych metod analitycznych.

Potwierdzenie struktury uzyskano za pomocą spektroskopii fotoelektronowej rentgenowskiej (XPS), natomiast rozmiar i ładunek powierzchniowy oceniono za pomocą dynamicznej dyfrakcji światła (DLS). Opracowano testy ilościowe w celu określenia stopnia funkcjonalizacji. Badania in vitro wykazały specyficzność docelową, internalizację i cytotoksyczność, natomiast pomiary relaksacyjności przy dwóch natężeniach pola magnetycznego ujawniły wpływ modyfikacji powierzchni na właściwości kontrastowe MRI. Obrazowanie *in vivo* PET/CT i MRI myszy z przeszczepami nowotworów PD-L1-dodatnich, a następnie biodystrybucja ex vivo wykazały szybką akumulację sond w układzie wątrobowo-żółciowym.

Aby umożliwić włączenie sond opartych na nanocząsteczkach do portfolio Zakładu Radiofarmacji i Obrazowania Laboratoryjnego PET (ZRO), konieczne było opracowanie i wdrożenie protokołów syntetycznych i analitycznych, które nie były wcześniej stosowane w ZRO. Metodologie ustalone w ramach tego projektu stanowią podstawę dla przyszłej adaptacji podobnych związków, różniących się izotopem lub wektorem docelowym, i przyczyniają się do rozszerzenia narzędzi radiofarmaceutycznych do zastosowań spersonalizowanych i teranostycznych.

Słowa kluczowe: PET/MRI, radiofarmaceutyki, środki kontrastowe, sondy bimodalne, immunoterapia, diagnostyka onkologiczna

Table of contents

Abbreviations:

1,5-DAN	1,5-diaminonaphthalene
2,5-DHAP	2,5-dihydroxyacetophenone
ADC	Antibody-drug conjugate
BCA	bicinchoninic acid assay
BFC	Bifunctional chelator
BP	Bisphosphonate
CA	Contrast agent
CT	Computed tomography
CTLA-4	Cytotoxic T Lymphocyte Antigen-4
CTW	Chelex-treated water
D_2O	Deuterium oxide
DFO	Deferoxamine
DHB	2,5-dihydroxybenzoic acid
DIPEA	N,N-Diisopropylethylamine
DLS	Dynamic light scattering
DMF	dimethylformamide
DMSO	Dimethyl sulfoxide
DMSO-d_6	Deuterated dimethyl sulfoxide
DOL	Degree of labelling
DOTA	2,2′,2′′,2′′′-(1,4,7,10-Tetraazacyclododecane-1,4,7,10-tetrayl)tetraacetic acid
DTPA	diethylenetriaminepentaacetic acid
EDTA	ethylenediaminetetraacetic acid
ESI-MS	Electrospray ionization mass spectrometry
Et_3N	triethylamine
FBS	Foetal bovine serum
FID	Free induction decay
FOV	field of view
FTIR	Fourier-transform Infrared spectroscopy

GBCA	Gadolinium based contrast agent
HEPES	4-(2-hydroxyethyl)-1-piperazineethanesulfonic acid
HIR	Heat-induced radiolabelling
HOPO	(3,4,3-LI(1,2-hydroxypyridinone
LAG-3	Lymphocyte Activation Gene-3
mAb	monoclonal antibody
MALDI-TOF	matrix-assisted laser desorption/ionisation time-of-flight mass spectrometry
MeCN	acetonitrile
MWCO	Molecular weight cut-off
NODAGA	1,4,7-triazacyclononane-1,4-diacetic acid
NSCLC	Non-small cell lung cancer
NOTA	1,4,7-triazacyclononane-1,4,7-triacetic acid
OI	Optical imaging
PBS	Phosphate buffer saline
PEG	polyethylene glycol
PET	Positron emission tomography
PMT	Photomultiplier tube
PTSA	p-toluenesulfonic acid
RCF	Relative centrifugal force
RCY	Radiochemical yield
RCP	Radiochemical purity
RF	radiofrequency
RIPA	Radioimmunoprecipitation assay
RPM	Revolutions per minute
RPMI	Rosewell Park Memorial Institute medium
RT	Radionuclide therapy
SA	Specific activity
scFv	Single chain variable fragment
SEC	size-exclusion chromatography

sdAbs	single-domain antibodies
SG	Silica gel
SPDP	succinimidyl 3-(2-pyridyldithio)propionate
SPECT	Single photon emission computed tomography
SPION	Superparamagnetic iron oxide nanoparticles
TCEP	tris(2-carboxyethyl)phosphine
TE	Time of echo
THF	tetrahydrofurane
TLC	Thin layer chromatography
TME	Tumour microenvironment
TMS	tetramethylsilane
TR	Time of repetition
$V_{H;}$	Heavy chain
V_L	Light chain

1. Introduction

Cancer remains one of the most pressing health challenges of the 21st century, often described as a 'civilizational disease' due to its increasing prevalence and complex aetiology. The World Health Organization reports that cancer is responsible for nearly 10 million deaths annually, making it the second leading cause of death worldwide. Over 180 000 new cases of oncological diseases were reported in Poland in 2022 alone [1]. The growing share of cancer in the pool of causes of death originates due to many factors, including genetic predisposition, lifestyle choices and environmental influences, especially environmental pollution and ultra-processed foods [2-4].

The heterogeneity of cancer - both inter- and intratumoural - necessitates tailored therapeutic approaches. There is no one-size-fits-all cancer therapy due to the enormous diversity of cases in terms of pathophysiology, location and tumour sensitivity to therapeutic agents. For example, solid tumours and haematological malignancies are fundamentally different disease entities, grouped together in the category of 'cancer' by their aetiology and the distinctive capabilities of cancer cells that enable tumour growth [2]. This diversity of forms that cancer can take emphasises the importance of precise diagnostic tools and personalised treatment strategies.

Early cancer diagnosis is crucial for improving patient outcomes, as it significantly enhances the effectiveness of treatment options available. Sensitive and specific diagnostic methods are a tool to facilitate detection of malignancies at an earlier stage when they are more amenable to treatment. This is particularly vital because many cancers, if diagnosed late, may lead to advanced disease stages that are harder to treat and have poorer prognoses.

Techniques such as positron emission tomography (PET) and single photon emission computed tomography (SPECT) provide non-invasive methods to visualise metabolic activity and physiological processes within tumours. Recent advancements in cancer diagnostics emphasise a multidisciplinary approach that integrates various imaging modalities alongside molecular profiling. Advanced imaging systems are now capable of combining modalities such as PET with computed tomography (CT) or magnetic resonance imaging (MRI), therefore adding spatial reference to metabolize-based information, allowing for more precise localisation of tumours and better assessment of treatment response. This can guide personalised treatment plans based on specific disease profiles. For instance, the use of radiotracers that target specific biomarkers can help in identifying tumours that may respond favourably to certain therapies, thereby minimising unnecessary treatments [5].

PET imaging relies on radiopharmaceuticals based on molecules labelled with positron-emitting isotopes that target specific biological pathways. In this dissertation, the term 'PET imaging agent' will be used interchangeably with 'radiopharmaceutical', 'radiotracer' or 'radioconjugate', therefore they should be treated as synonyms. The most commonly used radiotracer, [^{18}F]-fluorodeoxyglucose (FDG), reflects glucose metabolism, which is typically elevated in cancer cells. However, FDG lacks specificity, as it also may accumulate in inflammatory tissues, activated immune cells and organs of high glucose metabolism (e.g. brain, heart). To address this limitation, novel PET radiopharmaceuticals have been developed to target specific receptors, ligands or proteins. A particularly interesting application of this highly specific imaging method is immunoPET, a technique that enables monitoring of the response to targeted therapies, including immunotherapies, through the use of radiopharmaceuticals designed to bind immune checkpoint molecules and other relevant targets [6].

Immunotherapy has revolutionised cancer treatment by harnessing the immune system to target malignant cells. Immune checkpoint inhibitors (ICIs), such as anti-PD-1 and anti-CTLA-4 antibodies, have shown remarkable efficacy in melanoma, non-small cell lung cancer, and renal cell carcinoma [7]. Adoptive cell therapies, including CAR-T cells, further expand the therapeutic arsenal. Despite these advances, immunotherapy is not universally effective. Only part of patients achieves satisfactory responses, and immune-related adverse events can be severe. The variability in outcomes is caused by differences in tumour immunogenicity, microenvironment and immune cell infiltration [8].

ImmunoPET could offer a non-invasive way to stratify patients for immunotherapy by visualising immune activation and tumour-immune interactions. For example, programmed death ligand (PD-L1) expression can be quantified by immunoPET imaging with zirconium-89 (^{89}Zr) labelled anti-PD-L1 monoclonal antibody (e.g. ^{89}Zr-DFO-Atezolizumab). Moreover, immunoPET can detect atypical response patterns, such as pseudoprogression, which are common in immunotherapy and may be misinterpreted by conventional imaging. This capability is crucial for avoiding premature discontinuation of effective treatment [6].

In parallel with the rapid development of immunoPET, recent years have also seen the introduction of hybrid PET/MRI scanners into clinical practice. PET/MRI is a powerful hybrid imaging modality that combines the high sensitivity of PET with the superior soft-tissue contrast and functional information provided by MRI. This integration allows simultaneous acquisition of molecular, anatomical, and physiological data, offering a more

comprehensive picture of tumour biology. PET/MRI is particularly valuable in neuro-oncology, where precise delineation of brain tumours and their microenvironment is crucial. At the same time, it reduces radiation exposure compared to PET/CT, which is an important consideration in longitudinal studies and for younger patients. The development of probes specifically designed for PET/MRI has become a rapidly growing field, aiming to exploit the complementary strengths of both modalities.

In this context, the goal of this doctoral thesis was to design and evaluate PET/MRI probes that can advance precision imaging and better guide therapeutic strategies (**Scheme 1**). To achieve this, two main objectives were defined.

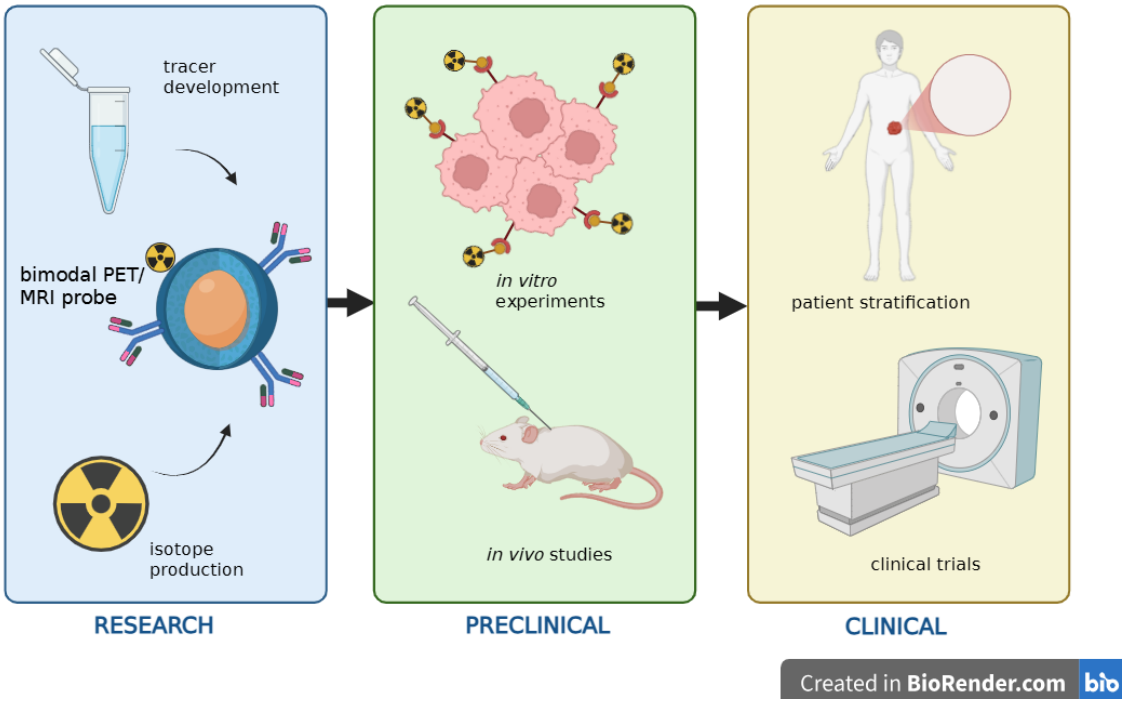

Scheme 1 – Stages of novel radiopharmaceutical development.

The first goal was to improve the stability of ^{89}Zr-based PET agents for immunoPET applications. It is well recognised that a major limitation of ^{89}Zr radiopharmaceuticals is the unsatisfactory stability of its complex with deferoxamine (DFO), the most commonly used zirconium chelator in clinical practice [9]. Due to ^{89}Zr half-life of 78 hours, which matches the biological half-life of monoclonal antibodies (mAbs), this isotope is often used in immunoPET agents [10, 11].

However, instability of the ^{89}Zr–DFO complex can result in isotope release and subsequent accumulation of the radioactivity in the bones, raising significant safety concern. To address this problem, a new, previously unreported chelator was designed and attempts were made to synthesise it. The idea of new DFO derivative incorporates a bisphosphonate group into the chelator's structure, expected to improve the stability of the isotope-chelator complex.

These studies are described in section **3.1 - Aim I: Development of novel DFO-based chelator for zirconium coordination.**

The second aim was to develop bimodal probes for combined PET/MRI, due to gaining popularity of PET/MRI and better possibility to use such probes for monitoring response to immunotherapy.

Nanoparticle-based bimodal probes, functionalised with a radioisotope and mAb, have been proposed for immune checkpoint targeting. Among them, superparamagnetic iron-oxide nanoparticles (SPION) have proven efficacy as a negative MRI contrast agent [12, 13]. In this project, their surface modification and radiolabelling were undertaken, followed by the evaluation of physicochemical properties, *in vitro* behaviour and proof-of-concept *in vivo* studies have been described in section **3.2. Aim II – Development of bimodal probe for simultaneous PET/MRI imaging.**

2. Theoretical background

2.1 PET imaging

PET imaging is based on the detection of coincidence of ɣ-ray quanta, each with energy of 511 keV, created by positron-electron annihilation (**Scheme 2**). A radioactive tracer, containing a radioactive isotope exhibiting β+ decay, administered in advance, is the positron donor in this process, while the electron comes from the environment (e.g. body tissues). Two quanta created in annihilation process are emitted in almost opposite direction (c.a. 180 °) and scintillators detect them simultaneously (so called coincidence). It allows for accurate and precise localisation of the source of the ɣ rays, therefore – region of interest being imaged.

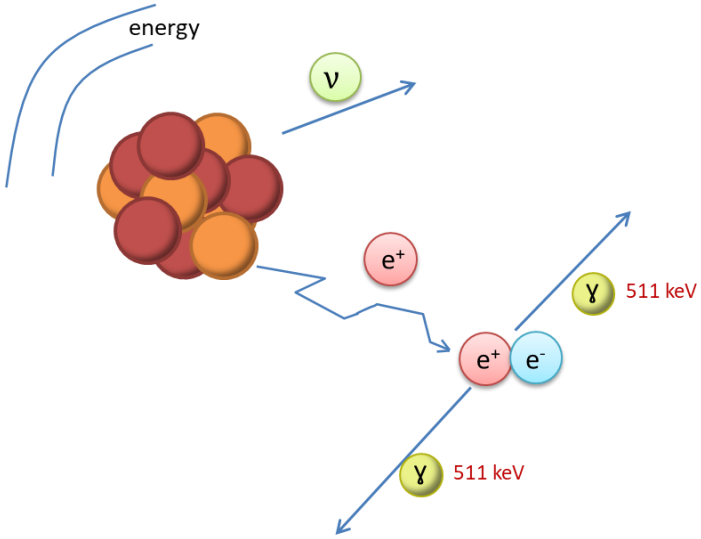

Scheme 2- β+ decay. In this transformation nucleus emits antineutrino (ν), energy and positron (e^+), which travels few mm in tissue before colliding with electron and undergoing positron-electron annihilation. In result, two ɣ-photons are emitted in opposite directions. This process is fundamental to PET imaging.

PET isotopes are radioactive nuclei, unstable due to excess of protons. Positron (e+) emission is triggered by such excess, resulting in **β+ radiation** [14]. The emission of the e+ particle occurs as a result of the transformation of one of the protons in the nucleus into a neutron and is accompanied by the emission of a neutrino (ν), a particle with properties similar to an antineutrino.

$$p^+ \rightarrow n + e^+ + \nu + \text{energy}$$

B+ isotopes for PET application are produced artificially, as they occur naturally only in trace amounts.

Detection

Detectors installed in PET scanners consist of scintillator and a photomultiplier [15]. Scintillators (solid scintillation detectors) have the unique property of emitting scintillation or flashes of light after absorbing γ or X-ray radiations. This interaction is the basis of radiation detection in PET technology. Important criteria to consider when selecting scintillator material are:

- scintillation decay time – time (in nanoseconds) during which the detector material excited by the ɣ ray emits energy through a flash of light. The lower this parameter, the higher the detector performance at high counts (high activity).
- Stopping power – a parameter that determines the distance the ɣ ray travels in the detector volume. In other words, it is the minimum thickness of the detector that allows the energy of a ɣ photon to be lost. In PET detection, stopping power is important for photons with energy of 511 keV.
- light flash power - a stronger flash of light produced by the scintillation process translates into an electric pulse of higher intensity, resulting in improved resolution of the image.
- energy resolution - this parameter is affected by imperfections in the crystal, which can interfere with the production of light signals. For PET detectors, this value is usually in the range of 15-20%.

The detectors used in PET scanners have been significantly developed and upgraded in recent years. Today, the mostly used crystals are NaI, bismuth germanate, lutetium based LSO and LYSO, and gadolinium oxyorthosilicate [16].

Photomultiplier tube (PMT) is needed to convert the light photons produced in the detector into an electrical pulse. Light pulses generated in the scintillator through the interaction of ɣ radiation with the detector crystal fall on the photocathode (usually made of a caesium-antimony alloy). After absorbing the photon, the photocathode emits electrons, which are then accelerated through vacuum in the tube and multiplied. This occurs by successive reflections of the electron beam from the dynodes, spaced along the length of the PMT, up to the anode. Currently there are some alternatives to PMT, like silicone photomultiplier or Geiger-mode avalanche photodiode [17]. Next, the signal is enhanced in the amplifier to a detectable pulse. The last step before arriving to the computer and being analysed, the pulse goes through PHA (pulse height analyser) where it is analysed by its size. Computer-enhanced reconstruction allows technicians to obtain images in minutes after scan, with typical resolution of 4-5 mm in the centre of the field of view.

A typical PET scanner setup has detectors arranged in an annular fashion around a computer-controlled bed that can move relative to the detectors. Currently, the most widely applied solution is combination of PET/CT, which almost completely replaced standalone PET systems. In such hybrid scanners both units are mounted on a common support with the CT unit in the front and the PET unit in the back next to the CT unit. Both units use the same gantry and imaging table (**Scheme 3**).

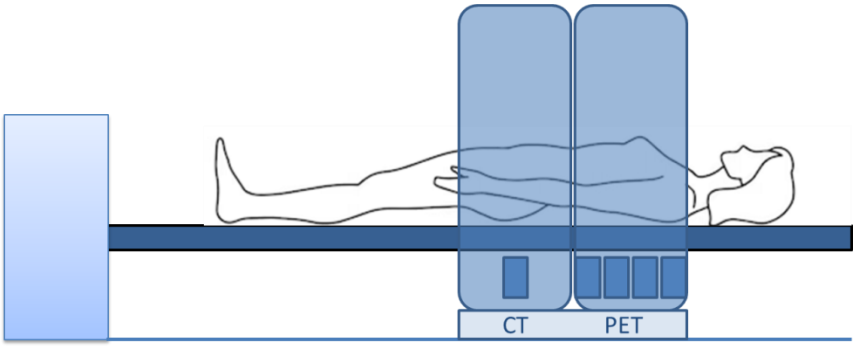

Scheme 3- Schematic illustration of a PET/CT scanner.

By combining different modalities, allow the acquisition of images with the high sensitivity for detecting biochemical and physiological processes owing to the PET technique (sensitivity: 10^{-11} - 10^{-12} mol/L) by combining it with the anatomical reference of high spatial resolution provided by CT imaging. Total effective dose delivered to patient's body during PET/CT scan is the sum of radiation originating from both radionuclides' decay and X-rays necessary to obtain CT scan. For typical ^{18}F-FDG scan (450 MBq injected) such a mean total effective dose was calculated to be 25 mSv, with 60% of dose coming from CT scan [18].

Rarer but still encountered combinations include PET/OI (optical imaging), CT/MRI, and PET/NIR [19-21]. A particularly noteworthy area of intensive development is the hybrid PET/MRI technique. In this combination, the MR technique replaces CT from the PET/CT combination. The rationale behind this substitution is the lack of ionising radiation dose from X-rays and the superiority of MRI in imaging the gastrointestinal tract, the nervous system including the brain, or the respiratory tract. High spatial resolution of this technique adds anatomical parameters to the sensitive with almost infinite penetration depth and quantitative capabilities of PET.

2.1.1 ImmunoPET

ImmunoPET is a molecular imaging modality that combines the high sensitivity of PET with the specificity of mAbs or antibody fragments to visualize and quantify biological targets

in vivo. It allows visualisation, characterisation, and measurement of immunological processes at the cellular and molecular level in living organisms, often before structural changes become apparent. Through the use of radiolabelled immunomolecules immunoPET enables early disease detection, determination of heterogeneity, and research into disease mechanisms, finding its application in screening, diagnosis, monitoring of therapy, prognosis of disease progression and also long-term follow-up [22].

The choice of targeting vector - whether full-length antibodies, engineered fragments, peptides, or immune checkpoint ligands - influences imaging performance, pharmacokinetics, and clinical applicability. Full-length mAbs were the first class of targeting agents employed in immunoPET due to their high affinity and specificity for tumour-associated antigens. These molecules (~150 kDa) exhibit prolonged circulation times and slow tumour penetration, necessitating the use of long-lived positron-emitting radionuclides such as ^{89}Zr ($t_1/_2 \approx 78.4$ h) or ^{124}I ($t_1/_2 \approx 100.2$ h). Pioneering research in field of immunoPET was targeted toward two receptors from epidermal growth factor family: human epidermal growth factor Receptor 2 (HER2) and EGFR. Monoclonal antibodies targeting these receptors were labelled with ^{89}Zr or ^{64}Cu. ^{89}Zr-trastuzumab has been used to image HER2-positive breast cancer, enabling assessment of receptor expression and therapeutic response, while ^{89}Zr-cetuximab and ^{64}Cu-panitumumab have been applied to visualize EGFR expression in colorectal and non-small lung cancer, respectively [23-25]. These early applications demonstrated the feasibility of antibody-based PET imaging and laid the foundation for more refined targeting strategies.

With the advent of immunotherapy, immune checkpoint proteins (ICPs) have emerged as critical targets for immunoPET. Radiolabelled antibodies and fragments directed against ICPs such as PD-1, PD-L1, and CTLA-4 enable visualization of immune cell infiltration, checkpoint expression, and response to immunomodulatory therapies [26]. Notable pathways include:

- Programmed Cell Death Protein 1 (PD-1) and its Ligands[1] (PD-L1 and PD-L2)
- Cytotoxic T Lymphocyte Antigen-4 (CTLA-4)
- Lymphocyte Activation Gene-3 (LAG-3)
- T -cell Immunoglobulin and Mucin Domain-3

[1] In order to keep the narrative consistent, the term ligand will be understood in a biomedical context (unless clearly stated otherwise). The term chelator will be used to refer to coordination compounds used to complex radiometal atoms.

Current immunotherapies in cancer treatment are very costly and benefit 20-50% of the total number of patients [27]. The probability of benefiting from immunotherapy depends on several factors, including the type of cancer, the presence of specific biomarkers (like PD-L1 expression), and the individual patient's immune system characteristics. Additionally, dynamic nature of immune response may make it more difficult to assess the therapeutic result [28]. With use of specially designed tracer, the response to therapy might be predicted and progress of treatment monitored.

Programmed Cell Death Protein (PD-1) and its Ligand (PD-L1)

Programmed Cell Death Protein 1 (PD-1) is a crucial immune checkpoint receptor that plays a significant role in regulating the immune system's response to cells of the human body [29]. It is encoded by the PDCD1 gene and primarily expressed on activated T cells, B cells, and myeloid-derived dendritic cells [30]. PD-1 consists of an extracellular immunoglobulin-like domain, a transmembrane region, and an intracellular tail that contains phosphorylation sites critical for its inhibitory function. Upon ligand binding, PD-1 recruits phosphatases like SHP-1 and SHP-2, leading to the down-regulation of T cell receptor signalling [31]. Its ligands, PD-L1 and PD-L2, are expressed on a variety of cell types, including tumour cells and antigen-presenting cells. Upon binding to PD-L1 or PD-L2, PD-1 transmits an inhibitory signal that attenuates T cell receptor signalling, leading to reduced cytokine production and impaired cytotoxic function. This pathway plays a critical role in maintaining peripheral tolerance and preventing autoimmunity, but it is also exploited by tumours to evade immune surveillance [32].

PD-1 functions based on two main mechanisms: promotion of apoptosis and regulation of regulatory T-cells. In the first process, receptor encourages programmed cell death (apoptosis) of antigen-specific T-cells within lymph nodes. It also influences regulatory T-cells, essential for maintaining immune homeostasis, by reducing apoptosis of those cells [33, 34].

The binding of transmembrane protein PD-L1 to PD-1 transmits inhibitory signals that reduce T-cell activation and proliferation by interfering with key signalling pathways such as ZAP70 and PKC-θ [22]. PD-L1 engagement with PD-1 inhibits IL-2 production and T-cell proliferation, crucial for maintaining immune tolerance during physiological events like pregnancy and tissue allografts. However, many tumours exploit PD-L1 expression to evade immune detection, making it a target for cancer immunotherapy. In clinical applications, PD-1 inhibitors (e.g. nivolumab, pembrolizumab or cemiplimab) have shown efficacy in treating various cancers, including melanoma, lung cancer, and renal cell carcinoma

[35-38]. They are often used in combination with other treatments to enhance their effectiveness. For instance, dual immune checkpoint blockade (e.g., combining PD-1 inhibitors with CTLA-4 antagonists) has demonstrated improved response rates in melanoma and non-small cell lung cancer (NSCLC), albeit with increased immune-related adverse events. Clinical trials have also explored combinations with cancer vaccines and oncolytic viruses to boost antigen-specific T-cell responses [39-41].

While PD-1/PD-L1 inhibitors represent a significant advancement in cancer therapy, their effectiveness can be limited, as presence of PD-L1 on tumour cells can vary significantly among different cases and even within different areas of the same tumour, affecting treatment response. For this reason, the issue that urgently needs to be addressed is the determination of the potential efficacy of the planned therapy, the choice of dose and the individual monitoring of the course of treatment. It turns out that the response of the immune system is different in each case and therefore requires testing for each patient first. Currently available methods to determine the presence of PD-1/PD-L1 receptors are mainly based on immunohistochemical tests, requiring the invasive removal of a piece of tumour tissue. Multiple first-in-human PET studies with ^{89}Zr-labelled antibodies (e.g., atezolizumab, durvalumab, nivolumab, pembrolizumab) have shown safety/feasibility, map whole-body target heterogeneity, and in some settings correlate with IHC or treatment outcomes [42-45] .

2.2 Radiopharmaceuticals

Radiopharmaceuticals play crucial role in modern nuclear medicine, serving both diagnostic and therapeutic purposes, providing non-invasive glimpse into processes at the molecular level or precisely delivering lethal rays [46]. Those radioactive drugs are administered into the patient's body (usually intravenously, but some may be taken orally) and target the desired tissue or organ due to biospecific moiety in their structure. Depending on the type of radionuclide used, radiopharmaceuticals allow to either detect targeted region of interest or deliver high-energy radiation in order to destroy or damage cancer cells while minimising exposure to surrounding healthy tissues. Moreover, radiopharmaceuticals play a significant role in monitoring new treatment regimens and understanding the pharmacokinetics of drugs, particularly in the fields of oncology and personalized medicine [47, 48]. An in-depth understanding of biodistribution, metabolism and pharmacokinetics is essential to develop optimal delivery methods and drug doses. Furthermore, it is necessary to optimise parameters such as excretion characteristics and binding affinity, depending on the desired diagnostic or therapeutic effect. By employing

novel radiopharmaceuticals, clinicians can optimize patient selection and treatment planning, ultimately improving personalised cancer care. The ability to track a compound by adding a radioactive element to its structure goes all the way back to the work of George de Hevesy and nowadays clinicians are utilising it to evaluate the expression of immune markers and assess changes in the tumour microenvironment (TME) over time.

Radiopharmaceuticals structure

Radiopharmaceuticals typically consist of a radionuclide, a linker and a targeting molecule. The role of the linker is usually fulfilled by a chelator (gr. *Chele* – ticks), which coordinates the radionuclide atom and provides a stable and permanent connection between the two parts (**Scheme 4**).

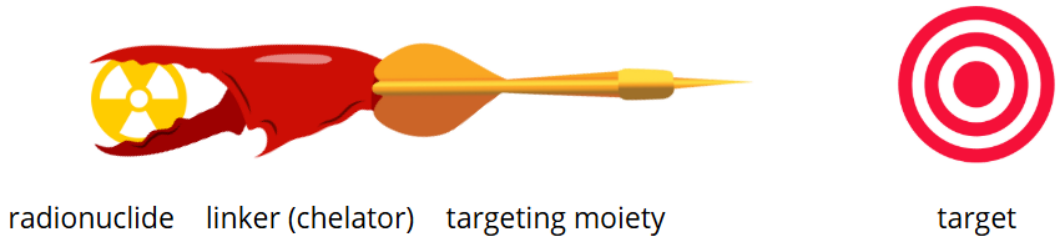

Scheme 4- Radiopharmaceutical – schematic representation

There are some examples that escape the above definition. Non-targeted radiopharmaceuticals do not have specific targeting moieties in their structure and their use is based on the general metabolism of the drug. The iodine isotopes (^{123}I, ^{124}I for SPECT and PET imaging respectively, while ^{131}I and ^{125}I are utilized for therapy) are examples of non-targeted radiopharmaceuticals, and their action (both diagnostic and therapeutic) is based on the naturally occurring metabolism of iodine by the thyroid organ [49]. The tracer most commonly used in clinical PET imaging (depending on the source estimated at 70 to 90% of all scans) is ^{18}F-fluodeoxy-D-glucose (FDG). Its prevalence is related to its versatility, as it allows glucose metabolism to be imaged, as its accumulation depends on the tissue's requirement for this monosaccharide. After internalization, FDG is phosphorylated by hexokinase in order to form FDG-6-phosphate, under the same mechanism in which glucose converts to glucose-6-phosphate. However, unlike glucose-6-phosphate, phosphorylated form of FDG is unable to proceed in glycolysis because it lacks the 2-hydroxyl group necessary for isomerization. Thus, radioactive isotope in form of FDG-6-phopsphate accumulates inside the cell and is not metabolized or exported, allowing PET scanners to detect its signal hours after administration [50]. Its use in oncology is based on the significantly higher glucose consumption of tumour

tissue, compared to healthy cells. Importantly, however, FDG is unsuitable for brain diagnostics (due to this organ's consistently high glucose consumption) and will also be non-specifically deposited in the heart or inflammatory states.

However, majority of modern radiopharmaceuticals utilise wide and constantly expanding library of targeting vectors, tailoring very specific biomolecules for personalised medicine.

2.2.1 Targeting vectors

Different biological structures or metabolic processes can be targeted, including: receptors, ligands, enzymes, differences in vascularisation, hypoxigenated tissues, gene products or transporters [51-57]. Because of this diversity of targets, the corresponding targeting molecules also differ in nature and function and may participate directly in these metabolic processes or act as a receptor agonist or antagonist. Depending on the molecule used, they will have different lipophilicity, charge and mass, all of which affect the circulation time, the way it interacts with the target present on the cell and the route of excretion from the body (**Scheme 5**). Larger molecules, like mAbs have a longer biological half-life and much slower systemic clearance, which simplify tumour accumulation. By contrast, smaller targeting vectors, including peptides or Ab fragments, are characterised by deeper tumour penetration. For macromolecules, receptor binding is generally restricted to the cell surface, whereas smaller vectors can access targets more effectively within the tumour mass. Clearance kinetics also differ, the smaller the vector, the shorter its residence time in the body. In terms of elimination pathways, molecules below 60 kDa pass through the kidneys, while larger constructs are eliminated via the hepatobiliary system.

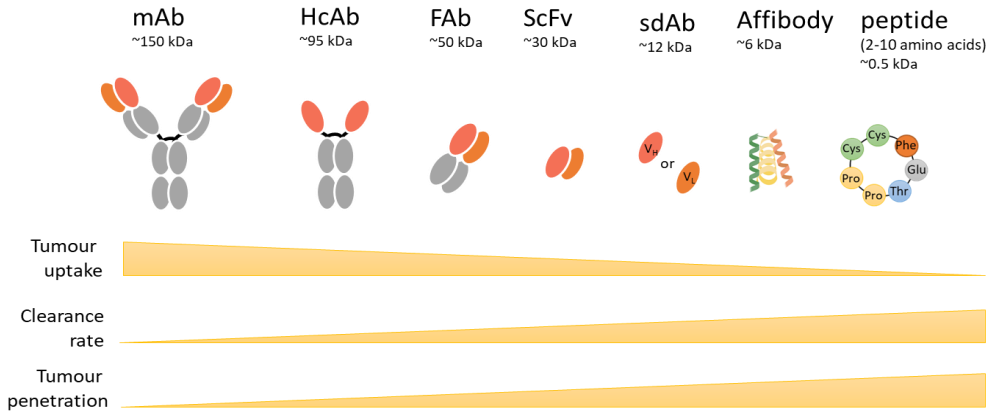

Scheme 5 - Vectors of different molecular weight: monoclonal antibody (mAb), heavy chain only antibody (HcAb), fragment antigen binding (Fab), single chain variable fragment (ScFv), variable fragment (Fv), single domain antibody (sdAb), affibody and peptide. Inspired by figure from Lin et [58]

mAbs owe their name to the way they are obtained, namely as clones of a single white cell. All antibodies are thus derived from the same cellular source. This gives them the unique ability to exclusively bind to a specific epitope (the part of the protein recognised by the mAb), unlike polyclonal (pAbs) or bispecific antibodies (BsAb). Monoclonal antibodies are used, among other things, in diagnostics and therapy (targeted therapy, immunotherapy), and because of their production method, it is possible to obtain a vector specific to almost any antigen. However, the path to the current state, in which 122 different antibodies and antibody-drug conjugates (ADCs) are FDA-approved has required decades of work of many specialists, especially in humanisation of mAbs, and extensive preclinal and clinical studies [58].

Multiple toxicological studies, as well as internal radiation dosimetry and pharmacokinetics studies were necessary for introducing radioimmunoconjugates into the diagnostic and therapy standard. High immunogenicity is still a problem for some mAbs [59-61]. It was theorised that variable domain is main cause of immunogenic issues, so smaller antibody fragments, stripped of this part were developed [62]. Enzymes papain or pepsin are used to digest mAbs in order to obtain antigen-binding fragments: F(ab) of molar mass in the range of 50-55 kDa or 'double' fragments $F(ab')_2$ weighing around 110 kDa (Scheme 5). Such a modification improves excretion (through the renal system, in contrast to intact antibodies with liver clearance and higher liver retention) and tumour penetration [63, 64]. However, this method is quite burdensome and requires large quantities of primary antibody, what cause the prices of such construct to remain high. Continuous growth of biotechnology field and methods of antibody modification allowed establishing another class of antibody fragments, namely single-chain variable region fragments (scFvs), single-domain antibodies (sdAbs, also called nanobodies) and affibodies [62, 65, 66]. The former scaffolds are not antibody fragments *per se*, but a fusion protein of the variable regions of the heavy (V_H) and light (V_L) chains, linked by dozen amino acids (usually 10 to 25 units). A reduction in protein mass (26 kDa) leads to an increase in affinity in comparison to intact antibody. Nanobodies on the other hand are characterised by half the molecular weight (12-15 kDa) than of scFvs, as they are derived from either V_H or V_L [67]. They present satisfactory stability, affinity and specificity in equilibrium to relatively low cost of production. Affibody molecules are small, engineered proteins (~6-7 kDa) derived from the Z-domain scaffold of Staphylococcal protein A. They consist of 58 amino acids arranged in a three-helix bundle, which provides high stability and the ability to tolerate diverse chemical modifications [66].

2.2.2 Radionuclides

Radioactive isotopes used in radiopharmaceuticals can be classified according to the ionising radiation emitted and the desired application (PET/SPECT imaging or radionuclide therapy (RT)). This classification, together with the most commonly used examples, is summarised in **Table 1**.

Table 1 - Radionuclides in various nuclear medicine applications

Application	Type of radiation	Medical application	Examples of radionuclides	Source
Diagnostics	β+ positrons	PET	^{18}F, ^{68}Ga, ^{89}Zr, ^{64}Cu	[68-71]
	ɣ photons	SPECT	^{99m}Tc, ^{123}I, ^{133}Xe	[72-74]
Radionuclide therapy	α particles	RT	^{225}Ac, ^{211}At, ^{227}Th	[75]
	β- electrons	RT, SPECT	^{177}Lu, ^{131}I, ^{90}Y	[76]
	Auger electron	RT	^{111}In, ^{67}Ga, ^{99m}Tc, ^{195m}Pt, ^{125}I and ^{123}I	[77]

In addition to matching an isotope of a particular radiation type to the desired application, the nature of the vehicle molecule must also be taken into account. The half-life must be matched to the biological half-life of the targeting vector. Typically, bigger molecules would have longer circulation times, and slow pharmacokinetics, hence they should be paired with longer-lived isotopes. These are worse suited for clinical purposes due to greater radiation doses and elongated wait times for imaging. Length of the labelling and other processes (e.g. purification, quality control) also must be taken into account while designing a radiopharmaceutical. Smaller proteins of shorter circulation times (hours rather than days) can be labelled with more clinically-relevant, shorter-lived PET radionuclides, which enable same-day imaging.

PET isotopes are characterized by the following definitions:

Activity or *total activity* (symbol *A*) - physical quantity defined as the number of radioactive decays per second. Quantitatively, activity is expressed in two units: *becquerel* (symbol Bq), which is understood as one decay per second; and *curie* (Ci), which is 3.7×10^{10} radioactive

decays per second [78]. The latter unit is older and not considered a SI-unit, however some materials still use it instead Bq.

Specific activity (SA) is defined as an activity per unit of mass. In context of radiopharmaceuticals the most common unit is MBq/mg (of protein or other vector moiety). A common unit is also MBq/mL of solution, called the activity concentration.

Adsorbed dose is defined as an energy absorbed per unit mass, measured in *grays* (Gy). 1 Gy = 1 J/kg. The older, non-SI unit rad is sometimes also used, predominantly in the USA (1 Gy = 100 rad) [79].

Decay constant: The decay constant λ represents the probability per unit time that a given atom will decay. This phenomenon can be described by exponential decay equation as shown below:

$$N(t) = N_0 e^{-\lambda t}$$

where N(t) is the number of atoms remaining at time t; N_0 is the initial number of atoms; *e* is the base of the natural logarithm.

Half-life ($t_{1/2}$) represents the time it takes for half of the radioactive atoms in a sample to decay [79]. Its relationship with decay constant is given by:

$$t_{1/2} = \frac{\ln(2)}{\lambda}$$

Isotope production

Isotopes for medical applications are obtained in one of the following three ways: in nuclear reactor, cyclotron or generator (**Scheme 6**).

Reactor

- Fission or neutron activation
- $^{98}Mo(n,\gamma)^{99}Mo$

Cyclotron

- Charged particles bombardment
- $^{89}Y(p,n)^{89}Zr$

Generator

- Decay of mother isotope
- $^{68}Ge + e^{-} \rightarrow {}^{68}Ga$

Scheme 6- Production of artificial radioactivity. (Source of pictures: Reactor - AI-generated image; cyclotron - own photo; generator – Eckert-Ziegler web page)

- Nuclear reactor
    - Fission Reactions: Many radioisotopes are produced via the fission of uranium-235 (^{235}U) in nuclear reactors. When ^{235}U undergoes fission, it releases neutrons that can interact with other materials placed in the reactor, leading to the formation of various radioisotopes, including isotopes of iodine, caesium, strontium, xenon and barium [80].
    - Neutron Activation: Another method involves neutron capture, where stable isotopes absorb neutrons and become radioactive. This process can yield high specific activity radioisotopes, which are essential in medical applications. For instance, molybdenum-99 (^{99}Mo) is produced in reactors and decays to technetium-99m (^{99m}Tc), widely used in diagnostic imaging. Interestingly, ^{99}Mo could be produced using both fission as well as neutron activation [81].
- Generator

  This method involves a parent radionuclide that decays into a daughter radionuclide. The parent is typically a longer-lived isotope, and as it decays, the daughter isotope can be extracted for use. The most commonly used isotope, ^{99m}Tc is obtained in generators from reactor-made molybdenum-99. ^{99m}Tc is then eluted for medical use (SPECT imaging). Another example is $^{68}Ge/^{68}Ga$ generator. Gallium-68, used in a range of PET radiopharmaceuticals has relatively short

half-life of 68 minutes, that is why its transportation is unprofitable and requires high initial activity.

- Cyclotron

  A cyclotron is a type of particle accelerator that uses a magnetic field to accelerate charged particles (typically protons) in a spiral path to high energies. These particles are then directed towards target materials to induce nuclear reactions that produce radioisotopes. The primary reactions involved in isotope production include (p,xn) reactions, where protons interact with target nuclei to produce radioisotopes. The energy of the protons typically ranges from 10 MeV to 30 MeV, depending on the specific isotope being produced. Some of the commonly produced isotopes involve ^{18}F, ^{11}C, ^{64}Cu. Fluorium-18 is produced in (p,n) reaction from liquid target: ^{18}O-enriched water ($[^{18}O]H_2O$). This PET isotope of half-life of 110 minutes is used for synthesis of FDG.

As **zirconium-89** is increasingly utilized in PET imaging, and its production methods primarily involve bombardment of yttrium targets, which can be configured as either solid or liquid targets [82, 83]. In the first case, natural yttrium (^{89}Y) is commonly used, undergoing the ^{89}Y(p,n)^{89}Zr reaction, where protons are accelerated and directed onto a solid yttrium disc or foil. This method generally requires higher energy (around 14-14.5 MeV) and longer irradiation times (up to several hours) to achieve significant yield. However, this results in higher production yields (up to 532 MBq) and purer product, in comparison with liquid target methodology. This second technique utilizes yttrium nitrate. Advantage of this approach is definitely improved safety of the operator, as it is usually possible to transfer irradiated liquid directly into the hot chamber, whereas solid target requires entering the accelerator's bunker to retrieve bombarded disc. Another benefit of employing this method is that purification of the target material is more straightforward and can be automated, further reducing radiation exposure. However, liquid target method is able to produce smaller amounts of activity and with lower radionuclide purity. This translates into lower ^{89}Zr concentration in final solution, which may influence the kinetics and efficiency of the labelling reaction.

Outside of different physical properties (decay) radionuclides differ in their chemical behaviour, which forces a highly specialised linker or radio-labelling method. The linker has the function of coupling a target molecule - be it a protein such as an antibody or a simpler and smaller molecule for example a peptide or sugar - to a radioactive isotope. Of particular importance in this function are bifunctional chelators (BFCs), which, in addition to their

metal-coordinating abilities, contain in their structure a functional group capable of attaching to the binding moiety.

2.2.3 Chelators

Many radionuclides used in PET imaging are metallic in nature and are much larger atoms compared to those that are usually the building blocks of organic compounds (carbon, hydrogen, oxygen, etc.). For this reason, introducing them into the structure of the tracer often requires the use of coordination compounds that bind such an atom. Atoms or molecules that are directly attached to the coordination centre in complex compounds are called ligands **in coordination chemistry**. In the light of Lewis's theory of acids and bases in a complex compound, the central atom is the acid (electron pair acceptor) and the ligand is the base (electron pair donor). A coordinate bond, also known as a donor-acceptor bond, is a covalent bond between a central atom and a ligand formed with the shared electron pair. Ligands bonded directly to the central atom constitute the inner coordination sphere, while counter ions balancing the charge of the complex ion are referred to as the outer coordination sphere. In contrast, from a biomedical point of view, a ligand is a compound capable of binding specifically to a receptor (such as the programmable cell death ligand PD-L1 described above). In order to keep the narrative consistent, the term ligand will be understood in a biomedical context (unless clearly stated otherwise). The term chelator will be used to refer to coordination compounds used to complex radiometal atoms.

When selecting or designing chelators for radionuclides several factors must be taken into consideration. Chelator must form a stable complex with the radionuclide, to prevent dissociation *in vivo* and loss of radioactivity from the construct. What distinguishes radiometal coordination chemistry from classical 'cold' metal ion chemistry is the extremely low concentration in the former case. Radiometal ions are generally used at nM to pM concentrations [84]. For this reason, fast complexation kinetics in extremely diluted conditions is crucial for effective radiolabelling process. Another requirement for such a compound is that it can be incorporated easily into the desired molecular target (antibody, peptide or other molecule). Commercial chelators currently on the market most often have moieties capable of readily attaching to amine groups (e.g. isothiocyanate group -NCS) or to a thiol group (e.g. maleimide) that are present in the vehicle molecule. Such chelators, consisting of reactive functional groups for covalent coupling with targeting vectors are BFCs. High thermodynamic stability is preferred to ensure that the complex remains intact under physiological conditions. The introduction of the chelator into the structure must not affect its binding affinity. Although with larger targeting molecules such as monoclonal

antibodies this condition is generally met, it is advisable to monitor the amount of attached chelator and the bioactivity of the bioconjugate [85]. Finally, selectivity of the chelator to chosen radionuclide might be preferred – however, in theranostic application chelator that binds both diagnostic and therapeutic isotope may be useful. In such case, the same molecule would be used for radionuclide therapy and monitoring the treatment with PET or SPECT imaging.

Radiochemists designing new radiopharmaceuticals have an extensive library of BFCs for the most commonly used radioisotopes [86]. Among the most commonly used are DOTA, DTPA, NOTA, DFO, HOPO (**Scheme 7**) and many others.

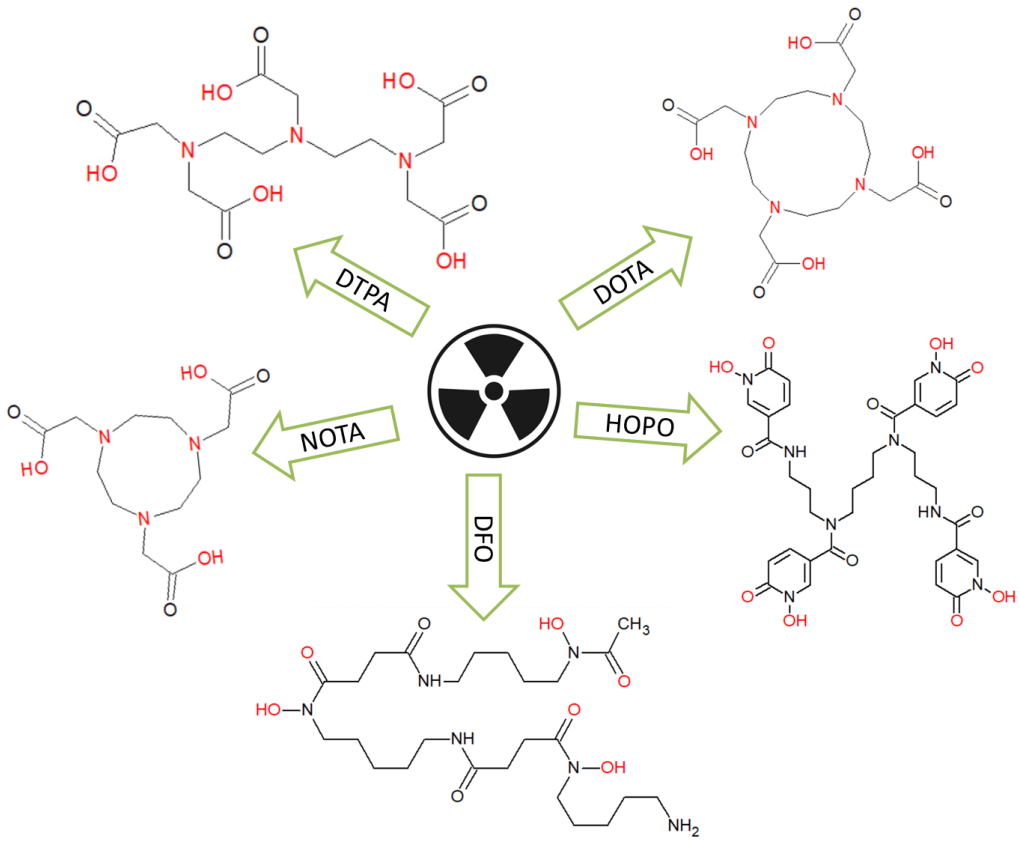

Scheme 7 – Popular chelators for radiometals. Potential coordination sites are marked with red colour.

DOTA (1,4,7,10-tetraazacyclododecane-1,4,7,10-tetraacetic acid) is used to bind several radiometals, including ^{44}Sc, ^{177}Lu, ^{225}Ac, ^{68}Ga and various isotopes of terbium. Its versatility and exceptional *in vivo* stability makes it very good candidate for theranostics, like ^{68}Ga-DOTA-JR11/^{177}Lu-DOTA-JR11 for neuroendocrine tumour imaging and therapy. However, it requires harsh condition for labelling (elevated temperature) which limits its use with biological vectors [86]. Another widely applicable chelating agents from the same family are NOTA (1,4,7-triazacyclononane-1,4,7-triacetic acid) and its modification

NODAGA (1,4,7-triazacyclononane-1,4-diacetic acid), macrocyclic compound most often seen in combination with gallium isotopes and ^{64}Cu or ^{177}Lu, as well as ^{111}In (NODAGA) and ^{99m}Tc (NOTA) [87]. While both chelators form stable complexes with metal ions, some studies suggest that NODAGA may exhibit lower *in vivo* stability compared to NOTA when used in peptide conjugates. This can affect the overall performance of radiopharmaceuticals in biological systems. In context of theranostic application, DTPA (diethylenetriaminepentaacetic acid) also is an attractive candidate, as it binds with a great stability ^{177}Lu and ^{99m}Tc, among others radioisotopes. This allows for monitoring with SPECT imaging the radionuclide therapy, for instance prostate-cancer targeted [88]. DTPA is octadentate, coordinating metal atoms through its three amine and five carboxylic groups, however it can also form stable complexes with metals which favour hexadentate coordination [89]. A macrocyclic chelator that features a spermine backbone with four hydroxypyridinone groups called HOPO (3,4,3-LI(1,2-hydroxypyridinone)) was specifically designed to form stable complexes with ^{89}Zr [90]. HOPO also shows strong binding affinity for actinides such as uranium and americium, which is beneficial for applications in nuclear waste management and decorporation therapies, as well as ferric anions Fe^{3+}[91, 92]. Its structure allows HOPO to act as an octadentate ligands and the hydroxypyridinone groups contain both hydroxyl (-OH) and carbonyl (C=O) functionalities, which serve as effective coordination sites for metal ions. Another chelator suitable to zirconium coordination is DFO (desferroxamine or deferoxamine), chelator of bacterial origin. Its primary application binds iron and aluminium in biochemical processes in *Streptomyces pilosus*. It is very well established in medical application field, as it is used as a chelator in iron poisoning, but it is also found useful as zirconium chelator in various PET tracers.

2.2.3.1 Coordination of zirconium

Zirconium has a half-life of 78 hours and is therefore a good radioisotope for labelling longer-circulating antibodies and nanoparticles. It is metallic in nature, located in the fourth group of the periodic table and forms Zr^{4+} ions. This relatively high charge (in comparison to many common radiometals, which form three-positive ions: Ga^{3+}, In^{3+}, Lu^{3+}) and in consequence: different charge and polarity of chelate-radiometal complex, is one of the reasons for which already established BFC's are not necessarily adequate for this atom. A number of different chelators have been employed to coordinate zirconium, from which DFO and its derivatives have been superior. Complexes of Zr-EDTA, Zr-DTPA and Zr-DOTA have been tested, however they all display some flaws in comparison to Zr-DFO [10]. ^{89}Zr-DOTA, despite promising stability is rarely utilized for zirconium-labelling of mAbs, because its requirement for elevated temperature during labelling conflicts with

the sensitivity of mAbs to such conditions [93]. DOTA coordinates central atom through four oxygen and four nitrogen atoms, EDTA: four oxygen and two nitrogen atoms and DTPA: five oxygen and three nitrogen atoms. As a hard cation, zirconium normally favours anionic oxygen donors and forms complexes with high coordination numbers [94]. For this reason, DFO which consist 3 hydroxamate groups, so 6 coordinating oxygen atoms exhibit preferred stability complexes with zirconium, despite only hexadentate character (in aqueous complexes two water molecules complete the coordination bonding).

To be applicable as a linker in radiopharmaceutical solutions, some modifications to DFO structure are necessary. Firstly, it must be able to easily attach to targeting moiety, through one of the functional groups as described above. The terminal amino group of deferoxamine, which is typically not involved in metal binding, provides a site for chemical modifications. Perhaps the best known example of such a modification is *p*-NCS-Bn-DFO[2], which isothiocyanate group binds readily with primary amine moiety (e.i. lysine groups of antibody) [95]. This approach is straightforward but no site-selective.

Another amine reactive chelator modification of deferoxamine is TFP-*N*-Suc-DFO (2,3,5,6-tetrafluorophenol *N*-succinyldesferrioxamine ester) [11]. It is introduced into the antibody in form of iron complex (Fe-TFP-N-Suc-DFO) and after bioconjugation Fe is removed in reaction with EDTA so the labelling with ^{89}Zr is possible. First ever described bifunctional version of DFO was SATA-DFO (*N*-(*S*-acetyl)mercaptoacetyldesferal) [96]. It showed excellent stability during *in vitro* studies (>99.5% over 24 hours). However, the further *in vivo* studies revealed decomposition of the thioether bond in biological conditions which eliminated the potential use of this system in clinical applications. Zeglis et al. reported on site-specific radiolabelling with ^{89}Zr through modified DFO [97]. This approach involved exposing terminal *N*-acetylglucosamine residues in heavy chain of antibody and introducing azide-modified *N*-acetylgalactosamine monosaccharides into the glycans of the antibody. DFO, modified with dibenzocyclooctane is then incorporated into antibody's structure by catalyst-free click conjugation and whole construct may be radiolabelled in the last step of radiopharmaceutical preparation.

While all the modifications described above concerned the way in which the chelator is attached to the protein, there are also known DFO modifications that alter the way

[2] Depending on the country of manufacture, this compound is referred to as *p*-NCS-Bn-DFO or *p*-NCS-Bz-DFO. Both names refer to N-[5-[acetyl(hydroxy)amino]pentyl]-N'-hydroxy-N'- [5-[[4-[hydroxy-[5-[(4-isothiocyanatophenyl)carbamothioylamino]pentyl]amino]-4-oxobutanoyl]amino]pentyl]butanediamide (CAS number 1222468-90-7). For clarity of the discussion in the rest of this dissertation and in the figures in Table 2, the moiety in question has therefore been designated as C_6H_4.

in which the zirconium atom is coordinated, mainly by introducing additional coordinating groups [85]. Among such modifications, mention should be made of DFO*, DFO-HOPO, DFOcyclo*, DFOSq and choice of tetrahydroxamate variations of this siderophore. All of these derivatives have been gathered along their structures in **Table 2**.

Table 2 - Hydroxamate-based zirconium chelators

Chelator name	Zirconium complex structure	Number and type of coordination bonds	Source
DFO	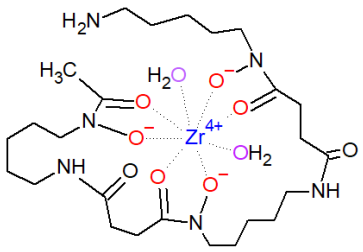	Hexadentate (3 hydroxamate groups)	[98]
DFO*	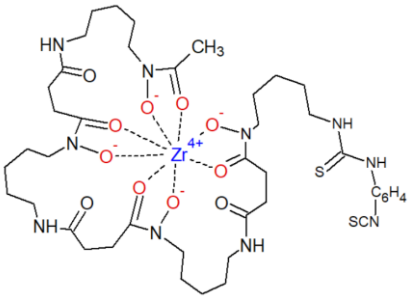	Octadentate (4 hydroxamate groups)	[99]
DFO-HOPO	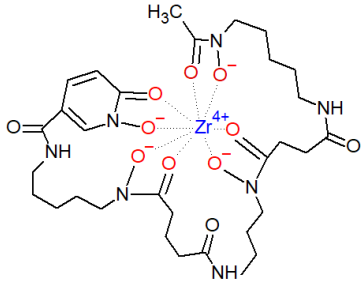	Octadentate (3 hydroxamate and hydroxypyridone group)	[100]
DFOcyclo*	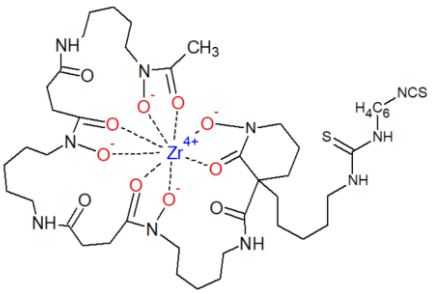	Octadentate (4 hydroxamate, including one cyclic hydroxamate group)	[101]

DFOSq	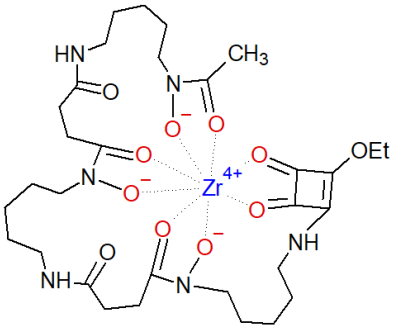	Octadentate (3 hydroxamate and squaramide group)	[102]
DFO*Sq	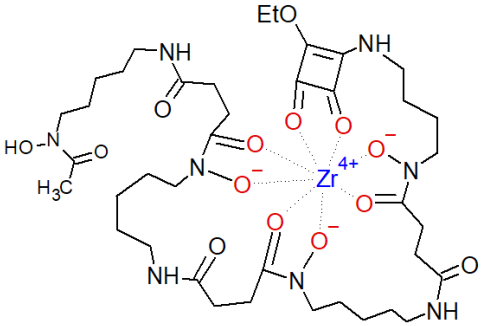	Octadentate (3 hydroxamate and squaramide)	[102]
DFO*Sq	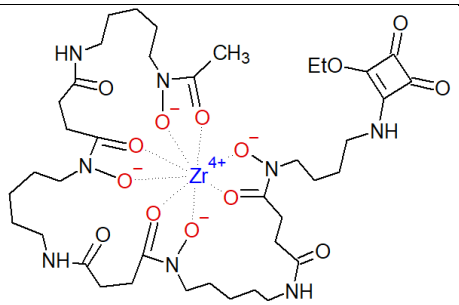	Octadentate (or 4 hydroxamate)	[102]
Iminodi-propiona-mide based tetrahydro-xamate chelators	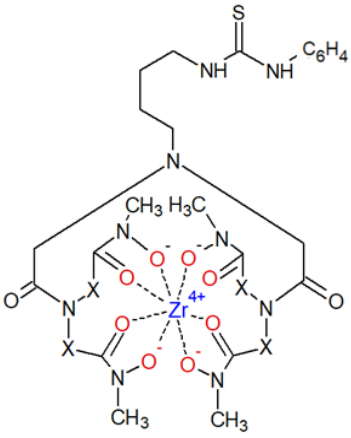 X = CH_2 or CH_2CH_2	Octadentate (4 hydroxamate groups)	[103]

CTH36	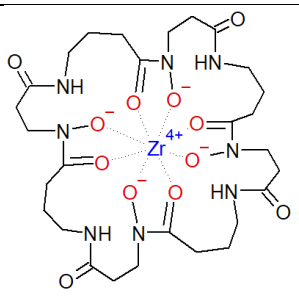	Octadentate (4 hydroxamate groups)	[104]
4HMS	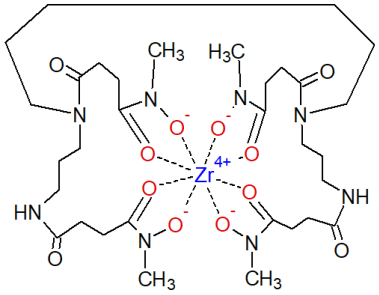	Octadentate (4 hydroxamate groups)	[105]

Vugts et al. reported detailed comparison of octadentate *p*-NCS-C_6H_4-DFO* with *p*-NCS-C_6H_4-DFO [99]. DFO* was synthesized by reaction of DFO mesylate salt with protected hydroxamic acid derivative [106]. After removing the protected groups DFO* was obtained with good yield. Introducing another hydroxamate group allowed two extra coordination bonds to form in complex with zirconium atom. Further biocongujation, labelling and *in vitro* test revealed superior stability of ^{89}Zr-DFO*-mAb in serum compared to ^{89}Zr-DFO-mAb, while maintaining a comparable *in vivo* tumour targeting and blood kinetics. Another octadentate DFO-derivative was obtained by adding a unit of hydroxypyridone moiety to its structure [100]. The final molecule, called DFO-HOPO by authors, also has superior zirconium complex stability compared to ^{89}Zr-DFO, both in EDTA (competitor) and in mouse serum. Raave et al. developed DFOcyclo*, in which basic molecular structure is extended with two coordinating groups by the addition of cyclic hydroxamate moiety [101]. Demetallation studies performed in parallel to DFO and DFO* complexes with ^{89}Zr showed similar stability as DFO*, much higher than of DFO. Derivatives including squaramide moiety were also reported. This functional group performs in those structures both as a linker (in place of NCS moiety) and donor of two extra coordination bonds. Although DFOSq showed slightly improved or comparable *in vitro* stability compared to the basic version of the chelator, the DFOSq* modification gave much better demetalisation resistance, at the level of DFO* and even slightly better [102]. Interesting approach was presented by Rousseau et al. Their proposed chelators, loosely inspired by deferoxamine, are based on iminodipropionamide chain. Two hydroxamate groups are located on both ends of the main backbone. Another two of them, as well as NCS linker

moiety, are attached as side chains. Unfortunately, zirconium complexes of both proposed models showed significant demetallation degree, while injected *in vivo* [103]. Those models were analysed by density functional theory methodology and it was theorized that longer arm length of side chains might improve complex stability. The same method was used by Seibold et al. to design tetrahydroxamate bifunctional chelator CTH36 [104]. Despite excellent stability, tested in presence of competitor EDTA, no further biological results were reported. Of the newer chelators that have not yet been fully investigated and evaluated, 4HMS, whose stability is on a similar level to DFO*, is still worth mentioning [105].

What makes it difficult to interpret the results and compare all available chelators based on hydroxamate groups is that, with isolated exceptions, they are only compared to the basic form of DFO. A thorough comparison of the stability of complexes with zirconium of all described BFCs using one experimental protocol and the same *in vitro/in vivo* model is lacking in the literature.

2.2.4 Nanoparticles as probes and carriers

Nanoparticles (NPs) have emerged as pivotal tools in both imaging and drug delivery, leveraging their unique properties to enhance therapeutic efficacy and diagnostic accuracy. The types of NPs utilized can be categorized based on their composition and application.

Lipid-based nanoparticles are among the most commonly used in drug delivery due to their biocompatibility and ability to encapsulate a variety of therapeutic agents. They include liposomes (spherical vesicles that can carry drugs while mimicking cell membranes, facilitating cellular absorption), solid lipid nanoparticles (composed of solid lipids that provide a controlled release of drugs) and nanostructured lipid carriers (a combination of solid and liquid lipids that improve drug loading capacity and stability) [107].

Another group are polymeric nanoparticles, versatile carriers that can be engineered for specific drug delivery applications. Key types include dendrimers, micelles and polymer-drug conjugates [108]. The former are highly branched (hence the name), star-shaped polymers that can be functionalized with various pending groups, adding therapeutic or diagnostic modality to the structure. Micelles are formed from amphiphilic block copolymers, they can solubilize hydrophobic drugs in aqueous environments [109]. The last group of polymer-drug conjugates involve covalently linking drugs to polymers to enhance solubility and reduce toxicity.

Inorganic nanoparticles are utilized for both imaging and therapeutic purposes due to their unique physical properties. Metallic NPs of gold and silver are used for imaging due to their

optical properties, while abovementioned iron oxide nanoparticles serve as contrast agents in MRI and as drug carriers (those are more extensively described below, in a subsection Magnetic nanoparticles) [107, 110]. Mesoporous silica NPs can be loaded with drugs and used for targeted delivery, also serving as imaging agents due to their tunable properties [109]. The last example of inorganic nanoparticles are quantum dots [108]. Those semiconductor particles exhibit fluorescence; they are primarily used in imaging applications but also show potential in drug delivery systems.

Magnetic nanoparticles, the last group of nanoparticles of medical application, are often made from iron oxide, and possess superparamagnetic properties that allow them to be guided to specific sites within the body using external magnetic fields. This means they can be magnetized in the presence of an external magnetic field but do not retain magnetism once the field is removed. The most commonly used types include superparamagnetic iron oxide nanoparticles (SPIONs), which are effective for both therapeutic and diagnostic applications due to their high magnetic susceptibility and biocompatibility. They are found useful in targeted drug delivery, to enhance the accumulation of drugs at tumour sites, and in imaging applications, serving as contrast agents in MRI [111]. It was also indicated, that tumour cells ability to phagocytize iron particles, can influence its accumulation in affected tissue and thus improve accuracy of tumour diagnosis [112]. Their magnetic and contrast inducing properties are explained in the section 2.3.1. *Contrast agents*. Magnetic nanoparticles have a lower tendency to aggregate compared to larger particles, which helps maintain their circulation time in the bloodstream and prevents complications like thrombosis [113]. They can be modified with various coatings to improve their interaction with biological systems, enhance drug loading capacity, and facilitate targeted delivery based on specific biomarkers [114]. Despite their promise, several challenges remain in the development and clinical application of magnetic NPs. These include issues related to biocompatibility, long-term stability in biological environments, and regulatory hurdles for clinical use. On-going research focuses on optimizing nanoparticle design and functionalization strategies to overcome these challenges and enhance their therapeutic potential.

2.3 Magnetic resonance imaging

Success of PET/CT and desire to decrease radiation dose inspired designing PET/MRI coupled modalities [115]. The technique is based on phenomenon called nuclear magnetic resonance (NMR). Certain atoms exhibit ability to absorb and re-emit radiofrequency energy when placed in strong magnetic field. The feature that allows the

resonance effect of the nucleus to occur is a non-zero spin. Almost all atoms with an odd number of nucleons have such quantum characteristic. These nuclei are characterised by magnetic moment and angular momentum, which in a simplified way can be explained as magnetic behaviour and rotational motion around a magnetic axis. Nuclides that undergo NMR effect are ^{1}H, ^{13}C, ^{19}F, ^{31}P and many more, however these listed above are found most frequently in organic matter therefore most significant in medical application. In practice, MRI scanners are tuned to prot nuclides (^{1}H), as they are most abundant in human body (99.985% of all hydrogen atoms are ^{1}H).

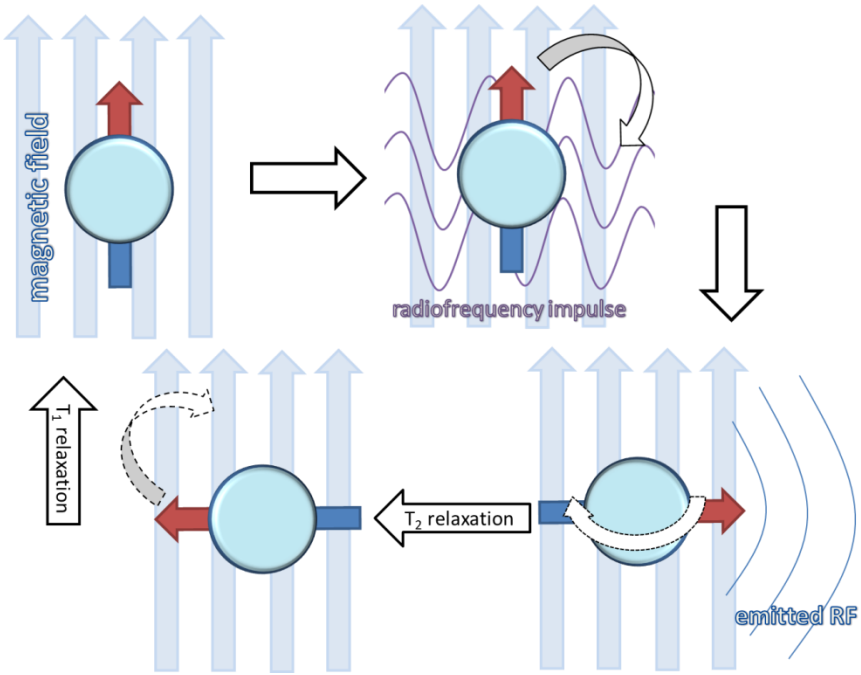

Scheme 8 - Schematic illustration of nuclear magnetic resonance effect

Atoms that undergo NMR behave like magnets in strong magnetic field (B_0) aligning with its direction, and precessing about the magnetic field (**Scheme 8**). Radiofrequency impulse (RF) knocks out nuclei from their equilibrium. Nuclei then precess about their own magnetic field, emitting their own RF signal in the process. The time at which the nuclei emit all the energy gained from the RF pulse is called the **T_2 relaxation time,** also known as spin-spin relaxation or transverse relaxation. The time required for the nucleus to return to its original alignment in line with the magnetic field is called **T_1 relaxation** time (spin-lattice or longitudinal). However T_2 is much shorter than T_1, both processes occur simultaneously, but in perpendicular planes**.** In practice, the process of destabilizing and collecting the signal from nuclei returning to their equilibriums is repeated until enough data is collected to reconstruct the image. Different tissues display different gyromagnetic ratios (γ) hence different relaxation times, which allow differentiating them on the image.

T_1 and T_2 values are dependent on the chemical environment of the sample and the mobility of water molecules there: soft tissue, fat and muscle tissue relax at different rates, yielding the image contrast in a typical scan.

Clinical MRI scanner is constructed in layered manner: most outer part is a magnet, inducing static magnetic field of 10 000 to 300 000 Earth's magnetic field, magnitude of a few Tesla (T) (**Scheme 9**). Middle layer consists of gradient coils, which alter B_0 field produced by electromagnet, allowing localization of RF signal emitted by nuclei undergoing NMR effect, and hence producing images of tissues. Its spatially varying magnetic field is of order of militesla [mT]. It is also used to provide contrast, such as diffusion or flow imaging. Innermost layer consists of RF coil, which produces and receives RF signals, using microtesla [μT] pulses for this purpose.

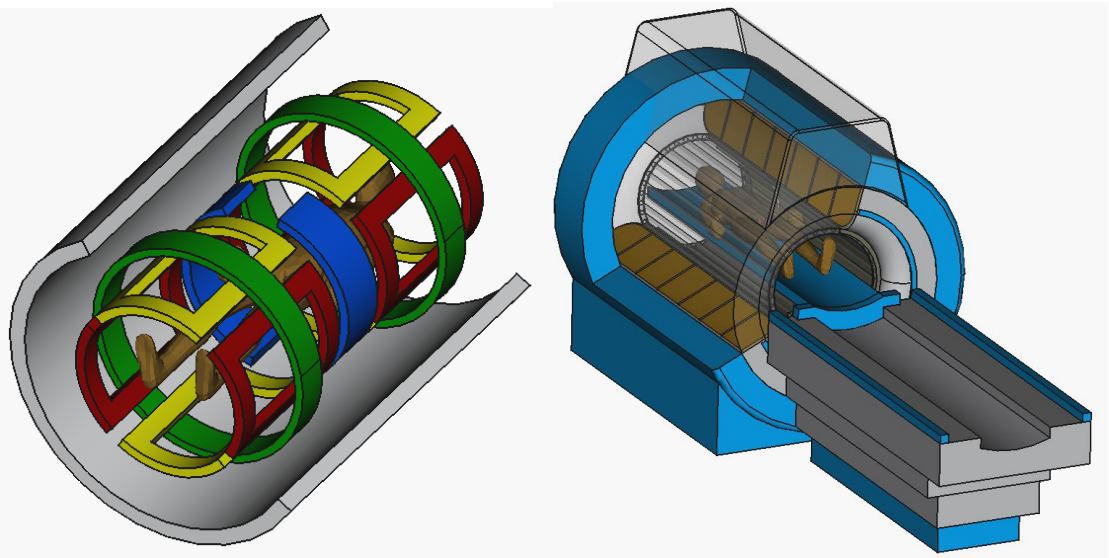

Scheme 9 - Schematic illustrations of an MRI scanner. Left image: positioning of coils in the scanner. Grey torus – electromagnet, green, yellow, red - gradient coils, blue - RF coil. Right image: schematic clinical setting.

Image reconstruction of the collected signal occurs in following way: as protons precess in B (combined resultant of B_0 and the magnetic environment of the resonating atoms), the magnetic flux of RF coil is changing sinusoidally in time, as per formula of $\Phi(t) = \sin(\omega t)$, where **Φ** – magnetic flux, **ω** – precession frequency (Larmor frequency) and **t** – time. Changing magnetic field near coil induces voltage in it, according to Lenz's law, which is than detected as a signal. Detected signal is a sinusoid of amplitude depending proportionally on magnetic field $\mathbf{B_0}$. It follows from Larmor equation $\left(\omega = \gamma \vec{B}\right)$ that protons of different **ɣ** will precess at different frequency in the same magnetic field, influencing frequency of electrical signal. Amplitude **A** (hence intensity) of the detected signal depends then on number of protons being observed, spin's flip angle, gyromagnetic

ratio and magnetic field. With time, protons lose their high coherence of the spin, as their experience not only the external magnetic field but also magnetic field of each of neighbouring protons. Such a dephasing leads to decreased intensity of signal, and sinusoid to decay exponentially. All of the above might be expressed in formula of $S(t) = A\ cos(\omega t)e^{-t/T_2}$; shortly, signal intensity in time **S(t)** depends on its amplitude A, precession frequency and free induction decay (FID), expressed as exponential part of the equation. Protons dephasing more quickly have shorter T_2 – tissues like bones (T_2 = 1 ms) or lungs (T_2 = 0.1 - 2 ms) - in opposition to those more fluid-like, staying in phase for a longer time (cerebrospinal fluid: T_2 = 160 ms; water: T_2 = 1000 ms), with all the other tissues exhibiting T_2 in between this range. To maximize the contrast one may choose appropriate echo time (TE), which is defined by the time between the delivery of the RF pulse and the peak of the signal (echo) received. This method of producing tissue contrast based on signal decays in different tissues is called T_2-weighting, and an imaged produced goes by the name of T_2-weighted image. Acquired signal needs to be reconstructed in order to obtain an anatomical map of the body. Frequency encoding is a reconstruction method which works by applying a gradient magnetic fields, which cause the resonance frequency to vary in a predictable pattern based on the position within the imaging slice. Shortly, signal emitted by nuclei vary in frequency, depending on the magnitude of magnetic field they are in. FID is detected as the sum of electrical signals of different frequencies and through the use of Fourier transform it is possible to subdivide it to initial components. Transforming FID gives an information of $V = f(\omega)$, instead of $V = f(t)$. In the context of MRI, each frequency corresponds to a specific position in space. In order to distinguish between these locations magnetic gradients are introduced in MRI machines.

First, gradient magnetic field $\overrightarrow{G_z}$ is superimposed on the main magnetic field, resulting in a $\vec{B}$ field, which induction increases linearly with increasing z-coordinate (in coronal plane). Slice selection is achieved by applying the RF impulses of ω_0, which induce resonance only in a given layer of the body (where the value of the field B_0 complies with Larmor's condition). The centre resonant frequency of entire slices would vary linearly as a function of position. The thickness of the resonance-sensitive layer depends on the size of the gradient and the width of the RF pulse – stronger gradient and longer RF impulse would give thinner slices, hence more accurate image.

To obtain an image of protons distribution in selected layer, one has to induce additional frequency-encoding and phase-encoding gradients in a given slice in the remaining two planes. Within a single plane selected by the $\overrightarrow{G_z}$ gradient, applied is the $\overrightarrow{G_y}$ field gradient

in the y-axis direction results in a resonance-sensitive line (row of pixels). This gradient causes the resonant frequency of the protons in this axis to vary, allowing the location of the protons along the y-axis to be determined, as each point in this axis has a unique frequency. The last step allowing localization of a single volume unit (voxel) in the x-axis is called phase encoding. After applying a frequency gradient, a magnetic gradient along the x-axis is applied. This gradient causes the phase of the resonant signal of the protons to change and different points along this axis have different phase shifts. By analysing the phase shifts in the received signal, the position of the protons in the last dimension is determined. Each voxel of such an image represents how quickly protons dephased with each other, creating anatomical map of the different tissue in the body.

T_1 relaxation is significantly longer than process of dephasing. Slow realignment of protons with magnetic field shows on the magnetization graph as a hyperbola tending towards M_0 (Boltzmann magnetization), at the rate determined by T_1, following the equation: $M(t) = M_0(1 - e^{-t/T1})$. T_1-weighted images rely on differences in T_1 relaxation in each tissue. Again, the optimal contrast depends on the time of the magnetization measurement, in this case called repetition time (TR). Whereas TE is the amount of time the scanner waits following spin excitation to detect the signal, TR is the amount of time the scanner waits in between excitation.

To obtain an image of satisfactory quality the process of excitation and relaxation of the process has to be repeated numerously until enough data is collected. MRI scan in clinical setting depends on the organ or part of the body being imaged, but typically it would last 30-60 minutes, with skeletal system and joints on the shorter side of the scan time, and the brain, cardiac system or abdomen taking up to two hours to perform a scan.

The advantages of MRI over X-ray imaging are its better sensitivity in the case of soft tissues (nervous, vascular or gastrointestinal systems) and the lack of exposure to ionising radiation, as opposed with the latter method. Spatial resolution depends heavily on various parameters of exact scans; namely: field of view (FOV), matrix size and slice thickness for MRI and FOV, focal spot /pixel size and pitch for CT [116]. Resolution of magnetic resonance imaging can go as low as 100 μm, however for full body scans it is usually in a range of 1 – 2 mm [117, 118]. CT scans are generally superior to MRI in terms of resolution (0.3 – 0.6 mm) [119].

2.3.1 Contrast agents

Even though scanning and image reconstruction described above is enough to obtain anatomical map of the body, frequently to enhance the diagnostic value of this modality the contrast agents (CAs) are used [120]. MRI Cas primarily function by affecting the relaxation times of water protons in tissues. They improve the visibility of internal structures, helping to differentiate between normal and abnormal tissues. The effectiveness of these agents is characterized by a property known as relaxivity, which varies depending on the chemical structure of the agent [121, 122]. These agents are paramagnetics or superparamagnetics, accelerating the polarisation decay of protons through a self-generated, oscillating magnetic field that affects the protons being imaged. This means, that when resonance scan is performed, the contrast agents itself are not directly recorded, but they influence their closest, surrounding water protons.

Paramagnetics are characterised by magnetisation in the direction of the external magnetic field when they are in it [122]. Superparamagnetics, on the other hand, are nanoparticles composed of paramagnetic crystallites. In the presence of a magnetic field, their behaviour resembles that of paramagnetic materials. However, while paramagnetism involves the magnetic moments of individual atoms responding to the field, superparamagnetism affects the magnetic moments of entire molecules or crystallites. The magnetic properties are caused by the presence of unpaired electrons in atoms such as Dy, Gd, Mn or Fe (4, 7, 5 and 5 unpaired electrons, respectively). These elements are most commonly used as Cas in magnetic resonance imaging technique. Following the separation into para- and superparamagnetics, contrast agents will therefore be divided into those based on lanthanides (paramagnetics; gadolinium, dysprosium) and on transition metals (superparamagnetics; iron, manganese mainly in the form of nanoparticles).

The most commonly used are gadolinium-based Cas (GBCAs), which play a crucial role in various diagnostic applications. GBCAs are paramagnetics so primarily, in low concentrations, they shorten the T_1 relaxation time of protons in tissues where they accumulate, resulting in brighter images on T_1-weighted MRI scans, and thus they are called positive contrast agents. As the concentration of the contrast compound increases, there is a T_2-shortening effect, darkening the contrasted areas, giving a so-called negative contrast. Unfortunately, as the concentration of the paramagnetic substance rises, the toxic effect on the body also increases. In the case of gadolinium-based compounds, their harmful effects on the excretory system have been well documented. Their use, particularly in patients with compromised renal function, raises significant concerns due to the risk of nephrogenic toxicity and the development of nephrogenic systemic fibrosis [123, 124].

To reduce these risks, newer GBCAs have been developed in form of chelates with increasingly stable hydrophilic or lipophilic complexes, such as Gd-DOTA, Gd-DTPA or Gd-BOPTA. Gadolinium(III)-based contrast agents follow into three categories: extracellular fluid agents, blood pool contrast agents and organ-specific agents.

A measure of a CA's ability to influence relaxation is relaxivity (r). It describes the relationship between relaxation times and CA concentration as follows: $\frac{1}{\Delta T_x} = r_x \cdot C$, where ΔT_x is a change of a given relaxation time (T_1 or T_2) and C is a concentration in mmol/L. Unit of relaxivity is then $L/mmol \cdot s^{-1}$. Relaxivity r is often used to describe CA's ability to improve contrasting; however it should be completed with the information of temperature and magnetic field strength used in measurement. Ratio of r_2/r_1 is often used to assess character of CA. Those demonstrating values in range 1-2 are considered good positive contrasts, as T_2 effects do not disturb image brightening, characteristic for positive CAs. Useful negative contrast should express r_2/r_1 of at least 20 [125].

Magnitude of contrast-induced relaxation is directly connected to number of adjacent water molecules coordinated to the paramagnetic centre *q* and residence lifetime τ_M, as presented on **Scheme 10**. This can be explained as a rate of water exchange near the coordination centre. Another factor influencing relaxivity is τ_R, which is the time needed for the change in orientation of the metal – proton vector [126]. Lastly, CA's longitudinal or transverse electronic relaxation times (T_{1e} or T_{2e} respectively) add up to the above-mentioned factors in affecting the proton relaxivity of gadolinium-complexes.

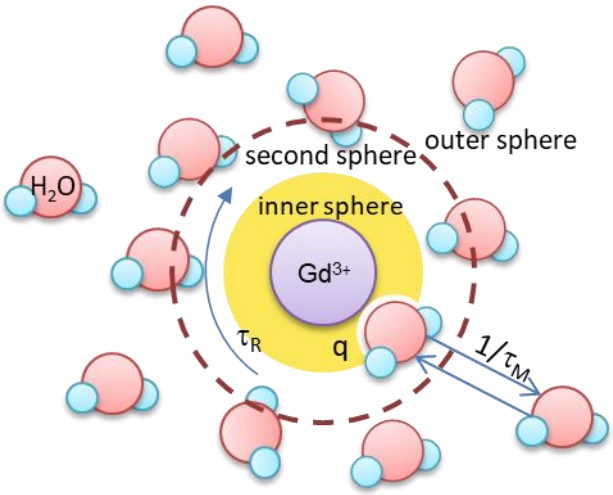

Scheme 10- Influence on relaxation of gadolinium-based contrast agents.

However, some more intricate mechanism has also been employed to T_1-weighted imaging. Receptor-induced magnetization enhancement (RIME) is a novel approach that utilizes specific receptor interactions to enhance the relaxivity of GBCAs (**Scheme 11**).

This technique aims to improve the sensitivity and specificity of MRI by leveraging biological interactions, making it particularly useful in detecting diseases at an early stage. The RIME effect is based on the principle that certain biological receptors can induce a change in the magnetic properties of gadolinium (Gd^{3+}) complexes when they bind to specific target molecules. This interaction leads to an increase in the longitudinal relaxivity (r_1) of the CA, enhancing the MRI signal in areas where these receptors are present. RIME allows for the development of targeted MRI contrast agents that can selectively bind to specific tissues or cells, such as cancer cells or inflamed tissues.

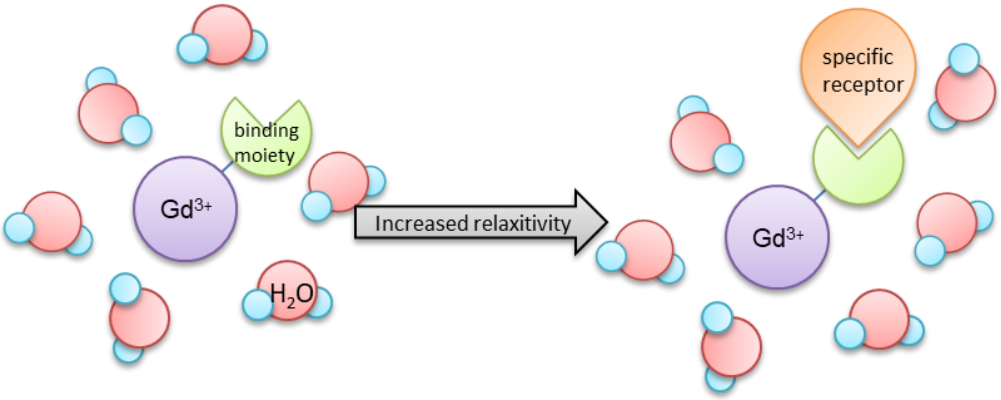

Scheme 11- RIME effect.

Two primary classes of iron oxide contrast agents exist: superparamagnetic iron oxide nanoparticles (SPION) and ultrasmall superparamagnetic iron oxide nanoparticles (USPION). Superparamagnetic CAs comprise colloidal suspensions of iron oxide nanoparticles. The crystallites consist of a core of nonstoichiometric metal oxides (usually iron), covered with a coating such as dextran, citrate, oleate, or other nonimmunogenic polymers to prevent aggregation and reduce toxicity. When exposed to an external magnetic field, the crystallites align with the field, creating a superspin that magnetizes the material [127]. The total spin of the particle significantly exceeds the sum of the individual metal ion spins, resulting in high relaxivity. Without the applied field, the material loses its magnetism. The initial superparamagnetic contrast agents exhibited high r_2/r_1 ratios and predominantly influenced T_2, hence were called T_2-agents or negative contrast agents due to their tendency to produce darkened MR images. However, numerous superparamagnetic iron oxide particles also possess substantial r_1 and can act as effective T_1 or T_2 CAs. While the contrast agent reduces T_1, the effect on T_2 is significant. The large magnetic moment of superparamagnetic relaxation agents generates local magnetic inhomogeneity and shortens the T_2* of tissues, causing signal loss in gradient echo T_2^*-weighted images. When these agents are employed in imaging procedures, they diminish the intensity of T_2 signals within tissues that accumulated the contrast material. The nanoscale dimensions and

specific morphologies of these contrast agents facilitate distinct biodistribution and applications that are not typical of other types of contrast agents.

2.4 PET/MRI bimodal probes

Techniques such as PET, CT, MRI, SPECT and OI (mentioned or extensively discussed in previous chapters) allow visualisation and description of physiological and pathological processes occurring in the body. Each of these modalities requires high-tech equipment, and often the pre-imaging administration of a substance that enables (PET, SPECT and OI) or facilitates (MRI, CT) the acquisition as a result of linking the signal to a molecular event. Also, each modality, due to its characteristics, has an advantage over the others in some aspect, but also carries its imperfections such as low sensitivity (CT) or spatial resolution (SPECT), dose of ionising radiation (PET, CT), long examination time and limitations for patients with pacemakers or other magnetic elements in the body (MRI). To reduce the negative features and improve the quality of the diagnostic process by complementing each other, a common technique is to combine the two modalities.

Recent developments in new contrast compounds, hybrid scanner technology and image reconstruction algorithms have significantly accelerated the introduction of this combination of modalities into routine use. This has prompted the need for a bimodal agent that will fulfil the function of paramagnetic contrast and PET radiopharmaceutical in the form of a single substance. An interdisciplinary army of scientists has begun to develop and test a variety of modifications and systems, including bioresponsive probes that respond to specific tumour microenvironments or supramolecular constructs that target specific receptors.

2.4.1 Probe preparation

In order to obtain such intricate molecules like bimodal probes requires multiple synthesis steps. Preparation of the nanostructure, surface functionalisation introducing vehicle moiety and radiolabelling is often a long, multi-step process. The more reaction steps, the more time the operator requires and this can affect reproducibility, which is why modular and one-pot synthesis is gaining popularity due to the short time to prepare the tracer and low cost.

Bioconjugation

The concept of personalized and targeted drugs relies deeply on highly specific bioconjugates. Process of bioconjugation is understood as attaching bioactive molecule (usually antibody or its fragment) to a different compound [128]. The effect of this process is creation of a new

compound, having the combined properties of each constituent, not normally found among naturally occurring substances. Bioconjugation is usually carried out using crosslinking agents or by the presence of a proper reactive group on one of the substrates to enable conjugation. A common practice is to use an agent that activates a functional group present in the structure to a more reactive form (e.g. an amine into an imide). Most of the reactive groups used in this process can then be combined with specific functional groups on one or more of the molecules to be conjugated. Among typical reagents for bioconjugation reactions there are: Sulfo-SBED, SATA, EDC, FITC, Sulfo-SMCC to name just a few. For the bioconjugation reactions one can choose from couple dozens of reactive functional groups, the most popular of which are primary amines, sulfhydryls, carbonyls, thioethers and imidazolyl groups, used in overwhelming majority of conjugates created.

The modification of SPIONs using EDC (1-ethyl-3-(3-dimethylaminopropyl) carbodiimide) as a coupling agent can lead to challenges, particularly concerning precipitation issues. EDC is often used to activate carboxyl groups on the surface of nanoparticles, facilitating the attachment of amine-containing molecules. This process can enhance the functional properties of SPIONs for various applications, including drug delivery and imaging [129].

Surface functionalization

Designing NPs to enhance tumour targeting for contrast agents and therapeutic drugs is a significant challenge in the field of nanomedicine [130, 131]. The pharmacological behaviour of NPs is influenced by their physical and chemical properties. Targeting efficiency rely on NP circulation time and tumour permeability, with both properties dictated by the coating type and particle size [132]. Adding vehicle molecule or chelator are also functionalization of the nanoparticle surface, however, they have been broadly described in other parts of this work. Various polymers, like dextran and polyethylene glycol (PEG), are utilized to modify magnetic NPs, leading to extended circulation times [133, 134]. PEG, known for being uncharged, highly hydrophilic, low in toxicity, and low in immunogenicity, renders these PEG-coated NPs "invisible," making them appealing for biomedical use. Despite the advantages of PEG, there are concerns about its non-degradability, product heterogeneity, and the accumulation of large linear PEG chains in the liver. Dextran coating also increases biocompatibility and stability in water. Attaching drug molecule to the nanoparticle adds therapeutic function. Common functionalization includes doxorubicin and other cytostatic drugs [135]. A study suggest that manipulating the composition of coating may improve SPION's permeability of blood-brain barrier (BBB), which gives promising perspective in bimodal PET/MRI imaging of neuro-oncological diseases [136].

Radiolabelling

Radiolabelling is a key step in the preparation of a radiopharmaceutical or multimodal probe involving radioisotope. It must be carefully planned in the process of obtaining the probe and carried out with great care in order to comply with the ALARA principle (as low as reasonably achievable, a basic principle of radiological protection, referring to the safety of personnel working with ionising radiation). The following methods of introducing a radioactive isotope into the structure of a compound have been described in the literature:

- During modular or single-pot synthesis

  Interesting example of this approach would be ferritin-based multimodal probe described by Yang et al [137]. This protein reversible ability to assembling and disassembling with pH change have been utilized in the process of loading its structure with ferric anions for MRI contrast, ^{64}Cu for PET signal and melanin nanoparticle (acting as both photoacoustic and chelating agent for Cu and Fe). Although relatively easy and not requiring many synthesis steps, such processes usually tend to have low reaction yields and poor repeatability. In this particular example, concern of increased cytotoxicity aroused, as disassemble of ferritin occurs in low pH. TME usually has lower pH than physiological standard, so it may cause the isotope or paramagnetic agent to escape from the structure.
- Physical absorption on the surface of the nanoparticle/polymer

  In this chelator-free approach isotope is attached directly to the surface of modified substance. An example of this methodology is heat-induced radiolabelling (HIR) of ^{89}Zr, ^{64}Cu or ^{111}In into feraheme (dextran coated iron oxide nanoparticles) [138-140]. Another example is germanium-69 introduced into the iron oxide, making it possible to prepare PET/MRI probe with this relatively exotic radionuclide [141].
- Through chelating agent introduced into structure

  The types of chelators and the basics of coordination are comprehensively described above. Importantly, however, in the context of bimodal probes, the introduction of a chelator into the structure is another step in the synthesis of the compound and is associated with lower overall process yields, often necessitating a change in the reaction environment. It is also highly advisable to determine the degree of functionalization, i.e. the number of chelator units introduced per tracer molecule. In this way, it is possible to control the progress of the reaction and to select the appropriate molar ratio of isotope and paramagnetic. All these steps affect

the complexity and time of compound preparation, which translates into availability and cost.

- Covalent bonding of non-metal radioisotopes

  As mentioned before, fluorine-18 is the most commonly produced and used PET isotope, but is rarely used in the context of bimodal PET/MRI probes. This is probably due to its short half-life, mismatched with the longer circulation times that larger structures (nanoparticles, antibodies) customarily employed for such applications. Nevertheless, introducing fluorine-18 into molecular structures can be quite challenging due to several factors related to its chemical properties and the conditions required for successful incorporation. Due to its half-life of 109 minutes reaction needs to be timely efficient (preferably less than 30 minutes). Nucleophilic character of $^{18}F^-$ anion requires typically aprotic solvents like DMSO or acetonitrile (MeCN) for nucleophilic substitution to occur, as well as decreased pressure and high temperature. Such harsh conditions may hinder the use of biomolecules that will not be resistant to such high temperatures.

Due to the specific nature of the radiolabelling reaction, it is generally the final stage in the preparation of a bimodal probe. However, as repeatedly pointed out, some methods require the use of elevated temperatures, which can damage the structure of more complex proteins. To overcome this problem, a twofold solution can be used. The first approach is to reverse the order of modification: labelling requiring elevated temperature is performed before bioconjugation. In this method, an essential aspect is that the half-life of the isotope is long enough to allow further modification to take place without losing a significant proportion of radioactivity. The bioconjugation process itself should also be as short as possible and not require repeated purification, which would expose the radiochemist to elevated exposure to ionising radiation. A second approach is pretargeting - an innovative strategy in radiopharmaceuticals that separates the processes of tumour targeting and radiolabel delivery, enhancing the efficacy and safety of imaging and therapeutic applications [142]. This concept requires two steps, first being administration of a tumour-targeting agent, often a bispecific antibody or a macromolecule. This agent binds specifically to antigens expressed on tumour cells. After allowing sufficient time for the targeting agent to localize in the cancer and for unbound agents to clear from circulation, a radiolabeled small molecule (the effector) is injected. It interacts with the targeting agent, leading to enhanced accumulation of radioactivity in the diseased tissue while minimizing exposure to healthy tissues. Various pretargeting mechanisms have been developed, including bispecific antibody-hapten systems, streptavidin-biotin systems

or 38iorthogonal chemistry [143]. Separating the targeting and imaging steps, pretargeting can achieve higher tumour-to-non-tumour ratios compared to direct labelling methods [144]. What is also of high importance, by minimizing the time that radioactivity is present in circulation before binding to the target, pretargeting can lower the overall radiation dose received by patients. This method however requires two injections, which may be uncomfortable for the patient, and require precise optimization of dosages and timing intervals between injections. Pretargeting strategies are being explored for both diagnostic imaging (e.g., PET scans) and therapeutic applications (e.g., RT) [143].

2.4.2 Application issues

2.4.2.1 Cytotoxicity

Although the advantages of MRI as a relatively safe form of diagnosis (non-invasiveness, absence of ionising radiation) have been highlighted above, contrast agents administered to enhance the diagnostic quality of the acquired image can have harmful effects on the body. Gadolinium-based contrast agents have confirmed toxicity in terms of nephrogenic system fibrosis. For this reason, it is necessary to follow guidelines to limit this effect. Despite these preventive measures, there are reports of accumulation of this lanthanide in the body, including in the brain. Turning to iron-based CAs was motivated, among other things, by the desire to eliminate this toxicity effect. However, oxide-based nanoparticles can induce local and systemic inflammation, genotoxicity or oxidative stress, with the intensity of the effect depending on the size, coating and even the method of synthesis of these constructs.

In the context of bimodal probes, it is important to consider the construct as a whole, as the final cytotoxic effect is not necessarily the simple sum of the cytotoxicity of the individual probe components. Examples of bimodal probes described in the literature are generally deliberately modified for enhanced biocompatibility, but their *in vitro* and *in vivo* properties are difficult to predict and must be confirmed experimentally. The need to compare the cytotoxic effects of bimodal probes described in the literature is difficult to fulfil, as the available data often lack information on the molecular weight of the probe. For this reason, it is impossible to convert the molar concentration into the mass of the potentially toxic substance. In general, many nanoparticle-based construct are reported to be relatively safe in terms of toxicity: several studies have reported that specific formulations of iron oxide nanoparticles used as bimodal PET/MRI probes exhibit minimal to no cytotoxic effects. For instance, research on Fe_3O_4–LDOPA–PEG–MANOTA nanoparticles showed that even at high concentrations (up to 300 μg/mL), cell viability

remained around 80-90%, comparable to control groups with no exposure to the nanoparticles [134]. Moreover, the mitochondrial enzymatic activity in liver cells (HepG2) was maintained after exposure to functionalized iron oxide nanoparticles, suggesting that these particles do not significantly impair cellular metabolic functions. This indicates a favourable safety profile for these nanoparticles *in vitro*. However, a little older report showed decreased viability (up to 50% in the conditions of highest iron amount) of a magnetite-based tracer of double PET/MRI modality [145]. However, this case is hard to compare with other as it reports amount of Fe used in cytotoxicity test and not its concentration.

To date, no construct containing a paramagnetic and a PET isotope has been approved, and even clinical trials of such a compound are not on-going. This is certainly indicative of the myriad difficulties encountered in the course of work to synthesise, optimise and determine the *in vitro* and *in vivo* behaviour of such constructs. A thorough and detailed understanding of the cytotoxic effects is a necessary and next step for the introduction of such compounds into the clinical routine.

2.4.2.2 Dose

For bimodal probes that combine PET and MRI, the doses must be optimized to ensure that both modalities can detect the probe effectively, while bearing toxic effects as low as possible. The balance between achieving sufficient imaging contrast and minimizing potential side effects is essential. The doses of injected radiopharmaceuticals in PET imaging are in the nanomolar range, which is several orders lower than that of contrast agents for MRI (c.a. 0.1 mmol/kg). This ratio should be taken into account when designing a bimodal probe. This dose of magnetic compound is a compromise between expected contrast enhancement and safety, but may not be sufficient at low magnetic fields. On the other hand, too high a concentration of CA (of the order of ~2 mmol/kg) may lead to contrast deterioration due to T_2 effects, not to mention potential toxicity. For this reason, compounds with one atom of magnetic substance per atom of radioisotope (as reported by Desbois et al. [146]) may not be useful for *in vivo* studies. A potential solution is to design particles that contain a core of magnetic substance and, on their modified surface, attach a correspondingly smaller amount of radionuclide [134]. This way also opens up other possibilities, such as modifying the surface by attaching drug particles or molecules that affect solubility or dispersibility. Ongoing research aims to refine dosing strategies further and explore new formulations of bimodal probes that could enhance imaging capabilities while reducing required doses. Meanwhile, biodistribution studies are crucial

for determining how well these probes localize in target tissues, which influences the dosing strategy.

2.4.2.3 Distribution, accumulation, clearance

The clearance of bimodal probes is primarily influenced by the particle size. Molecules that are smaller (≤ 60 kDa) are rapidly eliminated by the renal system, while larger molecules (≥ 60 kDa) exhibit prolonged circulation times and are cleared *via* the hepatobiliary system [147]. It is crucial for the conjugate to circulate sufficiently to reach the target region while swiftly clearing from normal tissues. Due to their substantial size, SPION-based bimodal probes remain in the vascular system for several hours, leading to significant accumulation in the liver and spleen, whereas gadolinium (Gd) complexes are quickly excreted through the kidneys.

Pharmacokinetic studies typically extend up to 48 hours, wherein mice are sacrificed and their organ-associated radioactivity is measured using a ɣ counter [133, 148]. Some studies have explored longitudinal clearance (up to six days) of bimodal probes, offering limited insight into their *in vivo* behaviour.

3. Research

3.1 Aim I – Development of novel DFO-based chelator for zirconium coordination

As described above, chelation of the zirconium(IV) cation by DFO proceeds using six coordination sites of the chelator and complementing the coordination sphere with two water molecules (**Scheme 12**).

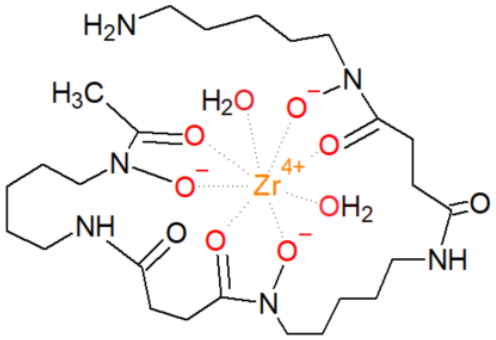

Scheme 12- DFO coordinating zirconium (IV) atom.

Many attempts were made to design and synthesize octadentate DFO derivatives, in hope that it would improve the Zr(IV) chelates stability. Majority of these proposed modification to DFO structure involve introduction of fourth hydroxamate group, filling coordination sphere with two additional coordination sites. In this work, entirely different approach has been taken – bisphosphonate group introduced to the deferoxamine structure would fill coordination sphere with two "missing" coordination sites (**Scheme 13**). This entirely novel attempt to synthesize more stable chelator for zirconium is inspired by propitious properties of bisphosphonate group.

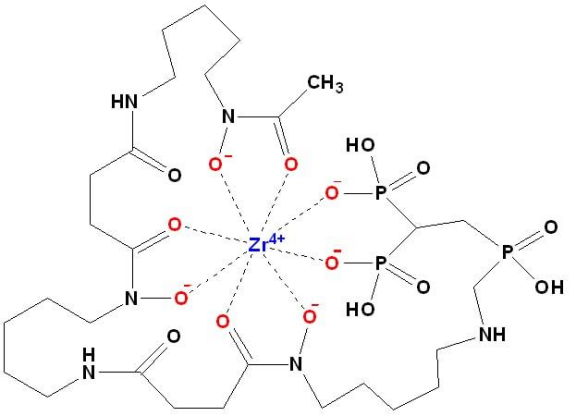

Scheme 13– Hypothetical bisphosphonate-modified DFO coordinating Zr(IV) atom.

Bisphosphonate group (BP) is known to have high bone affinity, as it forms very stable complex with calcium ions of hydroxyapatite [149]. Its excellent chemical stability (including resistance to enzymatic breakdown) is a consequence to the P-C-P bonds in the structure. Those features resulted in wide application of this class of chemical compounds, varying from bone disease therapy (including treatment of osteoporosis [150] and metastatic bone cancers [151], among many others), drug delivery with bisphosphonate group as a targeting vehicle [152], to the chelation of metal atoms [153]. It is worth noting, that despite some reports on BPs as chelating agents, this moiety has not been yet used in radiometal chelators. Moreover, bisphosphonates behaviour *in vitro* and *in vivo* has been extensively studied and this group of compounds is well established in clinical practice. All of the above led to the conclusion, that modifying DFO with BP might result in obtaining new chelator for ^{89}Zr of improved complex stability.

3.1.1 Synthesis of bisphosphonate-modified deferoxamine

3.1.1.1 Modification with H-phosphonate

Initial approach for synthesis of bisphosphonate-modified deferoxamine (DFO-BP) was inspired by work of Vitha et al [154]. In that study, BP group was introduced to the chelator DOTA, in order to add bone-seeking ability to the compound (**Scheme 14**). The resulting molecule would consist of Gd atom coordinated with bisphosphonate-DO3AP chelator (modified DOTA), finding its application as a bone targeting MRI CA.

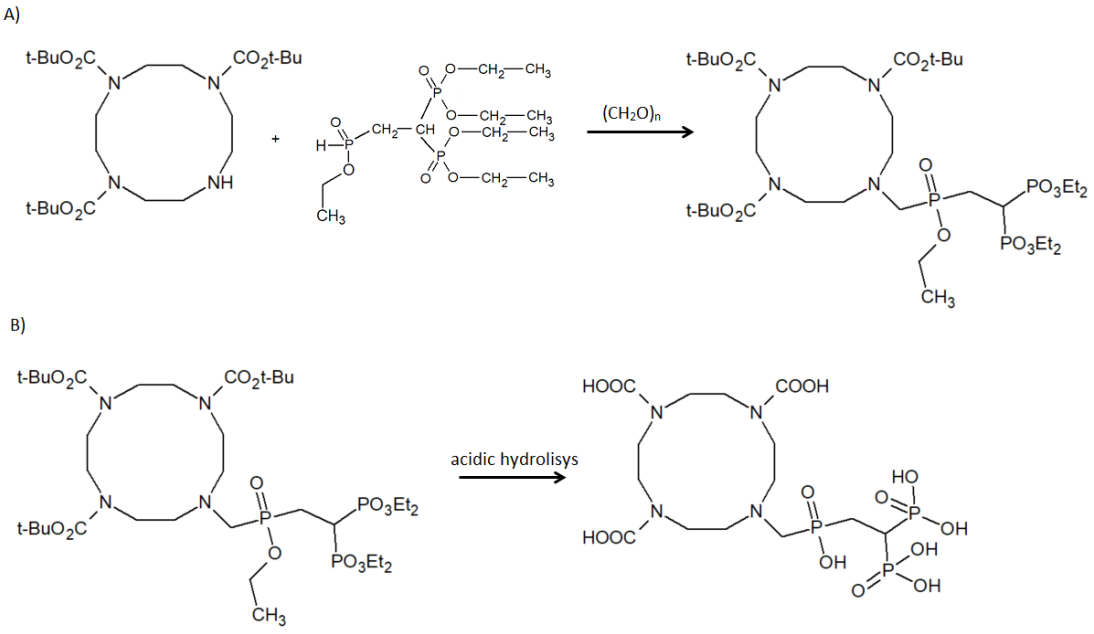

Scheme 14 - Synthesis of bisphosphonate-modified DO3A. A) Mannich reaction B) acidic hydrolysis

Based on this approach, DFO-BP synthesis was planned in three main process steps: (1) synthesis of an H-phosphonate containing a protected bisphosphonate group; (2) Kabachnik-Fields (phospha-Mannich) reaction, introducing the bisphosphonate group into the chelator structure; (3) hydrolytic deprotection of the bisphosphonate group.

Synthesis of H-phosphonate

H-phosphonates are esters or salts of phosphonic acid, containing the characteristic O=P-H system. They undergo the Mannich reaction, which in this variant is called the Kabachnik-Fields reaction. For the purposes of the present work, an H-phosphonate containing a bisphosphonate group was synthesised. Synthesis details of the tetraethyl[[(ethoxyhydrophosphoryl)methyl]methylene]bis-(phosphonate) (compound **G**) preparation process were adapted with minor modifications from the literature and are described in details in subsection 4.3.1 [154, 156]. Briefly, tetraethyl ethenylidenebis(phosphonate) (compound **B**) was prepared in reaction of substrate tetraethyl methylenebis(phosphonate) **A** with paraformaldehyde and diethylamine in methanol, and involved addition of ether-pendant into **A**. In the elimination reaction, ether group was then transformed into unsaturated C=C bond. Then the resulting intermediate product **C** was reacted with ethyl hypophosphinate **F** prepared *in situ* (**Scheme 15**). Final product was then analysed and purified.

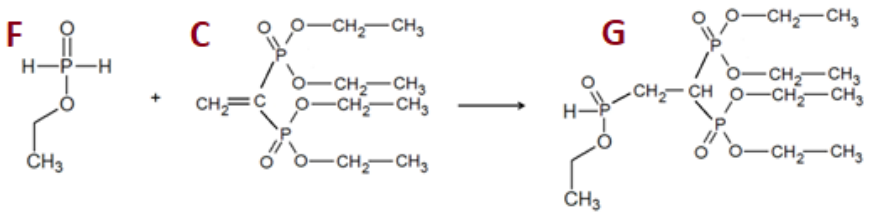

Scheme 15– Synthesis of G

Synthesis of tetraethyl ethenylidenebis(phosphonate)

Tetraethyl ethenylidenebis(phosphonate) **C** was prepared in two-step process. First step involved reaction of tetraethyl methylenebis(phosphonate) (substrate **A**) with paraformaldehyde and diethylamine in methanol, like presented in **Scheme 16**, in order to obtain intermediate product **B**.

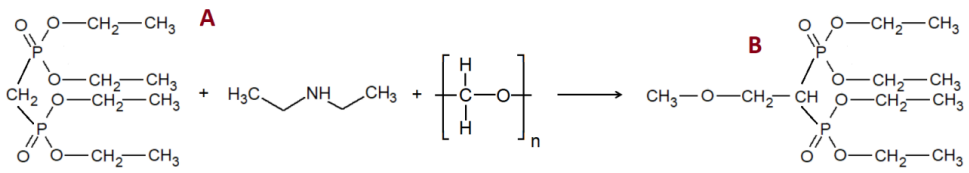

Scheme 16– Preparation of intermediate compound **B**.

The progress of this reaction was monitored by thin layer chromatography (TLC). Based on this assay, the reaction was either terminated to evaporate the solvent and collect the sample for NMR, or was left to react further. The stain originating from the bisphosphonate substrate appears at about 2/3 of the height. A sample from the reaction mixture showed stains from diethylamine (starting line), bisphosphonate substrate and intermediate **B** (about 1/2 of the height). The presence and intensity of **B**-derived stain was an indicator of the reaction progress.

To determine the degree of reaction yield, ^{1}H-NMR spectra were obtained after removing methanol. Sample of reaction mixture was dissolved in $CDCl_3$ and measurement was performed as described in 4.1.2. The recorded signals are gathered in **Table 3** and the symbols explained on a **Scheme 17**.

Table 3- Signals present in ^{1}H-NMR spectrum of compounds **A** and **B**.

Chemical shift δ [ppm]	Protons	Symbol
1.33 Triplet	Methyl protons –C**H**$_3$	e
2.40 Triplet	Methylene protons of bisphosphonate group P-C**H**$_2$-P (compound **A)**	c
2.5 Triplet	Methine proton of bisphosphonate group P–C**H**(CH_2)-P- (compound **B**)	c’
3.20 Singlet	Methyl protons of C**H**$_3$-O- group (compound **B**)	a
3.87 Doublet of triplets	Methylene protons of CH_3-O-C**H**$_2$- group (compound **B**)	b
4.18 Multiplet	Methylene protons –C**H**$_2$-CH_3	d

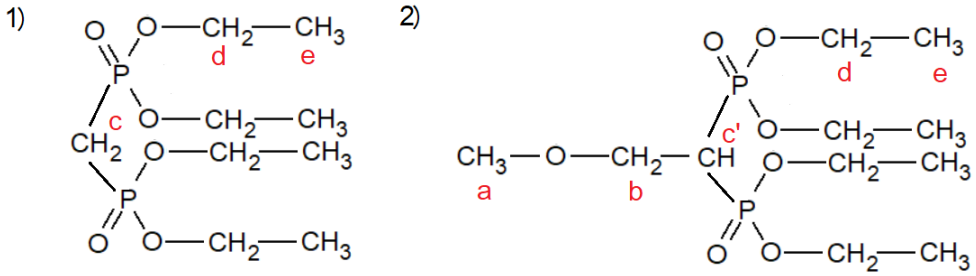

Scheme 17- Structure of 1) substrate **A** and 2) intermediate compound **B**

Reaction yield (Y) meant as percentage of an intermediate **B** in a reaction mixture was calculated from the equation below and was 91% for the 100 mg scale (**Figure 1** and **Figure 42**).

$$Y = \frac{\frac{I_b}{2}}{\frac{I_c}{2} + \frac{I_b}{2}} \cdot 100\%$$

where: I_b – intensity of a signal b; I_c – intensity of a signal c

Upscaling the process 100 fold resulted in decreasing the yield to 83%. The formation of compound **B** and the presence of unreacted substrate **A** were also confirmed by ^{31}P-NMR spectrum analysis (**Figure 2**) and confronted with spectral data available in literature [156]. The signal at 20.91 ppm corresponds to the phosphorus atoms of the intermediate **B**, and the signal with a chemical shift of 19.13 ppm corresponds to the substrate **A**. Interestingly, a signal at 12.68 ppm is also present, which can be attributed to phosphorus atoms close to the unsaturated bond, as in compound **C**.

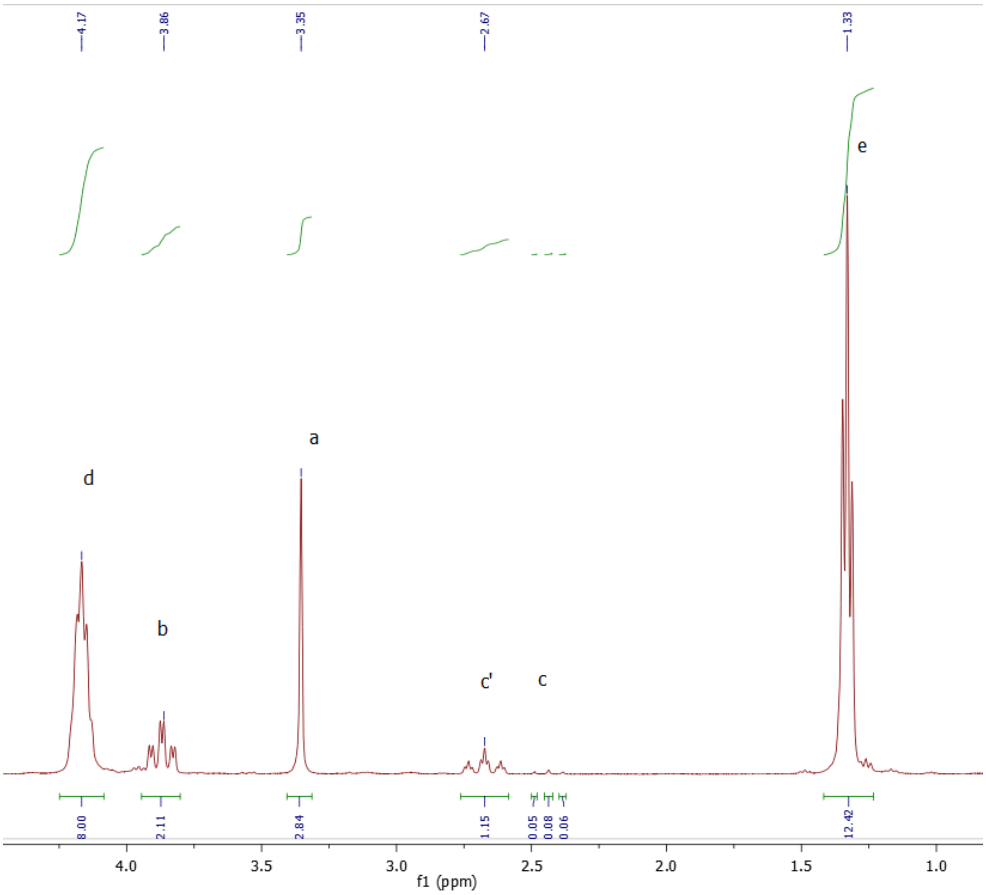

Figure 1– Excerpt of ^{1}H-NMR spectrum of reaction mixture containing intermediate **B** and substrate **A**. Full spectrum is presented on Figure 42.

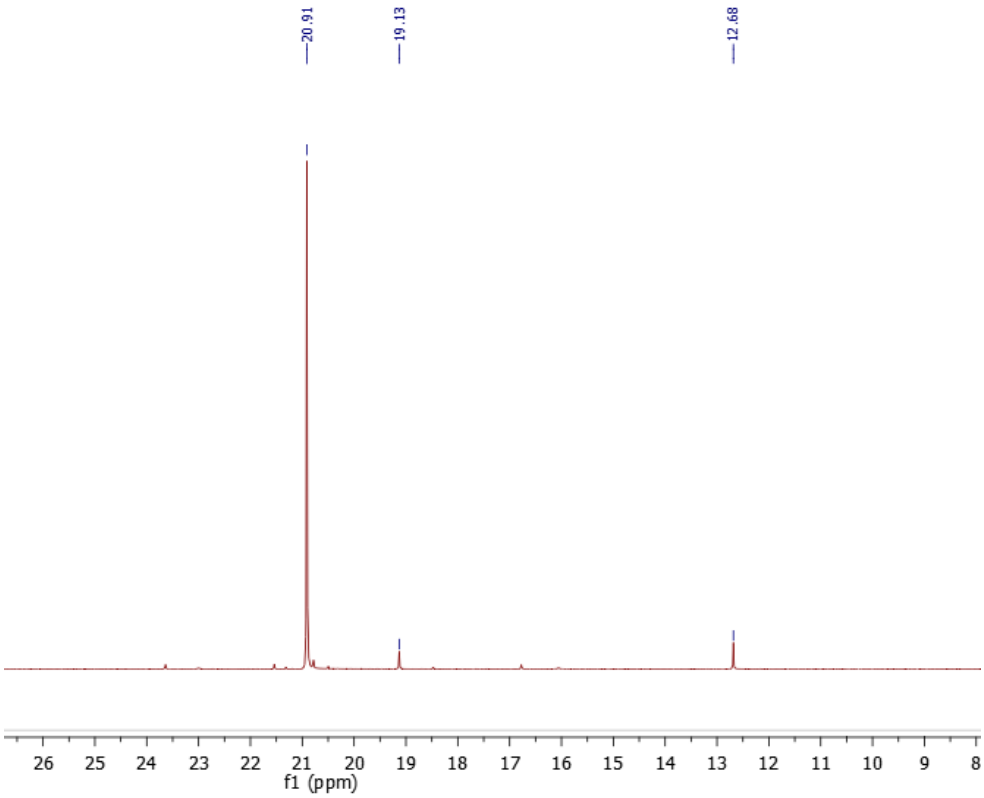

Figure 2- ^{31}P-NMR of reaction mixture containing intermediate **B** and substrate **A**.

Next step of the process was elimination reaction in order to obtain tetraethyl ethenylidenebis(phosphonate) ©, as presented on **Scheme 18**.

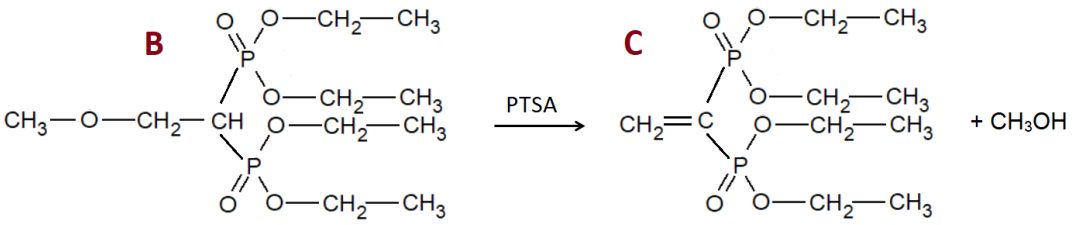

Scheme 18 – Second step of tetraethyl ethenylidenebis(phosphonat©(**C**) synthesis

The reaction mixture from the previous step was used without purification. Reaction was refluxed overnight in toluene with p-toluenesulfonic acid (PTSA) as catalyst, over dried sieves in order to remove methanol from the reaction mixture. After stopping the reaction and removing the reaction media, flushing with water and drying, samples of the crude product were dissolved in $CDCl_3$ for NMR analysis. The recorded signals are described in **Table 4** and the symbols explained on **Scheme 17** and **Scheme 19**.

Table 4 - Signals present in ^{1}H-NMR spectrum of compound B.

Chemical shift δ [ppm]	Protons	Symbol
1.33 Triplet	Methyl protons –C**H**$_3$	e
2.40 Triplet	Methylene protons of bisphosphonate group P-C**H**$_2$-P (compound **A)**	c
2.5 Triplet	Methine proton of bisphosphonate group P–C**H**(CH$_2$)-P- (compound **B)**	c’
3.20 Singlet	Methyl protons of C**H**$_3$-O- group (compound **B)**	a
3.87 Doublet of triplets	Methylene protons of CH$_3$-O-C**H**$_2$- group (compound **B)**	b
4.18 Multiplet	Methylene protons –C**H**$_2$-CH$_3$	d
6.97 Distorted doublet of doublets	Methylene protons C**H**$_2$=	f

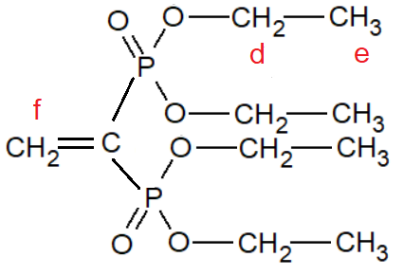

Scheme 19 - Structure of compound C

Reaction yield (Y) meant as percentage of product (compound **C**) in a reaction mixture was calculated from the equation below and was 80% for the 100 mg scale. Upscaling the process 100 fold resulted in decreasing the yield to 78%. The amount of the intermediate product (compound **B**) was constant in both batches (13%) and the amount of unreacted substrate increased with drop in product quantity.

$$Y = \frac{\frac{I_f}{2}}{\frac{I_c}{2} + \frac{I_b}{2} + \frac{I_f}{2}} \cdot 100\%$$

where: I_a – intensity of a signal *a*; I_c – intensity of a signal *c*, I_f – intensity of a signal *f*.

In order to obtain a product **C** of higher purity, a chromatography column was prepared. Each of the collected fractions was monitored using TLC, compared to the substrate sample. ^{1}H-NMR of samples in $CDCl_3$ was performed for two of the collected fractions. The NMR spectra obtained were analysed and the results are summarized in **Table 5**.

Table 5- Content of individual substances in subsequent fractions calculated from ^{1}H-NMR.

Fraction	Amount of product C	Amount of substrate A	Amount of intermediate B	Spectrum
1	78%	9%	13%	**Figure 43**
2	75%	7%	18%	**Figure 44**

The table above shows that separation on a conventional chromatography column is not sufficient to obtain pure compound **C**. For this reason, another part of the reaction mixture was separated on ISOLERA flash chromatography. Solvent from two fractions (6 and 13) was evaporated and ^{1}H-NMR of samples in $CDCl_3$ was performed. The NMR spectra obtained were analysed and the results are summarized in **Table 6.**

Table 6- Content of individual substances in subsequent fractions calculated from ^{1}H-NMR.

Fraction	Amount of product (compound C)	Amount of substrate A	Amount of intermediate (compound B)	Spectrum
6	94%	1%	5%	**Figure 45**
13	29%	52%	18.6%	**Figure 46**

Synthesis of tetraethyl[[(ethoxyhydrophosphoryl)methyl]methylene]bis-(phosphonate) (compound G)

Desired H-phosphonate **G** was prepared in reaction of an excess of ethyl hypophosphite (compound **F**) with tetraethyl ethenylidenebis(phosphonate) (**C**). First, **F** was prepared *in situ* due to its high reactivity, according to reaction presented on **Scheme 20**.

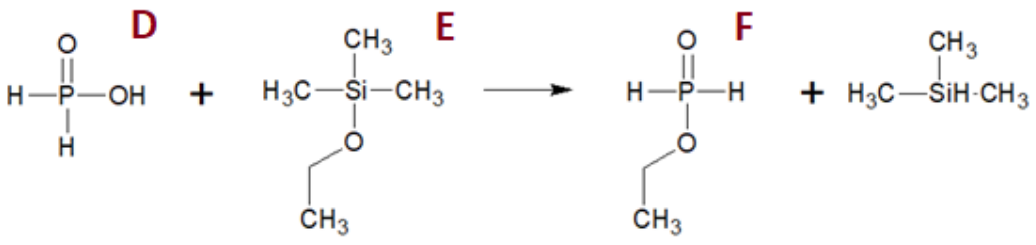

Scheme 20– Synthesis of compound **F**

Phosphinic acid **D** (old name hypophosphorous acid) was used in form of solid crystals. Complete dehydration of the phosphinic acid sample was confirmed by weighing the samples before and after lyophilization. A 10 mL, 12.06 g of 50% acid was placed

in a round-bottom flask. After freeze-drying, the weight of the sample was 5.95 g or 49% of the initial weight. Only one signal (multiplet) at 12 ppm was present in ^{31}P-NMR from the freeze-dried acid sample, proving that there is only one compound with an asymmetric phosphorus atom in the sample (**Figure 3** and **Figure 47**). Available literature data give the chemical shift of the acid as 15.2 ppm, but refer to a different solvent (deuterated nitromethane) [157].

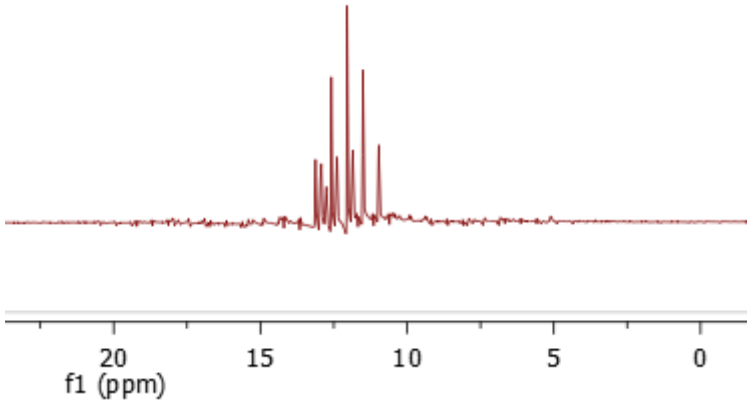

Figure 3- ^{31}P-NMR spectrum of phosphinic acid

White acid crystals were dissolved in tetrahydrofurane (THF) and reaction with ethoxytrimethylsilane **E** was carried out for two hours with mixing. Then, to the reaction mixture compound **C** of 94% purity was added in order to obtain final H-phosphonate product (**G**) in ethyl hypophosphinate addition to ethylidene group of a bisphosphonate (**Scheme 21**).

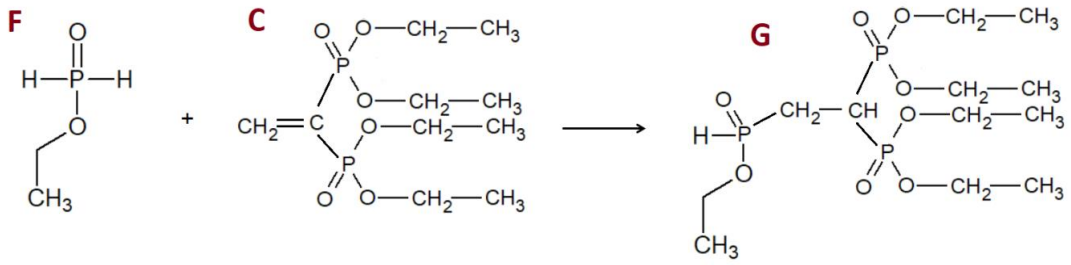

Scheme 21- Synthesis of compound **G**

After two-step reaction residue left after evaporating THF was redissolved in chloroform. Mixture was then extracted with H_2O and then aqueous phase was reextracted with chloroform twice. Combined organic phases were dried over MgSO4 and evaporated to dryness to give crude product, which was analysed with ^{1}H-NMR in $CDCl_3$. The recorded signals are described in

Table 7 and the symbols explained on a **Scheme 17, Scheme** 19 and **Scheme 22**.

Table 7- Signals present in ^{1}H-NMR spectrum of compound G.

Chemical shift δ [ppm]	**Protons**	**Symbol**
1.33 Triplet	Methyl protons –C**H**$_3$	e
2.26 Multiplet	Methylene protons of -P-C**H**$_2$- group (compound **G**)	g
2.40 Triplet	Methylene protons of bisphosphonate group P-C**H**$_2$-P (compound **A**)	c
2.5 Triplet	Methine proton of bisphosphonate group P–C**H**(CH$_2$)-P- (compound **B**)	c’
2.79 Multiplet	Methine proton of bisphosphonate group P–C**H**(CH$_2$)-P- (compound **G**)	c”
3.20 Singlet	Methyl protons of C**H**$_3$-O- group (compound **B**)	a
3.87 Doublet of triplets	Methylene protons of CH$_3$-O-C**H**$_2$- group (compound **B**)	b
4.18 Multiplet	Methylene protons –C**H**$_2$-CH$_3$	e
6.97 Distorted doublet of doublets	Methylene protons C**H**$_2$=	f
7.29 Doublet	Proton from group **H**-P- (compound **G**)	h

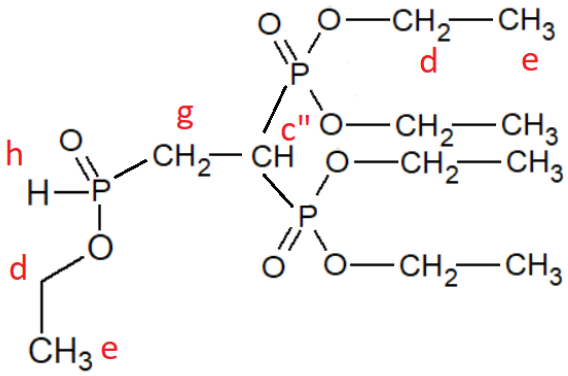

Scheme 22- Structure of compound **G**.

Reaction yield (Y) meant as percentage of product **G** in a reaction mixture was calculated from the equation below and was 86% for the 1 g scale, while amount of substrate was calculated to be 7% and intermediate product **B** – 7.4%.

$$Y = \frac{I_h}{I_h + \frac{I_b}{2} + \frac{I_f}{2}} \cdot 100\%$$

where: I_a – intensity of a signal *a*; I_c – intensity of a signal *c*, I_f – intensity of a signal *f*.

There were no signals indicating presence of compound **C** in reaction mixture (spectrum is presented on **Figure 48**). Quantitative analysis was performed based on ^{1}H-NMR spectra, although ^{13}C-NMR and ^{31}P-NMR spectra were also performed to confirm the structure obtained. Signals and their corresponding phosphorus/carbon atoms are collected in the **Table 8** and **Table 9.** Data obtained from actual measurements were compared with literature data.

Table 8- ^{31}P-NMR signals of bisphosphonate compounds.

Chemical shift δ [ppm]		Phosphorus	Compound	
Experimental	Theoretical			
10.0	15.8	H_2O**P**OEt	F	[158]
12.0		H_3**P**O_2	D	Figure 47
12.7	12.8	**P**-C(=CH_2)-**P**	C	[156] Figure 49
19.1		**P**-CH_2-**P**	A	Figure 49
20.9	21	**P**-CH(CH_2OCH_3)-**P**	B	[156] Figure 49
21.7	22.0-22.2	**P**-CH-**P**	G	[154] Figure 50
35.5	35.8	H-**P**		

As seen on **Figure 4**, ^{31}P-NMR spectrum of a product shows strong signals at 35.5 and 21.7 ppm, confirming presence of desired compound **G**. There is also signal corresponding to substrate **A** which is consistent with ^{1}H-NMR.

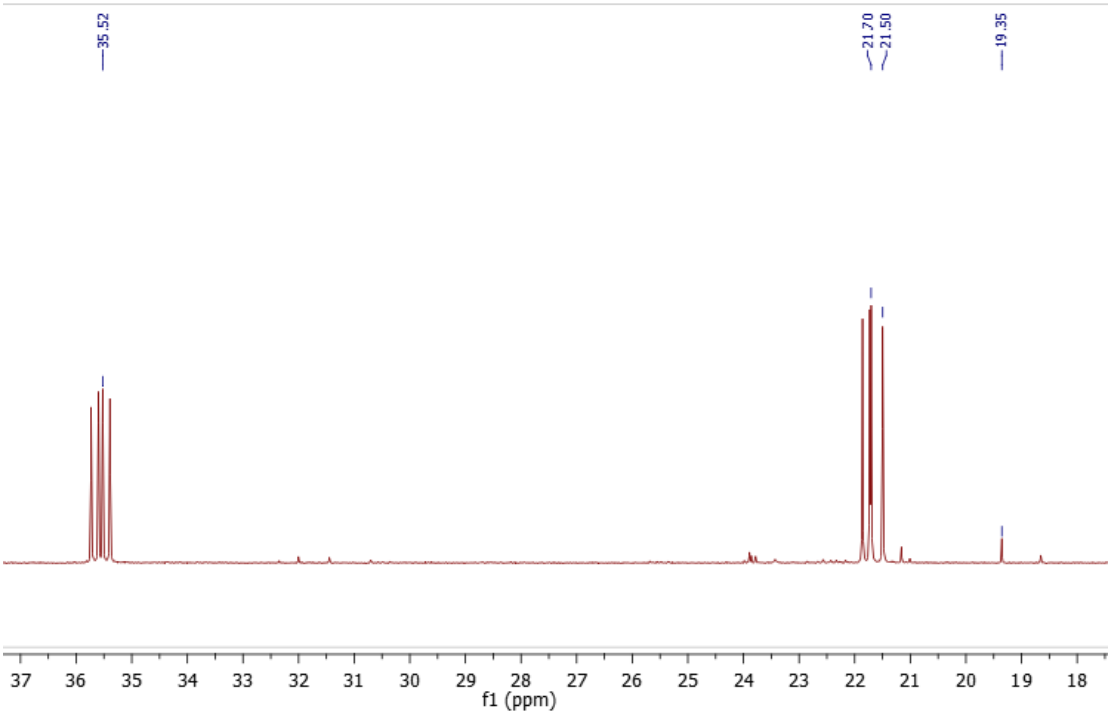

Figure 4- ^{31}P-NMR spectrum of compound G.

Table 9- ^{13}C-NMR signals of bisphosphonate compounds

Chemical shift δ [ppm]		Carbon	Compound	
Experimental	Theoretical			
16.01	15.72	CH_2-**C**H_3	G	[154] Figure 52
	16.0		B	[156]
16.29			A	Figure 51
25.37	24.36	P-**C**H_2-CHP_2	G	[154] Figure 52
25.39		P-**C**H_2-P	A	Figure 51
	30.08	P-**C**H-P	G	[154]
	38.50		B	[156]
	62.07	HP-O-**C**H_2-CH_3	G	[154]
	62.2	C-P-O-**C**H_2-CH_3	B	[156]
62.63	62.36		G	[154] Figure 52
62.52			A	Figure 51

	67.8	CH_3-O-**C**H_2-C	B	[156]
132.00		CH_2=**C**P_2	C	Figure 52
149.12		**C**H_2=CP_2		

Modification with H-phosphonate – Kabachnik-Fields reactions

The aim of this process was the introduction of a bisphosphonate group into DFO via a one-carbon spacer. Expected reaction of H-phosphonate **G** with protected bisphosphonate group would occur according to Kabachnik-Fields mechanism. This is a type of Mannich reaction involving an amine, a carbonyl group donor and an H-phosphonate.

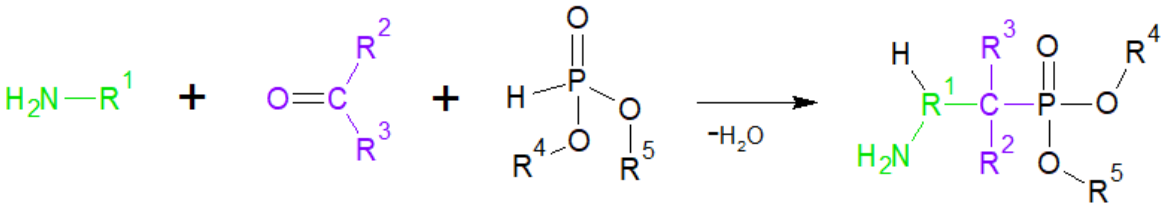

Scheme 23 - Kabachnik-Fields reaction – schematic route

The Kabachnik-Fields mechanism (**Scheme 23**) is a reaction that forms α-aminomethylphosphonates from three components: an amine (primary or secondary), a carbonyl compound and a dialkylphosphonate. The general mechanism involves the condensation of the abovementioned groups (amines, aldehydes or ketones and >P(O)H species), but the exact mechanism of the reaction is not completely elucidated. There are two alternative proposed mechanisms. The first one occurs via the formation of an imine (also known as Schiff's base) from a carbonyl compound and an amine. The dialkyl phosphine then attaches to the C=N bond of the imine intermediate by hydrophosphonylation. This addition follows a Pudovik-type reaction in which the P-H bond of the phosphonate is added to the C=N double bond. A second proposed reaction mechanism suggests the formation of α-hydroxyphosphonate by the addition of dialkylphosphine to the carbonyl group, followed by amine substitution to produce α-aminophosphonate.

Method used by the group of Vitha et al. to introduce a bisphosphonate group into the gadolinium chelator DO3A was adapted for Kabachnik-Fields reaction of deferoxamine with H-phosphonate (expected synthesis route at **Scheme 24**).

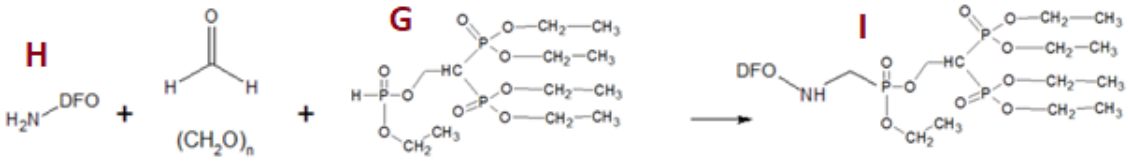

Scheme 24- Expected Kabachnik-Fields reaction of DFO and H-phosphonate

The ^{1}H-NMR of deferoxamine mesylate salt **H** was obtained in both DMSO-d_6 and D_2O, and signals assigned to corresponding protons, for easier analysis of the reaction mixture. Structure of **H** is presented on **Scheme 25** and corresponding peaks described in **Figure 53** and **Figure 54,** and **Table 10**.

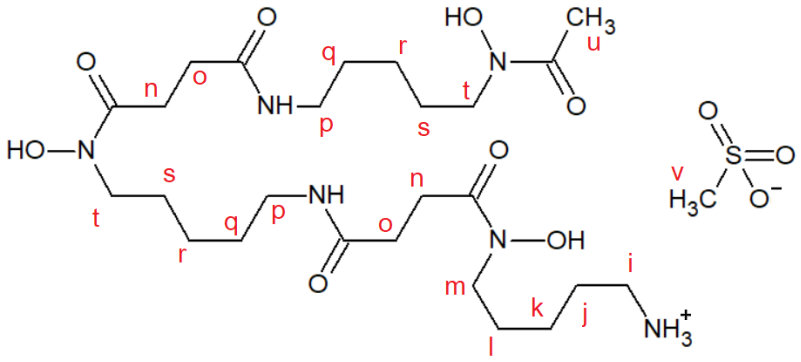

Scheme 25- Structure of DFO-Mes (compound H)

Table 10- Chemical shifts of H in D_2O and DMSO-d_6

Proton label	Chemical shift [ppm]	
	In D_2O	In DMSO-d_6
i	3.01	2.94
j	1.66	1.68
k	1.33	1.44
l	1.66	1.68
m	3.63	3.63
n	2.82	2.75
o	2.51	2.44
p	3.18	3.18
q	1.53	1.56
r	1.33	1.39
s	1.66	1.68
t	3.63	3.63
u	2.15	2.14
v	2.82	2.68

Expected ^{1}H-NMR spectrum of a product **I** (**Scheme 26**) would involve disappearance of a very characteristic signal from **H**-P proton (7.29 ppm; d, $^1J_{H\text{-}P}$ = 576.0 Hz) originating from

G. Also, migration of signal corresponding to -C**H₂-**NH_2 (3.0 ppm; t) would indicate reacting of the pendant amine group of DFO with the phosphonate.

Appearance of the new signals (corresponding to proton marked *x* and *i'* on **Scheme 26**) would also be confirmation of obtaining the desired structure.

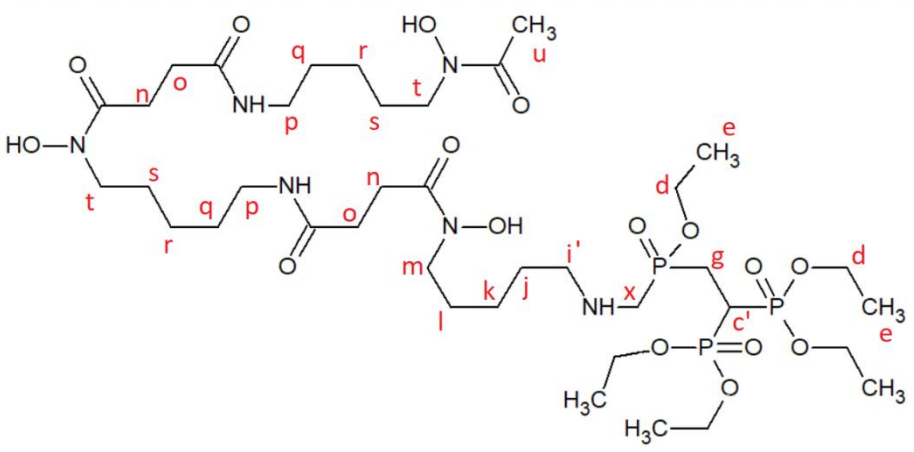

Scheme 26- Expected structure of I.

The experiments carried out in order to obtain the desired product included the use of both formalin and paraformaldehyde, solvents such as DMSO, water, methanol, benzene and lowering the pH. Variations of abovementioned conditions are gathered in **Table 11**.

Table 11 - Conditions for Kabachnik-Fields reaction of H with G and carbonyl donor.

Solvent	Carbonyl group donor *	Molar ratio of G:H	Molar ratio of carbonyl donor : DFO	Temperature [°C]	Time	other	Reaction
toluene	P	2	2	100	20 h		
methanol	P	2	2	70	20 h		
	P	1	1	70	20 h	Na_2CO_3	
	P	1	1	70	15 min	Na_2CO_3	
benzene	P	1	1	25	45 min	Na_2CO_3	
D_2O	F	1	1	80	15 min		I
	F	1	1	80	15 min	pH = 4	II
	P	1	1	80	15 min		III
	P	1	1	90	3 h	200 W microwave	IV
	F	1	1	100	20 h		V

DMSO	P	0.5	1	70	20 h		VI
	P	1	1	60	72 h	Et_3N 1 eq	VII
	P	1	1	60	72 h	Et_3N 0.2 eq	VIII

* - P – paraformaldehyde; F- formaldehyde

Reaction progress was monitored mainly by ^{1}H-NMR and ^{31}P-NMR. Efforts were made to establish combination of mobile and stationary phase to enable monitoring of the reaction progress by TLC. Even though many eluents were tested, none of it allowed of differentiating the spots corresponding to DFO from its derivatives. This problem, aside from impeding the tracking of the process was a harbinger of a problem with purification of the reaction mixture by chromatographic techniques.

Reaction in toluene

Process conditions adapted from the literature included toluene as reaction medium, so this solvent was the starting point. Paraformaldehyde was used as a carbonyl group donor and DFO was in the form of mesylate salt (DFO-Mes, compound **H**). Unfortunately, solubility of **H** in toluene remained very poor, despite increasing the reaction temperature up to 100 ^{O}C. After 24 hours reaction was stopped, solvent evaporated and the yellowish residue was analysed by NMR (in D_2O). ^{1}H-NMR spectra of the residue did not confirm creation of desired structure.

Deferoxamine in free amine form should have better solubility in toluene, than **H** in salt form. For this reason, an attempt was made to dissolve **H** in this non-polar solvent by adding in equal molar amounts of NaOH or Na_2CO_3 to two separate samples of **H** in toluene. Again, after refluxing overnight, clear supernatant was collected, solvent have been evaporated of toluene and samples for NMR collected. Both spectra did not confirm presence of **H**, proving this solvent's unsuitability for such a process.

Reaction in methanol

The first experiment was repeated in exact manner with methanol as a solvent. Reaction went on at solvent's boiling point, with twofold molar excess of **G** and paraformaldehyde over **H**. Analysis of the spectrum confirmed the dissolution of **H** in methanol under the above conditions, but the reaction did not take place, as it was evident from the lack of disappearance of the signal coming from the **H**-P proton. To liberate the free amine and hopefully improve reactivity of **H**, Na_2CO_3 was added to the reaction mixture before adding bisphosphonate substrate. Stirring with heating was continued until all the residue of **H** was

dissolved. Then, **G** was added and reaction went on for 15 minutes or overnight. Unfortunately, both of the reactions appear to have deviated significantly from the expected course. The obtained ^{1}H-NMR spectra show substantial discrepancies from the anticipated profile. Presence of doublet corresponding to **H-**P does not seem to decrease its intensity in comparison to some non-reacting groups. Signals that were expected to remain unaffected have shifted, and several new, unidentified peaks have emerged. The complexity of the spectral data makes it challenging to elucidate the underlying chemical processes or identify the resulting products with confidence. For the reasons above, efforts have been directed towards other solvents.

Reaction in benzene

Also, another non-polar solvent - benzene - was tested to be a suitable reaction medium for this process. As mentioned above, DFO in amine form should have better solubility than the mesyl salt. For this reason, a ^{1}H-NMR spectrum of a sample containing compound **H** and Na_2CO_3 dissolved in C_6D_6 was the first step on this experiment. Spectrum showed solely peaks from TMS, water and solvent residual peak. Verification was also carried out after further steps, i.e. after the addition of paraformaldehyde and compound **G**. The former compound also did not give a signal, while in the last sample a spectrum of only the **G** was obtained.

Reaction in water

Numerous attempts have been undertaken in aim to obtain the desired product in aqueous conditions. Experiments were performed in very small scale, involved changes in pH and utilization of microwaves.

Primarily, deuterated water was chosen as a solvent, due to small reaction scale (milligrams) and easy control of the process with ^{1}H-NMR. All the substrates were prepared in equal molar amounts for all the reactions, while pH and donor of carbonyl group varied between reactions (**Table 12**). Samples for ^{1}H-NMR were collected at three time points:

- a: After complete dissolution of **H**s and paraformaldehyde (for reaction III) in the solvent, before adding compound **G**
- b: In fifteen minutes after adding the **G** to the reaction mixture
- c: After 20 hours of reaction

Temperature was kept in 70 ^{O}C until second ^{1}H-NMR samples were withdrawn.

Table 12 – Conditions of experiments in water

Reaction symbol	Carbonyl group donor	pH
I	Formaldehyde	Neutral
II	Formaldehyde	Acidic (pH = 4.0)
III	Paraformaldehyde	Neutral

Reaction I: In second spectrum (Ib) there are some new signals in comparison to spectrum Ia, coming from **G**. There are some new, unidentified peaks, at 3.92 and 1.87 ppm. After several hours abovementioned peaks increased on intensity. The signal from the reactive **H**-phosphonate group reduced intensity (**Figure 5**). New doublet signal at 6.86 ppm (J = 41 Hz) of unknown origin appeared after adding bisphosphonate and increased after 20 hours of reaction.

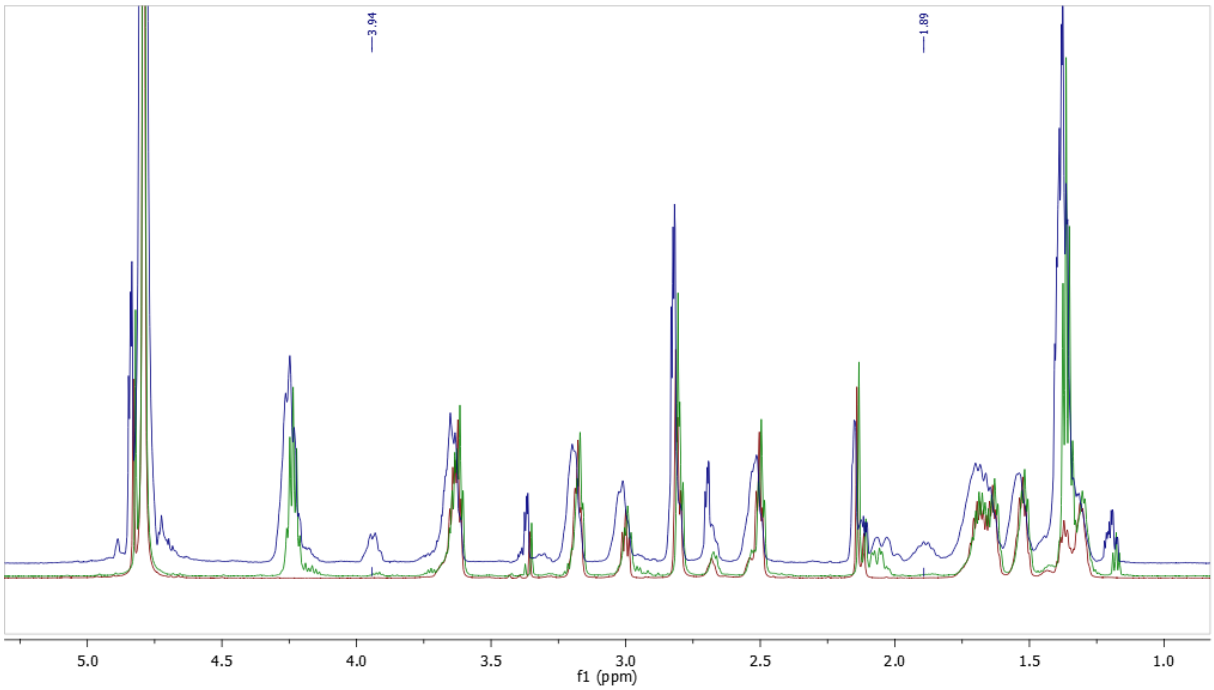

Figure 5 – Progress of reaction I. Colour red represents spectrum Ia; green: Ib and blue: Ic. Marked are new signals at 1.87 and 3.92 ppm.

Reaction II: The spectrum of the mixture of **H** and formalin under acidic conditions (IIa) was essentially no different from that of sample Ia (**Figure 6**). Similarly, the IIb spectrum and the Ib spectrum were identical. The reduction of intensity in signal at 7.3 ppm (compared to signal *d*) was even more significant, than in the reaction I.

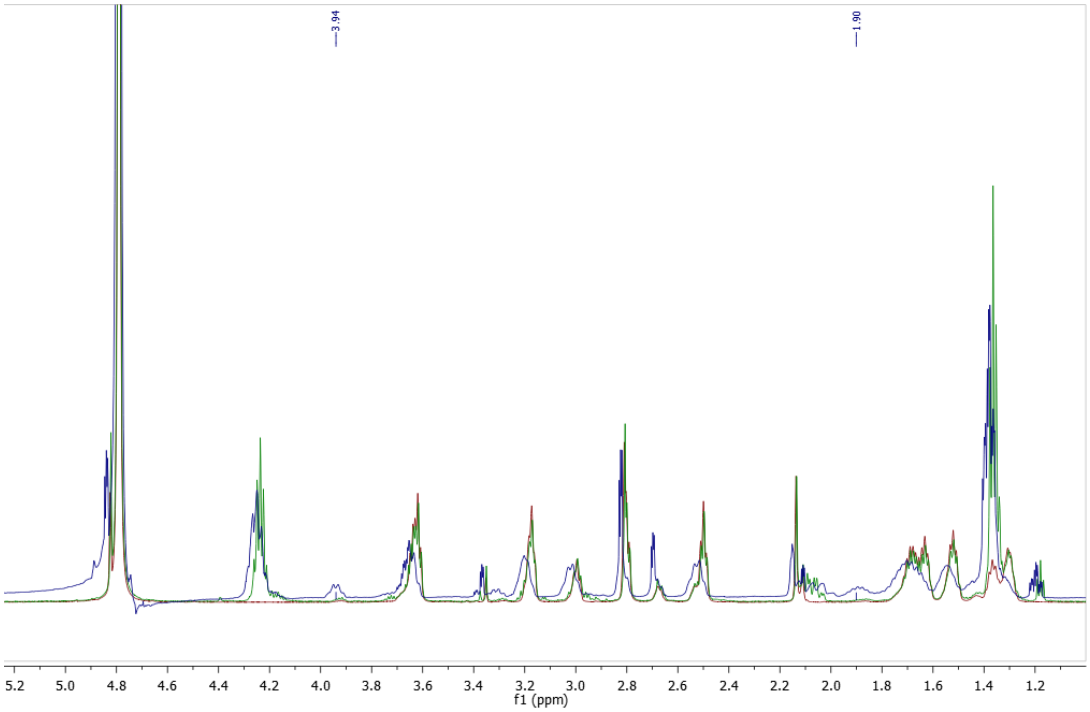

Figure 6- Progress of reaction II. Colour red represents spectrum IIa, green: IIb and blue: IIc. Marked are new signals at 1.90 and 3.94 ppm.

Reaction III: The absence of signal at 3.36 ppm, which was present in previous reactions (formaldehyde), was noted (**Figure 7**). Paraformaldehyde, as a formaldehyde polymer, can partially depolymerise in aqueous solution, releasing monomeric formaldehyde molecules. If it does not fully depolymerise, its signals may be weaker or difficult to detect in a standard ^{1}H-NMR spectrum. Aside from that difference, both IIIa and IIIb spectra are consistent with previous experiments. A reduction in the intensity of the signal from the reactive H-phosphonate group also occurred in this reaction, but not to the same extent as in the above experiments.

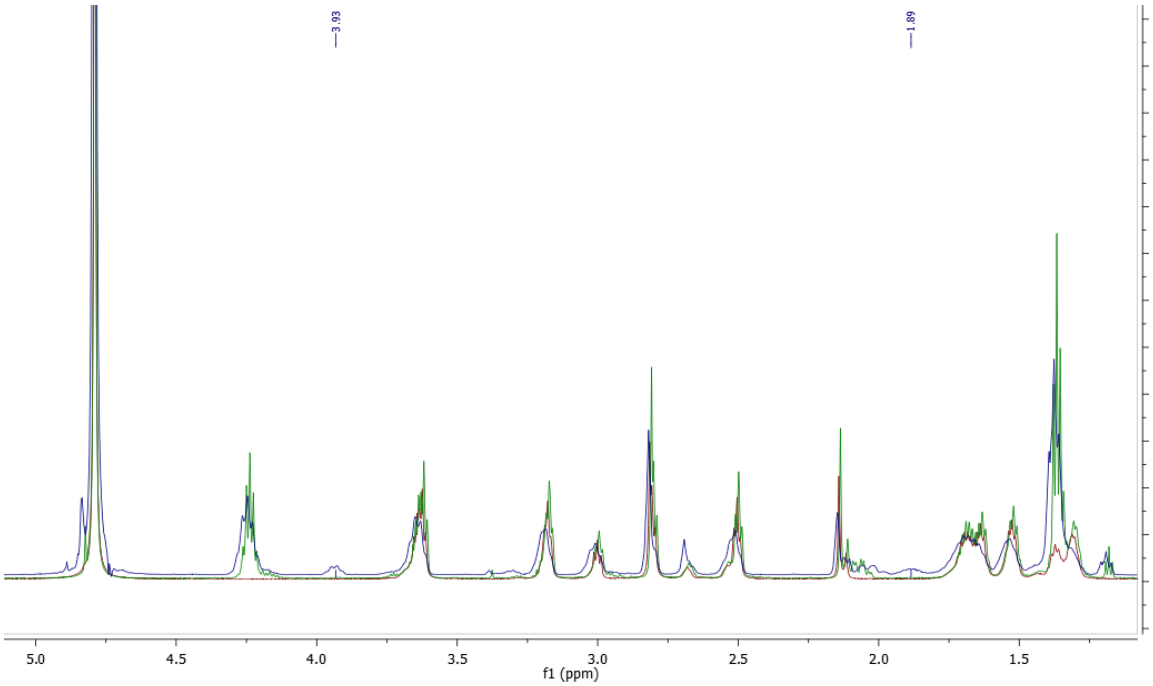

Figure 7- Progress of reaction III. Colour red represents spectrum IIIa, green: IIIb and blue: IIIc. Marked are new signals at 1.89 and 3.93 ppm.

The influence of microwave energy was then tried in the new reaction of **H** + formaldehyde + **G** (Reaction IV). Reaction was carried out at the lowest power setting for about 10 minutes (with stirring intervals). In the ^{1}H-NMR spectrum (**Figure 55**) there are no signals indicative of reaction progress (at 3.92 ppm and 1.87 ppm, which appeared for the previous reactions in water).

Next, Reaction V was carried out in D_2O, with equal molar amounts of **H**, formaldehyde and compound **G**. Reaction mixture was refluxed overnight. After reaching the target temperature reaction mixture turned colour of red/brown. At 20 hours of synthesis brown supernatant over pale looking sediment was observed. ^{1}H-NMR of the supernatant was performed and the signals analysed.

A disappearance of the signal originating from the **H**-P proton (signal *h* at 7.3 ppm) was observed in the spectrum (**Figure 56**), which may indicate a complete conversion (consumption) of the compound **G**. However, all the other signals indicate toward unsuccessful reaction or reaction according to unknown scheme (**Figure 8**). Signal *i* did not decrease its intensity (in relation to signal *n* or *p*). Some new signals have emerged, in the range of 3.36 to 3.73 ppm. Considering signal *x* to be the one at 3.73 ppm, yield of the reaction could be calculated to be 40%, when in comparison with the signal *u.* When comparing its intensity to signal *n*, theoretical yield would be 19%.

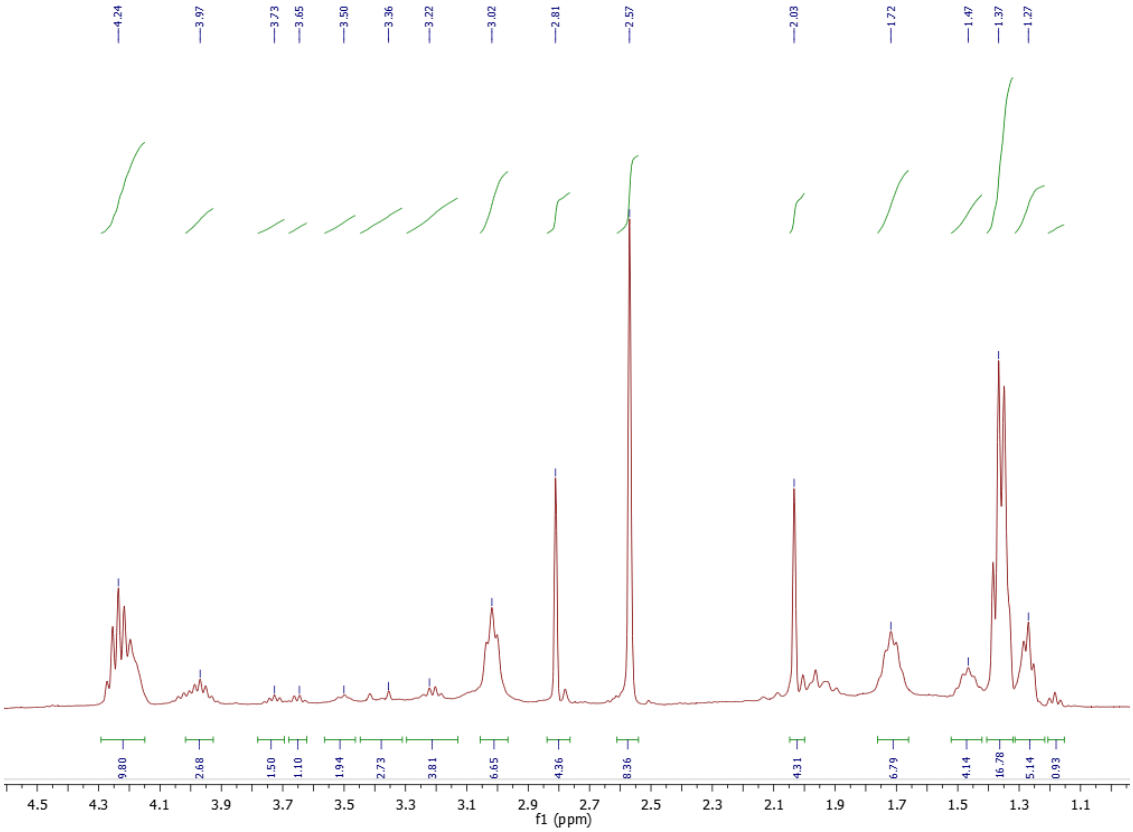

Figure 8– Excerpt of ^{1}H-NMR of reaction V.

Reaction in dimethyl sulfoxide

The mechanism of the Kabachnik-Fields reaction produces water as a by-product. For this reason, it was assumed that the reaction in an anhydrous environment could promote the formation of the desired product. All substrates of the DFO-Mes reaction with paraformaldehyde and H-phosphonate dissolve excellently in DMSO. Because of its unlimited miscibility with water, it was also possible to carry out the reaction with an aqueous formaldehyde solution.

As with the reactions in aqueous conditions, the first experiments were carried out in a deuterated solvent, for easy control of the process with the NMR technique. Analysis of the **Reaction VI** mixture after the addition of each substrate confirmed the good solubility of all components of the reaction mixture in this medium, and allowed the identification of signals from specific protons. The first of the ^{1}H-NMR spectra, obtained after brief (30 minutes) heating of **H** in DMSO-d_6 with stoichiometric addition of Na_2CO_3 showed a shift in the *i* signal (directly adjacent to the primary amine group) from 2.94 ppm (**Figure 54**) to 2.76 ppm (**Figure 9**). This may be indicative of the deprotonation of the neighbouring amino group into the free amine form, as in the case of the protonated amino group,

the deshielding effect is stronger due to the positive charge on the nitrogen. Protonation increases the electron-acceptor character of the nitrogen, resulting in a further signal shift.

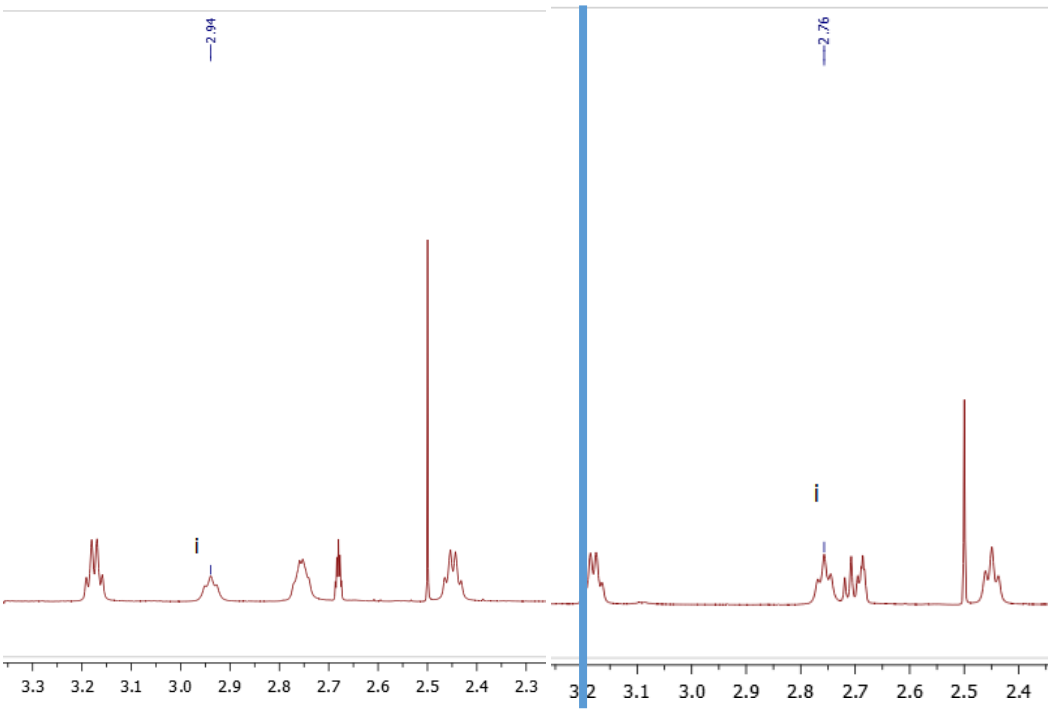

Figure 9 – Shift of signal *i:* left spectrum – **H** in DMSO-d_6, right spectrum – reaction **VI**

Similar, but weaker effect was observed for protons *j*, shifting from 1.68 to 1.55 ppm. Another process control was performed after the addition of paraformaldehyde and heating until dissolution. This action resulted in emerging a signal at 7.97 ppm (which corresponds to depolymerized formaldehyde) and peak from H_2O at 3.52 ppm. Next spectrum was obtained after adding **G** to the reaction mixture. Signals at 1.40 and 4.24 ppm, as well as characteristic doublet at 7.24 ppm emerging in spectrum confirmed good solubility of **G** in this solvent. Interestingly, a new triplet and a doublet were observed at low chemical shift values. These are likely to originate from other bisphosphonate derivatives (compounds **A, B**) present in small amounts in the **G** sample. Heating overnight did not result in the disappearance of the **G**, a weakening or shift of the *i* peak, nor the appearance of new peaks in the expected range of 3.7 -3.9 ppm (**Figure 57**).

Another two reactions were carried out in deuterated DMSO with Et_3N as an activator of the amine to increase its nucleophilicity. **H**, **G** and paraformaldehyde were added in equal molar amounts, while Et_3N was added in equal (Reaction VII) or 0.2 molar equivalents (Reaction VIII). Both processes were carried out for 24 hours at room temperature after which a sample was taken from each reactor for ^{1}H-NMR and ^{31}P-NMR analysis. The reaction temperature was then raised to 60 ^{O}C and the processes were run at this temperature for

72 hours, followed by ^{1}H- and ^{31}P- NMR of final reaction mixtures. Interpretation of obtained data is collected in

Table 13 and

Table 14.

Reaction VII: ^{1}H-NMR spectrum obtained after 24 hours (**Figure 58**) at room temperature indicated that the desired reaction product was not obtained. There was no loss of the *h* signal (*d,* 7.19 ppm, $^{1}J_{H\text{-}P}$ = 501 Hz) relative to the methylene protons of the bisphosphonate (peak *e*): for the pure substrate this ratio was 1:10 (**Figure 48**), in the investigated sample - 1:7.14 (**Figure 58**). It might be due to the fact, that Et_3N did not cause deprotonation of the amine group in room temperature, as its chemical shift did not decrease. However, there are some new signals at: 3.88 ppm, 1.68 ppm and 8.00 ppm. Especially the former is suspected to originate from *x* protons. Broad band at 3.5 ppm originates from water, which may be a by-product of the desired reaction or the result of an insufficiently hermetic reactor. After another 72 hours in elevated temperature a shift of the *i* and *j* signals towards lower chemical shift values was found (**Figure 59**), which, as described earlier, may be a confirmation of deprotonation of the amine group. Significant loss was observed for *h* peak intensity, ratio *h:e* equals 1:21.89, which can be interpreted as yield of 68%. Signal at 3.88 ppm increased in intensity 2.4 times, which roughly corresponds with loss of *h* signal. Numerous peaks of unknown origin emerged in the range of 4.70 – 5.50 ppm.

In ^{31}P-NMR lack of signal at 35 ppm (originating from **G**) is observed, in both time points (**Figure 60, Figure 61, Figure 64, Figure 65**) even when there are still peaks coming from H-P proton in ^{1}H-NMR spectrum. Unknown signal at 15 ppm is observed after 24 hours; however it is doubtful that it originates from a phosphorus atom of a newly formed

–NH_2-CH_2-**P**- compound. Peak at 23.8 ppm is present in both reactions in all the time points, and for that reason it is possibly also not an effect of desired reaction.

Table 13 - Results of reactions VII and VIII in DMSO-d_6 with Et_3N – ^{1}H-NMR interpretation.

Reaction	**Et_3N eq***	**Results after 24 hours**		**Results after 96 hours**		**Figures**
		***h* signal**	**New peaks [ppm]**	***h* signal**	**New peaks [ppm]**	
VII	1	no loss	1.68 3.88	significant loss (68% yield)	2.07 3.91 4.78 4.86 5.07 5.50	**Figure 58** **Figure 59**
VIII	0.2	no loss	2.09	complete disappearance (100% yield)	1.23 2.21 2.58 3.10 3.79	**Figure 62** **Figure 63**

* regarding to DFO-Mes

Reaction VIII: After 24 hours ^{1}H-NMR spectrum was similar to that of Reaction VII at the same time point. Likewise, there is no decrease at signal *h* intensity (1: 8.76); however half of this dublet was hidden by peak at 7.96 ppm. Lower intensity of the signals at 1.32 and 3.25 ppm corresponds to the lower molar ratio of triethylamine added to the reaction. Nothing indicates formation of DFO-BP. After another 72 hours in elevated temperature, complete loss was observed for *h* peak intensity, what indicates that all **H**-P-groups reacted or degraded due to temperature or pH, because H-phosphonate esters under alkaline conditions can readily undergo hydrolysis or transesterification [159]. Signal at 3.79 ppm, suspected to originate from *x* emerged. Signal *i* decreased threefold, and new peak of chemical shift higher by 0.16 ppm appeared. It was interpreted as *i'*, confirming creation of desired structure. Data obtained from ^{31}P-NMR spectra is consistent with the above reasoning. There is new triplet at 24.58 ppm emerging after 96 hours of synthesis, which might be signal corresponding to phosphorus atom from newly created DFO-BP. Signals from H-P group is absent, and peak at 19.85 and 22.55 ppm are present in both time points. This indicates the disappearance of the H-phosphonate and the presence

of a bisphosphonate group in the reaction medium, although this may come from the substrate, the product or another, unforeseen by-product.

Table 14- Results of **I** synthesis in DMSO-d_6 with Et_3N – ^{31}P-NMR interpretation.

Chemical shift [ppm]	Phosphorus atom / compound	Present in reaction VII		Present in reaction VIII	
		After 24 hours	After 96 hours	After 24 hours	After 96 hours
15.34	unknown	✓	×	×	×
19.85	**P**-CH_2-**P** compound **A**	✓	✓	✓	✓
22.55	**P**-CH-**P** compound **G** & product	✓	✓	✓	✓
23.8	Unknown	✓	✓	✓	✓
24.58	NH-CH_2-**P**-CH_2 Product?	×	×	×	✓
35.52	H-**P**, compound **G**	×	×	×	×

A sample of the VIII reaction mixture after 96 hours of reaction was analysed by positive-field ESI-MS (electrospray ionization mass spectrometry). The masses of the expected components of the reaction mixture were calculated and collected in **Table 15**. The mass of the expected product as $[M+H]^+$ was calculated to be 967.4682 Da. Whole spectrum and enhanced area of 850-1000 Da are presented on **Figure 66** and **Figure 67**. There are no signals corresponding to desired structure, however in the region of interest there is a peak of 953.4584 m/z, which might be molecular ion of compound $C_{38}H_{79}N_6O_{15}P_3$. A compound related to the desired DFO-BP with such a molecular formula would have to lose an oxygen atom and gain two hydrogen atoms in the course of chemical reactions. This is certainly not the loss of an oxygen atom from the ester groups, as it would also involve the loss of an ethyl group, thus a final mass lower by c.a. 29 Da. Also, the detachment of the carbonyl oxygen seems unlikely, as these are known to be very stable. The loss from the structure of the oxygen derived from the hydroxamate group and its conversion to an amide group would be a reduction reaction, which seems unlikely to occur under the conditions described.

Table 15- Molecular formulae and masses of the compounds expected in the reaction VIII mixture

Compound	Molecular formula	Molecular weight [Da]
G - H-phosphonate	$C_{12}O_8P_3H_{29}$	394.1075
H - DFO-Mes	$C_{26}H_{52}N_6O_{10}S$	640.3466
I - DFO-bisphosphonate	$C_{38}H_{77}N_6O_{16}P_3$	966.9698
G without ethyl groups	$C_2H_9O_8P_3$	254.0093
I without ethyl groups	$C_{28}H_{57}N_6O_{15}P_3$	810.3095
Et_3N	$C_6H_{15}N$	101.19

The promising results obtained in the small-scale and deuterated solvent experiment led to another attempt, in larger quantities. Unfortunately, the separation of the reaction products from dimethyl sulfoxide proved problematic. The high boiling point of DMSO (189°C) made it impossible to remove the solvent from the reaction mixture using a vacuum evaporator. The poor solubility of DFO in other organic solvents immiscible with DMSO (like toluene, ethyl acetate or chlorinated solvents) precluded extraction of the reaction products. An attempt to precipitate the substances contained in the reaction mixture by adding large amounts of sodium chloride was not successful. Also, the addition of diethyl ether and the cooling of the reaction mixture did not allow the separation of DMSO from the other components.

3.1.1.2 Modification with tetraethyl [(2-chloroacetamido)methylene]bisphosphonate

After numerous unsuccessful experiments were performed according to Kabachnik-Fields reaction mechanism, the idea of modifying deferoxamine with H-phosphonate **G** was abandoned. Different bisphosphonate substrate, a tetraethyl [(2-chloroacetamido)methylene]-bisphosphonate (compound **J**) was received from another research group at Department of Organic Chemistry, Bioorganic Chemistry and Biotechnology in collaboration with Professor Jakub Adamek, PhD and Dominika Kozicka, M.Sc. Structure of substrate is presented in **Scheme 27**.

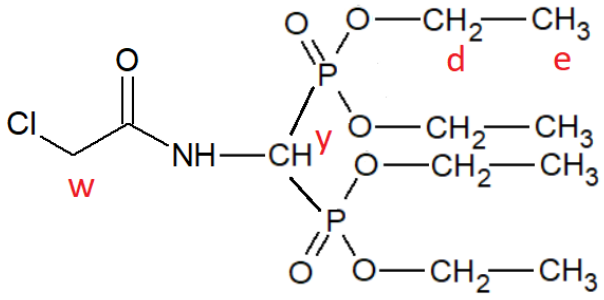

Scheme 27- Structure of tetraethyl [(2-chloroacetamido)methylene]bis(phosphonate) - **J**

Compound **J** was analysed in ^{1}H-NMR (in DMSO-d_6) and results are presented in **Table 16**.

Table 16- Chemical shifts of J DMSO-d_6.

Proton label	Chemical shift [ppm]
y	4.80
d	4.05
e	1.23
w	4.20

The reaction of this compound with DFO mesylate would proceed according to the S_N2 mechanism of bimolecular nucleophilic substitution (**Scheme 28**). A double-substituted derivative DFO(BP)$_2$, marked as **L** in the diagram, may be formed.

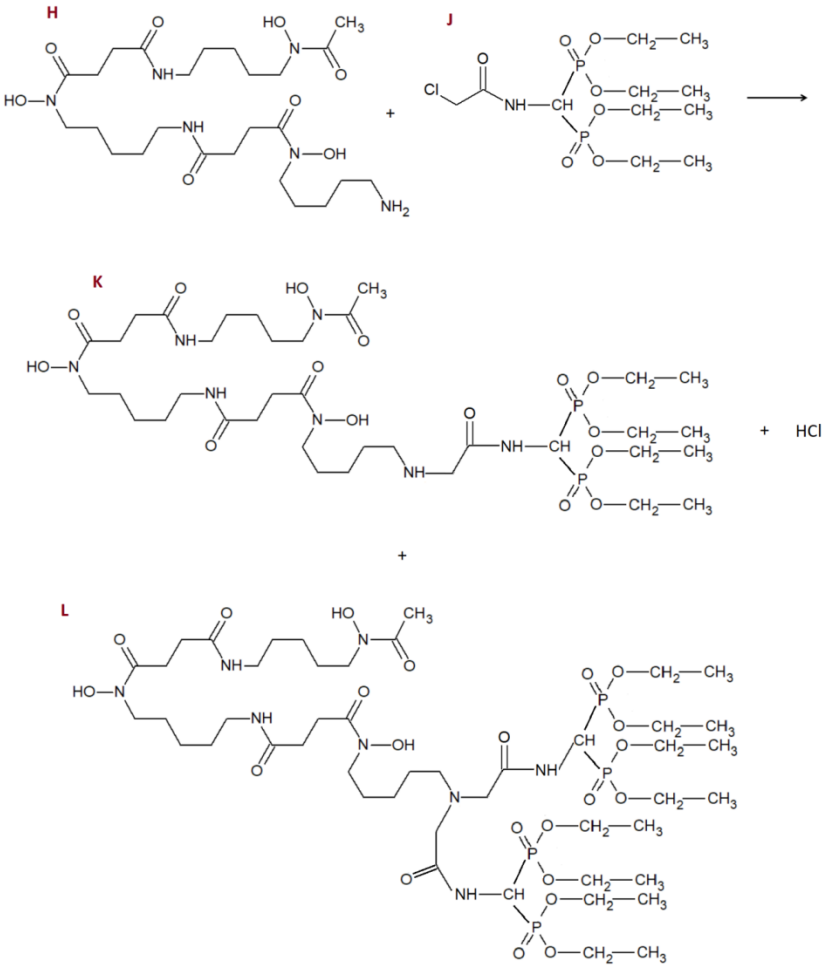

Scheme 28– Schematic representation of S_N2 reaction of **H** with **J.**

Once again, the choice of solvent proved problematic. DMSO provided good solubility for all substrates, but the separation of DFO and its derivatives was impossible. Additionally, presence of signal corresponding to proton *w* in post-reaction ^{1}H-NMR analysis suggests that the reaction did not occur in this solvent.

Heterogeneous reaction (water-chloroform)

For this reason, a **heterogeneous reaction** was attempted, in the expectation that the DFO-BP reaction product would have greater solubility in the chlorinated solvent. Shortly, **H** was dissolved in distilled water and 5 M KOH was added dropwise until pH reached value above 8.0. Trifold molar excess of H-phosphonate **J** in chloroform was added into the aqueous phase, while controlling pH of reaction mixture (maintained in range 8.40-8.76). Reaction was carried out with constant mixing (both in presence and without Et_3N) in 80 ^{O}C. Heterogeneous reaction mixture was separated. Aqueous phase was extracted with chloroform four times and solvent was combined with organic phase. Chloroform was removed under vacuum and residue was dissolved in deuterated solvent ($CDCl_3$ or CD_3OD).

However, using ^{1}H-NMR spectrum analysis of samples in both solvents, the presence of DFO or its derivatives in organic phase was ruled out. Also MS analysis (positive field) confirmed only presence of compound **J** in the sample.

Reaction in dimethylformamide (DMF)

Next, DMF as reaction medium was tested. Solubility of **H** in this solvent was an issue, because DFO-Mes forms a suspension (opaque mixture), rather than dissolves completely in DMF in room temperature. Complete dissolution of small amounts of **H** (up to 40 mg) was achieved in 80 ^{O}C, and this temperature was maintained through process. The reactions were carried out with a threefold excess of bisphosphonate towards **H** or in a stoichiometric ratio, with or without the addition of Et_3N. The reaction conditions are summarised in the **Table 17**.

Table 17 – Conditions of reactions X – XII in DMF

Reaction	Molar ratio of H:J	Et_3N eq
X	1:3	0.3
XI	1:1	0.1
XII	1:3	None

The chemical shift of protons *w* was observed in the ^{1}H-NMR spectrum. In substrate **J**, they are strongly deshielded both by the proximity of the chlorine atom and the amide group. In the product (either singularly or doubly substituted **K** or **L** compounds) the environment of this methyl group changes. A shift of the signal (~0.5 ppm) towards lower δ values would be expected due to the disappearance of the strong influence of the chlorine atom's neighbouring. In the case of the double-substituted compound **L**, this effect could be even more significant. However, in all reactions carried out in DMF, the *w* signal was present in the ^{1}H-NMR spectrum at its original location, and its intensity suggested no or negligible reaction. Mass spectra were obtained in the positive ion mode for the described reaction mixtures. In reactions X and XII, in which the bisphosphonate substrate was in excess relative to DFO-Mes, a signal corresponding to the DFO-$(BP)_2$ compound was identified (**Figure 68** and **Figure 70**,

Table 18), but the desired product **K** was not present. Reducing the excess to a stoichiometric ratio, as in reaction XI (**Figure 69**), did not result in the desired modification product, neither **K** nor **L**.

Table 18- Molecular formulae and masses of the compounds expected in the reaction mixture

Compound	Molecular formula	Molecular weight [Da]
J - bisphosphonate	$C_{11}O_7P_2H_{24}Cl$	379.7113
H - DFO-Mes	$C_{26}H_{52}N_6O_{10}S$	640.3466
K - DFO-BP	$C_{36}H_{71}N_7O_{15}P_2$	903.9344
L - DFO-$(BP)_2$	$C_{47}H_{94}N_8O_{22}P_4$	1247.1847

Again, none of the many experiments in different solvents and reagent ratios yielded the expected result. Further studies on the introduction of BP to DFO and its hydrolysis to the appropriate phosphonic acid were carried out by Dominika Kozicka under the supervision of prof. Jakub Adamek and are described in her dissertation.

3.1.1.3 Hydrolysis of the protecting ethoxy groups

The final reaction step in the synthesis of DFO modified by the introduction of a bisphosphonate group would be the hydrolysis of the protective ester groups. There are many reports in the literature on the hydrolysis of phosphonates [160]. Acidic hydrolysis is often applied, utilizing both mineral and Lewis acids, among which hydrochloric acid is by far the most widespread. On the other hand, sodium hydroxide is often used in processes occurring in basic pH. However, alkaline hydrolysis requires additional step – obtaining a phosphonate salt before final group in the acid form. Harsh conditions required in hydrolysis reaction (large amounts of acid/base, elevated temperature) might damage molecule structure. In order avoid this, the process of acidic hydrolysis was optimised to determine the conditions under which the bisphosphonate groups became exposed, while ensuring that the structure of the overall compound was not degraded.

Experiment involved two sets of samples, H-phosphonate **G** and DFO-Mes **H** each prepared in triplicate. Hydrolysis and possible degradation under different conditions was assessed by ^{1}H-NMR spectrum of the samples taken in respective time points.

Samples **H** consisted of DFO-Mes in D_2O, whereas samples **G** – bisphosphonate substrate in DMSO-d_6. Group 1 was treated with 6 molar excess of HCl and group 2 with 20 molar excess of this mineral acid. Control group 3 had no hydrochloric acid added. All the groups

(1-3) were heated to 60 ^{O}C for 22 hours, then at 95 ^{O}C for the next 23 hours. The parameters of the experiment are summarised in a

Table 19.

Table 19- Experiment parameters

	Conditions at 0 – 22 hours	**Conditions at 22-45 hours**
1	6 eq HCl, 60 ^{O}C	6 eq HCl, 95 ^{O}C
2	20 eq HCl, 60 ^{O}C	20 eq HCl, 95 ^{O}C
3	60 ^{O}C	95 ^{O}C

Organoleptic observations of the samples in the experiment: after 22 hours, a specific odour appeared in samples G1, G2 and G3. Sample H3, on the other hand, contained a white-yellow precipitate (suspension). On the following day, samples H1 and H2 still showed no change in appearance or smell from the initial condition. All samples in group G continued to emit an odour, while sample G2 emitted a sound when opened, which may indicate the release of gas stored in the reactor in the reaction. Sample G3 turned an intense yellow colour, while maintaining the clarity of the solution.

^{1}H-NMR spectra was obtained with 60 MHz Benchtop NMR Spectrometer (Nanalysis). The analysis of spectra from three time points of samples containing DFO in D_2O (group H) was preceded by aligning all spectra against the signal derived from the solvent residual peak (4.79 ppm).

Samples H1 and H2 revealed signals shift of approximately +0.2 ppm (at 22 h); +0.3 ppm (at 45 hours) and signal disappearance at 3.38 ppm. This signal corresponds to protons *t* (C**H**$_2$-N(OH)=O), which may indicate structural changes in hydroxamate group, crucial for chelating process. Sample H3 also showed signals shift of approximately +0.25 ppm (at 22 and 45 hours); however signal at ~3.5 ppm was still present. In samples G1 and G2 partial signal shift at 3.9 ppm (-O-C**H**$_2$-CH_3) towards lower δ values was observed, which did not occur in G3.

Experiment was repeated and after 24 hours samples for 400 Hz NMR were collected.

The presence of a signal at 2.4 ppm (P-C**H**$_2$-P, *c''*) and the absence of signals at 1.3 ppm and 4.2 ppm, corresponding respectively to the methyl *e* and methylene *d* protons of the departing group, confirm the full hydrolysis of the ester groups, in both G1 and G2.

However, there are no peaks corresponding to ethanol, as a byproduct of this reaction. There is also signal at 13 ppm of unknown origin. In the ^{31}P-NMR spectrum analysis, those samples showed a signal shift from ~20 ppm to ~17 ppm, indicating a change in the chemical environment of the phosphorus atom. The reduction in the chemical shift may confirm the disconnection of the ethyl groups.

3.1.2 Stability studies

Stability of ^{89}Zr-chelator complex was conducted on DFO modified by the introduction of a bisphosphonate group, obtained and isolated by Dominika Kozicka and detailed description of the synthesis and preparation of the compound **M** is provided in her dissertation. Shortly, DFO-Mes was reacted with succinic anhydride in pyridine, resulting in the opening of the anhydride ring. The resulting *N*-(3-carboxypropanoil)deferoxamine was then reacted with tetraethyl(1-aminomethylidene-1,1-)bisphosphonate. Structure of final bisphosphonate-modified DFO (compound **M**) is shown on **Scheme 29**.

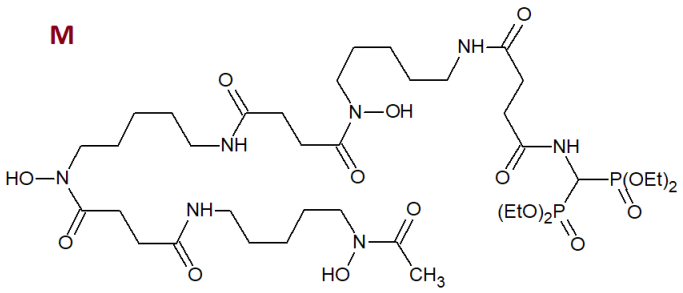

Scheme 29– Structure of compound M.

Unfortunately, compound **M** has a bisphosphonate moiety protected by ethoxyl groups, due to difficulties in selecting the optimal hydrolysis conditions for this compound. Even though, stability of complex ^{89}Zr-**M** was conducted in comparison to commercial *p*-NCS-C_6H_4-DFO labelled with ^{89}Zr. In this context, stability is understood as ability to retain the radiocation in the coordination structure.

Stability in HEPES (4-(2-hydroxyethyl)-1-piperazineethanesulfonic acid) buffer

The radio-labelling (complexation) reaction of zirconium-89 with DFO and its derivatives occurs at a pH close to 7. The radiometal is usually obtained as a solution of ^{89}Zr-oxalate in oxalic acid, so neutralisation of this mixture is necessary [83]. In laboratory practice, HEPES buffer is often used, as it stabilises the pH and makes the reaction system immune to possible changes (additives, small differences in substrate quantities). The stability of ^{89}Zr-chelator complexes at pH 7 and room temperature is therefore a fundamental requirement for such a chelator. To test the suitability of the new chelator DFO-BP,

a labelling reaction was performed using ^{89}Zr-oxalate in 0.1 M oxalic acid. Labelling reaction of both chelators was very quick, with over 90% of isotope complexed at start of the reaction and almost full labelling at 2 hours, as confirmed with radioTLC. Their stability was then controlled in various time points. For DFO-BP radiometal remained fully coordinated for 96 hours, showing slightly improved complex stability in comparison with commercial equivalent (**Figure 10**).

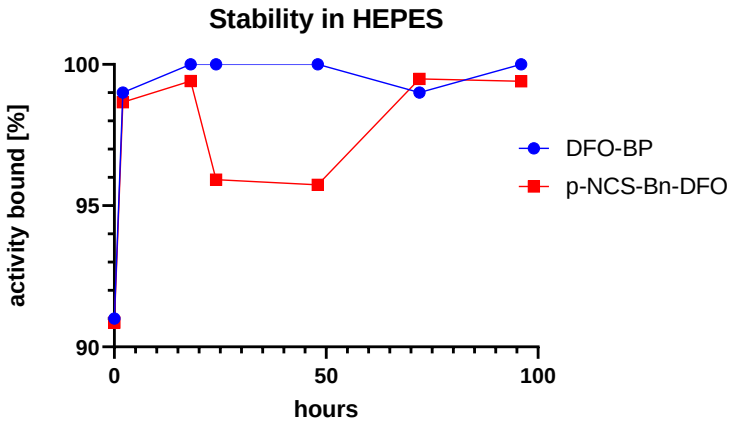

Figure 10– Stability of ^{89}Zr-**M** in comparison to ^{89}Zr-(*p*-NCS-C$_6$H$_4$-DFO)

Stability in quasi-physiological conditions

The behaviour of the radiometal-chelator complex under conditions corresponding to physiological conditions is expected to confirm the safety of use in *in vitro* and *in vivo* experiments. This may differ significantly from stability in buffer, as serum (e.g. human) contains a multitude of different components (proteins, lipids, electrolytes, antigens or hormones) that may interact differently with the complex or its components. For this reason, the behaviour of the radiometal-chelator complex in the presence of human serum and at physiological temperature is tested. For this experiment, 1.5 MBq of each radioconjugate (145 μL of 50 μM solution) was mixed with 400 μL of human serum and incubated with gentle mixing in 37 ^{O}C. RadioTLC for bound activity ratio was performed in numerous time points over 5 days and the results are gathered on **Figure 11**.

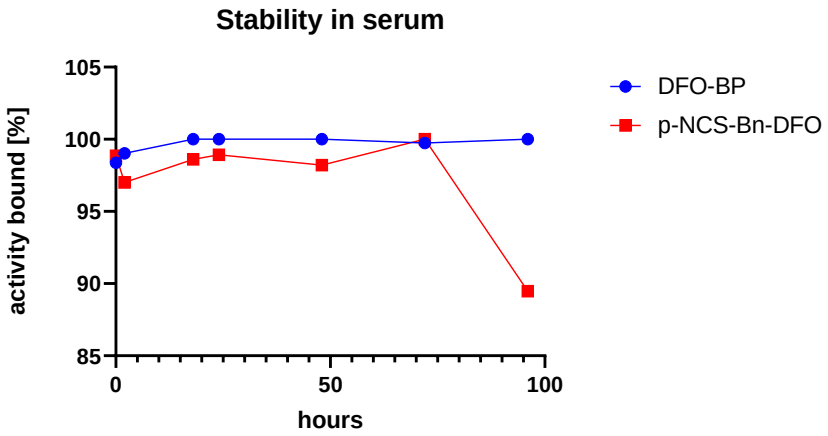

Figure 11 – Stability of ^{89}Zr-DFO-BP and ^{89}Zr-DFO-C_6H_4-SCN in quasi-physiological conditions

The experiment confirms the high stability of both complexes under quasi-physiological conditions over 5 days. DFO modified with a bisphosphonate group shows a slight advantage over *p*-NCS-C_6H_4-DFO, as manifested by the release of 10% of free zirconium-89 into the reaction mixture after 5 days from the commercial chelator.

Demetallation studies

Complexes stability was challenged against 100-fold molar excess of EDTA. Briefly, to 1 MBq of each radioconjugate (8.93 nmol), 89.3 µmol of EDTA dissolved in HEPES buffer was added. Mixture was incubated in room temperature and radioTLC of mixture was performed in various time points (**Figure 12**). After 18 hours, half of the activity from ^{89}Zr-DFO-BP radioconjugate was removed from the complex, and mixture remained in such equilibrium for the rest of the experiment.

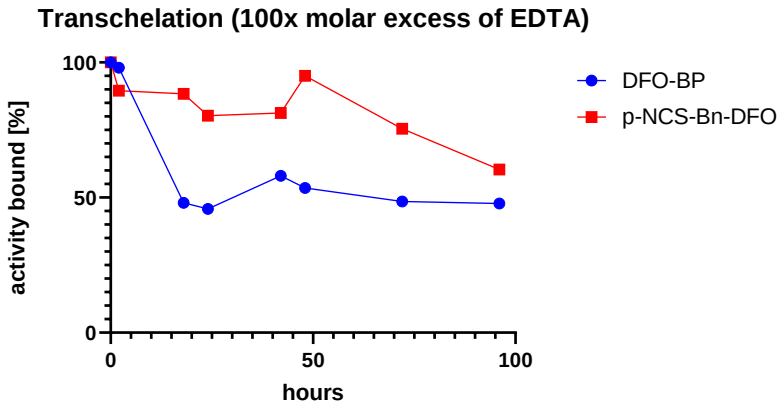

Figure 12 - Stability of ^{89}Zr-**M** versus ^{89}Zr-(*p*-NCS-C_6H_4-DFO) in 100x molar excess of EDTA

3.2 Aim II – Development of bimodal probe for simultaneous PET/MRI PD-L1 imaging

In this Aim a bimodal PET/MRI imaging probe were designed and characterized. Multifunctional and water-soluble ^{89}Zr-SPION-Atezolizumab / ^{89}Zr-DFO-SPION-Atezolizumab (**Scheme 30**) conjugates contain:

- SPIONs coated with dextran for better biocompatibility and dispersion stability.
- Atezolizumab, anti-PD-L1 mAb that targets protein expressed on both cancer cells and lymphocytes. Monoclonal antibody is conjugated onto the SPIONs to enhance their tumour-targeting ability.
- Aside, SPIONs also carry, PET radioisotope ^{89}Zr to follow their distribution by PET *in vivo*. ^{89}Zr was chosen due to its relatively long half-life that matches the biological half-life of large molecules like mAbs. For *in vitro* evaluation of their uptake an Alexa-Fluor 647 fluorochrome was conjugated to the structure.

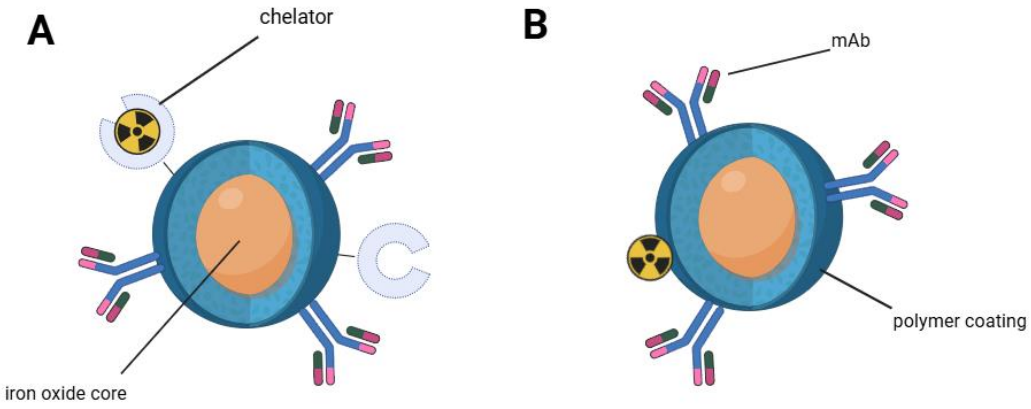

Scheme 30 - Bimodal PET/MRI probes: A: ^{89}Zr-DFO-SPION-Atezolizumab and B: ^{89}Zr-SPION-Atezolizumab

Feridex® (AMAG Pharmaceuticals), dextran-coated superparamagnetic iron oxide nanostructures was FDA-approved in in the U.S. in 1996, and soon after its equivalent Endorem® (Guerbet S.A) was introduced in Europe. Ferumoxides (non-stoichiometric magnetite core of superparamagnetic iron oxide coated with dextran) like Endorem and Feridex were used as negative MRI contrast for detecting liver lesions; however they were discontinued in 2008, followed by other iron-based contrast agents like Resovist, Sinerem and Gastromark. Currently, no iron-based contrast agents are in use, and Ferumoxytol (SPION coated with polyglucose sorbitol carboxymethylether) is approved as iron-deficiency drug. However, in second decade of XXI century the idea of repurposing SPIONs as targeted or bimodal contrast agent emerged [135, 139, 161-164].

Thus, Feraheme® was used off-label in numerous researches, because its carboxymethyl dextran polymer coatingincreased biocompatibility of nanoparticles and allowed their further modification and functionalization. Unfortunately, purchasing Feraheme® in Europe was not possible. Thus, reagent-grade dextran-coated superparamagnetic iron oxide nanoparticles were selected for the scientific purpose of this work. Unfortunately, the manufacturer does not provide information about molar weight of the SPIONs. Molecular formula and weight have been taken from Boros et al.: $Fe_{5874}O_{8752}C_{11719}H_{18682}O_{9933}Na_{414}$; MW ~ 796 kDa [139]. Thus, any further molar calculations of SPION should be taken as approximation.

Dextran functionalized iron oxide(II,III) nanoparticles of 5 nm average particle size (determined by TEM) in concentration of 10 mg/mL were initially purchased from Sigma Aldrich (cat. no 900147), as a product from external manufacturer, Ocean Nanotech. After the product was discontinued by Sigma Aldrich, another batches of supposedly identical substrate were imported directly from manufacturer (cat. no. SHP05). However, how it will be proved in the following chapters, the acquired product batches were not identical and consistent throughout the project, which significantly hampered the development of synthesis methods and the interpretation of *in vitro* results.

Throughout the duration of this project, modifications and studies were also carried out on dextran coated SPIONs with a larger radius of 20 nm. The reasoning behind this idea was that larger nanoparticles have better relaxivity and therefore their application in preclinical and clinical contexts may be facilitated compared to 5 nm SPION due to their improved MRI contrast capabilities. Unfortunately, after initial studies, these nanostructures were found to have a higher tendency to aggregate, higher cytotoxicity and higher non-specific binding to cells. However, data on structural and relaxation studies of 20 nm SPION samples have been retained in the following chapters as a comparison to leading models based on smaller nanoparticles.

As mentioned above, the gold standard for labelling compounds with ^{89}Zr is using of a macrocyclic chelating agent – usually DFO or its derivatives [161, 165]. Interestingly, there are reports on heat-induced radiolabelling (HIR) of SPIONs using a chelator-free labelling method [139, 140]. However, this method requires more severe temperature conditions (120 ^{O}C), which could affect the mAb structure, when ^{89}Zr is introduced at the end of conjugation. Therefore, the first probe was obtained by incorporating ^{89}Zr to the surface of the nanostructure (HIR) and then mAb was attached (**^{89}Zr-SPION-Atezolizumab**). The second conjugate was prepared by attaching the mAb and DFO

to the nanostructure and then the obtained structure was radiolabelled (**^{89}Zr-DFO-SPION-Atezolizumab)**, in reaction that does not require heating. Schematic illustration of conjugation and labelling route for both bimodal probes are presented in **Scheme 31** - Synthesis route of ^{89Zr} -SPION-Atezolizumab and $^{89Zr\text{-}DFO\text{-}SPION\text{-}Atezolizumab}$..

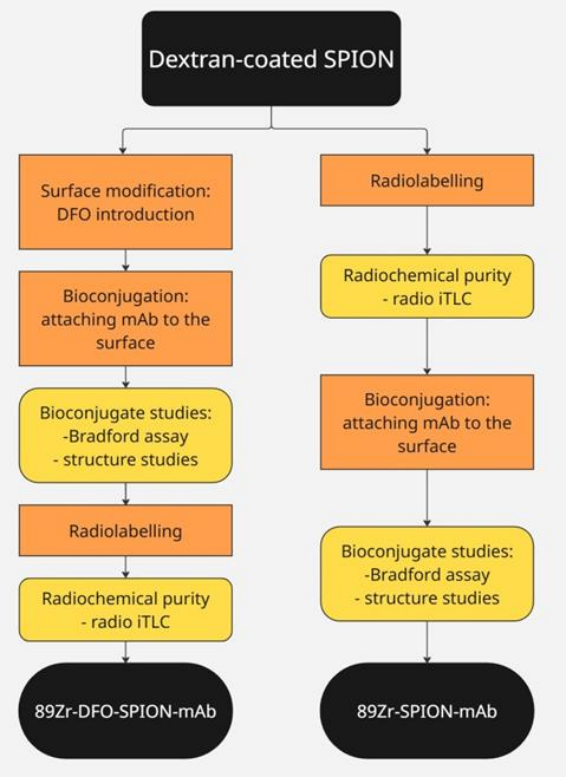

Scheme 31 - Synthesis route of ^{89}Zr -SPION-Atezolizumab and ^{89}Zr-DFO-SPION-Atezolizumab.

In the following parts of this work, SPIONs and their modified derivatives will be addressed to as 'nanoparticles', 'nanostructures' or 'functionalised SPIONs', which all should be treated as synonyms.

3.2.1 Bioconjugation

The introduction of a monoclonal antibody into the structure of a nanoparticle can be carried out in a number of different ways. This process will be referred to as bioconjugation, due to the biological nature of this protein molecule. The original idea was to use disulphide bridges to link the Atezolizumab to the nanoparticle. However, this would have required:

- Modification of the surface of SPION nanostructures (or SPION-DFO conjugates) by introducing a thiol group.
- Modification of the monoclonal antibody or purchase of a suitably modified protein

- Attachment of the modified antibody to the nanostructure by reaction of two thiol groups and formation of disulphide bridge

Modifying the surface of dextran-coated SPIONs to introduce pending thiol groups can be achieved using carbodiimide chemistry (e.g., EDC/NHS) to introduce reactive sites that can then be conjugated with thiol-containing molecules. However, modifying the antibody is already much more complicated. Due to the need to preserve the nature of the antibody binding sites, conventional non-specific thiolation strategies cannot be used. These include, for example, the reduction of existing disulphide bridges in the structure, which would expose the free thiol groups. However, this may affect the structure or affinity of the antibody. The safest option is site-specific antibody engineering. However, it requires in-depth planning of the modification site, genetic modification, expression of a new version of antibody in mammalian cells and its purification, characterisation and optimisation [166]. All of the above processes require specialised knowledge and equipment that are beyond the scope of this work.

Functionalization of the nanoparticle surface to incorporate isothiocyanate groups was also considered. This group combines easily with a free amine group, such as the lysine group of a monoclonal antibody. This approach is used in the bioconjugation of the *p*-NCS-C_6H_4-DFO chelator into monoclonal antibodies.

Proposed way of –NCS group introduction is presented on **Scheme 32**:

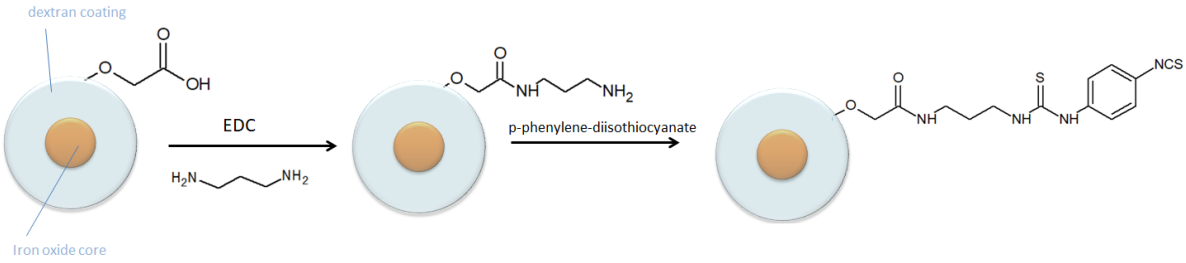

Scheme 32- Schematic representation of –NCS group introduction

Shortly, first step of reaction was EDC-mediated introduction of amine group into dextran coating of nanoparticle. This reaction occurs in following way: EDC forms unstable *O*-acylisourea intermediate in reaction with carboxylic group. Intermediate compound is highly reactive and reacts easily with primary amine, present in reaction mixture. Isourea by-product is released into reaction mixture and bond between carboxylic and amine group is formed. In second step, *p*-phenylene diisothiocyanate would react with newly introduced pendant amine groups.

Amine introduction was carried out in aqueous solution and slightly acidic conditions to promote efficient crosslinking reaction. MES buffer was chosen as a reaction medium, because it is carboxyl- and amine-free, thus would not interfere with the coupling reaction. Unreacted EDC and diamine were removed from reaction mixture with Amicon 50kDa centrifuge filtration, and medium was changed to bicarbonate buffer (BC, pH = 9.0). Presence of amine groups was confirmed with Fourier-transform Infrared Spectroscopy (FTIR) (3.2.3.3 *Fourier transform infrared spectroscopy*.)

However, as isothiocyanate substrate is poorly soluble in water, it was dissolved in MeCN and added to reaction mixture in second step of this process. Reaction incubated overnight and in room temperature, and after reaction end precipitation was observed. It was removed with numerous MeCN washes on Amicon 50 kDa filter.

Reddish-brown residue of SPION was then analysed by FTIR. The presence of a new signal at a wave number of 2280-2000 cm^{-1} would confirm the introduction of an isothiocyanate group into the structure, as the stretching vibration bands originating from the cumulative bonds are in this range [167]. The isothiocyanate group, R-N=C=S, is an example of cumulative double bonds. Absence of this additional bond confirmed that expected structure was not obtained, probably due to *p*-phenylene diisothiocyanate poor solubility in aqueous media.

Finally, it was decided to simplify the process and perform an EDC-mediated reaction between the carboxyl group of the dextran coating and the lysine groups of the monoclonal antibody. A schematic representation of the bioconjugation and purification process is shown in **Scheme 33**. Determination of the amount of unreacted protein in the supernatant would enable the calculation of the protein attached to the NPs surface.

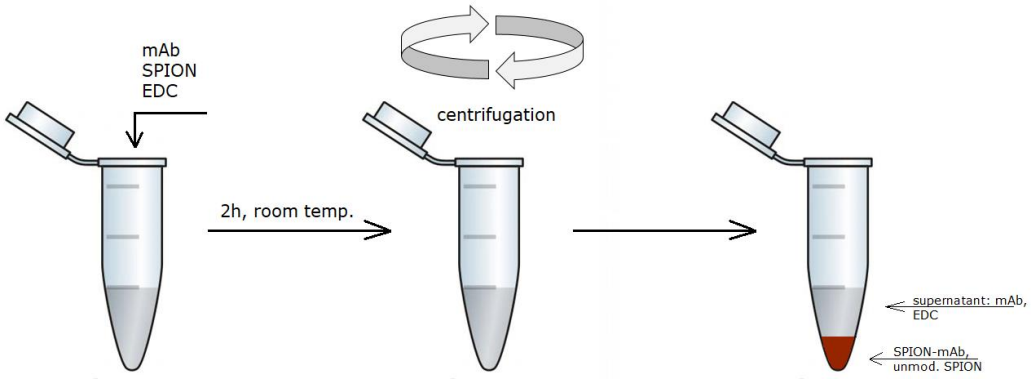

Scheme 33- Conceptual representation of bioconjugation process.

In initial experiments, Atezolizumab concentration was measured by UV/Vis spectrophotometric measurements, performed in NanoDrop One. However, supernatant

contained unreacted EDC and isourea by-product, which interfered with measurement. That was confirmed by A260/A280 ratio value of 0.74, with protein amount calculated to be higher than the initial amount in the reaction mixture. Filtration of supernatant on 50 kDa MWCO centrifugation filter removed EDC and its by-product. Repeated absorbance measurement revealed 13% of protein reacted, however filtration could have led to unwanted loss on protein, due to high antibody's adhesion.

However, it was observed that high amounts of EDC caused irreversible precipitation of nanoparticles. This effect was especially observed in one specific nanoparticle batch. Probable explanation is that high concentrations of EDC can lead to increased ionic strength, promoting aggregation and subsequent precipitation of the nanoparticles. Precipitation problems were mostly eliminated by heating both SPION solution and EDC dissolved in adequate medium to 27-30 ^{O}C. EDC solution was then added dropwise to the SPION dispersion with constant mixing. After purchasing another batch of reportedly same product, precipitation problems did not occur. This led the author to believe that nanoparticles differed in physicochemical properties between batches.

In order to improve the degree of bioconjugation (understood as the amount of antibody attached to the nanoparticle, mAb units per nanoparticle), the effect of adding N-hydroxysulfosuccinimide (sulfo-NHS) to the reaction mixture was tested. Sulfo-NHS (or NHS, for non-aqueous conditions) is often included in EDC crosslinking protocols, because it forms more stable esters with very reactive *O*-acylisourea intermediate [168]. Last step of a process is amide bond formation with primary amine, resulting in the same product like in EDC chemistry. A comparison of processes using EDC alone and EDC/sulfo-NHS combinations as coupling agents, showed no significant differences in the amount of protein incorporated into the nanoparticle structure.

Initially, the ratio of protein to nanoparticles in reaction mixture was 3:1 (weight ratio), what equals to approximately 5.6:1 molar ratio. Increasing the amount of monoclonal antibody to 10-fold molar excess resulted in doubling the amount of protein introduced into surface. Calculated degree of bioconjugation at this stage of research was c.a. 2.0.

Unfortunately, despite the above modifications, the bioconjugation reaction still did not occur with sufficient efficiency. First attempts in specificity of binding study showed, that nanoconstruct does not bind specifically to the PD-L1 receptors. It was hypothesised weak efficiency of bioconjugation reaction might be due to the process taking place in a slightly acidic environment, when the isoelectric point (pI) of Atezolizumab is approximately 8.6-8.8 [169]. The isoelectric point is the value of pH at which the population of ampholytic

molecules contains, on average, as many positive as negative charges, resulting in the total charge of the entire population being zero. The isoelectric point depends on the presence of charged amino acids in the antibody structure and will therefore be slightly different for each monoclonal antibody. Antibodies typically have pI values in the range of 6-9 due to the charged amino acid residues. At pH values below the pI, antibodies tend to have a net positive charge due to protonation of amine groups. Lysine residues have a pKa around 10.5, meaning that at neutral and acidic pH values below the lysine pKa, the ε-amino groups on lysine become increasingly protonated, reducing their nucleophilicity and reactivity in conjugation reactions [155]. This characteristic is taken advantage of in the bioconjugation of Atezolizumab with *p*-NCS-C_6H_4-DFO, as described in several papers. Atezolizumab is conjugated to the chelator DFO by reacting the ε-amino groups on surface-exposed lysine residues in a pH = 9.0 (in BC buffer) to maximize lysine reactivity [42, 170].

Based on the above considerations, an experiment was designed to compare different pH conditions in the two-step bioconjugation of Atezolizumab to dextran-coated SPION via EDC-mediated crosslinking (**Scheme 34**).

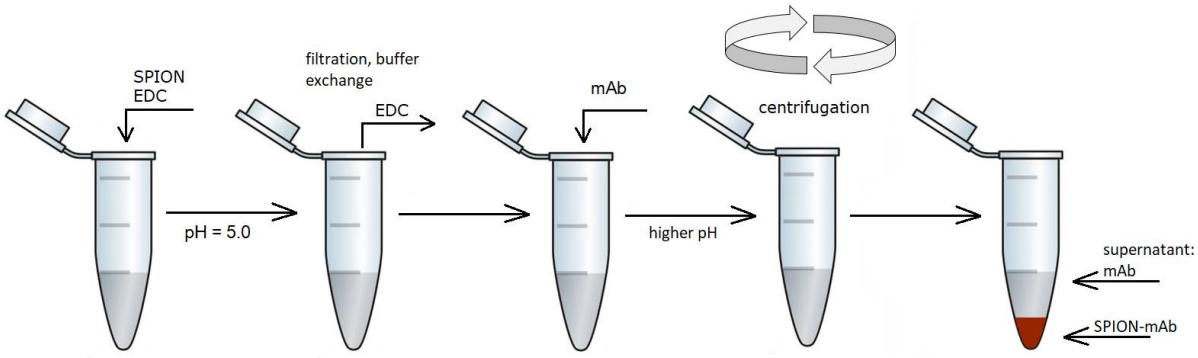

Scheme 34- Schematic representation of bioconjugation process with pH change

First, activation of the nanostructure surface was carried out at pH = 5.0 and in the presence of an excess of EDC. Then, the solvent, unreacted EDC and possible by-products were filtered out using 50 kDa MWCO filters and activated nanoparticles were washed and transferred to three different buffers: phosphate buffer saline (PBS), HEPES buffer (both pH = 7.0) and BC buffer pH = 9.0. The use of PBS buffer was inspired by the Gawęda et. al., as author performed Trastuzumab-ferrite nanoparticles conjugation in analogous way [171]. The HEPES buffer was chosen because the labelling reaction of Atezolizumab occurs in this buffer and its neutral effect on this antibody is known. The BC buffer with the highest pH was chosen because of Atezolizumab's comparable pI. Monoclonal antibody in 30-fold molar excess was added to each sample. After several hours while gently shaken in room temperature, samples were centrifuged, supernatant collected, then brown residue was

washed with adequate buffer and centrifuged again. Supernatants were joined and amount of unreacted protein was measured according to BCA assay. This time the assay was possible to conduct, because EDC was removed from reaction mixture during filtration and buffer exchange. Results revealed the highest degree of bioconjugation of 2.78 for sample, which reacted in the highest pH.

3.2.1.1 Assessment of the amount of amine groups introduced

FTIR spectroscopy, however helpful in confirming presence of pendant amine groups, does not give any quantitative information. Accurate determination of degree of functionalisation is necessary to optimise reaction conditions, ensure compound properties and understanding of the process.

Colorimetric titration – recoverable method

Initial idea of quantitative determination of amount of amine moiety introduced was based on simple and recoverable titration method, originally developed for amine-modified carbon nanotubes (**Scheme 35**) [172]. Nanotubes were reacted with known amount of HCl, filtered and unreacted HCl was titrated with NaOH of known concentration in presence of phenolphthalein as indicator. Difference in HCl amount (initial vs. unreacted acid) corresponds to the number of moles of amino groups. Nanoparticles containing an amine group on the surface in salt form are then recovered to the amine form by reaction with NaOH.

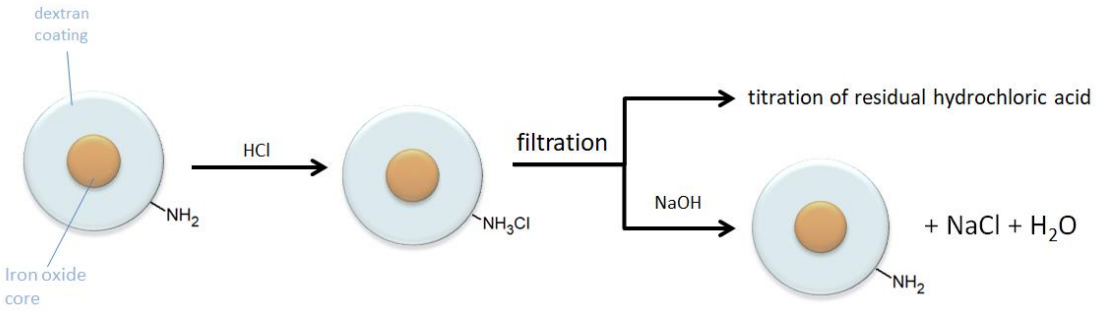

Scheme 35- Amine group titration

Amount of primary amine groups was calculated from the following formula: $n_{NH_2} = V_a \cdot C_a - V_B \cdot C_B$, where V is volume of acid (A) or base (B) and C is concentration. Degree of functionalization (DOF) is defined as number of amine groups per one nanoparticle unit and was obtained by comparing molar amounts of amine and SPION, with formula: $\frac{n_{NH_2}}{n_{SPION}}$. Prior to titration, concentration of HCl was standardized with NaOH used in experiment (colorimetric titration), in order to obtain exact concentration value.

Unfortunately, despite the use of a titrator, which should have better accuracy than manual titration, the results were not reliable (**Table 20**).

Table 20- Results of colorimetric titration

	V_A [173]	C_A [M]	V_B [173]	C_B [M]	n_{NH2} [mmol]	DOF
A	10	0.054	10.6	0.05	2.600	2094
B	1.5	0.058	1.769	0.05	- 0.002	**negative**
C	1.5	0.058	1.263	0.05	0.023	9.2
D	3	0.057	3.3	0.05	0.005	2160
E	5	0.063	6.606	0.05	- 0.015	**negative**

Twice, a negative result was obtained, meaning that the amount of titrant solution exceeded the amount of analyte. This was probably due to several factors, including: dilution of the titrant in the titrator system, analyte losses during the filtration step and very small amounts of analyte, which drastically increases the contribution of errors (including droplet error) to the final result. An attempt was made to reduce the error by reducing the volume of samples analysed, thus increasing the acid concentration. Unfortunately, treating the nanoparticles with 2M hydrochloric acid affected their structure - a flocculent precipitate was observed. Results B and C analyse the same sample at different stages of functionalization. Result B refers to the SPION-NH_2 sample, which was further modified after the determination of the amine groups. After reaction with the chelator *p*-NCS-C_6H_4-DFO, the sample was retested for the amount of free amino groups. As presented, the result obtained after the first modification step indicates a measurement error, which may have various causes. The introduction of the chelator, which reacts withsome of the amino groups, increased the DOF according to the above determination. This indicates, as well as the subsequent negative result of the E, that the method is unreproducible and unsuitable for the chosen application. Thus, efforts have been directed towards other methods.

Fluorescamine assay

The suitability of the method using fluorescamine was then tested. This compound reacts rapidly with primary amines to form a fluorescent derivative, as presented on **Scheme 36**.

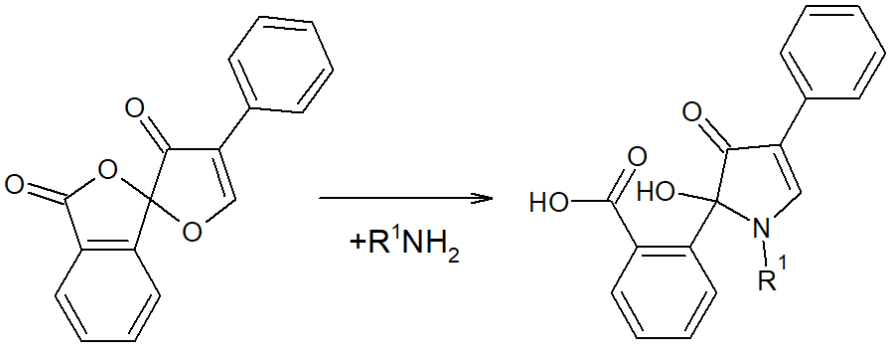

Scheme 36- Reaction of fluorescamine with primary amine. Final compound is fluorescent.

When excited with 365 nm UV light, it emits light at a wavelength of approximately 470 nm. For this reason, it is also often used for the quantification of proteins and peptides, alongside assay such as BCA and Bradford. However, in this case the method has been adapted for the indirect determination of amino groups introduced on the surface of the nanoparticle. Briefly, a calibration curve was prepared containing fixed concentrations of 1,3-diaminopropane and EDC. The reaction mixture containing the excess diamine, coupling agent and nanoparticles was filtered through a 50 kDa MWCO filter. The supernatant (containing the diamine and EDC), and a calibration curve were added to a black 96-well plate, followed by the addition of a 1% (*w*/*v*) fluorescamine solution. Excitation with UV light and measurement of the amount of light emitted allowed calculation of the amount of unreacted amine in the supernatant.

First, it was necessary to establish the concentration range over which the method is linear. Different dilutions of the amine used in the process were prepared and the fluorescence of the mixture was studied after the addition of a fixed amount of 0.1% fluorescamine solution. In the range of 0.231 to 1.16 M of 1,3-diaminopropane, the values of the emitted fluorescence did not show linearity, nor did they in the range of 0.07 - 0.7 M. Decreasing the concentration to millimolar range finally allowed for linear calibration curve to be obtained in the range of 0.5 - 3.7 mM.

Amine functionalization process was carried out like described in experimental section (4.4.1. *SPION surface modification*). Briefly, SPION solution was exchanged to 0.1 M MES buffer, then EDC in same buffer was added. After short activation, diamine was added and pH adjusted to 6.0. In parallel, the reference sample was prepared in the same way as the samples, minus the nanoparticles: to the same volume of EDC solution was added diamine, HCl to lower the pH and MES in appropriate amounts. The reference sample and SPION samples were then mixed at for 2 h. After this time, the nanoparticles were filtered, followed by a buffer wash and the supernatants were combined. The volume

of the supernatant was measured and the concentration of unreacted amine in the supernatant was determined.

For this purpose, the reference sample and supernatant were diluted 10-fold to achieve a concentration within the linearity range of the method. Reference sample was added in appropriate amounts (0 - 20 µL) to the wells of a 96-well black plates obtain a five-point calibration curve in the range 0 - 2.0 mM, topping up the volume to 190 µL with MES buffer. Supernatant samples of 20 µL were added to further wells and 170 µL of MES buffer was added to each well. All samples (tested and calibration curve) were prepared in triplicate. The same amount of 0.1% fluorescamine solution was then added to all samples and the fluorescence of the solutions was immediately tested.

A trend line was drawn from the calibration curve by linear regression and the concentration of 1,3-diaminopropane in the supernatant was calculated. The results of the functionalization reaction are summarised in **Table 21**. DOF was calculated from measured SPION amount in sample (UV/Vis absorbance) and indirect amine group quantification.

Table 21- DOF calculated from fluorescamine assay method.

Substrates			**Supernatant**			**Product**			
SPION		**amine [µmol]**	**amine [mM]**	**Volume [mL]**	**Unreacted amine [µmol]**	**SPION**		**Amine [µmol]**	**DOF**
[mg]	**[nmol]**					**[mg]**	**[nmol]**		
1	1.25	95	77.37	1.213	93.85	0.907	1.13	1.15	1017
1	1.25	95	96.60	0.825	79.70	0.980	1.23	15.30	12490
1	1.25	95	101.34	0.798	80.87	0.946	1.18	14.13	11946

The results posted above indicate a significant degree of surface functionalization of the nanoparticles, which enabled further modifications. Finally, the selected bimodal probe model and its synthesis route did not require an amino-modification step on the surface, but the developed test method may be useful for future syntheses of nanoparticles with different characteristics.

3.2.2 Radiolabelling

3.2.2.1 Labelling through DFO

Introduction of DFO into the nanoparticles structure

Introducing chelators into nanostructure has been broadly described in scientific literature and addressed in previous parts of this dissertation.

Initial idea was inspired by study by Thorek et al. [161] and presented on **Scheme 37** below:

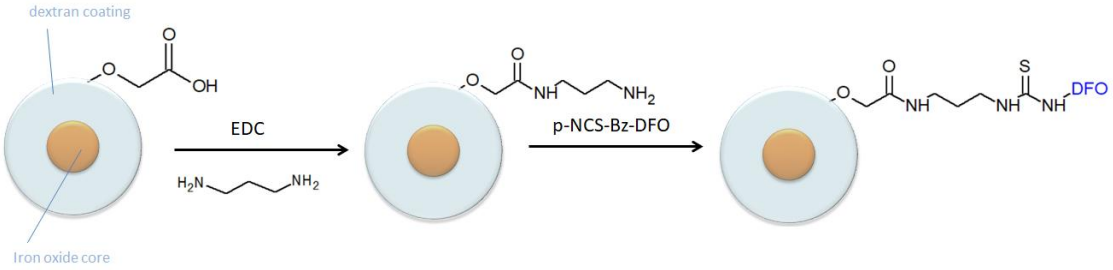

Scheme 37 - Reaction of modification using EDC and *p*-NCS-C_6H_4-DFO

Presented manner requires two-step reaction: firstly introducing amine group through EDC-mediated reaction of carboxyl moiety with diamine. Next step would be an introduction of modified deferoxamine (*p*-NCS-C_6H_4-DFO). Isothiocyanate group of the modified chelator reacts easily with primary amine group introduced in previous step. After some experiments according to scheme above, the following issues have arisen:

a) two-step reaction requires two assessments: the number of amines conjugated and later on, the number of chelators introduced
b) multistep reaction entails numerous purification steps hence reduces the final process efficiency, as some of the product is lost during these stages
c) quantitative determination of DOF by isotopic dilution method showed very poor reaction yield.

For the above reasons, it simplification of the process was proposed. Instead of two steps, the reaction would take place in a single-step reaction, in which the carboxyl group of the nanoparticle coating would react with the amine group of the DFO-Mes (**Scheme 38**).

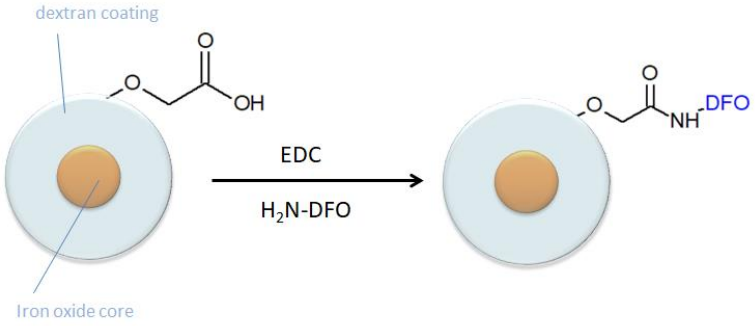

Scheme 38- Simplified, one-step process of DFO introduction

The resulting advantages of such a single-step process include:

- use of DFO-Mes instead of the more expensive *p*-NCS-C_6H_4-DFO derivative,
- smaller loses on the nanoparticles, due to singular purification of the reaction mixture;
- singular assay characterization (quantification of the amount of chelator introduced).

Assessment of the amount of chelator incorporated into the structure

Determining the amount of chelator incorporated into the nanoparticle surface is important for several reasons. Firstly, it allows an estimation of the reaction yield and, if the value is too low, a modification of the reaction conditions to obtain better results. Secondly, in relation to the rate and efficiency of the labelling reaction, it allows determining what amount of chelator is sufficient to completely label the nanostructure.

Conductometric titration

Deferoxamine mesylate is registered as an iron-chelating drug, used as a treatment in acute iron and aluminium intoxication (generic name: Desferal). Thus, it is described in the Pharmacopoeia European, and the quantitative method for the determination of DFO-Mes was taken from this source [174]. The described conductometric titration method is based on reaction of a deferoxamine with sulphuric acid (titrant) with a ferric ammonium sulphate solution (titrate). The end point is determined potentiometrically, using a platinum standard electrode and a suitable reference electrode. This methodology however encountered similar problems as another titration assay, described above for determination of amine groups introduced. In addition, with the use of electrodes available at site it was impossible to determine end-point confidently. For this reason, this methodology has not been used in the synthesis of functionalised bimodal probes.

Isotopic dilution

Isotopic dilution method was inspired by work of Deri et al. [175]. The basic concept of this method is to add an isotopic counterpart to the test sample and determine their ratio in the final mixture. In this particular application, number of chelators in sample is determined by labelling known amount of conjugate with increasing volumes of ^{89}Zr and ^{nat}Zr mixture ('working solution'). Amount of $^{89}Zr^{4+}$ cations in working solution is negligible; it is therefore assumed that the amount of zirconium ions is approximately equal to the ions originating from the 'cold' compound. Increasing the volume of working solution per sample changes the amount of $^{nat}Zr^{4+}$ cations significantly, but not the $^{89}Zr^{4+}$ (due to its low concentration in the mixture). Hence, as the amount of $^{nat}Zr^{4+}$ ions in the sample increases, the probability of the conjugate being labelled with a radioactive isotope decreases. Number of chelators per nanoparticle is calculated as ratio of bound to unbound ^{89}Zr x total amount of zirconium cations in sample per amount of nanoparticle-based conjugate in a sample:

$$N_{chel} = \frac{\frac{bound\ ^{89}Zr}{unbound\ ^{89}Zr} \times moles\ of\ Zr^{4+}}{moles\ of\ nanoparticles}$$

Experiments were performed like it is described in experimental section 4.4.2. *Quantitative assays.* Briefly, studied sample was prepared in triplicate, in equal and known amounts. To each sample increasing volumes of working solution was added (20, 25 and 30 µL). After incubation, ratio of bound to unbound ^{89}Zr was determined by radioTLC (method *b*). In **Table 22** an exemplary calculation for the SPION-DFO sample is shown.

Table 22- Calculation of number of chelators per nanoparticle for SPION-DFO-Atezolizumab sample.

No	Nanoparticle [mol]	Working solution			radioTLC		Number of chelators per nanoparticle
		Activity [MBq]	Volume [µL]	Zr^{4+} [mol]	Activity bound [%]	Activity unbound [%]	
1	$4.28 \cdot 10^{-11}$	0.46	20	$8 \cdot 10^{-8}$	19.96	80.04	2.33
2		0.59	25	$1 \cdot 10^{-9}$	9.41	90.59	1.76
3		0.71	30	$1.2 \cdot 10^{-9}$	15.49	84.51	4.06
						Average:	**2.72 ± 0.98**

Results from multiple assays of different samples are gathered in **Table 23**.

Table 23- Number of chelators per nanoparticle for different batches of DFO-modified SPIONs.

Chelators per nanoparticle	3.10	2.72	2.78	2.82	1.70	2.52	1.80	2.03
Standard deviation	0.90	0.98	0.39	1.06	0.65	0.90	0.19	0.67

The average number of DFO molecules introduced into the nanoparticle structure is 2.43 +/- 0.49. This is lower than in the literature (7 chelators per particle in the study by Thorek et al. [161]), but both the methodology of the nanostructure modification and the method of testing the amount of DFO introduced were different in the referenced studies.

Assuming that at least one chelator molecules of a nanoparticle is occupied by the radionuclide during the radio-labelling process, the ratio of paramagnetic to radionuclide would be 6000:1. Taking into account the difference in sensitivity between MRI and PET techniques (10^{-6} mol/L and 10^{-11} - 10^{-12} mol/L, respectively [176]) this ratio might be a satisfactory equilibrium in paramagnetic substance and radionuclide for simultaneous PET/MRI imaging.

Radiolabelling of DFO-modified SPION

At the stage of planning the radiolabelling method, it was assumed that labelling via the DFO chelator would be a simple process. It is well documented in the literature, including the study of Thorek et al. (which was the starting point for this research project). However, the process of labelling through a chelator proved to be an unpredictable reaction with low yields.

Certainly, the rate and yield of this reaction was influenced by the degree of modification, i.e. the amount of DFO molecules introduced on the surface of the nanoparticle. Furthermore, significant differences were observed when using ^{89}Zr of different origins. In the course of the present study, isotope from three sources was used, including on-site production on IBA Cyclone 18/9 cyclotron. Radioactive material varied in purity and activity concentration, significantly influencing RCP (radiochemical purity) and RCY (radiochemical yield).

Highest RCY was obtained for SPION-DFO-Atezolizumab with number of chelators per nanoparticle calculated to be 2.78 (determined by isotopic dilution). Reaction was

performed with ^{89}Zr-oxalate obtained from PerkinElmer (The Netherlands), neutralized to pH = 7.0. To 25 µL of radioactive solution (7.82 MBq at the start of the reaction), 57 µL of SPION-DFO-Atezolizumab dispersion (c.a. 142.5 µg SPION) was added. Reaction was carried out in 30 ^{O}C on a thermoblock with shaking. RadioTLC was performed after 30 min in order to determine the degree of labelling (**Figure 13**). Due to low percentage of activity bound to the nanoconstructs, reaction was left overnight, resulting in 94.73% RCY after 20 hours.

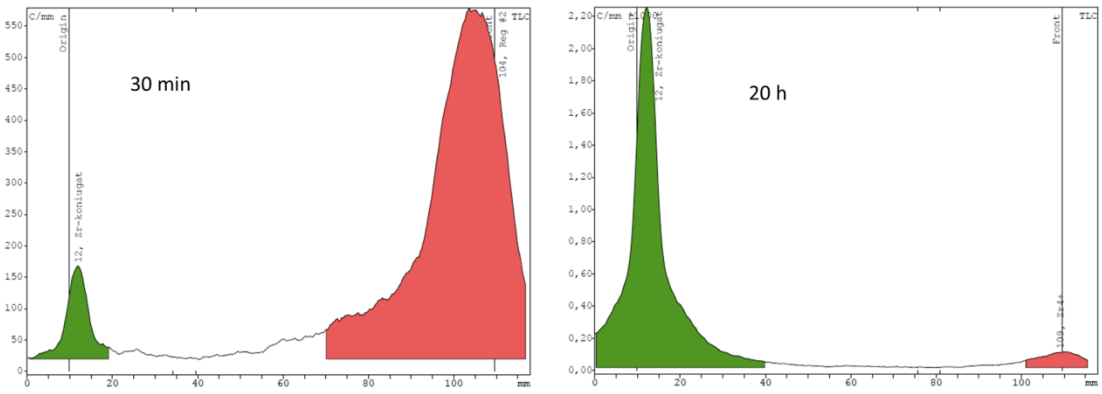

Figure 13 - Reaction progress of DFO-labelling (radioTLC)

High yield of this reaction is probably due to the high concentration of radiocation (95 MBq/mL) and chelator-modified nanoparticle in reaction mixture. However, reaction times of 20 hours are highly impractical in context of radiolabelling, due to radioactive decay. Moreover, for larger reaction volumes and/or lower initial activities, radiochemical yields often remained below 5%, generally ranking in the region of 50% labelling after 20 hours of reaction.

3.2.2.2 Heat-induced radiolabelling

Chelator-free labelling was adapted from *Nature* protocol [140]. Shortly, ^{89}Zr oxalate was neutralized to pH = 7.5 – 9 with 1 M Na_2CO_3 and diluted with Chelex-treated water (CTW). Radioactive solution was then added to nanoparticles in glass vial with magnetic stirrer and reaction went on for 2 hours at 120 ^{O}C in silicon oil bath. Reaction progress was monitored by radioTLC (method *a)* described in 4.2. Unbounded ^{89}Zr was quenched with DFO solution and reaction mixture purified with PD-10 chromatography column.

Recommended TLC method involved strongly acidic cation exchange silica gel (SG) plates, soaked in CTW and dried well prior to use, and CTW as developing phase. The expected separation was that free zirconium-89 and ^{89}Zr-DFO would remain at the start of the strip, and that the labelled nanoparticles would move with the phase front (Rf ~1.0). However, due to their orange-brown colour, it was possible to observe that the nanoparticles partially

remain at the start of the strip, which disrupts the ratio of bound and unbound activity to nanoparticles obtained in the radioTLC measurement. In order to avoid this problem, which affects the value of RCY, two more TLC systems were tested.

Both methods were taken from the literature. The first was described in the context of HIR of dextran-coated SPIONs, and involved separation on SG 60 F_{254} on aluminium strips, using a DTPA solution as the mobile phase [139]. The second method, applicable to the determination of the RCY of zirconium-89-labelled monoclonal antibodies, uses SG impregnated glass paper and NH_4OAc/EDTA as the mobile phase [42]. Both of these methods are based on the complexation of free zirconium-89 present in the reaction mixture by a chelator (DTPA/EDTA). Thus, in both TLC methods ^{89}Zr–SPION and ^{89}Zr–DFO-SPION remained at the baseline (Rf = 0.0) whereas unbound $^{89}Zr^{4+}$ cations coordinated as ^{89}Zr–DTPA or ^{89}Zr–EDTA eluted with the solvent front (Rf = 1.0). All the methods are presented in **Table 24**.

Table 24 - RadioTLC methods and expected R_fs.

Method	**TLC plate**	**Mobile phase**	**Expected R_f**
a	SG with strongly acidic cation exchange resin	Chelex-treated water	^{89}Zr – 0,0-0,2 ^{89}Zr-SPION – 0,9-1,0
b	Glass microfiber chromatography paper impregnated with SG	0.1 M ammonium acetate, 25 mM EDTA	^{89}Zr-SPION – 0,0 ^{89}Zr – ~1,0
c	SG 60 F_{254} on aluminium strips	DTPA solution	^{89}Zr-SPION – 0,0 ^{89}Zr – ~1,0

Both tested methods (*b* and *c*) proved useful and, due to the shorter plate development time in method *b*, it was used in further studies.

Subsequently, an attempt was made to lower the reaction temperature and verify the effect of this modification on the labelling rate and final RCY. Carrying out the reaction in an aqueous solution, at a temperature above the boiling point of water, implies the necessity of a condenser or the use of venting. For reactions carried out in such a small volume as the radiolabelling (up to 500 μL), the use of a condenser is not possible. A boiling reaction mixture can also be a source of radioactive contamination. When hermetic reactors (e.g. glass vial with screw cap) were used, leakage or deformation of the plastic components has occurred. On the other hand, reaction in open reactor (allowing the aqueous phase to evaporate) led to drying and burning of the mixture. Lowering the HIR temperature

to 95 ^{O}C allowed the transfer of the reaction from the glass vial in the silicon oil bath to the plastic vial (eppendorfs) in the thermoshaker. Fortunately, RCY did not decrease significantly by lowering the reaction temperature. The change in a heating method has also affected the way of mixing. With the introduction of shaking on the thermoshaker, the need for a magnetic stirrer was removed. Due to their magnetic behaviour, the nanoparticles aggregated on this element reducing the quantitative yield of the reaction. The reaction mixture of one of the HIR reactions (carried out in glass vial with magnetic stirrer, in silicon oil bath) had an activity of 7.75 MBq. When it was transferred from the glass reactor to the eppendorf, it was shown that the loss of activity on the reactor + magnetic stirrer was 3.85 MBq (50%). An attempt was made to overcome the problem by sonicating the sample and the stirrer in the reactor. Some of the labelled nanoparticles transferred back into disperssion, improving the RCY to 65%. Using radioTLC, it was confirmed that sonication did not desorb zirconium-89 from the surface of the nanoparticles (100% bound activity; bottom graph on **Figure 14**). However, the lowering of the reaction temperature and the resulting change in reactor and mixing method allowed the loss on the labelled product to be minimised.

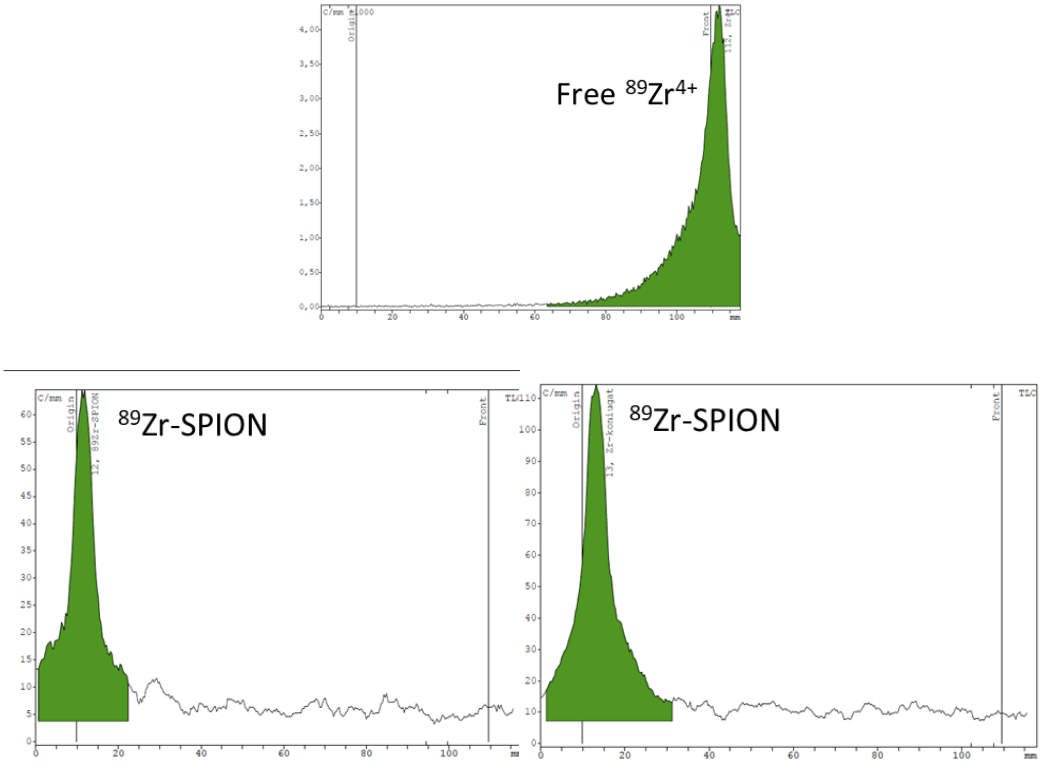

Figure 14 – RadioTLC of ^{89}Zr-oxalate (top), reaction mixture after heat-induced radiolabelling (bottom left) and reaction mixture after sonification (bottom right).

Crucial step for successful HIR is pH control. As mentioned above, desired are slightly basic conditions and deviation into both neutral and too high pH seriously decelerate or even stop

the reaction. Reaction of 17.85 MBq of ^{89}Zr solution with 0.5 mg SPION (20 nm) was carried out in pH = 7.0 and in temperature of 95 ^{O}C. Such temperature proved to be sufficient for complete radiolabelling in 60 minutes in pH 8.0 (**Figure 14**), however in neutral pH it slowed down significantly, achieving 85% RCP in 110 minutes (**Figure 15**).

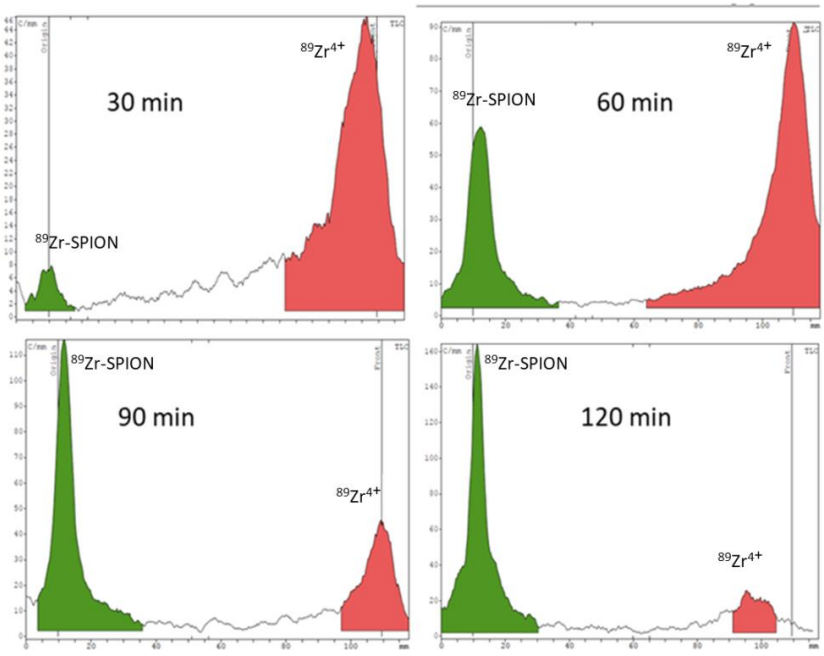

Figure 15– Reaction progress of HIR at neutral pH (radioTLC)

The effect of pH exceeding 9.0 proved even more significant: the same amount of SPION (0.5 mg, SPION 20 nm) was labelled with 7 MBq of ^{89}Zr-oxalate in 95 ^{O}C and pH = 9.5. After 100 minutes degree of labelling was 1.5% (**Figure 16**).

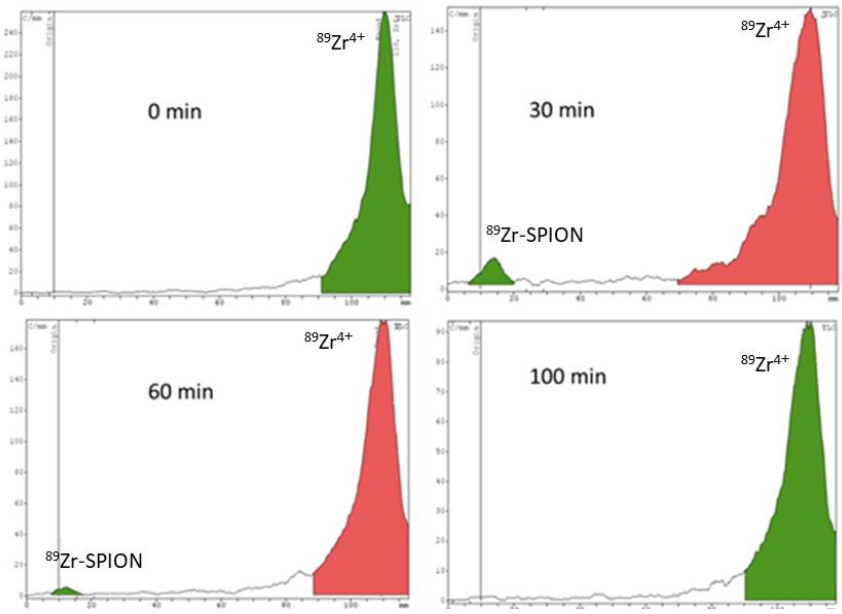

Figure 16- Reaction progress of HIR at pH=9.5 (radioTLC)

3.2.3 Structure studies

Physical properties like potential and size of nanoparticles have a significant impact on biocompatibility of structures. Thus, an in-depth understanding of their characteristics, including size, potential and confirmation of surface decoration composition is necessary to predict their *in vitro* and in *vivo* behaviour. The size of nanoparticles affects their pharmacokinetics and *in vitro* behaviour, which translates into their *in vivo* biological activity - including accumulation, biodistribution and clearance. Surface potential (charge) indicate their tendency to form aggregates. Techniques like FTIR, Raman spectroscopy and XPS give insight into chemical composition of nanostructures, confirming successful modification.

A number of nanoparticle models were prepared to facilitate the interpretation of the data obtained and to confirm the structural changes at different stages of the bimodal probe synthesis, the designation and detailed description of which are summarised in **Table 25** below. Due to the availability of measurement equipment for these studies, in some cases nanostructures containing natural (non-radioactive) zirconium were used to reflect its physicochemical character without the risk of ionizing radiation. For clarity, such exchange was marked by use of the '^{nat}Zr' (as in natural zirconium) instead of '^{89}Zr'.

Table 25- Nanoparticle models prepared for structural studies

Sample	Description
20_S	dextran coated SPION, Ø 20 nm (unmodified)
5_S	dextran coated SPION, Ø 5 nm (unmodified)
5_SD	dextran coated SPION Ø 5 nm, conjugated with DFO
5_SZr	dextran coated SPION Ø 5 nm, with zirconium adsorbed on NP's surface
5_SA	dextran coated SPION Ø 5 nm, conjugated with Atezolizumab
5_SAD	dextran coated SPION Ø 5 nm, conjugated with Atezolizumab and DFO
5_SAZr	dextran coated SPION Ø 5 nm, conjugated with Atezolizumab and zirconium adsorbed on NP's surface
5_SADZr	dextran coated SPION Ø 5 nm, conjugated with Atezolizumab and ^{nat}Zr-DFO

3.2.3.1 Hydrodynamic size

Accurate knowledge of the nanoparticle's hydrodynamic diameter is essential, especially in the context of the medical application. The study of nanoparticles by the dynamic light scattering (DLS) technique makes it possible to determine not only their hydrodynamic diameter, but also their size distribution. The hydrodynamic diameter is understood as the diameter of a hypothetical sphere that diffuses at the same rate as the particle in solution. The result of this study cannot be directly related to the dimensions of nanoparticles determined by microscopic techniques. The hydrodynamic diameter is derived from the particle's diffusion behaviour in the liquid, calculated using the Stokes-Einstein equation. Therefore, it represents an effective size of the particle as it moves through the solvent [177].

Average diameters of SPION-based samples are gathered in **Table 26**, alongside diffusion coefficient. Size distribution (by intensity) is presented on **Figure 71** and **Figure 72**. Interestingly, sample of unmodified SPION is heterogeneous, a distribution of hydrodynamic diameter values was observed. The more complex the surface composition of the sample is, the more often the size distribution is close to a Gaussian normal distribution. A large difference in sample size of 5_SADZr compared to other 5 nm SPION-based nanoconstructs is observed, reaching as much as 200 nm.

Table 26 - Average hydrodynamic diameter and diffusion coefficient for SPION-based nanostructures

Sample	Average diameter [nm]	Diffusion coefficient [μ^2/s]
20_S	108.5	4.54
5_S	40.14	12.3
5_SD	45.47	10.8
5_SZr	24.92	19.8
5_SA	43.94	11.2
5_SAD	73.18	6.73
5_SAZr	75.37	6.53
5_SADZr	198.1	2.48

3.2.3.2 Zeta potential

Zeta potential provides important information about the surface charge of particles and their colloidal stability in suspension [178]. Specifically, it measures the electrostatic potential at the slipping plane surrounding a particle, which reflects how strongly particles repel or attract each other in dispersion. Nanoparticles with high magnitude zeta potentials (greater than +30 mV or less than −30 mV) are strongly charged and tend to repel each other, leading to good colloidal stability and resistance to aggregation or flocculation. Conversely, nanoparticles with zeta potentials between about −10 mV and +10 mV are nearly neutral and prone to rapid aggregation due to insufficient electrostatic repulsion. Zeta potential is also important due to another factor, as it may indicate nanoparticles interaction with cells. Cellular membranes are generally negatively charged, hence cationic nanoparticles often have increased cellular uptake. Additionally, they may also cause higher cytotoxicity, due to membrane disruption [179].

The pH strongly influences the ionization state of surface functional groups on SPIONs, thereby affecting their surface charge and zeta potential. Changes in pH can lead to shifts in zeta potential, which in turn affect nanoparticle dispersion and aggregation behaviour [180]. In order to exclude mentioned effects, all samples of different SPION-based models were prepared in deionized water, without any buffering additives. Measurement was carried out in temperature of 25 ^{O}C. Zeta potential distribution is showed in **Figure 73Figure** 74, and values are collected in **Table 27**.

Table 27- Zeta potential of different SPION models.

Sample	20_S	5_S	5_SD	5_SZr	5_SA	5_SAD	5_SAZr
Zeta potential [mV]	- 29.0	- 44.7	- 41.0	- 47.0	- 26.2	- 25.8	- 29.5

All samples tested have a negative charge and the functionalization of the nanoparticle surface does not drastically affect this value. The manufacturer of the nanoparticles provided information on both the 5 nm and 20 nm diameter nanoparticles that the expected Zeta potential is in the range of -30 to -45 mV, which is consistent with the data obtained. It is noteworthy that commercial nanoparticles with a diameter of 20 nm have a lower absolute potential value (less negative, closer to neutral) in comparison with unmodified 5 nm SPIONS (sample 5_S). This may indicate lower stability of dispersion, and agrees with observation of 20 nm SPION's behaviour *in vitro*.

Introducing chelator or metal cation to SPION's surface did not change its potential drastically, as these differences are 3.7 and 2.3 mV, respectively. It is consistent with data available in literature [161]. Interestingly, structures which contain monoclonal antibody on their surface (namely: 5_SA, 5_SAD and 5_SADZr) all have a lower absolute zeta potential value (less negative) compared to the starting material (5_S). These values are less negative than – 30 mV and might indicate aggregation tendencies. Monoclonal antibodies generally have low magnitude zeta potentials (are less polarized, often between about −10 mV and +10 mV), reflecting their complex surface chemistry and tendency to aggregate unless stabilized by formulation conditions [181]. Introducing such biological compound has had the expected effect on electrokinetic properties of such a complex structure as multifunctionalised SPIONs.

3.2.3.3 Fourier transform infrared spectroscopy

FTIR has been adapted to qualitatively assess the structure of nanoparticles. This method is able to identify characteristic absorption bands, corresponding to individual bonds and functional groups [182]. Therefore, it was used to confirm the structure of commercial dextran-coated nanoparticles, and the introduction of amino groups on the surface of the functionalised nanoparticle was also determined. The spectrum of unmodified and amine-functionalised SPIONs obtained in the 4000 - 600 cm^{-1} range contains multiple bands, collected and interpreted in **Table 28** and presented on **Figure 75**. The shift of the band corresponding to the O-H vibration at about 3200 cm^{-1} to around the 3400 cm^{-1} value (**Figure 17**), confirms the reaction of the carboxyl groups of the dextran coating and the introduction of primary amine groups onto the nanoparticle surface. Data is consistent with literature regarding FTIR spectrum for iron-oxide nanoparticles and their dextran-coated derivative [180, 183].

Table 28- Interpretation of FTIR spectrum bands

Wave number [cm^{-1}]	Band
3440	N-H stretching
3200	H-O vibrations
2920; 2850	Asymmetric and symmetric C-H stretch in methyl groups
1600	C-H vibrations
1400	C-H asymmetric bends
1160	C-O-C stretch in the dextran group
1020	C-O vibrations
760 - 910	Glucopyranose ring vibrations
600	Fe-O

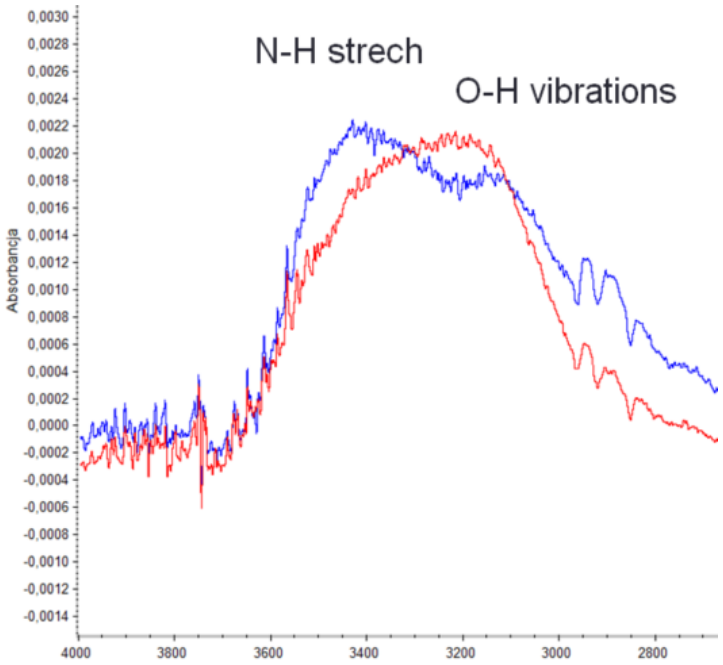

Figure 17- FTIR spectrum spectrum presenting band shift confirming amine-functionalization of dextran-coated SPION

3.2.3.4 X-ray Photoelectron Spectroscopy

This spectroscopic method uses the energy of X-rays to determine the surface composition of the material under investigation - hence the name X-ray Photoelectron Spectroscopy (XPS). By analysing the kinetic energy of the photoelectrons emitted by the sample under X-rays, the chemical composition of the surface can be determined. XPS has a penetration of approximately 5-10 nm, which translates to 50-60 atoms deep into the structure. For this reason, it is used for the analysis of nanoparticles and other larger structures as well as surface films. In order to analyse the nanostructures, they were applied to a silicon wafer and a solvent (water) was evaporated.

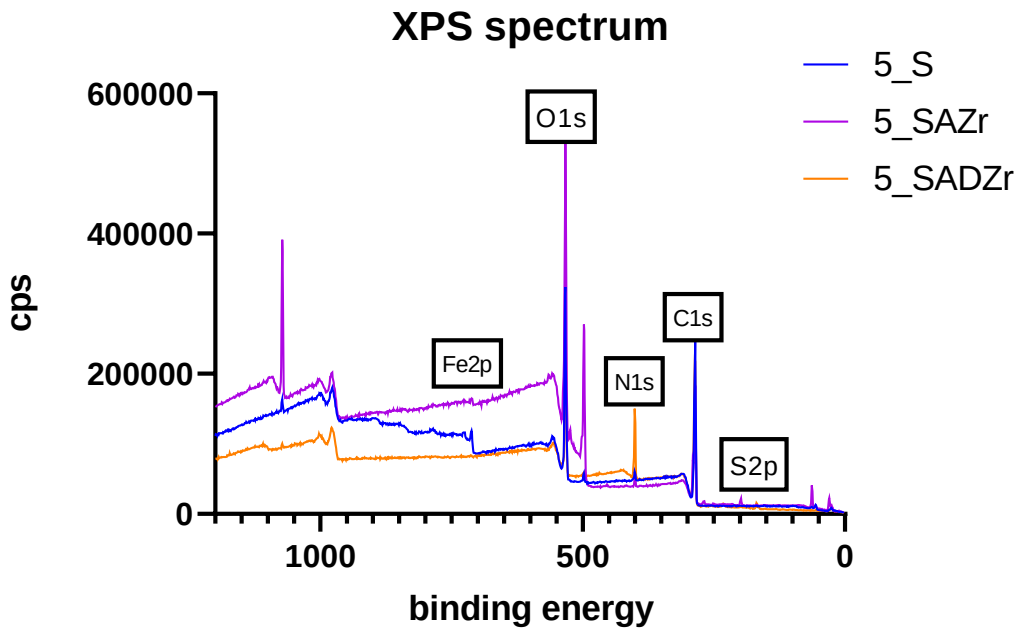

Figure 18 – XPS spectrum for samples 5_S, 5_SAZr and 5_SADZr

Figure 18 presents the broad overall spectrum of sample 5_S. The visible signals are Fe (Fe2p signals at 710-730 eV), O (O1s signal at about 530 eV, OKLL at about 980 eV), C (C1s at about 285 eV), N (N1s at about 400 eV). In addition, sodium, potassium, chlorine, and a silicon signals (from the wafer) are observable. The spectra of the other samples (5_SA, 5_SDA) were similar to these above, differing in the ratio of the individual signals.

Spectrum of Fe2p shows $Fe2p_{3/2}$ signals at about 710 and 713 eV and $Fe2p_{1/2}$ signal at 723 and 726 eV, confirming presence of both iron(II) and (III) in the nanoparticles (**Figure 19**). Also presence of satellite peak at 719 eV (omitted on the spectrum) is a strong indicator of Fe(III). This data correlates with literature and shows non-stoichiometric ratio of both iron forms in the SPIONs [184].

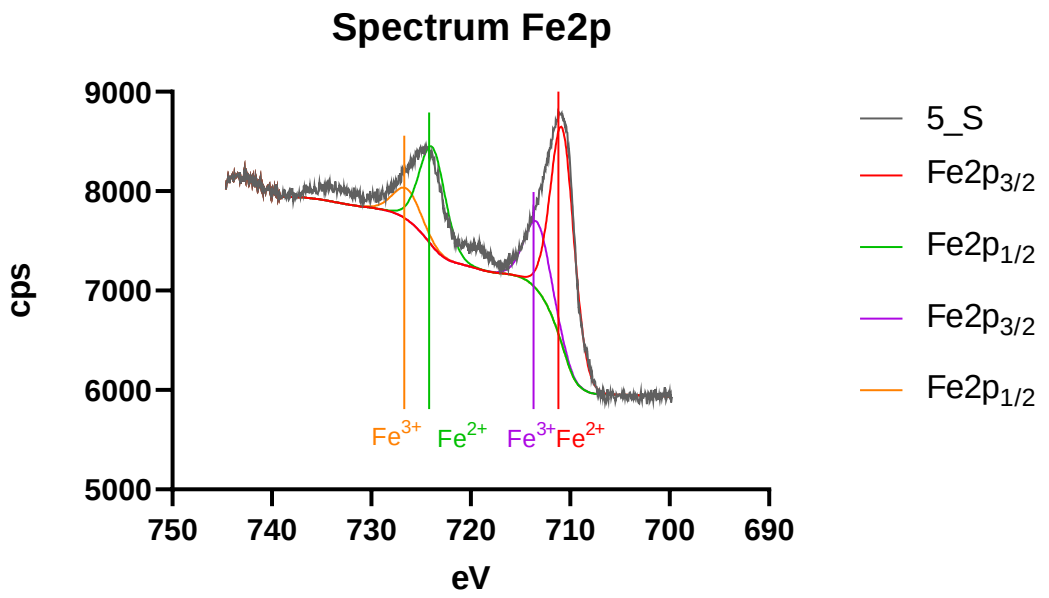

Figure 19 – High resolution XPS Fe 2p spectral region. Signals corresponding to sample 5_S (grey line) and fitting curves.

Sulphur-derived signals (S2p) were present in samples 5_SA, 5_SAD, 5_SAZr and 5_SADZr; this signal was not observed in unmodified 5_S (**Figure 20**). The sulphur originates from the disulphide bridges and cysteine groups present in the structure of the monoclonal antibody, confirming the presence of these proteins in the mentioned samples.

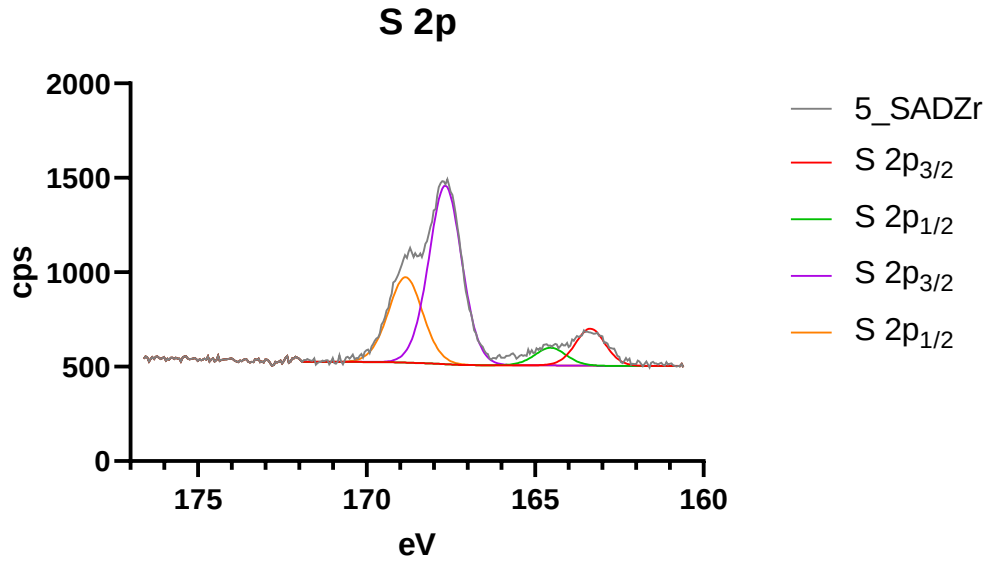

Figure 20 - High resolution XPS S 2p spectral region. Signals corresponding to sample 5_SADZr (grey line) and fitting curves.

Signals corresponding with oxygen (in a range 531 – 536 eV) represent presence of C=O and C-O bonds (from dextran coating) and Fe-O in the paramagnetic core of the nanostructure.

For samples 5_SAZr, 5_SADZr and 5_SZr peak at 184 eV was observable (**Figure 21**), what confirmed effectiveness of heat-induced zirconium adsorption as well as DFO-introduction and further complexation of zirconium atom through chelator.

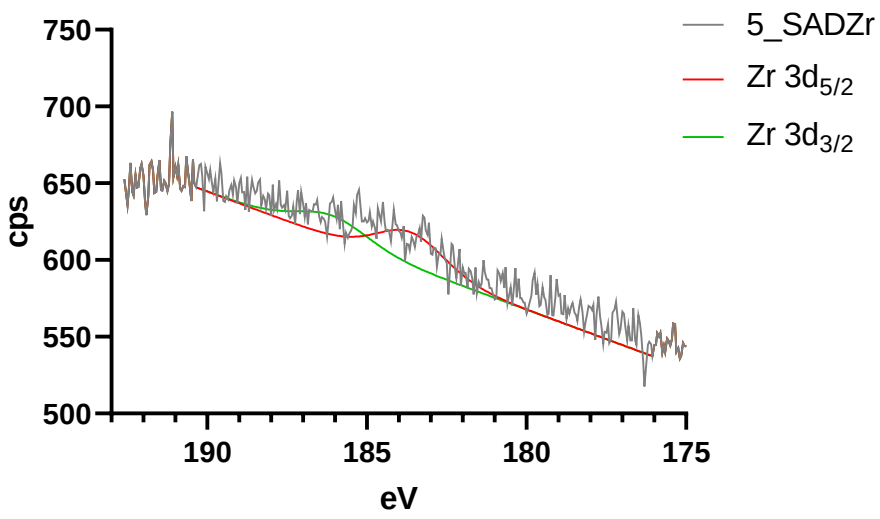

Figure 21 - High resolution XPS Zr 3d spectral region. Signals corresponding to sample 5_SADZr (grey line) and fitting curves.

Unexpectedly, there are signals corresponding to the energy absorbed due to the presence of nitrogen in all of the samples. In the sample containing unmodified SPION of 5 nm there are bands at 399.9 and 402.1 eV. A rational explanation would be that they correspond to the amide group of nanoparticle's polymer coating. In antibody modified samples (5_SA, 5_SAD, 5_SADZr and 5_SAZr) nitrogen-derived signals increase in intensity, and a new signal at 398.3 eV emerges.

3.2.3.5 MALDI-TOF

An attempt was made to assess the size of nanoparticles using the matrix-assisted laser desorption/ionisation time-of-flight mass spectrometry (MALDI-TOF) technique. Obtaining molecular weight information of the nanostructures would be extremely valuable and would allow an easy assessment of the degree of modification at different stages of probe functionalization. Samples of unmodified SPIONs of both studied sizes (5 nm and 20 nm) were deposited on a Ground Steel plate (MTP 384 target plate ground steel BC).

Samples were concentrated using Amicon 50 kDa centrifuge filters. Buffer was exchanged to 0.1% TFA (trifluoroacetic acid) and sample of 45 µL (22 mg/mL) was obtained. Four array systems were tried: 2,5-DHAP (2,5-dihydroxy acetophenone) dried droplet, 1,5-DAN (1,5-diaminonaphtalene) dried droplet, SA (trans-3,5-dimethoxy-4-hydroxy cinnamic acid) double layer and S-DHB (90:10 mixture of 2,5-dihydroxy benzoic acid and

2-hydroxy-5-methoxy benzoic acid), and applied to the steel target in the manner recommended by the manufacturer (details of this technique are described in the experimental section 4.4.3. *Structural studies*).

However, none of the matrices was adequate and spectra did not show any significant signals.

3.2.4 *In vitro* evaluation

3.2.4.1 Cell lines characterisation

In vitro studies were performed using cell lines expressing PD-L1 (H292 and ES2) and their PD-L1 knockout equivalents ($H292_{PD\text{-}L1KO}$ and $ES2_{PD\text{-}L1KO}$). The difference in binding of the resulting functionalized SPIONs to PD-L1 positive and negative lines would indicate the specificity of the compound towards this molecular target. The level of PD-L1 expression was measured by flow cytometry and Western blot techniques. Flow cytometry is a single-cell analytical technique in which cells suspended in fluid are hydrodynamically focused into a narrow stream and interrogated individually by one or more laser beams. For each event, two light-scattering parameters are recorded: forward scatter (FSC), which correlates primarily with cell size, and side scatter (SSC), which reflects internal complexity or granularity (e.g., cytoplasmic granules, organelles). In parallel, fluorescence emission from fluorophore-conjugated probes enables multiparametric immunophenotyping and functional readouts (e.g., cell cycle, viability, proliferation, phospho-signalling) at single-cell resolution.

Western blot is an immunoassay for the detection and semiquantitative analysis of specific proteins in cell or tissue lysates. Proteins are denatured in sodium dodecyl sulfate (SDS), typically with a reducing agent such as DTT or β-mercaptoethanol, separated by SDS–PAGE (polyacrylamide gel electrophoresis) according to apparent molecular mass, and electrophoretically transferred to a nitrocellulose or polyvinylidene fluoride (PVDF) membrane. After blocking nonspecific binding sites using milk or bovine serum albumin, the membrane is incubated with a target-specific primary antibody and a species-matched secondary antibody conjugated to horseradish peroxidase or a fluorescent dye. Signals are visualised by chemiluminescence or near-infrared fluorescence and recorded. Subsequently, band intensities are normalised to a housekeeping protein (e.g., GAPDH - glyceraldehyde 3-phosphate dehydrogenase) to control for loading and transfer.

Western blot

Cell lysates were prepared for all four tested cell lines, and Western blotting was performed according to experimental details described in section 4.5.2. *Cell lines characterisation.* Western blotting for PD-L1 (~45–50 kDa) reveals a strong band in ES2 cell lysates, a markedly weaker band in H292, and no detectable signal in $ES2_{PD\text{-}L1\text{-}KO}$ and $H292_{PD\text{-}L1\text{-}KO}$ samples (**Figure 22**). Uniform intensity of the loading control across cell lines confirms comparable protein loading. These data demonstrate high PD-L1 expression in ES2, lower expression in H292, and successful knockout in both KO lines, validating them as appropriate negative controls for subsequent *in vitro* assays.

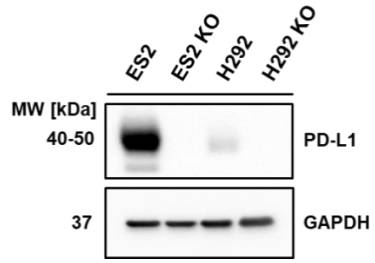

Figure 22 – PD-L1 expression levels in cell lysates assessed via Western blot.

Flow cytometry

Analysis of membrane PD-L1 expression levels in investigated cell lines was performed as described in 4.5.2. *Cell lines characterisation*

Representative histograms of fluorescence are shown in Figure 23Figure 24. Staining with a dye-conjugated anti-PD-L1 antibody produced a clear rightward shift for ES2 and a weaker but distinct shift for H292 (red), indicating surface PD-L1 expression (higher in ES2) compared to the control groups (orange) (**Figure 23Figure 24**). In contrast, $ES2_{PD\text{-}L1\text{-}KO}$ and $H292_{PD\text{-}L1\text{-}KO}$ overlapped with controls. The isotype control in every line gave fluorescence at control (baseline) level, indicating minimal non-specific binding and background, so the positive shifts observed with the anti-PD-L1 antibody reflect specific epitope binding.

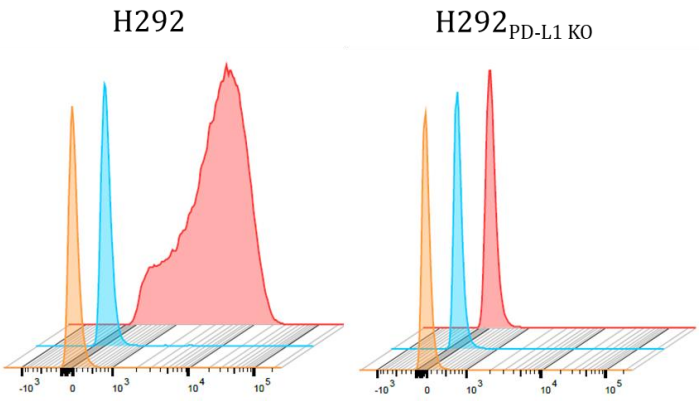

Figure 23 – Representative fluorescence histograms showing PD-L1 expression levels on H292 and $H292_{PD\text{-}L1\ KO}$ cells. Orange signal represents unstained control, blue – stained with isotype IgG, and red – cells stained with fluorophore PE-Cyanine7.

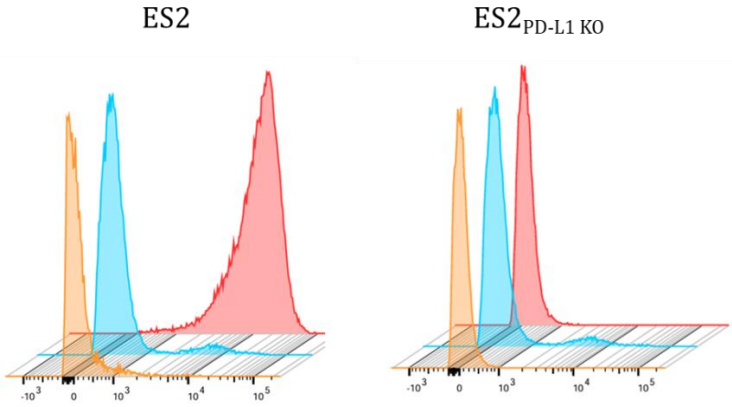

Figure 24– Representative fluorescence histograms showing PD-L1 expression levels on ES2 and $ES2_{PD\text{-}L1\ KO}$ cells. Orange signal represents unstained control, red – cell stained with fluorophore PE-Cyanine7 and blue – stained with isotype IgG.

Median fluorescent intensity (MFI) values for all groups are gathered in **Table 29**. The flow cytometry data corroborated with the Western blot results.

Table 29– MFI values for PD-L1 positive and negative cell lines (data are mean ± SD; n= 3 independent experiments)

Cell line	Unstained cells	Isotypic IgG-PE-Cy7	Anti-PD-L1-PE-C7
H292	127 ± 43	157 ± 30	5941 ± 1193
$H292_{PD\text{-}L1\ KO}$	147 ± 51	184 ± 48	167 ± 79
ES2	181 ± 26	299 ± 30	16107 ± 1932
$ES2_{PD\text{-}L1\ KO}$	155 ± 33	250± 26	195 ± 5

3.2.4.2 Specificity

Flow cytometry

In order detect SPION nanoparticles using fluorescence techniques such as flow cytometry and confocal microscopy, it was necessary to prepare them with a fluorescent dye in their structure. The fluorophore AlexaFluor (AF647) was chosen and the SPION-Atezolizumab-AF647 model was prepared as described in the experimental section (4.4.1. *SPION surface modification*). *In vitro*, a bimodal probe comprising SPION nanoparticles conjugated to Atezolizumab and Alexa Fluor-647 (SPION-Atezo-AF647), designed to approximate the cellular behaviour of the final imaging construct. To differentiate specific from non-specific interactions Atezolizumab-AF647 (antibody without nanoparticle) was prepared to serve as a positive control for PD-L1-specific binding. The binding was next evaluated using flow cytometry and fluorescence microscopy.

Specificity of binding

In these studies, cells were incubated in 4 °C with 10 nM of each fluorescent conjugate; unstained cells served as negative controls. Flow cytometry revealed a shift to higher fluorescence intensity (increased MFI) in H292 and ES2 stained with SPION-Atezolizumab-AF647 and with Atezolizumab-AF647, consistent with specific binding to surface PD-L1 (**Figure 25**). MFI for all conditions are summarised in **Table 30**, providing a quantitative comparison of binding across cell lines and conjugates.

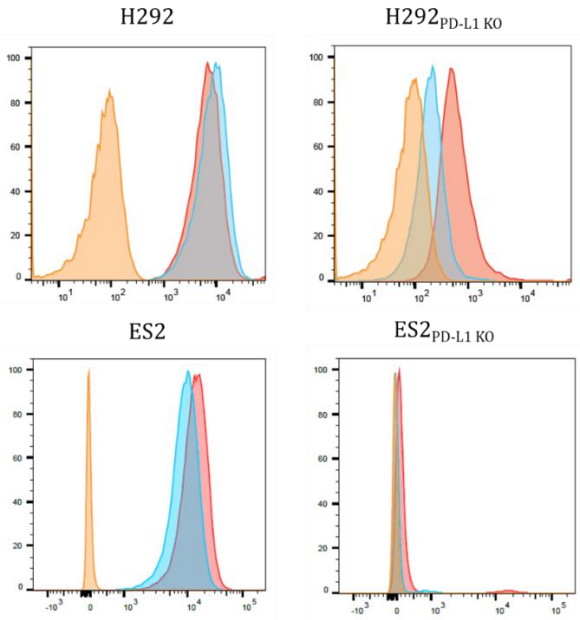

Figure 25 - Representative fluorescence histograms showing binding in 4 °C of SPION-Atezolizumab-AF647 (red) and Atezolizumab-AF647 (blue), in comparison to unstained control (orange).

Table 30 - MFI values for control, Atezolizumab-AF647 and SPION-Atezolizumab-AF647 stained cells (data are mean ± SD; n = 3 independent experiments

Cell line	unstained	Atezolizumab-AF647 (10 nM)	SPION-Atezolizumab-AF647 (10 nM)
H292	113 ± 37	1621 ± 576	5240 ± 330
$H292_{PD\text{-}L1\ KO}$	122 ± 47	142 ± 39	205 ± 24
ES2	139 ± 1	12894 ± 34	22378 ± 220
$ES2_{PD\text{-}L1\ KO}$	138 ±2	152 ± 1	155 ± 4

For H292 cells, the fluorescence increase is slightly greater with Atezolizumab-AF647 than with SPION-Atezo-AF647and almost comparable between H292 and ES2. In both PD-L1-positive lines, no fluorescence band shift is observed for the unstained groups. In the PD-L1 knockout lines ($H292_{PD\text{-}L1\ KO}$ and $ES2_{PD\text{-}L1\ KO}$) a small shift to higher fluorescence is observed, but not as strong as for PD-L1-expressing lines. The effect is more profound in the SPION-Atezolizumab-AF647 stained group. This likely reflects non-specific nanoparticle association (surface adsorption and/or uptake) related to the particles' larger hydrodynamic size and surface properties, rather than PD-L1-specific binding.

Confocal microscopy

Specificity determined by confocal microscopy required the use of AlexaFluor 647 fluorochrome constructs, prepared in the same manner, as those used in the flow cytometry. PD-L1 positive and negative cell lines were incubated with one of the SPION-based fluorescent constructs. Cell nuclei were then stained with Hoechst 33258 reagent. Cells incubated with the sample were washed to remove unbound nanoparticles. Fluorescence was then excited on a confocal microscope ($\lambda_{ex} \approx 650$ nm) and the emitted signal was recorded. A markedly higher membrane-associated signal in PD-L1-positive versus negative cell line confirmed the specificity of the SPION-Atezolizumab construct (**Figure 26**)

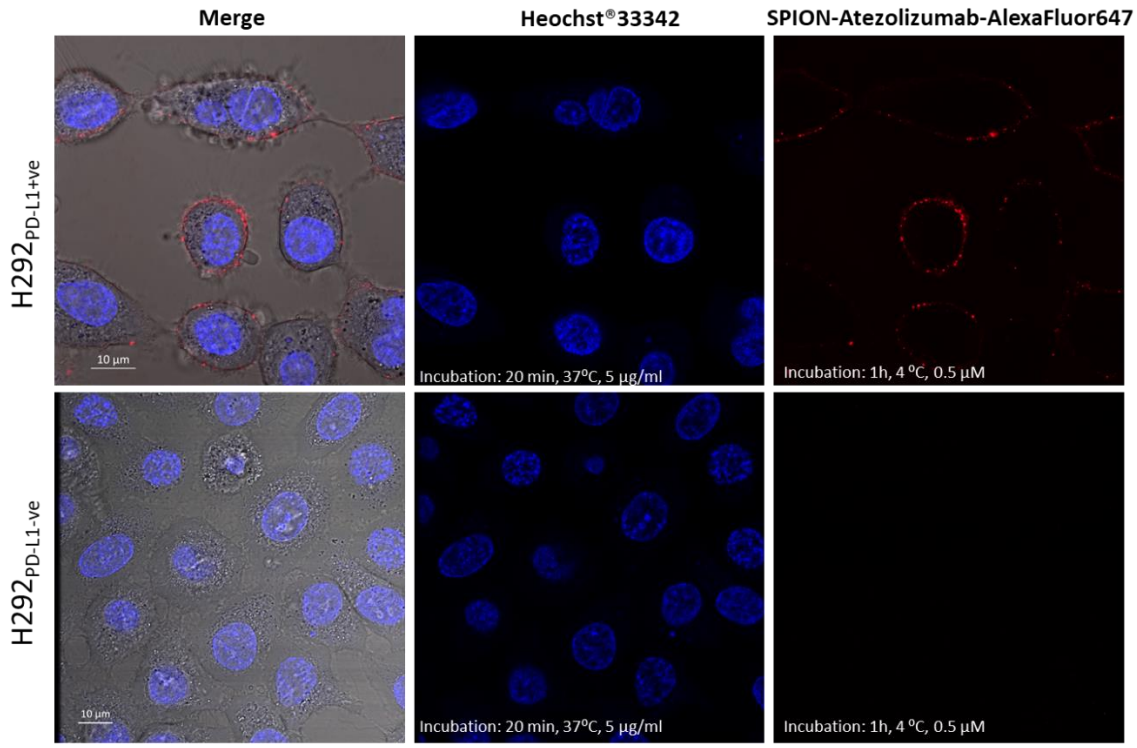

Figure 26 – Images from confocal microscope (63x) of H292 and H292$_{PD\text{-}L1\ KO}$ cells

Similar results were obtained for Atezolizumab-AF647 that was used as a positive control in this study. **Figure 27** shows similar accumulation of fluorochrom-labelled antibody on cellular membrane of H292$_{PD\text{-}L1+ve}$ cells, and lack of this binding on knock-out cells.

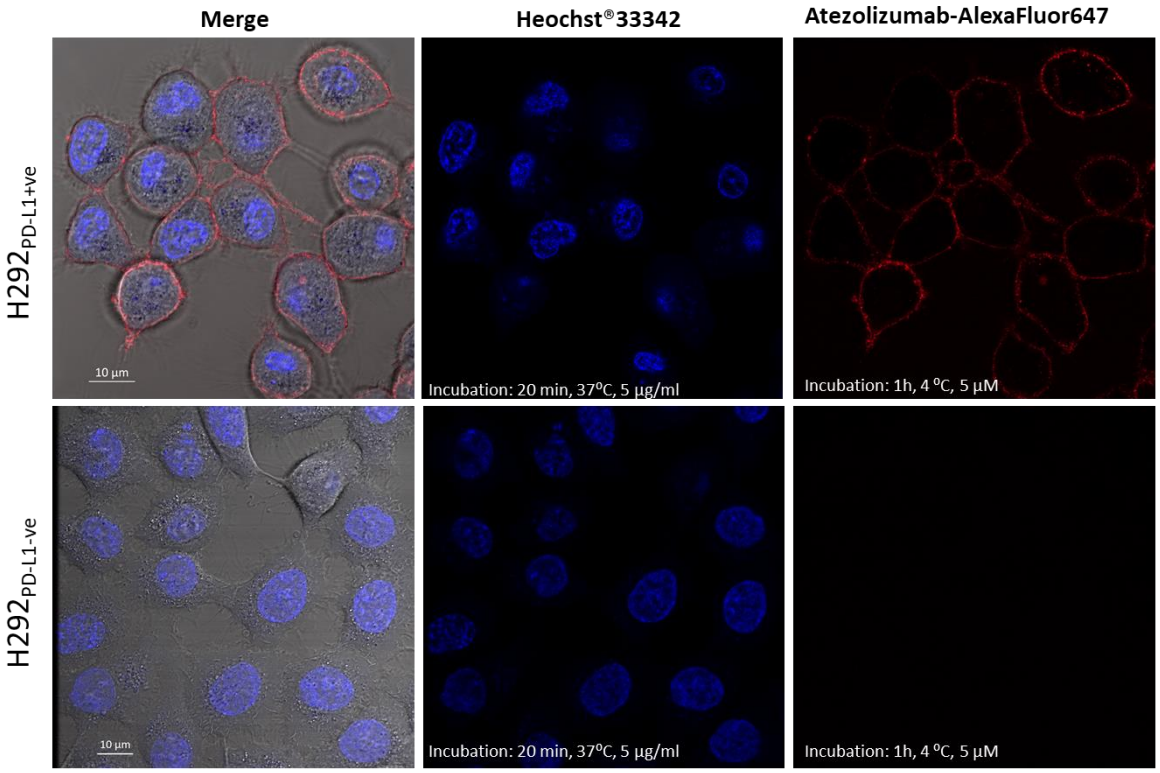

Figure 27 - Images from confocal microscope (63x) of H292 and H292$_{PD\text{-}L1\ KO}$ cells

Cellular uptake

Cellular uptake is distinct from surface binding. The former is a dynamic, often energy-dependent process in which cells internalise extracellular material via endocytosis or membrane transporters. The latter refers to the reversible association of a molecule or nanoparticle with the plasma membrane (non-specific adsorption or specific receptor–ligand binding) without internalization.

Cellular uptake of SPION-Atezolizumab-AF647 was tested using flow cytometry. PD-L1 positive and negative cells were incubated for 1 hour at 37 ^{O}C with 1 nM of SPION-Atezolizumab-AF647 or with Atezolizumab-AF647 alone (positive control). After incubation samples were washed three times with PBS to remove unbound fluorescent conjugates and analysed on flow cytometer.

Representative fluorescence histograms are shown in **Figure 28** (PD-L1 positive cells (left) and PD-L1 negative (right), corresponding median fluoresce intensities are summarised **Table 31**. After 1 h incubation at 37 °C, both SPION-Atezolizumab-AF647 and Atezolizumab-AF647 produced a clear shift to higher fluorescence in ES2(PD-L1^{+}) compared with unstained controls, consistent with PD-L1-dependent cellular uptake.

In $ES2_{PD\text{-}L1KO}$ cells fluorescence distributions overlapped the controls, indicating absence of specific binding.

Despite being matched for Atezolizumab concentration, SPION-AtezolizumabAF647 yielded a greater signal in ES2 than Atezolizumab-AF647 (higher MFI), indicating rapid internalisation of the nanoparticle conjugate, which is consistent with nanoparticle-mediated endocytosis. No right-shift was observed in the PD-L1-negative line, supporting the specificity of the interaction under these conditions.

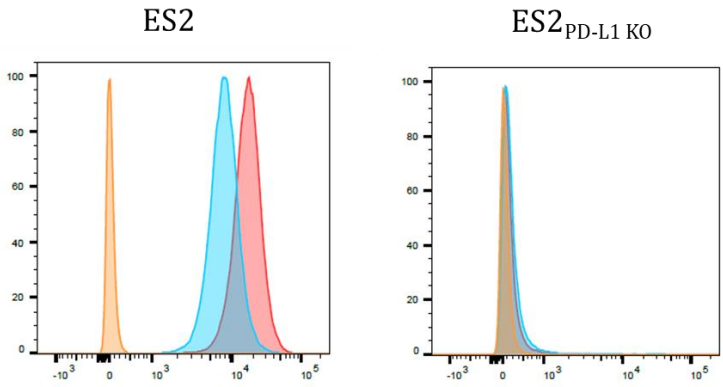

Figure 28 – Representative fluorescence histograms of unstained (orange), stained with Atezolizumab-AF647 (blue) or SPION-Atezolizumab-AF647 (red) cells.

Table 31 - MFI values for control, Atezolizumab-AF647 and SPION-Atezolizumab-AF647 stained samples in 37 °C (data are mean ± SD; n = 3 replicates)

Cell line	unstained	10 nM Atezolizumab-AF647	10 nM SPION-Atezolizumab-AF647
ES2	139 ± 1	12874 ± 30	22343 ± 190
$ES2_{PD\text{-}L1\ KO}$	138 ±2	154 ± 1	156 ± 3

Specificity of binding

The radiolabelled nanoparticles ^{89}Zr-DFO-SPION-Atezolizumab and ^{89}Zr-SPION-Atezolizumab were also subjected to *in vitro* specificity of binding testing. The methodology for this assay is described in 4.5.3. *Specificity and cellular uptake*. In brief, ES2 and $ES2_{PD\text{-}L1\ KO}$ cells were treated with ^{89}Zr-DFO-SPION-Atezolizumab, ^{89}Zr-SPION-Atezolizumab or ^{89}Zr-DFO-Atezolizumab (as a control) with or without prior blocking with 'cold' Atezolizumab. After one hour of incubation at 4 °C, the cells were washed multiple times to remove unbound compounds. Radioactivity of samples was then measured by gamma-counter, along the same amount of radioconjugate (treated as 100% of activity). Percentage

of activity bound to cells per mass unit was calculated. Numerous attempts were undertaken, however only one study (10 nM ^{89}Zr-DFO-SPION-Atezolizumab) demonstrated specificity and it is shown on **Figure 29.** For this experiment, statistical analysis showed significant ($p \leq 0.05$) difference among groups. In the remaining experiments, other nanostructures were not specific. Representative experiments, including concentrations of 10 and 1 nM of both radiolabelled nanostructures are also shown**.**

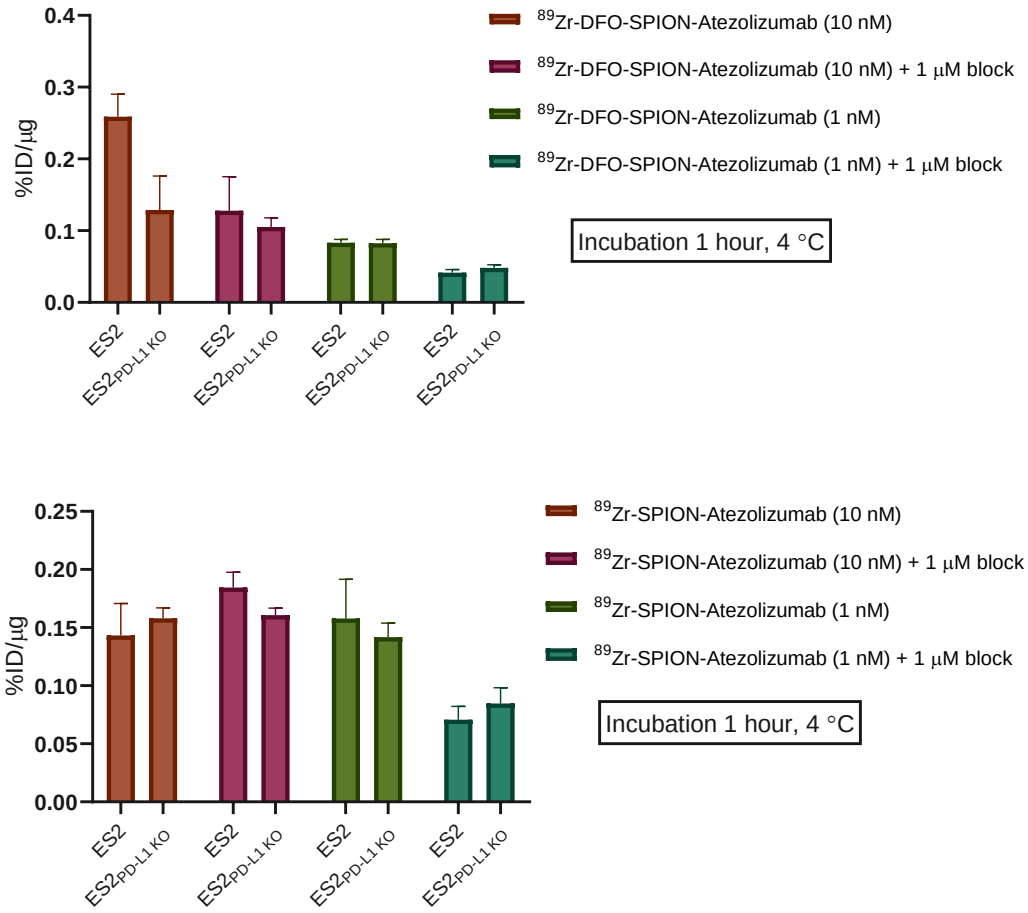

Figure 29 - Binding specificity of radioconjugates (n= 3 replicates for each group). Top: ^{89}Zr-DFO-SPION-Atezolizumab; bottom: ^{89}Zr-SPION-Atezolizumab.

In comparison, specificity of binding for 'typical' radiolabelled monoclonal antibody (^{89}Zr-DFO-Atezolizumab), hence without SPION, is presented on (**Figure 30**).

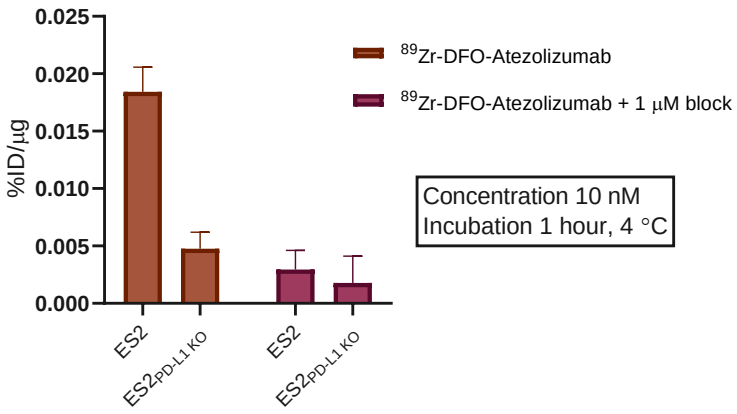

Figure 30 - Specificity of binding – ^{89}Zr-DFO-Atezolizumab (10 nM, incubation for 1 hour at 4 ^{O}C, n= 3 for each group)

3.2.4.3 Cytotoxicity

The cytotoxicity of a compound (diagnostic, drug) is a measure of its negative effect on cells. As a rule, cytotoxicity is defined as the inverse of the survival rate of cells treated with a particular concentration of a given compound, relative to an untreated control group. For iron oxide nanoparticles, intrinsic toxicity primarily depends on hydrodynamic size, surface charge (electrical potential), and the resulting colloidal stability/aggregation propensity, as well as by surface chemistry/coating [185]. These physicochemical parameters for the tested nanostructures were quantified as described in 3.2.3. *Structure studies*, allowing us to interpret viability data in the context of material properties.

Due to the fact the evaluated nanoparticles-were modified with ^{89}Zr, initially a non-radioactive zirconium counterpart was used, to remove contributions from ionising radiation (radiolysis/radiotoxicity) and focusing on chemistry-driven effects. At activities typical for diagnostic studies with ^{89}Zr, radiation dose to cells is expected to be negligible compared with chemical toxicity; nonetheless, using the cold analogue ensures that the cytotoxicity readout reflects the nanostructure and surface modification rather than radionuclide emissions.

Accordingly, the viability results presented here should be interpreted as a function of particle size/aggregation state, and surface functionalisation (including Atezolizumab and DFO), independent of radioactive dose.

Cytotoxicity of SPION-based formulations was assessed using CellTiterGlow® assay according to manufacturer's protocol. Assay is based on quantitative determination of ATP present in a sample, due to reaction of ATP with luciferin present in the reagent. Product of this reaction emits luminescent light, amount of which is proportional to viable cells

in tested well. ES2 and $ES2_{PD\text{-}L1\text{-}KO}$ cells were exposed for 24 h or 48 h at 37 °C to each formulation over a concentration range of 0.1 - 1.0 µM Fe (corresponding to 0.014 - 0.136 mg SPION mL^{-1}), selected from prior *in vitro* cytotoxicity data and *in vivo* dosing reports. For each condition, four replicate wells were assayed, untreated cells served as controls (100% viability). Luminescence signals were background-subtracted and normalised to the untreated control to yield per cent viability. Results are presented on **Figure 31** and**Figure 32**.

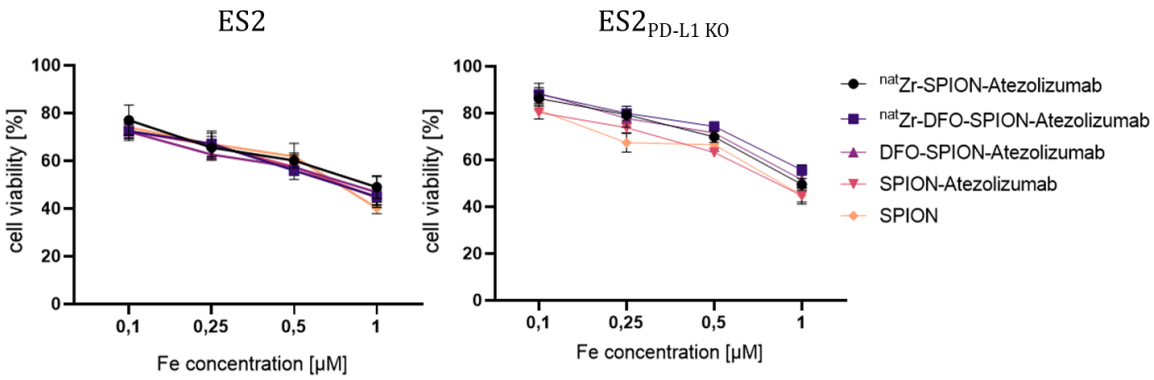

Figure 31– Viability of ES2 and ES2 $_{PD\text{-}L1\ KO}$ cells after 24 hours of incubation with various SPIONs (data represent n = 4 replicates ± SD).

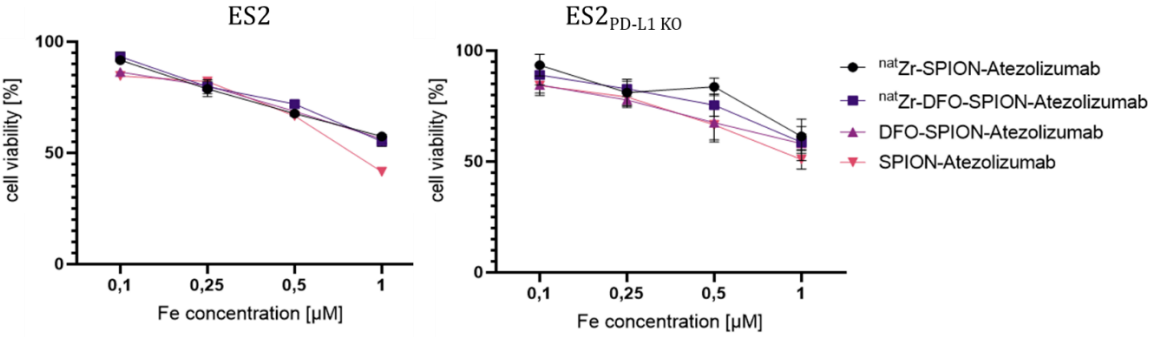

Figure 32– Viability of ES2 and ES2 $_{PD\text{-}L1\ KO}$ cells after 48 hours of incubation with various SPIONs (data represent n = 4 replicates ± SD).

Across experiments, viability assay yielded very similar data. All SPION-based formulations exhibited similar cytotoxicity over 0.1 - 1.0 µM Fe, indicating that cell death is driven predominantly by the iron oxide dose, rather than by surface modifications (antibody, chelator, or metal atom). Interestingly, samples incubated for 48 h showed a slightly higher survival rate than those tested after one day.

3.2.5 Application studies

After determining the physicochemical properties of the bimodal probes obtained, the next stage of their implementation is preclinical studies, which in this case included relaxometry studies and an animal model experiments. The former aims to examine the contrasting abilities of the various probes described, taking into account different magnetic field strengths and concentrations. The second research task examined the pharmacokinetics and specificity of the chosen probes *in vivo.*

3.2.5.1 Magnetic studies - relaxivity

Relaxivity is a measure of the ability of a CA to enhance contrast in MRI, as described in more detail in section 2.3.1. *Contrast agents.* Obtaining information of this value is important in assessing suitability of a substance with potential use in clinical practice. Mathematically, relaxivity is the relationship between the concentration of a paramagnetic substance (potentially accelerating relaxation) and the inverse of the relaxation time, as shown by the formula below:

$$\frac{1}{T_x} = r_x \cdot C$$

In practice, the determination of relaxivity involves measuring the T_x time at different concentrations of CA. Determination of the T_x time, in turn, involves measurement at different TR or TE parameters (for T_1 and T_2, respectively with chosen sequence). The next step is to calculate the slope of the linear regression curve of the relationship of $1/T_x$ to C, resulting in r_x [mg/mL/s]. Current NMR spectroscopes and MRI scanners generally have the option of mapping relaxation times to given parameters, leaving the operator only to mathematically transform the dependence of the inverse of this time to the CA concentration. Nanoparticles that were subject of this work were analysed in two magnetic fields strength: 1.4 T (benchtop NMR spectrometer) and 7 T (preclinical MRI scanner). T_2 and T_1 mapping on BioSpec Maxwell MRI (Bruker) was performed by analysing samples of studied nanoparticles (e.i. ^{nat}Zr-DFO-SPION–Atezolizumab) in different concentrations with sequence T1_T2map_RARE (parameter of this sequence are listed in 4.6.1. *Relaxometry*). After determining regions of interest (ROI) in the cross-sections of the examined samples, the software returns T_2 and T_1 values [ms] together with the standard deviation for the designated areas. To determine the transverse relaxation rate r_2 for each sample T_x values were transformed to $1/T_x$ [s]. Then, simple linear regression was drawn for each compound. A representative graph of the $1/T_2$ to c correlation for ^{nat}Zr-DFO-SPION–Atezolizumab is presented **Figure 33.**

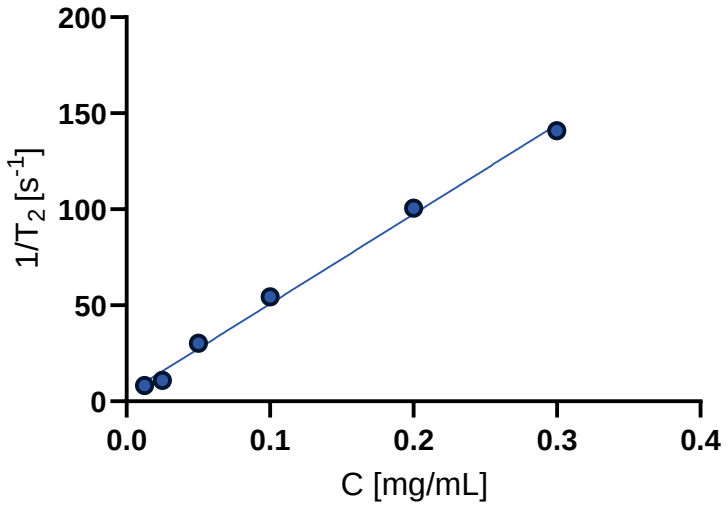

Figure 33– Relaxivity of ^{nat}Zr-DFO-SPION-Atezolizumab measured in a 7.0 T magnetic field (on BioSpec Maxwell MRI Bruker). From linear regression curve relaxivity was calculated to be 467.2 mg/mL/s.

Relaxivity of CA, despite its concentration, depends mainly on magnetic fields strength, temperature and solvent. In order to obtain the most comparable measurements, all samples were dispersed in deionised water and measured at room temperature. Relaxivity of different Ø 5 and Ø 20 nm based SPION nanostructures calculated based on measurement on 7 T MRI scanner are summarised in **Table 32** and visually compared in **Figure 34**.

Table 32- Relaxivity of different functionalised SPIONs, determined with 7.0 T MRI (data are slope of linear regression ± standard error of slope)

	SPION Ø 5 [nm]		**SPION Ø 20 [nm]**	
Nanoparticles	**r_1 [mg/mL/s]**	**r_2 [mg/mL/s]**	**r_1 [mg/mL/s]**	**r_2 [mg/mL/s]**
SPION	5.03 ± 0.08	316.2 ± 0.9	2.16 ± 0.68	1158.0 ± 107.4
^{nat}Zr-SPION	4.10 ± 0.16	315.8 ± 14.1	5.11 ± 0.40	1741.0 ± 749.7
SPION-Atezolizumab	2.65 ± 0.02	316.8 ± 0.6	2.33 ± 0.44	964.6 ± 52.1
^{nat}Zr-SPION-Atezolizumab	2.99 ± 0.13	469.1 ± 14.2	2.73 ± 0.62	1553.0 ± 76.2
SPION-DFO-Atezolizumab	2.23 ± 0.08	392.7 ± 6.0	2.12 ± 0.07	928.8 ± 50.0
^{nat}Zr-DFO-SPION-Atezolizumab	1.06 ± 0.03	467.2 ± 16.18	1.29 ± 0.15	1318.0 ± 53.5

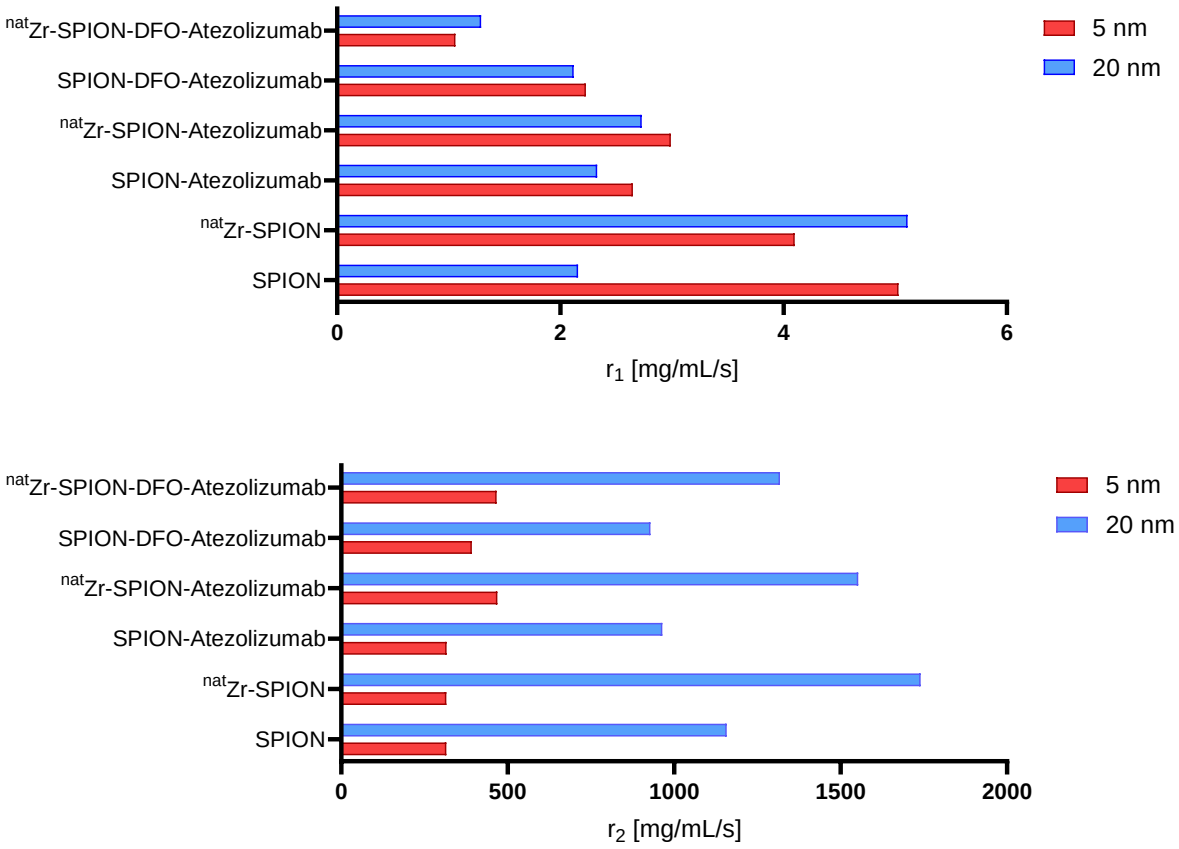

Figure 34 – Comparison of relaxivity r_1 (upper figure) and r_2 (bottom) for different 5 nm and 20 nm SPIONs (measured on 7 T MRI)

Representative images (of ^{89}Zr-DFO-SPION-Atezolizumab) obtained in T_1 and T_2-weighed sequences are shown in **Figure 35** and **Figure 36**.

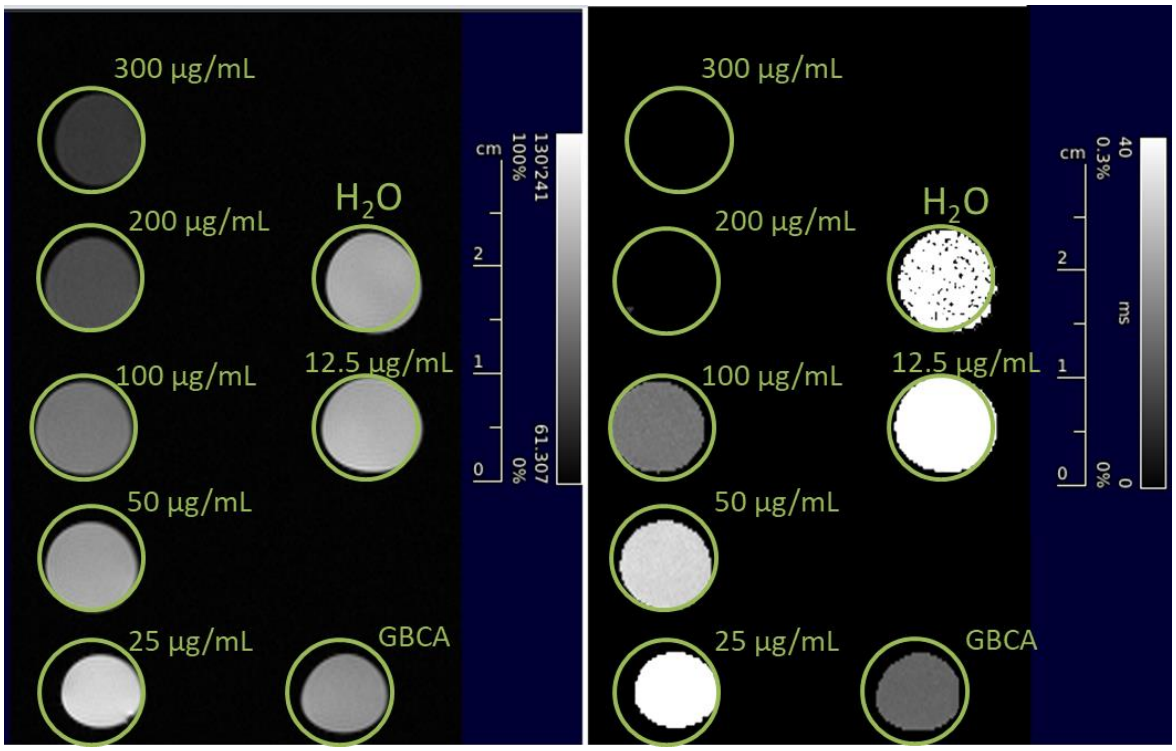

Figure 35 – Images of T_1 (left) and T_2-weighted (right) MRI sequences of ^{nat}Zr-DFO-SPION-Atezolizumab (based on SPION Ø5 nm) in different concentrations. Samples of water and Dotarem (Gd(III) based CA) were added as controls.

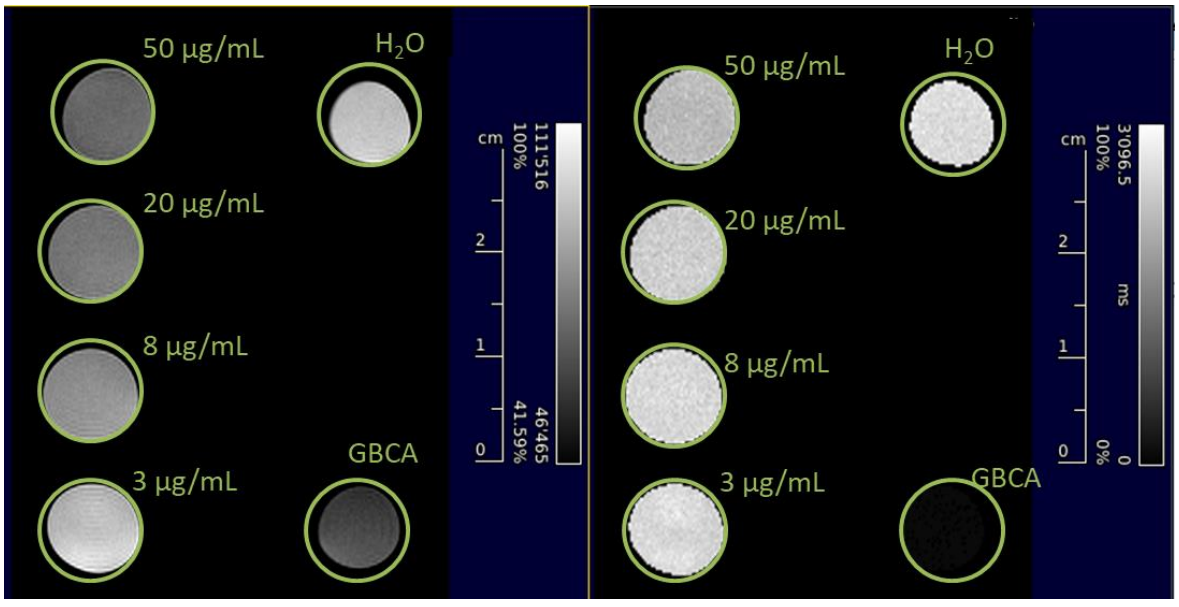

Figure 36 – Images of T_1 (left) and T_2-weighted (right) MRI sequences of ^{nat}Zr-DFO-SPION-Atezolizumab (based on SPION Ø 20 nm). Samples of water and Dotarem (Gd(III) based CA) were added as controls.

Both groups of nanoparticles meet the condition of r_2/r_1 above 20, which is imposed on negative CAs [125]. NPs of 5 nm show ratio r_2/r_1 in the range of 60 – 420, while the larger nanoparticles of 20 nm diameter – 370 up to 1000. Latter nanoparticles have stronger

relaxivity effects, however they showed greater toxicity, were prone to aggregation and lacked specificity. Contrasting effects of 5nm however more subtle, are still promising for MRI imaging. The data provided shows that the presence of zirconium atoms has a measurable effect on the r_2 effect of 20 nm nanoparticles. Relaxivity r_2 of SPION 5 nm is the highest (ergo, the contrasting is most effective) for probes modified with Atezolizumab and zirconium atom. The aforementioned RIME effect is not expected in r_2 relaxation, as it is mostly reported in T_1-weighted sequences, where the magnetisation effect is positive [186, 187]. T_2 relaxation is strongly dependent on local magnetic field inhomogeneities, which can be amplified by clusters of magnetic nanoparticles [188]. Therefore, T_2-weighted imaging is susceptible to many parameters, and precise differentiation of molecular effects (e.g., receptor effects like RIME) might be problematic, especially when the CA is not enhancing T_2 significantly. Moreover, based on current academic literature, there is no direct evidence or published study confirming that the PD-L1 ligand specifically induces a RIME effect. Determining whether this effect actually occurs in the case of the PD-L ligand requires further research and confirmation of whether PD-L1 binding could influence magnetic properties in a receptor-mediated fashion.

Superparamagnetics like SPION are primarly T_2 CAs, and as proved above r_2 relaxivity is much higher than r_1. Thus, following experiments and measurements were concentrated on the former value. To compare results from preclinical 7 T MRI scanner, T_2 measurements were also conducted on 1.4 T NMR spectrometer (Nanalysis-60). Calculated relaxivity r_2 of different 5 and 20 nm based SPIONs are gathered in **Table 33**.

Table 33 - Relaxivity r_2 [mg/mL/s] of different SPIONs determined with 1.4 T NMR (data are slope of linear regression ± standard error of slope)

Nanoparticles	**Relaxivity r_2**	
	Ø 5 nm	**Ø 20 nm**
SPION	113.8 ± 34.4	3548 ± 38
^{nat}Zr-SPION	189.9 ± 12.2	4955 ± 146
SPION-Atezolizumab	203.7 ± 3.91	1552 ± 248
^{nat}Zr-SPION-Atezolizumab	267.1 ± 65.0	2920 ± 43
DFO-SPION-Atezolizumab	290.9 ± 49.21	1386 ± 103
^{nat}Zr-DFO-SPION-Atezolizumab	285.1 ± 6.9	974 ± 123

Additionally, obtained data were compared with literature in **Table 34**, where relaxivity was determined for series of SHP nanoparticles of different radius (manufacturer's name for nanomaterial used in this project) [189].

Table 34 – Relaxivity of unmodified SPIONs compared for different magnetic field strength (data for 0.47 T taken from Zhang et al. [189])

Magnetic field strength		**7 T**	**1.4 T**	**0.47 T**
SHP05 5 nm	r_1 [mg/mL/s]	5.0	3.1	8.6
	r_2 [mg/mL/s]	316.2	113.8	28.5
	r_1/r_2	**0.016**	**0.027**	**0.30**
SHP20 20 nm	r_1 [mg/mL/s]	2.16	41.7	16.8
	r_2 [mg/mL/s]	1158	3548	156.9
	r_1/r_2	**0.002**	**0.012**	**0.11**

As can be observed, the r_2 relaxation determined for SPION Ø 5nm increases with the magnetic field in which it was measured. This is very good information in the context of the development of increasingly technologically advanced scanners with higher achievable magnetic field strengths. The obvious benefit of technological development and improving this parameter of MRI scanners is higher-resolution imaging and shorter scan duration. However, as the above determinations indicate, superparamagnetic contrast agents have higher relaxation in higher magnetic fields, and therefore will provide better contrast in higher magnetic fields.

A general trend shows that the r_1/r_2 ratio decreases with increasing magnetic field, where this effect is more significant for superparamagnetics than for lanthanide-based CAs [190]. The data presented above is consistent with the literature data.

3.2.5.2 In vivo experiments

Proof-of-concept animal studies were performed in order to evaluate biodistribution and accumulation of the investigated ^{89}Zr-DFO-SPION-Atezolizumab. This probe was chosen for *in vivo* studies due to its superior specificity in *in vitro* context and safer order of modification and radiolabelling (compared to ^{89}Zr-SPION-Atezolizumab). Specificity and pharmacokinetics of ^{89}Zr-DFO-SPION-Atezolizumab were evaluated in comparison

to non-targeted ^{89}Zr-DFO-SPION by PET/CT and MRI in mice bearing PD-L1- expressing (H292) subcutaneous tumours. As the ES2 xenograft model is not well established, the *in vivo* studies were performed in the well-characterised H292 subcutaneous model, previously validated within our group [191]. All animals studies (including intravenous administration of nanoparticle formulations, PET/CT and MRI scans and biodistribution studies) were performed by Marlena Golec, PhD. Author's contribution in this part of the project involved preparation of the nanoparticle formulations, assistance during administration and scans, and data analysis.

Radioconjugates preparation

Bimodal probes (^{89}Zr-DFO-SPION-Atezolizumab and ^{89}Zr-DFO-SPION) for *in vivo* experiments were prepared in sterile manner, in laminar flow hot chamber. Synthesis details are described in 4.4.1. *SPION surface modifications*. Shortly, 1.5 mg of SPION (5 nm) for each nanoparticle model was transferred to MES buffer with centrifuge filter, followed by addition of EDC and DFO-Mes. After overnight incubation both reactions were processed through centrifuge filters. The first was exchanged into MES buffer for the bioconjugation process, while the latter into HEPES buffer, closed tightly in sterile eppendorf tube and stored in the 4 ^{O}C. Two-step bioconjugation of Atezolizumab was performed, like described in the experimental section. Quantitative assays (isotopic dilution and Bradford assay, 4.4.2. *Quantitative assays*) were performed in order to characterise obtained DFO-SPION-Atezolizumab and DFO-SPION.

Radiolabelling of both models with zirconium-89 oxalate was carried out in room temperature overnight, with stirring, with RCP controlled with radioTLC. Both reactions reached 100% RCP, however after purification (centrifuge filter MWCO 50kDa) some radioactivity was present in the supernatant. Nanoparticles were then stripped off the filter with 400 µL of normal saline and filtered through 0.22 µm syringe filters. SPION concentration was measured and SA for each radioconjugate was calculated.

Animal PET/CT and MRI

Female BALB/c Nude- Foxn1 nu/nu, mice were injected with $8 \cdot 10^6$ cells and their tumour growth monitored twice a week. After tumours reached desired volume, four mice (M1 – M4) were injected intravenously (i.v.), via the tail vain, with 1.47-1.99 MBq of ^{89}Zr-DFO-SPION-Atezolizumab or ^{89}Zr-DFO-SPION (85 – 134 µg SPION) in a normal saline 0.9% saline (100 µL). Amount of protein in the injected volume was calculated to be 77.35 – 104.65 µg. Another cohort of three mice (M5-M7) received 1.80 – 1.97 MBq of ^{89}Zr-DFO-SPION (122-134 µg SPION). Mice were scanned using PET/CT and MRI

scanners (both from Bruker) at 24, 48 and 72 hours post-injection. After the last scan mice were immediately sacrificed and their organs collected, imaged *ex vivo* and the radioactivity measured in gamma-counter.

At 24 hours post-injection, the biodistribution patterns of both bimodal probes were similar. Prominent accumulation was observed in the liver and spleen, whereas tumour uptake in the PD-L1 positive xenografts was minimal to absent. (**Figure 37**). In some cases, additional activity was detected in axillary and mandibular lymph nodes. Differences in nanoparticles were apparent not only between tumours within the same group, but also within individual tumour masses. The tumour-associated signal did not increase in the later time points, showing virtually no difference in comparison to imaging 24 hours post injection. In contrast, bone uptake was observed in both groups at all points, consistent with partial release of zirconium-89 and its known affinity for hydroxyapatite. MRI showed a negative contrast effect in the liver, corroborating that the radioactivity signal remained associated with the nanoparticle structure.

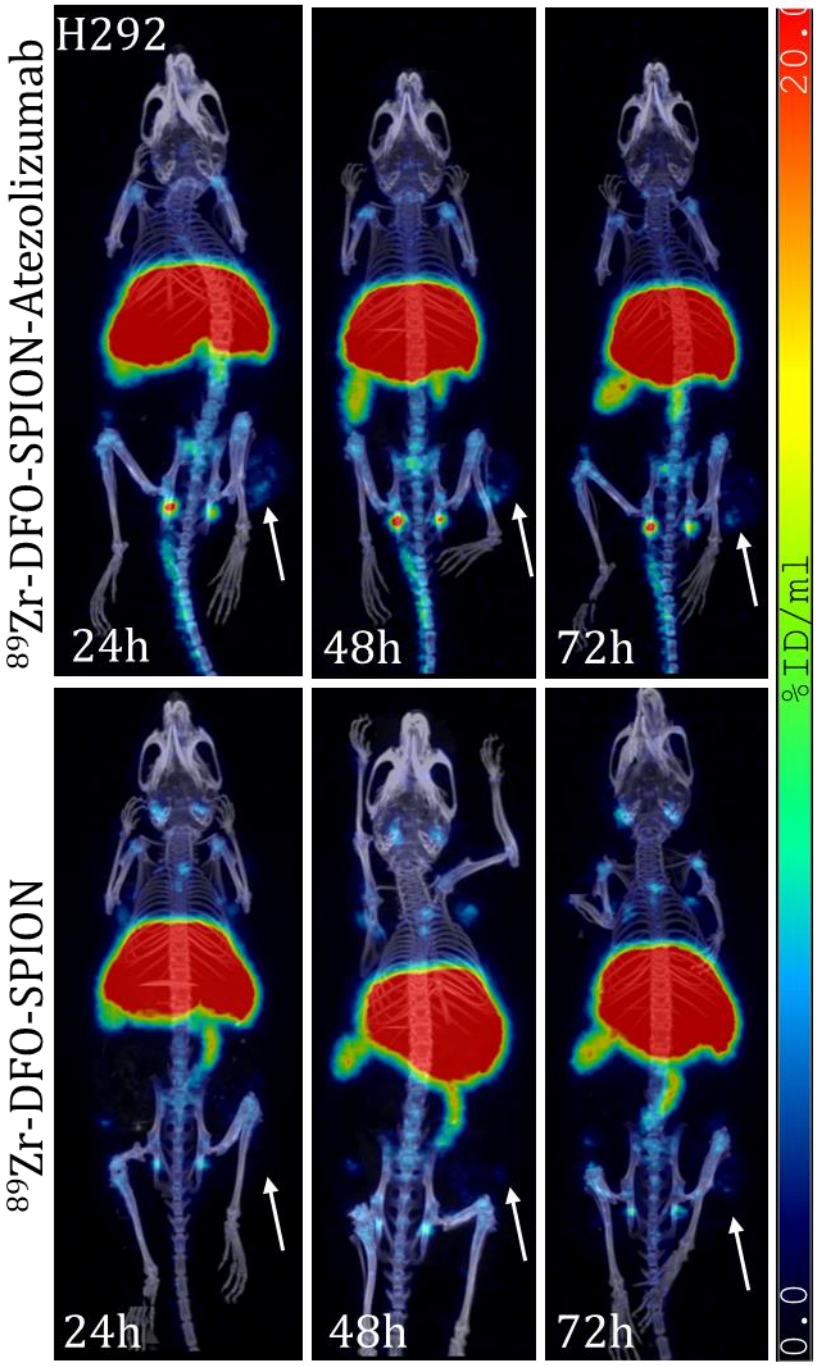

Figure 37 - Accumulation of ^{89}Zr-DFO-SPION-Atezolizumab (M3) and ^{89}Zr-DFO-SPION (M7) in H292-tumour bearing mice at 24, 48 and 72 hours post injection. Tumour localization is marked with an arrow.

Even though longer circulation time was expected, given the nanoparticle mass and diameter (198 nm hydrodynamic size), the biodistribution data suggested that the peak accumulation in non-hepatic organs may have occurred prior to the first scheduled imaging time. To investigate this possibility, an additional cohort of three mice was co-injected with similar doses of ^{89}Zr-DFO-SPION and the gadolinium-based contrast agent (Gadovist, 0.3 mmol/kg body weight). Sequential imaging was then carried out at 10 min

post-injection (MRI), 3 hours (PET), 24 h (PET) and 48 hours post injection (PET and MRI). The comparison of obtained images from this cohort is presented on **Figure 38.**

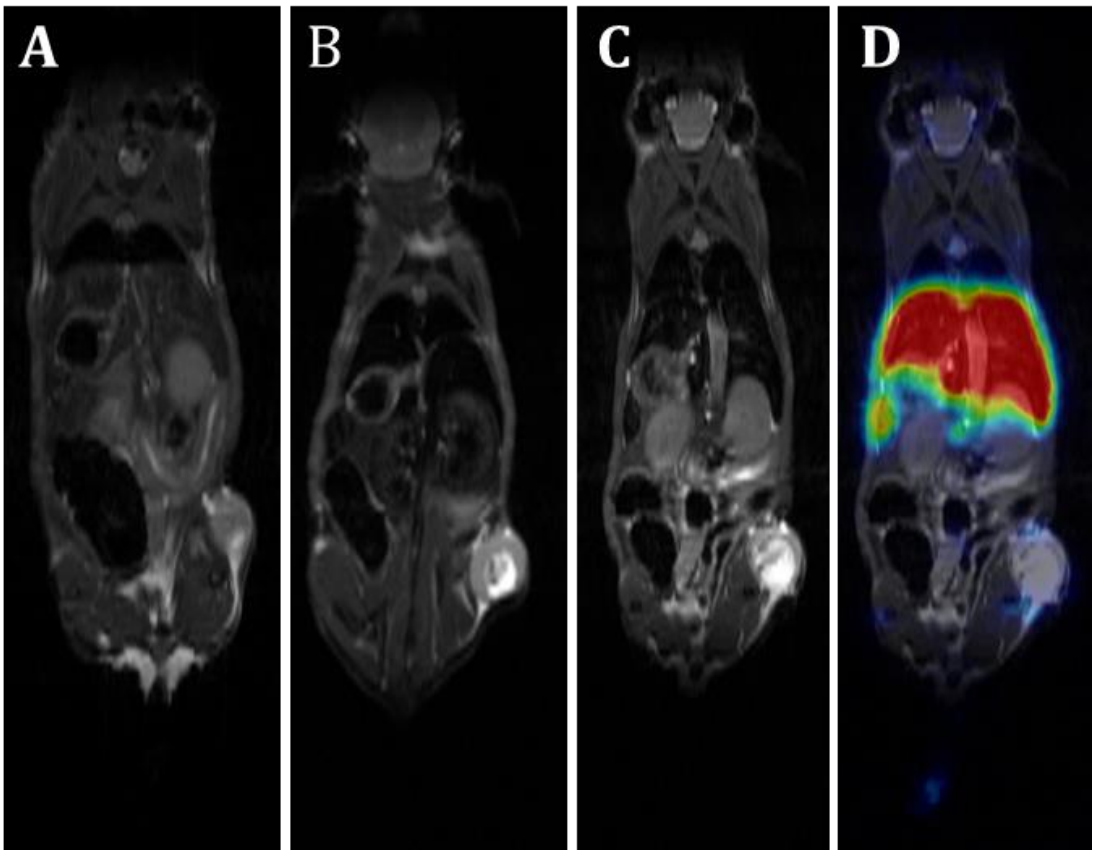

Figure 38 - Accumulation of ^{89}Zr-DFO-SPION in H292-tumour bearing mouse (M10). **A** –24 h pre-injection of ^{89}Zr-DFO-SPION, T_2-weighted MRI; **B** – 10 min post-injection, T_2-weighted MRI; **C** – 48 h post-injection, T_2-weighted MRI; **D** – 48 h post-injection, T_2-weighted MRI + PET (fusion). T2_TurboRARE sequence was used.

At 10 minutes and 48 hours post-injection MRI revealed a clear negative contrast enhancement of the liver, indicating that the nanoparticles accumulated in this organ both immediately after injection and persistently over time. In **Figure 38 B,** a similar effect was observed in the kidneys, most likely reflecting the rapid renal clearance of GBCA rather than nanoparticle retention. PET at 3 hours post injection did not differ significantly from images shown at **Figure 37.**

Finally, axial tumour slices (mouse M10) demonstrated no discernible contrast enhancement with either the GBCA or the radiolabelled SPIONs, confirming the lack of detectable tumour accumulation (**Figure 39**).

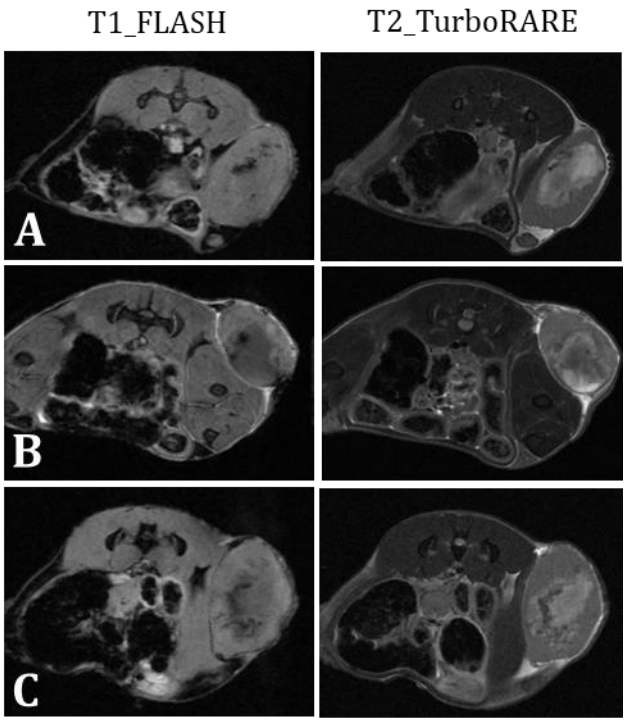

Figure 39 – T1_FLASH and T2_TurboRARE MRI of H292-tumour bearing mouse (axial plane)**. A** – 24 h pre-injection of ^{89}Zr-DFO-SPION; **B** – 10 min post-injection (^{89}Zr-DFO-SPION + GBCA); **C** – 48 h post-injection.

Biodistribution *ex vivo*

Following imaging, uptake of ^{89}Zr-DFO-SPION at 48 and 72 hours and ^{89}Zr-DFO-SPION-Atezolizumab at 72 hours post-injection performing biodistribution studies was assessed. Quantitative organ measurements (**Figure 40Figure 41; Table 35**) showed prominent uptake in liver, spleen and bone for both formulations at both time points. Blood, heart, lung and kidneys activity was very low at 48 hour and remained low at 72 hours. In case of ^{89}Zr-DFO-SPION bone and liver uptake were lower at 48 and increased by 72 hours. Notably, tumour uptake assessed at 72 hours was higher with the non-targeted ^{89}Zr-DFO-SPION than with the antibody-conjugated particles.

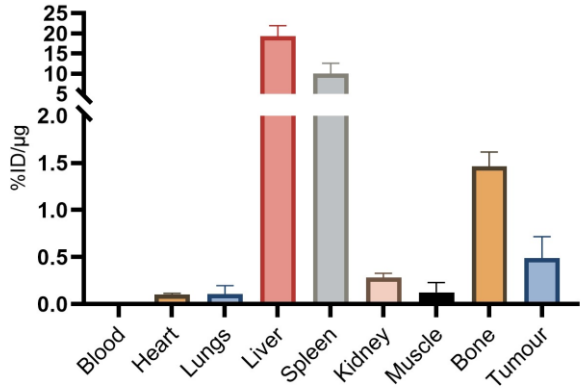

Figure 40 - Biodistribution of radioactivity in major organs after 48 hours post injection of ^{89}Zr-DFO-SPION (data are presented as mean ± SD for n = 3 animals in the group)

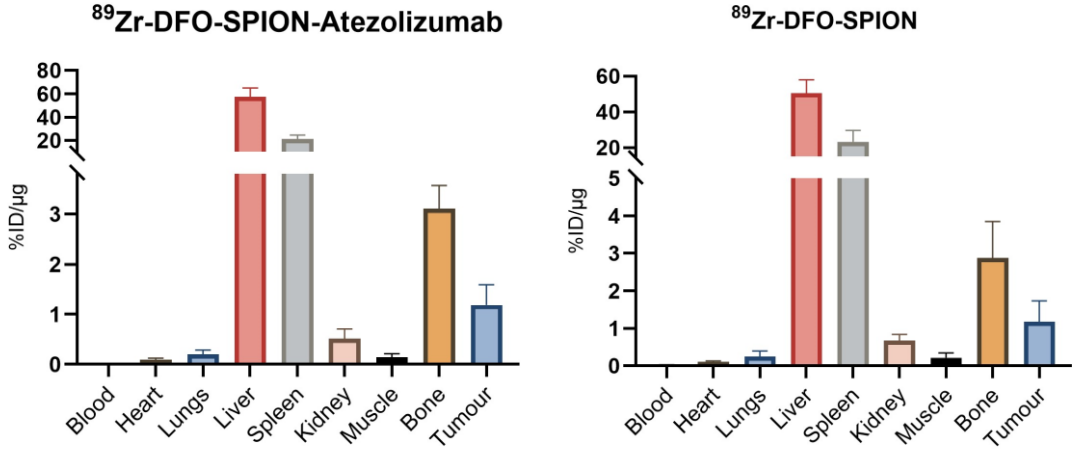

Figure 41 - Biodistribution of radioactivity in major organs after 72 hours post injection (data are presented as a mean ± SD for n = 4 [^{89}Zr-DFO-SPION-Atezolizumab) or 3 (^{89}Zr-DFO-SPION) animals in the group

Table 35 - Radioconjugate uptake in organs [%ID/g] (data are presented as mean ± SD for n = animals in group)

Tissue	^{89}Zr-DFO-SPION (n = 3)	^{89}Zr-DFO-SPION (n = 3)	^{89}Zr-DFO-SPION-Atezolizumab (n = 4)
	48 h p. i.	72 h p. i.	72 p. i.
Blood	nd*	nd*	nd*
Heart	0.10 ± 0.01	0.10 ± 0.03	0.09 ± 0.02
Lungs	0.11 ± 0.09	0.25 ± 0.15	0.20 ± 0.11
Liver	19.24 ± 2.65	50.42 ± 7.66	56.28 ± 8.8
Spleen	10.03 ± 2.54	23.35 ± 6.31	21.78 ± 3.90
Kidney	0.28 ± 0.04	0.68 ± 0.16	0.42 ± 0.02

Muscle	0.12 ± 0.11	0.22 ± 0.13	3.21 ± 0.51
Bone	1.46 ± 0.15	2.88 ± 0.97	3.21 ± 0.51
Tumour	0.49 ± 0.23	1.18 ± 0.56	1.05 ± 0.37

* - not detectable

The strong liver and spleen signals are characteristic of nanoparticles cleared by the mononuclear phagocyte system (MPS) [192]. After intravenous injection, SPIONs rapidly adsorb plasma proteins, which flag them for uptake by Kupffer cells in hepatic sinusoids and macrophages in the spleen. Antibody conjugation increases hydrodynamic size (and often alters surface chemistry). This makes easier for blood proteins to coat the nanoparticles, which in turn speeds their capture by liver/spleen macrophages reducing blood half-life and tumour delivery. The progressive bone signal is consistent with ^{89}Zr released from the nanostructure binding to hydroxyapatite in the bone matrix over time [193]. Our sampling at 48 and 72 h post-injection cannot resolve very early kinetics (e.g., lung transit, blood clearance) reported by others. Nonetheless, the pattern of high liver/spleen, low blood, rising bone signal, and size-dependent tumour delivery is internally consistent and mechanistically explained by mononuclear phagocyte system capture and chelate stability. Future optimisation should focus on nanoparticles modifications that will extend circulation, reduce off-target effects, and sustain tumour exposure.

4. Experimental methods

4.1 Reagents

Purchased reagents

Reagents were used as received, unless stated otherwise.

- Tetraethyl methylenebis(phosphonate) - Acros Organics
- Parafolmaldehyde – POCH, Gliwice, Poland
- Diethylamine – Acros Organics
- PTSA – POCH, Gliwice, Poland
- hypophosphorous acid - Acros Organics
- ethoxytrimethylsilane - Acros Organics
- Deferoxamine mesylate – Acros Organics
- *N,N*-diisopropylethylamine (DIPEA) – Acros Organics
- Formaldehyde- RCI LabScan, Thailand
- Triethylamine – Acros Organics
- *p*-NCS-C_6H_4-DFO - Diverchim, France
- Magnesium sulphate (VI) - Chempur, Piekary Śląskie, Poland
- Silica gel 60 – Merck, Germany
- Molecular sieves 4Å – Sigma Aldrich, Germany
- TLC plates Silica gel 60 F_{254} – Merck, Germany
- Dichloromethane – Chempur, Piekary Śląskie, Poland
- DMSO – Merck, Germany
- DMF – Sigma Aldrich
- Chloroform - Chempur, Piekary Śląskie, Poland
- Methanol - Honeywell, Germany
- THF - Sigma Aldrich, Germany
- Toluene - POCH, Gliwice, Poland
- DMSO-d_6 – Euroisotope, France
- D_2O – Polatom, Poland
- Human serum – Sigma Aldrich, Germany
- EDTA – Sigma Aldrich, Germany
- Dextran coated superparamagnetic iron oxide nanoparticles – Ocean Nanotech, USA

- Monoclonal antibody Atezolizumab used for bimodal probe synthesis steps (bioconjugation) and as blocking solution for *in vitro* studies was obtained as Tecentriq® (Roche).
- Radioactive solution of ^{89}Zr was received in form of ^{89}Zr-oxalate in 1 M oxalic acid. Isotope was either purchased from external producer (Revvity, The Netherlands; or Voxel, Poland) or produced in on-site cyclotron IBA Cyclone 18/9.
- Amicon centrifuge filters – Merck, Germany
- EDC – Ambeed, USA
- 1,3-diaminopropane – Sigma Aldrich, Germany
- Fluorescamine – Apollo Scientific, UK
- AF647, NHS ester – Lumiprobe, Germany
- Chelex 100 sodium form (200-400-mesh particle size); Fluka, USA

Reagent and solvent preparation

- Diethylamine was distilled from zinc dust, under nitrogen.
- Metallic sodium was added to methanol few hours prior distillation of the solvent.
- THF was dried by distillation over sodium dispersion/benzophenone ketyl.
- Molecular sieves were prepared by drying in 300 °C for 24 hours and cooled down in desiccator.
- Triethylamine (Et_3N) was left over KOH overnight, than distilled under a nitrogen atmosphere and stored above KOH.
- DMSO (and DMSO-d_6) was stored over dried molecular sieves.
- MES buffer 0.5 M: 9.76 g (0.05 mol) of MES free acid was dissolved in c.a. 80 mL of deionized water. pH was checked and adjusted to 5.0 with 10 M NaOH. Then, solution was filled to final volume of 100 mL.
- Sodium bicarbonate-carbonate (BC) buffer 0.1 M: BC buffer consists of sodium bicarbonate and sodium carbonate, with molar ratio dependent of desired pH (for pH = 9.0: 0.092 M $NaHCO_3$ + 0.008 M Na_2CO_3). Sodium carbonate solution 0.1 M was prepared: 529.94 mg of anhydrous Na_2CO_3 was dissolved in 50 mL of deionized water. Then, 0.1 M sodium bicarbonate was prepared by dissolving 4.2 g of $NaHCO_3$ in 0.5 L of deionized water. Final buffer was prepared by adding 43.48 mL of sodium carbonate to 500 mL of 0.1 M sodium bicarbonate. Desired pH (9.0) was confirmed with pH indicator paper.

- HEPES buffer: 59.757 g HEPES was dissolved in 200 mL of deionised water. 10 M NaOH was added until pH reached 7.0. The solution was filled to final volume of 500 mL.
- Fluorescamine (0.1% (w/v)) was prepared by dissolving 1 mg of solid fluorescamine in 1mL of MeCN.

4.2 General techniques

Nuclear magnetic resonance spectroscopy

Two NMR spectrometers were used to perform ^{1}H NMR, ^{31}P-NMR and ^{13}C NMR analyses:

- Varian Unity Inova 300 MHz
- Agilent Technologies 400 MHz
- Nanalysis-60 60 MHz

The measurements were carried out at room temperature.

Mass spectroscopy

A mass spectrometer used for MS analysis was 400 QTrap (Appled Biosystems/MDS Sciex), with the electrospray ionisation (ESI) method.

Microwave reactor

Discover ® CEM reactor was used for Kabachnik-Fields reaction in water.

Radioactivity handling

All work involving radioactive compounds (radiolabelling, stability studies) was carried out in a laboratory located in a controlled area. The operator was authorised to work with open radioactive sources (category A). Manual work with radioactive samples was carried out in hot chambers (equipped with lead shields) with laminar airflow and an ACS (air compressing station) system, in compliance with all radiological protection requirements.

RadioTLC

All radioTLC assessments were conducted using Raytest thin layer radiochromatograph (TLC-scanner), with Gina Star software.

a) Method based on *Nature* protocol on HIR [140]

- Plate: strongly acidic cation exchange silica gel (Sorbent Technologies), plates were soaked in Chelex-treated water (CTW) and dried well prior to use
- Developing phase: Chelex-treated water
    - Chelex resin is washed several times, until the neutral pH of the washings. Deionised water (500 mL, Milipore) was then purified by incubating with 25 g of Chelex resin, stirring overnight at room temperature. CTW was filtered through a 0.22 μm filter and brought to pH 7-8 with diluted Na_2CO_3. Aliquots of CTW were stored at 4 °C up to 1 year.
- Retention factors:
    - ^{89}Zr-oxalate – R_f = 0,0
    - SPION $R_f \sim 1.0$

b) Method used for ^{89}Zr-DFO-Atezolizumab [42]

- Plate: iTLC (instant TLC) silica gel impregnated glass fibre strip
- Developing phase: 0.1 M ammonium acetate + 25 mM EDTA 1:1 (*v:v)*
    - 5 M NH_4Oac (ammonium acetate stock solution) : 19.27 g of ammonium acetate was weighed, transferred to a 50 mL volumetric flask and 30 mL of deionised water was added. Solution was mixed until the salt was dissolved, then the flask was filled with deionised water.
    - Mobile phase: 365.3 mg of EDTA was weighed and placed in a 50 mL volumetric flask. Then 1 mL of ammonium acetate stock solution was added, then 30 mL of deionised water and pH checked with a strip (desired pH = 5.5). If pH was too low, small volume of 10 M sodium hydroxide solution was added. Mobile phase was mixed carefully until the precipitate dissolved, then filled up to 50 mL with deionised water.
- Retention factors:
    - ^{89}Zr-oxalate – $R_f \sim 1.0$
    - SPION – R_f = 0.0

Statistical analysis

Viability, flow cytometry and specificity of binding were analysed by ANOVA method with Sidak's multiple comparisons tests using GraphPad 10.0 (Graphpad Inc., San Diego,CA. The correlation between measured T_x time and concentration of bimodal agents was performed by simple linear regression.

4.3 Bisphosphonate-modified DFO – experimental details

4.3.1 Synthesis of H-phosphonate

Synthesis of tetraethyl ethenylidenebis(phosphonate) (compound B)

Compound **B** was prepared by reaction of tetraethyl methylenebis(phosphonate) (**A**) with paraformaldehyde and diethylamine in methanol [156]. Paraformaldehyde (5.02 g/172 mmol) was added to 250 mL round-bottom flask and dissolved in 100 mL of methanol with heating and stirring. After complete dissolution of paraformaldehyde, diethylamine was added (3.57 mL / 2.52 g / 34.5 mmol) following compound **A** (8.6 mL/10 g/ 34.5 mmol). The mixture was refluxed for 24 hours. Reaction progress was monitored by TLC ($CHCl_3$: MeOH 10:1 V/V; SG on aluminium plates). The reaction mixture, the substrate and the mixture of both were spotted on the plates. They were developed, dried with a stream of lukewarm air and then developed in an iodine chamber. Once product formation was confirmed by the above TLC method, the reaction was stopped and methanol was removed under vacuum. Residue was dissolved in 50 mL of toluene and solvent was removed under vacuum, to ensure complete removal of methanol. Yield of reaction was confirmed by ^{1}H-NMR.

Intermediate product (compound **B**) was dissolved in 50 mL of toluene and PTSA was added (25 mg/0.15 mmol). The mixture was refluxed overnight in presence of dried molecular sieves 4 Å. The next day toluene was removed under vacuum. Crude product was dissolved in 50 mL chloroform and washed twice with water (20 mL each washing). Organic phase was then dried with $MgSO_4$ and chloroform was evaporated under vacuum. The composition of the reaction mixture was determined by ^{1}H-NMR.

The reaction mixture was separated by chromatographic methods:

- Separation on a SiO_2 bed column: 1.14 g of a sample was placed on top of a column and eluted with a 10:1 (V/V) chloroform:methanol mobile phase. The content of compound B in consecutive fractions was monitored by TLC.
- *Isolera* flash chromatography system: Separation was done on Biotage® SNAP KP-Sil 25 g cartridge using gradient of chloroform 100%→80% and methanol 0%→20%. Separation was based on absorbance at 254 and 400 nm.

Synthesis of compound G

Compound **G** was prepared by reaction of an excess of **F** with **C**, as decribed in Vitha et al [154]. Firstly, solid phosphinic acid (compound **D**) was prepared from 50% acid solution by freezing a 10 mL with liquid nitrogen and lyophilisation overnight. Purity of a substrate was confirmed by ^{31}P-NMR to be 100%. Solid **D** (5.98 mmol, 0.39 g) in form of flat, whitish crystals was dissolved in 5 mL of tetrahydrofurane. 11.95 mmol (1.41 g) of **E** was added and the reaction was carried out for two hours in room temperature, with mixing and amid nitrogen [158].

The mixture was used in the next reaction step without purification due to the high reactivity of ethyl hypophosphinate (compound **C**). To the round-bottom flask the mixture was already in, 1.04 mL (0.77 g; 5.98 mmol) of DIPEA as catalyst was added, as well as 1 g of compound B. Reaction occurred overnight, in room temperature and with stirring. The next day solvent was evaporated and the crude product was dissolved in 10 mL of dichloromethane. Organic phase was flushed with 15 mL of distilled water and water was re-extracted with CH_2Cl_2 twice, using 10 mL each time. Combined organic phases were dried with $MgSO_4$ and the solvent was evaporated. Sample of a crude product was examined with ^{1}H-NMR, ^{31}P-NMR and ^{13}C-NMR.

4.3.2 Synthesis of bisphosphonate-modified deferoxamine

Reaction with H-phosphonate

Reaction of deferoxamine with synthesised **G** was expected to occur according to Kabachnik-Fields mechanism (phospha-Mannich) – **Scheme 39.** Numerous attempts were undertaken in different variations of conditions: solvents, molar ratio of substrates, temperature, carbonyl group donor (formalin or paraformaldehyde), as described in Research section – 3.1.1.1.

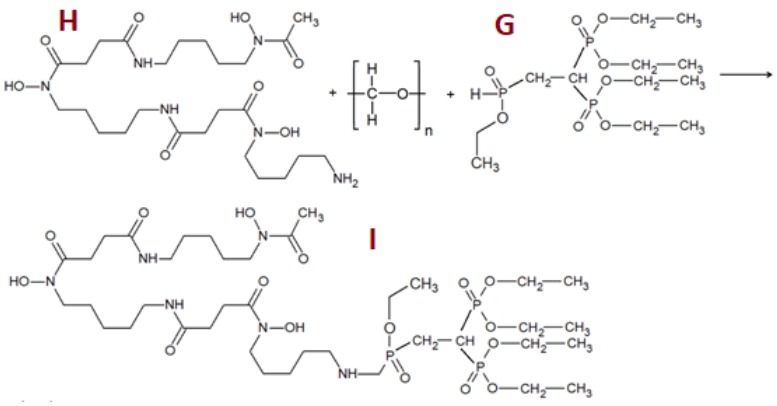

Scheme 39- Expected Kabachnik-Fields reaction (n = 1 – formalin; n = 8-100 – paraformaldehyde)

Reaction in DMSO

Substrate G**,** Et_3N and solvent were purified before use as described in 4.1.1. Compound **H** (20 mg, 0.03 mmol) was added to glass vial with small magnetic stirrer, followed by 0.9 mg (0.03 mmol) of paraformaldehyde. DMSO-d_6 was added to the vial (3 mL) as well as 4 µL (0.03 mmol) of triethylamine (with a Hamilton syringe). After complete dissolution of **H** and paraformaldehyde, 12 mg (0.03 mmol) of compound **G** was added, dissolved in 500 µL of DMSO-d_6. Reaction went on for 24 hours amid nitrogen in room temperature (23 ^{O}C). After 24 hours, aliquot of 50 µL was withdrawn for NMR analysis. Reaction temperature was then increased to 60 ^{O}C and reaction proceeded another 72 hours. Sample for NMR was taken without further purification.

4.3.3 Hydrolysis of the protecting ethoxy groups

The experiment was designed to determine what conditions are necessary for the complete hydrolysis of the ester groups protecting the bisphosphonate, and whether the required conditions will not degrade the DFO chelating structure. Two groups of samples were prepared, each in triplicate. The reaction was carried out in glass vials closed with screw caps and in deuterated solvents, for easy evaluation of the structure of the reaction mixture by ^{1}H-NMR technique. The first group tested was a solution of **H** (50 mg, 0.076 mmol) in 3 mL D_2O. The second group of samples was 0.076 mmol (22 mg) of **G** in the same volume of DMSO-d_6.

The reaction was carried out for two days, in three different sets of conditions, with the temperature increase after 24 hours. Samples for ^{1}H-NMR were withdrawn from the test tubes at 0, 22 and 45 hours.

4.3.4 Stability studies

Radiolabelling of DFO-BP and *p*-NCS-C_6H_4-DFO

^{89}Zr-oxalate (38 µL, 17.76 MBq) in 1 M oxalic acid was neutralized with 8 µL of 2 M Na_2CO_3. Then, pH of radioactive solution was stabilized by addition of 50 µL of HEPES buffer. Final volume of radioactive solution was 96 µL. Both DFO-derivatives (compound **M** and *p*-NCS-C_6H_4-DFO, Diverchim, France) were prepared as a 4.2 mM solution in DMSO. Of each chelator solution, aliquot of 15 µL was prepared in 1.5 mL centrifuge tube (eppendorf) and 45 µL of radioactive solution was added, followed by mixing with the pipette tips. RadioTLC of radioactive solution and both reaction mixture was performed at time T = 0 h.

Stability in serum

From each of the two reaction mixtures 17 μL (2 MBq) aliquote was withdrawn and added to 1.5 mL centrifuge tube (133ppendorf) containing 200 μL of normal human serum (Sigma Aldrich). Tubes were carefully closed and incubated in 37 ^{O}C with shaking (in a thermoshaker placed in shielded hot cell). RadioTLC was performed at selected time points.

Stability – transchelation

From each of the two mixtures 8.5 μL (1 MBq, 8.93 nmol) was withdrawn and added to centrifuge tube (133ppendorf). To each 133ppendorf 100 μL of HEPES buffer was added, followed by 89.3 μL of 0.01 M solution of EDTA in HEPES buffer (0.893 μmol, 100 x molar excess). Tubes were carefully closed and incubated in room temperature. RadioTLC was performed at selected time points.

Stability in HEPES

From each of the two reaction mixtures 30 μL was taken and 285 μL of HEPES buffer was added, resulting in final DFO concentration of 100 μM. Reactions were then incubated in lead shielded container for radiological safety and radioTLC was performed at selected time points.

4.4 Bimodal probes – experimental details

4.4.1 SPION surface modifications

Amine introduction

Amine functionalization was performed according to a protocol from literature [161]. Amicon filter (50 kDa MWCO) was conditioned by washing it twice with 500 μL of deionized water, and centrifuged for 5 minutes. 100 μL (0.5 mg) of dextran-coated SPION (5 mg/mL) was added to the filter unit, filled with 0.1 M MES buffer and centrifuged for 20 minutes. Nanoparticles were then washed twice with the same buffer. Nanoparticles were then recovered with 200 μL of buffer, by placing the filter 'upside' down and centrifuging. Filter was then washed with another 200 μL of MES buffer and the volume was added to the nanoparticles, resulting in ~400 μL of SPION in MES buffer. The mixture was sonicated to obtain a homogeneous dispersion. Meanwhile, EDC solution in MES buffer was prepared, by adding 0.5 mg EDC·HCl to 200 μL 0.1 M MES buffer, and stirring with heating to 30 ^{O}C on a heat block. After complete dissolution, EDC was added to nanoparticles and sample was

mixed in 30 ^{O}C for 20 minutes. Next, 17.2 µL (0.7 µmol) of 1,3-diaminopropane was added and reactions' pH was adjusted to 6 with hydrochloric acid. Reaction was incubated in 30 ^{O}C for 120 minutes. Then, reaction mixture was filtered through conditioned Amicon filter. Brownish precipitate was washed 4 times with 0.1 M MES buffer and then recovered with appropriate media (depending on batch's next modification).

Two-step bioconjugation

First, activation of the nanostructure surface was carried out at pH = 5.0 and in the presence of a 4000 molar excess of EDC for 3 h at room temperature. Then, the solvent, unreacted EDC and possible by-products were filtered out using 50 kDa MWCO filters. Nanoparticles were washed twice BC buffer pH = 9.0.

Activated nanoparticles were then stripped from the filter with adequate buffer and 30-fold molar excess of Atezolizumab was added to the reaction mixture. Reaction was carried out for 17 hours at room temperature, with gentle shaking. Next, samples were centrifuged at high force (15 000 RPM, 20 879 RCF) for several hours, in order to separate nanoparticles from the mixture. Supernatant from above the brown residue was collected; residue washed with adequate buffer and samples again was centrifuged.

DFO introduction

Amicon filter (50 kDa MWCO) was conditioned by washing it twice with 500 µL of deionized water, and centrifuged for 5 minutes. 100 µL (0.5 mg) of dextran-coated SPION (5 mg/mL) was added to the filter unit, filled with 0.1 M MES buffer and centrifuged for 20 minutes. Nanoparticles were then washed twice with the same buffer and recovered with 200 µL of buffer, by placing the filter 'upside' down and centrifuging. Filter was washed with another 200 µL of MES buffer and the volume was added to the nanoparticles, resulting in ~400 µL of SPION in MES buffer. SPIONs were sonicated in order to obtain aggregate-free dispersion. Meanwhile, EDC solution in MES buffer was prepared, by adding 0.5 mg EDC·HCl to 200 µL 0.1 M MES buffer, and stirring with heating to 30 ^{O}C on a heat block. After complete dissolution, EDC was added to nanoparticles and sample was mixed in 30 ^{O}C for 120 minutes. To the activated SPIONs 0.5 mg of DFO-Mes was added (80 µL of 9 mM stock solution in MES buffer). Reaction was carried out overnight in 35 ^{O}C on a heat block with shaking. After 20 hours, reaction was filtered on conditioned Amicon 50 kDa MWCO filter and SPION-DFO transferred to appropriate buffer for further modification or deionized water for structure studies.

Synthesis of fluorochrome-labelled SPIONs

Conjugation of AlexaFluor 647 dye was performed according to manufacturer's protocol. Dye was purchased in form of NHS ester, and was used in bioconjugation reactions in 8-fold molar excess over protein.

Atezolizumab-AF647

Monoclonal antibody was transferred into BC buffer using 50 kDa MWCO filter. Its concentration was measured with UV/Vis Nanodrop. Desired amount of mAb was diluted to concentration of 2 – 10 mg/mL with BC buffer, and appropriate excess of AF647 NHS ester in DMSO was added. Reaction was carried out in room temperature for 2 hours. Then, reaction mixture was added to centrifuge filter 50 kDa MWCO and centrifuged for 15 minutes, 13.4 kRPM. Supernatant was discarded, bioconjugate washed with 400 µL of BC buffer. Last step was repeated until the supernatant was colourless. Protein-dye conjugate was then stripped-off of filter with 2 portions of 200 µL of PBS. Absorbance was measured at wavelengths λ = 280 nm and λ = 680 nm, and the values obtained were used to calculate the degree of labelling (DOL).

SPION-Atezolizumab-AF647

SPION-Atezolizumab was prepared and characterised like it is described in 4.4.1 *Two-step bioconjugation.*. Nanoparticles were then transferred into BC buffer (pH = 9.0) and diluted to protein concentration of 2 – 10 mg/mL. Appropriate excess of AF647 NHS ester was dissolved in small amount of DMSO and intensely blue solution was added to nanoparticles dispersion. Reaction was carried out in room temperature for 2 hours. Then, reaction mixture was added to centrifuge filter 50 kDa MWCO and centrifuged for 15 minutes, 13.4 krpm. Supernatant was discarded, nanoparticles washed with 400 µL of BC buffer. Last step was repeated until the supernatant was colourless. Nanoparticles were stripped off of the filter with 2 portions of 200 µL of PBS. SPION-Atezolizumab-AF647 nanoparticles in aqueous solution are dark green in colour.

Heat-induced radiolabelling

Neutralization of ^{89}Zr-oxalate: solution of ^{89}Zr-oxalate was delivered in 1M oxalic acid. Appropriate volume of 2M Na_2CO_3 for neutralization was calculated as $0.44 \cdot V_{^{89}Zr\text{-}oxalate}$. Reaction mixture was mixed by pippeting after addition of sodium carbonate solution and pH was measured with pH-indicator paper (pH-Fix; Macherey-Nagel). Desired pH for HIR is in range 7.5 – 9.0.

Radiolabelling: 0.5 mg of SPION was diluted with 300 µL of CTW in 1.5 mL eppendorf tube. Radioactive solution was added to SPION solution and pH verified before labelling start. For too low pH (< 8.0) small aliquots of 2 M Na_2CO_3 was added; in case of pH over 9.0 it was lowered by adding small volumes of 1 M oxalic acid. Then, reaction tube was placed in Thermoshaker pre-heated to 95 ^{O}C and incubated for 2 h with shaking.

Reaction progress monitoring: Radiolabelling progress was measured with radioTLC (method b in 4.4.2.). Briefly, reaction tube was removed from thermoshaker and placed in ice water for few minutes. Then, 1 – 2 µL of reaction mixture (depending on activity concentration in reaction mixture) was placed on the start line of TLC plate and developed in appropriate mobile phase. Developed plate was scanned with radioTLC scanner.

Quenching/filtration: In the case of incomplete binding of zirconium-89 to the nanoparticles, purification of the reaction mixture was carried out. In order to do so, 4 µL of DFO solution (4.2 mM) was added and incubated with stirring for 15 minutes at room temperature. Then, ^{89}Zr-SPION was separated from ^{89}Zr-DFO with centrifuge filtration 50 kDa MWCO.

Labelling through DFO

Neutralization of ^{89}Zr-oxalate: solution of ^{89}Zr-oxalate was delivered in 1M oxalic acid. Appropriate volume of 2M Na_2CO_3 for neutralization was calculated as $0.44 \cdot V_{89Zr\text{-}oxalate}$. Reaction mixture was mixed by pippeting after addition of sodium carbonate solution and pH was measured with pH-indicator paper (pH-Fix; Macherey-Nagel). For pH stabilization, 200 µL of HEPES buffer was added to the reaction mixture. Desired pH for radiolabelling through DFO is in range 7.0.

Radiolabelling: SPION-DFO in HEPES was mixed with neutralized radioactive solution and incubated in room temperature. Reaction progress monitoring and quenching/filtration were performed in the same manner as for heat-induced radiolabelling.

Natural zirconium 'labelling'

For experiments requiring ^{nat}Zr in the nanoparticle structure, 20 µL of 0.1 mM solution of $^{nat}ZrCl_4$ in 1M oxalic acid was used (instead of ^{89}Zr-oxalate in 1 M oxalic acid). Then, the protocols were followed like in HIR or chelator-radiolabelling, excluding radioTLC / activity measurements. Final product was filtered with Amicon 50 kDa MWCO filters with multiple washings, to ensure complete removal of unbound zirconium cations from the reaction mixture.

4.4.2 Quantitative assays

Isotopic dilution

0.1 mM solution of $^{nat}ZrCl_4$ was prepared by dissolving 2.33 mg of zirconium (IV) chloride in 100 mL of 1 M oxalic acid. Next, 100 µL of this solution was added to 20 µL of ^{89}Zr in 1 M oxalic acid (Perkin Elmer). Mixture's pH was then adjusted to 7.0 by adding 2 M Na_2CO_3 and 0.1 M HEPES buffer in order to create ~250 µL of working solution. Analysed conjugates (DFO-modified SPIONs) were prepared in triplicates, of equal and known mass. Volumes of 20, 25 and 30 µL of working solution were added to each three samples of analysed conjugate. Labelling was conducted overnight in room temperature, with gentle mixing. The next day radioTLC of all the samples was performed to determine the ratio of bound to unbound ^{89}Zr (method b).

SPION concentration – UV/Vis measurement

SPION concentration was measured by determination of their absorbance at 600 nm. Measurements were conducted on UV1900 Shimadzu in Quantitative protocol, having previously completed calibration. Calibration was performed by measuring absorbance of 5 solutions of known and increasing concentration and determining the calibration curve in the spectrophotometer's control software. Unknown samples were then measured and their concentration calculated by the control software.

Protein concentration

Nanodrop One was used for monoclonal antibody concentration measurement. The Protein A280 method was created for Atezolizumab, including extinction coefficient of $16.21\frac{100\ mL}{g\cdot cm}$. Method calculates concentration based on sample absorbance at 280 nm. It also verifies if sample was pure protein based on A260/A280 ratio (absorbance at 260 nm and 280 nm, respectively). An ideal 260/280 ratio for common proteins is 0.6, and higher values may indicate contamination with nucleic acids or other compounds.

To determine amount of unreacted protein in bioconjugation reaction supernatant was analysed with BCA or Bradford assays, according to manufacturer's protocol. Calibration curve of Atezolizumab consisted of 8 points between 25 and 2000 µg/mL of mAb.

4.4.3 Structural studies

DLS

DLS and Zeta potential measurements were performed by Professor Grzegorz Dzido (Department of Chemistry, Silesian University of Technology). DLS measurements were carried out at Zetasizer S. Nanoparticles were dispersed in deionized water, and measured in temperature of 25 ^{O}C. Results were mathematically modelled with a general-purpose model which is suitable for most samples with a normal grain distribution. It was assumed for calculations that the addition of solid magnetite does not significantly affect the solution of the mathematical model. Final result was averaged from five measurement repetitions.

Size measurements parameters: Sample stabilisation time was 300 s. The refractive index was taken for the laser wavelength of 632 nm (R=2.358), and the absorption coefficient 0.300, as for coloured samples (indications of the manufacturer of the apparatus). The instrument's operating parameters were selected automatically. Measurements were performed in disposable cuvettes model DTS0012.

Zeta potential

Nanoparticles were dispersed in deionized water, and measured in temperature of 25 ^{O}C on Zetasizer Z apparatus, with red laser of wavelength 632 nm . It was assumed, that sample viscosity is not affected by the addition of magnetite (viscosity of water). Mathematical model for calculation of Zeta potential was Smoluchowski model approximating Henry's function F(κa)=1.5. Final result was averaged from five measurement repetitions.

Size measurements parameters: Sample stabilisation time was 300 s. The instrument's operating parameters were selected automatically. Measurements were performed in measuring cell model DTS1070

FTIR

FT-IR spectra were obtained on NICOLET iS50 with ATR module and software OMNIC and TQ Analyst. Before measuring the samples in aqueous solution, the spectrum of water was subtracted as a blank.

X-ray Photoelectron Spectroscopy

XPS measurements were performed by Professor Agata Blacha-Grzechnik (Department of Chemistry, Silesian University of Technology). Measurements were conducted on AXIS Supra+ (Kratos Analytical), monochromatic Al(Kα) C-ray source (150 W, 10 mA, 15 kV).

System base pressure:pb = $4.1 \cdot 10^{-9}$ Torr. The pass energy was set to 160 eV (scanning step: 0.9 eV) for survey scans and 20 eV (scanning step: 0.05 eV) for high-resolution spectra acquisition. The Kratos charge neutralization dual-beam system was used for charging effect compensation. Binding energy scale was calibrated relative to the C-C component of C1s signal (284.8 eV). Samples were applied to a silicon wafers and air-dried before measurements. The recorded spectra were analysed using CASA XPS® software and embedded algorithms. The components of the high-resolution spectra were given as Gaussian (70%) and Lorentzian (30%) lines, while for the background the Shirley's function was used.

MALDI-TOF

Samples of SPIONs were transferred to 0.1% TFA (aqueous solution) and applied into the steel target in following ways:

- 2,5-DHAP dried droplet

  Matrix solution preparation: 1.52 mg of 2,5-DHAP was dissolved in 75 µL of EtOH. Next, 25 µL of DAC (diammonium hydrogen citrate, 18 mg/mL) solution was added. Sample in 0.1% TFA was mixed with 2% TFA in equal volumes (5 µL). Then, 5 µL of the matrix solution was added. Samples were mixed until the crystallization started (visible opacity of the sample). Drop of 0,5 µL of the crystal suspension was placed on the target.
- 1,5-DAN dried droplet

  Matrix solution was freshly prepared 1,5-DAN saturated solution in 50:50 (v/v) acetonitrile : TFA 0,1% in water. Sample was then mixed with matrix solution in a ratio of 1:2 (v) and the 0.5 µL of the mixture was applied to the target.
- SA double layer

  Two matrix solutions were prepared: SA saturated in EtOH and SA saturated in solution of 30:70 (v/v) acetonitrile: 0.1% TFA in water. On the target was applied thinlayer of first matrix solution (in EtOH) and dried. Sample was then mixed in equal volumes with second matrix solution and mixture was applied to previously prepared layer in volume of 0.5 µL.
- S-DHB

  Matrix solution preparation: 2.5 mg of S-DHB was dissolved in 100 µL of solution (50:50 (v/v) 0.1% TFA in water and MeCN). 0.5 µL of the sample was applied to the target, and after drying equal volume of matrix was added.

After completing sample preparation, samples on steel target were analysed on MALDI Ultraflex TOF/TOF mass spectrometer, Bruker, MA, US.

4.5 *In vitro* studies

4.5.1 General methods for cell culture

Human non-small cell lung cancer derived cell lines H292 and $H292_{PD\text{-}L1KO}$ were cultured in RPMI medium (RPMI Medium 1640 (1X) + GlutaMAX™-I, Gibco) supplemented with 10% foetal bovine serum (FBS) (Gibco). The ES-2 cell line, human ovarian cancer cell line and its PD-L1 knock-out variant were cultured in the same medium (RPMI with 10% FBS). The cells were routinely tested and found to be negative for Mycoplasma contamination. They were cultured in 75 cm^2 cell culture flasks and used while in passages 3-10. All the utilized cell lines were obtained from the Medical Oncology Laboratory, University Medical Centre, Groningen (UMCG). Cell lines were passaged when reached 80-90% confluency. After removal of cell medium, cells were washed with DPBS (Gibco) and lysed with TryplE™ Express Enzyme (Gibco). Process of lysis was controlled with optical microscopy, and TryplE was neutralised with double volume of medium after all cells were dissociated. Cell suspension was then transferred into 15 mL centrifuge tube and centrifuged at 200 RCF for 5 minutes. Supernatant was then removed, cells resuspended in fresh cell medium and adequate amount placed in new culture flask. Cells were incubated in humidified chamber at 37 ^{O}C supplied with 5% CO_2.

Surplus of cells was preserved in liquid nitrogen. To do so, cells were washed with DPBS and resuspended in RPMI, DMSO and FBS mixture. Cell suspension was transferred into cryovials and placed in placed in a Mr. Frosty™ Freezing Container (Thermo Fisher Scientific), which allows for a gradual cooling at a rate of -1°C/ min when stored at -80 ^{O}C for at least 24 hours. After that time, cryovials were transferred into liquid nitrogen for long-term storage.

In order to prepare experiments with known amount of cells, concentration of cells was counted with Bruker's chamber. Cells were collected and resuspended in medium, ensuring the sample is homogeneous. When needed, cells were dyed with Trypan Blue 0.5% solution (Sartorius), added in equal volume to cell suspension. Portion of 10 µL of the cell suspension was added into chamber and cells counted under a microscope. The cell concentration (cells/ mL) was calculated using the following formula:

$$\frac{cells}{ml} = \frac{counted\ cells}{counted\ squares} \cdot dilution\ factor\ \cdot 10^4$$

4.5.2 Cell lines characterization

Western Blot

Reagents and solutions

- RIPA buffer

Recipe for preparation of 2 mL of reagent: to 1956 µL of RIPA buffer (radioimmunoprecipitation assay buffer) (Pierce™ RIPA Buffer, Thermo Scientific™) was added: 4 µL of EDTA (0.5 M, Sigma Aldrich), 20 µL of phosphatase inhibitor (Halt™ Phosphatase Inhibitor Cocktail (100X)) (Thermo Fisher Scientific) and 20 µL of phoshoSTOP cocktail 100X. Ingredients were thoroughly mixed.

- Running buffer

To 900 mL of distilled water, 50 mL of 20X NuPage MOPS SDS Running Buffer (20x) (Invitrogen) was added. Ingredients were thoroughly mixed.

- Transfer buffer

To 700 mL of distilled water, 100 mL of 10X Transfer buffer and 200 mL of methanol was added.

- Tween-Tris Buffered Saline (TTBS) 0.5 M

Prepared by diluting 50 mL of Tris Buffered Saline Solution (10x) (Sigma-Aldrich (Merck)) in 450 mL of deionized water, followed by addition of 250 µL of Tween 80 (Sigma-Aldrich (Merck)).

- Stripping buffer

To 67.5 mL deionized water was added 12.5 mL Tris Buffer Solution 0.5 M, pH 6.8 (Thermo Scientific), 20 mL of SDS (Sodium Dodecyl Sulfate 10% solution (Invitrogen)) and 0.8 mL of β-mercaptoethanol (Bioultra, for molecular biology (Merck Life Science)).

Preparation of lysates

Lysates of each of the cell lines were prepared in the following manner. Cell culture of 80 - 100% confluence was washed with PBS with 10% FBS after media aspiration. Cells were then dissociated with 2 mL TryplE Enzyme. The process was followed by neutralization of the dissociation enzymes with equal amount of adequate medium, collection of the cell suspension into the 15 mL centrifuge tube. Cells were centrifuged for 5 min at 200 RCF.

Supernatant was aspirated and 250 – 350 µL of RIPA complete buffer was added, depending on the amount of cell pellet. Incubation with RIPA lysis buffer went on for 30 min on ice. Samples were then sonicated and centrifuged at 4 ^{O}C, 10 000 rpm for 10 min. Lysates were then transferred to two cryovials (aliquots of 125 µL each), snap frozen in liquid nitrogen and stored in -20 ^{O}C until needed. 100 µL of lysate obtained was used for BCA assay (bicinchoninic acid assay, Pierce™ kit, Thermo Fisher Scientific) for protein concentration determination, using the manufacturer's protocol.

Sample preparation

Samples were prepared in 1.5 mL Eppendorf tubes in a total volume of 35 µL. For each sample, 20 µg of protein (calculated based on the concentration determined by the BCA assay) was loaded per well. The sample mixture contained NuPage™ LDS Sample Buffer (4X) (Invitrogen), NuPage™ Sample Reducing Agent (10X) (Invitrogen), and lysates. Samples were incubated in a Thermomixer (Eppendorf) at 70 °C for 10 min to ensure protein denaturation.

Electrophoresis

The proteins in the samples were separated by polyacrylamide gel electrophoresis (PAGE). Each sample was loaded onto a NuPAGE™ 4-12% Bis-Tris gel (Invitrogen, Thermo Fisher Scientific) in established order. Molecular Weight Marker (BLUelf Prestained Protein Ladder (MW Standard) (Simply)) was loaded as a control. NuPAGE™ Antioxidant (#NP0005) (1 mL) was added to prevent proteins from re-oxidizing. PowerPac™ HC High-Current Power Supply (Bio-Rad Laboratories Inc, USA) was set for constant voltage of 120 V. Electrophoresis went on for ~2 hours.

Transfer

The gel was recovered, and the proteins were transferred from the gel onto a nitrocellulose membrane (Nitrocellulose Western blotting membrane 0.45 µm, 150 mm x 4 m; Amersham Protran, GE Healthcare) previously soaked in transfer buffer. The transfer chamber was filled with cold transfer buffer and the transfer was performed at constant current of 330 mA for 3 hours. Completion of the transfer was confirmed visually by appearance of the molecular ladder on the membrane.

Antibody incubation

Membrane was blocked by incubation in 5% skimmed powdered milk (Gostyń) dissolved in TTBS for 1 hour in room temperature. Then it was washed twice with TTBS before adding

primary antibody solution. Anti-PD-L1 (E1L3N®) XP®, Rabbit mAb, IgG isotype, unconjugated (Cell Signaling Technology) antibody was diluted 1000x in 5% milk in TTBS. Membrane was incubated with primary antibody solution overnight in 4 ^{O}C with gentle orbital shaking. Following day membrane was washed three times with TTBS and incubated with secondary anti-rabbit antibody. Similarly, HRP-linked Anti-rabbit Antibody, IgG isotype (Cell Signaling Technology) was prepared in 1000x dilution in 5% milk solution and incubated with the membrane for 1 hour in 4 ^{O}C. Membrane was then washed three times with TTBS (10 minutes each wash) and once with deionized water.

Protein visualisation

SuperSignal™ West Pico PLUS Chemiluminescent Substrate Kit was used to visualize signals present on the membrane. Incubation with substrate was carried out in darkness (in black, opaque plastic box) for 5 minutes, followed immediately by imaging of immunoblots on Syngene G:BOX system.

Stripping

In order to remove previously introduced antibodies from the membrane, it was inbucated with stripping buffer for 20 minutes in 60 ^{O}C. After heating, membrane in stripping buffer was shaken on orbital shaker for 10 minutes, and then heating and shaking was repeated. Stripping buffer was removed, and the membrane was washed with deionized water followed by TTBS.

Antibody incubation

Incubation was performed in the same manner like the one after the transfer. Briefly, after blocking with 5% milk solution primary anti-GAPDH antibody was added (in 1000x dilution; GAPDH (D16H11) XP®, Rabbit mAb, IgG isotype, unconjugated (Cell Signaling Technology)) and incubated overnight. After washing with TTBS, secondary Anti-Rabbit HRP antibody was added and incubated for 1 hour, followed by three TTBS washings. GAPDH protein visualization was performed as described above.

Flow cytometry – PD-L1 expression

Cells were harvested, washed twice with PBS to ensure complete removal of cell culture medium, and their concentration measured. Suspension of 1.5×10^5 cells was prepared in 1.5 mL microcentrifuge tube, in triplicate for each line. Cells were then centrifuged at 400 RCF at 4 ^{O}C for 2 minutes, supernatant was discarded, and cells were resuspended in antibody solution. For each cell line, one sample was left unstained (negative control),

one stained with PD-L1 monoclonal antibody (CD274 (PD-L1, B7-H1), monoclonal antibody (MIH1), PE-Cyanine7 conjugated, mouse IgG1κ (eBioscience)) and last one was stained with isotypic control (CD223 (LAG-3) monoclonal antibody (11C3C65), PE-Cyanine7 conjugated, mouse IgG1 κ (BioLegend). Samples were incubated with gentle mixing for 1 hour at 4 ^{O}C in complete darkness. After incubation, cold PBS with 2% FBS (500 µL) was added to the cells which were centrifuged, twice. Each time, the supernatant was discarded. After last washing, cell pellet was resuspended in 200 µL of PBS and cells analysed on flow cytometer BD FACSCanto II. Data was analysed on FlowJo software (BD). The median fluorescence intensity (MFI) was calculated to assess the PD-L1 expression levels.

4.5.3 Specificity and cellular uptake

Specificity of binding (radioconjugates)

ES2 and ES2$_{PD\text{-}L1KO}$ were collected from cell culture flasks, washed and counted. Aliquots of 2×10^5 cells in PBS per sample were prepared in Eppendorf in triplicate for each line. Cells for group with blocking were prepared in the same manner. Radioactive solution was 10 nM (or 1 nM) solution of protein in radioconjugate, calculated for volume of 300 µL per well, but prepared in 200 µL per sample. Blocking solution was 1 µM solution of unlabelled Atezolizumab. Amount of antibody for blocking was also calculated for volume of 300 µL per sample, but prepared in 100 µL per sample.

Samples were centrifuged and PBS was discarded. Next, 100 µL of blocking solution was added to the blocking group samples, and 100 µL of FBS-free medium was added to all the other samples. After 20 minutes of incubation on ice, 200 µL of radioactive solution was added to all test samples. Samples were incubated for 1 hour in 4 °C and after that time samples were centrifuged, and supernatants were discarded. All the samples were washed four times with 200 µL of cold PBS. Samples were measured in gamma counter (Wizard) in open protocol for zirconium-89. Except for the test vials, background was measured, as well as 200 µL of radioactive solution (each in triplicate).

Of each cell line, three eppendorfs were prepared for protein concentration determination. These samples were treated in the same manner (addition of 300 µL of media, washings) and cells were collected with 200 µL RIPA for BCA protein measurements.

Confocal microscopy

Cells were seeded in glass bottom petri dishes NuncGlass™ Base Dish (12 mm) 24 hours prior to the experiment (4×10^5 cells in 600 µL per dish) and kept overnight in a carbon

dioxide incubator. On the following day the cells were washed with PBS and incubated with SPION-Atezolizumab-AF647 (0.5 μM protein) or Atezolizumab-AF647 (5 μM) at 4 ^{O}C for 1 hour. Samples were washed twice with PBS post-incubation and Hoechst®33342 (5 μg/mL) was added for nuclear counterstaining for 20 minutes in 37 ^{O}C right before imaging. Again, the samples were carefully washed twice with PBS and images were captured using a Zeiss LSM980 Airyscan 2 confocal microscope (Carl Zeiss Inc, Oberkochen, Germany). Samples were illuminated with 405 and 655 nm lasers and appropriate filters. Data was analysed using the Zen2009 software (Carl Zeiss Inc, Oberkochen, Germany).

Flow cytometry – specificity of binding and uptake studies

Cells were harvested, washed twice with PBS to ensure complete removal of cell culture medium, and their concentration counted. Suspension of 5×10^5 cells was prepared in 1.5 mL microcentrifuge tube, in triplicate for each line. Cells were then centrifuged at 400 RCF at 4 ^{O}C for 2 minutes, supernatant was discarded and cells were resuspended in solution of Atezolizumab-AF647 or SPION-Atezolizumab-AF647.

To evaluate the specificity of Atezolizumab-modified SPION models, cells were incubated with fluorescent conjugates (10 nM) at 4 °C for 1 hour. For uptake studies, cells were incubated with the 1 nM of conjugates for 1 hour at 37 °C. After incubation cells were washed then resuspended in 200 μL of PBS with 2% FBS. During an experiment 10,000 events per sample were collected, and fluorescent emission was captured using the BD FACSCanto II. Single cell populations were gated and analysed using FlowJo v10 software.

During apprenticeship at Institute of Cancer Research, London, experiments were conducted using BD LSRII flow cytometer (Becton Dickinson and Company, USA) at Flow Cytometry Core facility.

4.5.4 Cytotoxicity

Cytotoxicity of different compounds was tested with CellTiter-Glo® Luminescent Cell Viability Assay (Promega). Experiments were carried out according to producent's protocol. Shortly, cell were seeded in 96-well plate 24 hours prior to adding tested sample, in 200 μL of RPMI with 10% FBS.

In the day of experiment, tested compounds were prepared at specified concentrations in a normal medium with addition of FBS (10% v/v of final mixture). Then, the media from test cells was aspirated and 100 μL of samples was added to each well. Each concentration of a given compound was tested in quadruplicate. Untreated wells (control) were handled

accordingly – media was aspirated and 100 µL of RPMI with 10% FBS was added to each well.

Few hours before the end of incubation, CellTiter-Glo® buffer and substrate were removed from the freezer and allowed to thaw in room temperature. Appropriate volume of buffer was transferred to amber vial containing lyophilised substrate and mixed until homogenous solution (CellTiter-Glo® reagent).

To each test well, 100 µL of CellTiterGlo® reagent was added (volume equal to the culture medium present in the well). Plate was then placed in an orbital shaker for 2 minutes to induce cell lysis. Meanwhile, white 96-well plate with opaque bottom was prepared. Blank wells were prepared in quadruplicate, containing 50 µL of RPMI with 10% FBS and equal volume of CellTiterGlo® reagent. After lysis was completed, 100 µL of sample and reagent mixture was transferred into corresponding well in the white 96-well plate. Plate was then left for 10 minutes in room temperature in order to stabilize luminescent signal and the plate was analysed in Tecan infinite 200Pro plate reader. Software Tecan i-control, 1.8.20.0 was used to perform scan in luminescence mode, with automatic attenuation and with 500 ms integration time.

4.6 Application studies

4.6.1 Relaxometry

Relaxometry studies in high magnetic field (7 T) were conducted on BioSpec Maxwell MRI 7T (Bruker), in assistance of Bartłomiej Gawełczyk, MSc and Artur Tomasik, MSc. For determination of T_1 and T_2 relaxation times samples of 6 concentrations were prepared for each tested compound. They were then analysed with sequence T1_T2map_RARE, created by the manufacturer and available in ParaVision 360 V3.6 software. T1_T2map_RARE sequence consists of 5 scans of different TE: 8, 24, 40, 56, 72 ms for T_2 determination and 5 scans of different TR: 5500, 3000, 1500, 800, 424.973 ms (for TE 8 ms). Excitation angle 90 ^{o}, refocusing angle 180^{o}, dummy duration 5500 ms. T_1/T_2 maps were obtained in the form of axial cross-sections through eppendorfs with tested SPION samples. Five slices with a thickness of 2 mm were made. The middle one was taken for the analysis. A circular region of interest (ROI) was drawn, and the programme displayed calculated and averaged T_1 and T_2 values. FOV was 68.54x42 mm and the slice images had 256x192 pixels each. Mathematical operations were performed in GraphPad Prism version 10.2.3 for Windows (GraphPad Software,). For T_1 and T_2 relaxation times measurements in lower magnetic field (1.4 T) 60 MHz benchtop NMR Spectrometer, Nanalysis-60 was used.

T_2 experiment parameters: Experiment: T2; Solvent: D_2O; Spectral width: 14 ppm, spectral centre at 6.00 ppm. Number of TE points was set to 16, within range of 5 – 800 ms, with 4 scans per point. Scan delay was set to 3 s. Each measurement lasted for 9 minutes. Samples were measured in triplicate and T_2 (FD Max) averaged from these values.

T_1 experiment parameters: Experiment: T1; Solvent: D_2O; Spectral width: 14 ppm, spectral centre at 6.00 ppm. Number of TR points was set to 16, within range of 2000 – 10000 ms, with 4 scans per point. Scan delay was set to 5 s. Each measurement lasted for 11.4 minutes. Samples were measured in triplicate and T_1 (FD Max) averaged from these values.

4.6.2 *In vivo* studies

All experiments were performed in compliance with the licence issued by local Bioethical Comitee (Resolution no 48/2024, from 15.11.2024: „*Badanie nowych radioznaczników i środków kontrastowych jako biomarkerów obrazowania z wykorzystaniem modeli zwierzęcych*"). The *in vivo* experiments were performed by Marlena Golec, PhD, who held valid permits for planning and performing such experiments as well as for animals' euthanasia procedures.

The 3Rs (replacement, reduction and refinement) principle in animal research were taken into consideration. Female BALB/c Nude- Foxn1 nu/nu, mice were purchased from Animal Facility of Advanced Technologies Centre (Centrum Zaawansowanych Technologii – Zwierzętarnia (at Adam Mickiewicz University in Poznań at the age of 6 weeks are stayed under quarantine for 10 days. The animals were kept in the animal facility of the Centre for Translational Research and Molecular Biology of Cancer, Maria Skłodowska-Curie National Research Institute of Oncology - State Research Institute, Gliwice Branch, in conditions fully compliant with the requirements of the 'Act on the protection of animals used for scientific or educational purposes'. Animals were housed in ventilated cages, with constant access to food (Total Pathogen Free feed by Altromin) and water. Mice were kept in the experimental groups of up to 5 in a cage with aspen wood bedding (Maxi LTE E-004 by Abedd, dust fraction content (<0.09 mm) not exceeding 0.003%, intended for individually ventilated cages) and enrichment to reduce stress and the risk of aggression within the group (wooden blocks serving as chew toys, tubes, nesting material).

H292 cells (8×10^6 in 100 µl PBS with 50% Matrigel™) were injected in the right flank of each mouse. Subcutaneous tumour growth was monitored by calliper measurements twice per week. The tumour volume was estimated applying the ellipsoid formula:

$$V = height\ (h) \times width\ (w) \times length\ (l) \times \pi/6$$

Animals were imaged once tumours reached approximately 100 mm^3 (1 week after injection of H292 cells).

For imaging studies, animals were anaesthetised with isoflurane (3-4% induction, 1-2% maintenance v/v in O_2 at 1 L/min) and injected intravenously, via the tail vain, with 1.47-1.99 MBq of ^{89}Zr-DFO-SPION-Atezolizumab or ^{89}Zr-DFO-SPION (85–134 μg SPION) in a normal saline 0.9% saline (100 μL).

Mice were imaged under anaesthesia (PET/CT or MRI) in chosen time-points.

PET/CT scans were performed on system PET/CT Si78 (Bruker), using 2 min CT sequence (*Anatomical Reference Standard*). High-resolution CT scans were performed with the X-ray tube set-up at a voltage of 50 kV, current of 598 μA, FOV of 79.4 x 100 mm, 256 projections (45 ms per projection), and a pixel size of 100 μm. The CT images were reconstructed using a filtered-back-projection (FBP) algorithm. CT scan was followed by whole body 10 minute static PET scan (*Static 10 min*), performed with a 357.7 and 664.3 keV energy window. PET images were reconstructed using a maximum-likelihood expectation-maximization (MLEM) algorithm (18 iterations) with a voxel size of 0.5 x 0.5 x 0.5 mm^3. Image analysis was performed using the PMOD software package (PMOD Technologies Ltd., Switzerland).

MRI studies were obtained in imaging system BioSpec Maxwell 70/17 (Bruker). Sequence parameters:

- **T2_TurboRARE** (T_2-weighted imaging): TE = 35 ms, TR = 3000 ms; 3 averages; echo spacing 7.0 ms, slice thickness: 0.7 mm; resolution 0.625 x 0.156 mm; fat suppression, trigger on (to synchronise data acquisition with animal's breath, to prevent motion-related artefacts and produce clear image).
- **T1_FLASH** (T_1-weighted imaging): TE = 4.5 ms; TR = 175 ms; 5 averages; slice thickness: 0.7 mm; resolution 0.104 x 0.104 mm; fat suppression; trigger on.

After completion of the experimental procedures, mice were euthanized by cervical dislocation, performed in accordance with institutional and international ethical guidelines for the humane treatment of laboratory animals. Immediately after euthanasia their major organs were collected, weighted, and the radioactivity content measured in gamma-counter. The decay-corrected data were expressed as a percentage of injected dose per gram of tissue (%ID/g).

5. Summary and conclusions

5.1 Development of DFO-based chelator for zirconium-89

It is currently well recognised that DFO is not an ideal chelator for ^{89}Zr, primarily due to its insufficient *in vivo* stability and the risk of transchelation or demetallation [194, 195]. These limitations can lead to the release of free ^{89}Zr, which accumulates in bone and contributes to non-specific background signal and increased radiation dose. To address these issues, novel chelators such as DFO*, DFO-cyclo, and HOPO derivatives are being developed, offering enhanced thermodynamic stability and kinetic inertness, and thus providing safer and more reliable ^{89}Zr radioconjugates for clinical applications. In line with this urgent need a novel chelator was designed, based on DFO scaffold with a bisphosphonate group to enable the formation of a more stable complex with ^{89}Zr.

The initial idea involved modifying DFO with H-phosphonate, inspired by a publication of Vitha et al [154]. To achieve that goal, bisphosphonate with reactive H-phosphonate moiety (compound **G**) was synthesised and attempts were made to incorporate it into the DFO structure via Kabachnik-Fields mechanism. The experiments carried out in order to obtain the desired product included the use of both formalin and paraformaldehyde as a carbonyl group donor, in solvents such as DMSO, water, methanol, benzene. Non-polar solvents such as toluene and benzene were eliminated due to the insufficient solubility of DFO-Mes, despite attempts to overcome this limitation by adding NaOH or Na_2CO_3.

Reaction in methanol did not lead to desired effect. ^{1}H-NMR spectra show substantial discrepancies from the anticipated profile, including shifting the signals that were expected to remain unaffected, and several new, unidentified peaks have emerged. The complexity of the spectral data makes it challenging to elucidate the underlying chemical processes or identify the resulting products with confidence. For the reasons above, efforts have been directed towards other solvents.

Next, an attempt was made to carry out this reaction in water. This ensured good solubility of DFO. Comparative tests showed that paraformaldehyde is more useful than formalin. However, despite the disappearance of the H-P signal, the reactions in the aqueous environment did not result in the formation of the desired product with sufficient yield – depending on the interpretation of the NMR spectra, a yield of 19–40% can be assumed. The use of microwave energy to improve reaction yield was also eliminated.

Since the product of the Kabachnik-Fields reaction is water, it was assumed that anhydrous conditions could promote product formation by shifting the reaction equilibrium. Indeed, reactions in DMSO, which ensured good solubility of all reaction components, yielded the closest results to the desired effect. The addition of Et3N as an amine activator was evaluated to increase its nucleophilicity. This effect was not observed at room temperature, but raising the reaction temperature to 60 degrees was sufficient to achieve this effect, observed by a decrease in the chemical shift value for the proton adjacent to the terminal amino group of DFO.

After 72 hours of reaction at 60 ^{O}C, a complete loss of intensity of the peak *h* was observed, indicating that all **H**-P- groups reacted or degraded under the influence of temperature or pH, as H-phosphonate esters can easily undergo hydrolysis or transesterification under alkaline conditions. ^{1}H-NMR and ^{31}P-NMR confirm the formation of a new compound under these conditions (with the addition of 0.2 molar equivalent of Et_3N). To verify this, MS was performed, which did not confirm the optimistic conclusions from NMR analysis. The expected reaction product **I** would have a mass of $[M+H]^+$ 967.4682 Da, but such signals are not present in the mass spectrum. Furthermore, it proved impossible to separate the reaction products from DMSO, as all the methods tried failed: evaporation of the solvent under vacuum, extraction to another solvent immiscible with DMSO, precipitation with NaCl or diethyl ether.

Another bisphosphonate substrate (compound **J**) was tested in order to functionalise DFO-Mes. It was received from Dominika Kozicka M.Sc at another research group and its synthesis is decribed in her dissertation. The reaction of DFO-Mes and compound **J** was expected to occur according to S_N2 mechanism, between terminal amine group of **H** as a nucleophile and tertiary alkyl chloride (**J**). The reaction did not occur in DMSO, and moreover, it would not have been possible to extract DFO derivatives from reaction mixture, as it was proved in previous studies. Next, an interfacial $CHCl_3$-water reaction (DFO was dissolved in water, bisphosphonate substrate in chloroform) was performed. However, no reaction occurred at the phase boundary, and after extraction of the aqueous phase with chloroform, no solubility of DFO or its derivatives in $CHCl_3$ was found. Next, DMF was tried, as DFO-Mes dissolves in this solvent (however, only after increasing reaction temperature). Influence of addition of Et_3N to reaction mixture was also tested, but it did not seem to affect the course of the reaction. The signal of the proton adjacent to the chlorine atom did not migrate in the ^{1}H-NMR spectra of the reaction mixture, which may suggest no (or negligible) product formation. However, the MS spectra of the two distinct reaction conditions suggest, that the di-substituted product DFO-$(BP)_2$ (**L**) was formed,

but the desired mono-substituted product DFO-BP (**K**) was not achieved despite attempts to reduce the BP:DFO ratio in the reaction mixture.

Although the proposed synthesis route did not lead to the expected result, the research provided valuable information on the limitations and potential of the methodology used. The concept of developing a bisphosphonate-modified DFO remains promising and deserves further exploration using alternative synthetic strategies. Further studies on the introduction of BP to DFO and its hydrolysis to the appropriate phosphonic acid were carried out by Dominika Kozicka under the supervision of prof. Jakub Adamek and are described in her dissertation.

Obtained compound **M** was still in a protected form, so it cannot be stated with certainty whether the coordination of ^{89}Zr occurred in the form of a hexa- or octadentate complex. However, stability studies performed for ^{89}Zr-**M** complex confirmed slight advantage of this chelator over commercially available *p*-NCS-C_6H_4-DFO, Significant difference in stability was observed in quasi-physiological conditions (incubation in 37 ^{O}C in normal human serum). However, in transchelation competition ^{89}Zr-**M** did not show increased stability over ^{89}Zr-(*p*-NCS-C_6H_4-DFO).

Further studies on the hydrolysis of the bisphosphonate group in the compound **M** should be conducted, followed by further verification of the complex's stability. Once such a complex has achieved improved stability in comparison to hexadentate DFO, the next step would be to add a functional group to the structure that would allow for easy attachment to the targeting vector. As described in the 'chelators' section, this could be, for example, *p*-NCS-C_6H_4- or maleimide group, depending on the chosen vector. Such modification would confirm its place among the BFCs and open up opportunities to further investigate this compound in *in vitro* and *in vivo* contexts.

5.2 Development of bimodal probe for simultaneous PET/MRI imaging

Two bimodal probes were proposed for future simultaneous PET/MRI imaging of PD-L1 expression, ^{89}Zr-DFO-SPION-Atezolizumab and ^{89}Zr-SPION-Atezolizumab. The design and synthesis of these constructs (**Scheme 40**) were based on an extensive literature survey, which resulted in a review of targeted bimodal probes developed for PET/MRI imaging [125].

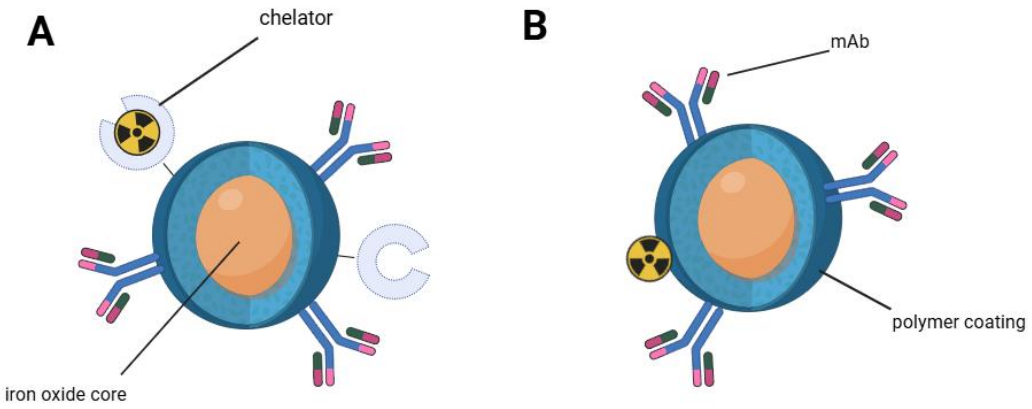

Scheme 40 - Bimodal PET/MRI probes: A: ^{89}Zr-DFO-SPION-Atezolizumab and B: ^{89}Zr-SPION-Atezolizumab

In addition to comparison of these two imaging techniques, the review article focused on the practical aspects of developing bimodal probes and their preclinical application. Previously published data on bimodal PET/MRI probes were compared, including both small molecules and nanostructures containing a radioactive isotope. Important practical issues were identified, including the challenges of synthesising and radiolabelling such structures. The cytotoxicity of different models was compared, and possible solutions to problematic dosing issues (CAs vs. PET isotope, given the different sensitivities of these two techniques) and the expected behaviour of such constructs in the body were considered. Using the information gained from this literature study, two bimodal probe models were designed, based on SPIONs and conjugated to the anti-PD-L1 antibody Atezolizumab.

Dextran-coated SPIONs, with a declared diameter of 5 nm (as determined by TEM), were chosen as the basis for bimodal probes due to their favourable MRI contrast properties and carbohydrate coating, which enables surface modification. The two investigated probe models differ in the method of incorporating ^{89}Zr into the nanoparticle structure. In the first approach SPION surface was functionalised with DFO, and subsequent radiolabelling

through this molecule. In the second approach, a chelator-free HIR method was applied, prior to incorporation of into the nanoparticle structure.

First, a bioconjugation method was developed to incorporate Atezolizumab into the SPION surface. Several approaches were evaluated, including functionalisation with a *p*-phenylene-diisothiocyanate linker. This method was rejected due to the reagent's poor solubility in an aqueous medium. Instead, efforts focused on EDC-mediated bioconjugation, which involves the formation of a highly reactive intermediate molecule, which then reacts with the carboxyl groups present in the nanoparticle polymer coating. The process was optimised by including a large molar excess of antibody relative to SPIONs and using a two-step conjugation procedure. This process is based on the assumption that the antibody will be most reactive at pH = 9.0, as its pI is also within this range. Hence, the first step of the reaction (formation of the highly reactive intermediate) which requires a slightly acidic pH (~5), was conducted in MES buffer. Binding Atezolizumab on the activated coating was conducted in BC buffer of pH = 9.0. The amount of mAb incorporated into the nanostructure was determined indirectly. For this purpose, the reaction mixture was centrifuged multiple times, and the protein concentration in the supernatant was measured, determining the amount of unreacted mAb. This process was lengthy and tedious, especially for 5 nm nanoparticles – as separating nanoparticles from the supernatant required high speed (15 kRPM) and prolonged centrifugation (four 2-hour cycles). After optimisation, the amount of mAbs per nanoparticle was determined to be approximately 3:1, resulting in a mass ratio of approximately 1:2 (mAb:NP).

A method for incorporating DFO into the antibody structure was then developed, reducing the procedure to a single-step process compared with methodologies previously described in the literature [161]. Determining the amount of chelator incorporated into the structure proved problematic, as the methods reported in the literature were ineffective for such small-scale reactions and, consequently, samples with low analyte concentrations. Therefore, the conductometric titration method described in Ph. Eur was rejected. Ultimately, the amount of DFO incorporated into the structure was calculated using the isotopic dilution method, adapted from the literature, where it was used to determine the degree of modification (amount of incorporated chelator) of mAbs [175]. The average number of DFO molecules incorporated into the nanoparticle structure was defined to be c.a. 2.5. This is lower than the literature (7 chelators per particle in the study by Thorek et al. [161]), but both the nanostructure modification procedure and the method for measuring the amount of DFO incorporated differed in the cited studies. Assuming that at least one chelator nanoparticle molecule is occupied by the radionuclide during the

radiolabelling process, the paramagnetic-to-radionuclide ratio would be 6000:1. However, this estimation does not take into account the very low concentration of ^{89}Zr ions in the mixture, so this ratio may shift even further towards the advantage of paramagnetic over radionuclide. Considering the difference in sensitivity between MRI and PET techniques (10^{-6} mol/l and 10^{-11} - 10^{-12} mol/l, respectively), this ratio may represent a satisfactory balance of paramagnetic substance and radionuclide for simultaneous PET/MRI imaging.

Importantly, there were significant differences in the behaviour of the nanoparticles between the purchased batches. Some production batches precipitated during synthesis, for example, when pH was changed or ionic strength was increased by adding EDC. This significantly complicated and prolonged the optimisation of functionalisation conditions. Purchasing the nanoparticles from an external supplier was intended to ensure consistency of the starting material, but instead it became a source of synthesis problems.

Two methods of radiolabelling have been compared. First of them was radiolabelling through chelator DFO. Surprisingly, it proved to be an unpredictable process with lower than expected yields (in comparison to radiolabelling of DFO-conjugated Atezolizumab alone). The process depended significantly on the concentration of ^{89}Zr in the reaction mixture. However, the compound typically showed complete labelling after an overnight reaction. An undoubted advantage of this method of radiolabelling was the ability to prepare the compound in advance and characterize the DOF, which allowed for the prediction of labelling speed and efficiency. Furthermore, in this synthetic route, radiolabelling was almost the last step of synthesis (preceding product purification and filtration), which allowed limitation of activity losses and minimising the risk of radiological contamination.

The second method was HIR, a chelator-free labelling technique using elevated temperature. The protocol available in the literature was modified, introducing an alternative radioTLC method, more suitable for the current research [140]. The effect of lowering the temperature from the initial temperature of 120 °C to 95 °C was also examined. Lowering the HIR temperature under the boiling point of water allowed the reaction to transfer from the glass vial in the silicon oil bath to the plastic vial (eppendorfs) in the thermoshaker. This improved process safety and did not significantly reduce RCY. Furthermore, changing the reactor increased yield, by avoiding losses associated with ^{89}Zr-SPION deposition on the magnetic stirrer. The effect of the reaction medium pH on the radiolabelling reaction rate was also examined. Lowering the pH to approximately 7.0 and increasing it above 9.0 slowed or even stopped the HIR reaction, confirming desired

range of pH for HIR to be between 7.5 and 9.0. A major drawback of this labelling method when using mAbs is the high reaction temperature, which precludes radiolabelling of SPION-Atezolizumab nanostructures due to mAb's degradation at temperatures above 40°C. Therefore, HIR radiolabelling was the first step of the modification, followed by bioconjugation with Atezolizumab. This resulted in greater exposure to ionizing radiation, increased the risk of contamination (especially during the purification), and required significantly higher initial activity to obtain similar final intended dose, than with ^{89}Zr-DFO-SPION-Atezolizumab. Therefore, in preclinical *in vivo* studies, a bimodal probe labelled through the DFO chelator was used. However, both bimodal probes were characterised by similar, very high stability in serum for up to 4 days after synthesis (no free ^{89}Zr was detected at any time point).

Structural and *in vitro* studies were conducted on functionalised SPION samples, including 'single' modified SPIONs (i.e., containing only mAb, DFO, or ^{nat}Zr) as well as more complex constructs, up to bimodal probe targets. Due to the availability of measurement equipment, nanostructures containing natural (non-radioactive) zirconium were used to reflect its physicochemical character without the risk of ionizing radiation. In some studies, the properties of SPION Ø 20 nm were also examined for comparison. The larger nanoparticles were at some point considered as a potential alternative to the leading SPION Ø5 nm.

The hydrodynamic size of the nanoparticles was examined and described. Unmodified SPIONs Ø 5 nm have a hydrodynamic diameter determined of approximately 40 nm, and single modifications (SPION-Atezolizumab, SPION-DFO, ^{nat}Zr-SPION) did not significantly affect this value. Attaching two different structures to a nanoparticle almost doubled this value (approximately 75 nm), while the ^{nat}Zr-DFO-SPION-Atezolizumab construct yielded a surprising result of almost 200 nm. The zeta potential of these samples was also determined. All tested formulations exhibited a net negative surface charge, with nanoparticle functionalisation having only a modest impact on this parameter. Notably, samples bearing mAbs on their surfaces (specifically 5_SA, 5_SAD, and 5_SADZr) displayed a reduced absolute zeta potential (i.e. less negative) in comparison to the unmodified reference material (5_S). These values, falling above –30 mV, may suggest a propensity for particle aggregation. This observation aligns with the known characteristics of monoclonal antibodies, which typically exhibit low zeta potential values (ranging approximately from −10 mV to +10 mV), owing to their intricate surface chemistry and inherent tendency to aggregate unless appropriately stabilised.

Interesting results were obtained by examining the nanostructures using XPS. The presence of both forms of iron (Fe(II) and Fe(III)) in the nanoparticles was confirmed. Oxygen signals were also present in all samples, further verifying declared structure, as signals originating from the presence of Fe-O bonds (nanoparticle core) and C=O and C-O bonds (shell) were observed. The presence of sulphur-derived signals in samples containing Atezolizumab is consistent with expectations, as the mAb's structure contains disulphide bridges between cysteine groups. In samples containing ^{nat}Zr, signals confirming the incorporation of this metal into the probe structure are noticeable.

In vitro evaluation was conducted on cell lines expressing PD-L1 (ES2 and H292) and their knockout equivalents ($H292_{PD\text{-}L1KO}$ and $ES2_{PD\text{-}L1KO}$). Expression of PD-L1 ligand on cell membranes (or its absence) was confirmed using Western blot and flow cytometry. To investigate the specificity of binding and internalisation of the constructs using fluorescence methods (such as flow cytometry and confocal microscopy), a SPION-Atezolizumab-AF647 structure was prepared, in which the fluorophore AlexaFluor647 (AF647) was attached to the lysine groups of the mAb. The Atezolizumab-AF647 conjugate was used as a positive control. In the specificity of binding and internalisation studies, cells were incubated at 4 or 37 °C with the aforementioned constructs (SPION-Atezolizumab-AF647 or Atezolizumab-AF647), respectively. Specificity of binding and internalisation of both structures was observed, with higher binding for ES2 than for H292 cells. This corresponds to the results obtained during cell line characterization, where ES2 cells showed higher expression of the PD-L1 ligand than H292 cells.

Specificity of binding was also confirmed by confocal microscopy. H292 and $H292_{PD\text{-}L1KO}$ cells were treated with fluorescent SPION-Atezolizumab-AF647 or Atezolizumab-AF647. Fluorescence was then excited using a laser ($\lambda\_ex \approx 650$ nm) and the emitted signal was recorded with confocal microscope. A markedly higher membrane-associated signal in PD-L1-positive versus negative cell lines confirmed the specificity of the SPION-Atezolizumab construct.

The *in vitro* binding specificity of the ^{89}Zr-DFO-SPION-Atezolizumab and ^{89}Zr-SPION-Atezolizumab conjugates was also examined. Regardless of the concentrations and experimental conditions used, results confirmed some level of unspecific binding to the cell membranes. The discrepancy between these results and the data obtained with the fluorescent conjugate likely arises from differences in conjugates chemistry and surface properties, such as conjugation geometry and loading (AF647 vs DFO/^{89}Zr), hydrodynamic size/aggregation state, surface charge, and net lipophilicity, as well as potential radiolysis effects. These factors can reduce effective epitope accessibility and

increase non-specific interactions, leading to lower apparent specificity in the radiolabelled formulations.. In line with these considerations, simply adding a metal centre is unlikely to be the primary driver of the mismatch. Our Zeta potential data indicate that incorporation of ^{nat}Zr via DFO leaves the particle surface potential essentially unchanged within experimental error. Most likely it is due to sample heterogeneity in the fluorescent arm during AF647 labelling. As any Atezolizumab not stably presented on the SPION surface (carry-over "free" mAb from bioconjugation or early degradation) would readily acquire dye. Fluorescence readouts would then disproportionately report the behaviour of AF647–Atezolizumab species (mAb alone or weakly associated) rather than the intended SPION–Atezolizumab-AF647 construct, inflating apparent specificity and masking the non-specific membrane association observed with the radiolabelled formulations.

These factors can reduce effective epitope accessibility and increase non-specific interactions, leading to lower apparent specificity in the radiolabelled formulations

The cytotoxic effect of the bimodal probes was evaluated using formulations containing non-radioactive zirconium, ensuring that observed effects were attributable to the nanoparticle structure and surface chemistry rather than radiological impact. Given that diagnostic levels of ^{89}Zr typically result in minimal radiation exposure, the use of its cold analogue allowed for a clearer assessment of chemical toxicity. Experimental results showed consistent cell viability across assays, with all SPION-based variants demonstrating comparable cytotoxicity within the 0.1-1.0 μM iron concentration range. This suggests that cellular damage is primarily linked to the iron oxide content, rather than to differences in surface functionalisation. Notably, cells exposed for 48 hours exhibited slightly improved survival compared to those assessed after 24 hours.

It was also crucial to determine the effect of modification of superparamagnetic structures on their relaxation. Magnetic studies involved T_1 and T_2 measurements of differently modified SPIONs Ø 5 and 20 nm in different magnetic fields (1.4 and 7 T). Both groups of nanoparticle models meet the condition of r_2/r_1 above 20, which is imposed on negative CAs. As demonstrated in 3.2.5.1. *Magnetic studies – relaxivity*, the strength of the magnetic field in which relaxivity measurements are performed influences the results of this assay. For this reason, a meaningful comparison should include r_2 measured in the same magnetic field. Relaxivity r_2 (measured in 1.4 T) for various SPIONs based on 5 nm nanoparticles was assessed in this research in the range of 113 – 290 mg/mL/s, with the highest values over 250 mg/mL/s for ^{nat}Zr-DFO-SPION-Atezolizumab and ^{nat}Zr-SPION-Atezolizumab. Such contrasting effect is comparable with available literature data on bimodal probes based on nanoparticles. For instance, dextran-coated iron oxide nanoparticles labelled

with ^{64}Cu through DOTA, had r_2 measured in 1.4 T of 279 mg/mL/s [196]. Introduction of zirconium atom increased r_2 for nanoparticles of both diameters, and this effect was more significant in 7 T magnetic field. Similar effect of improved r_2 was observed also for antibody-modified nanoparticles. However, it is not clear whether this is due to the RIME effect or whether the modification of the nanoparticles causes the inhomogeneous nature of the bimodal probe. Especially the T_2 relaxation time is susceptible to such inhomogeneities. However, this data could have a significant impact on the design of similar bimodal probes in the future. Importantly, the r_2 relaxation value (for SPION Ø 5 nm) increased with the magnetic field in which it was measured. This is very promising tendency, as superparamagnetic contrast agents will provide better contrast in higher magnetic fields, improving efficiency of contrasting together with development in scanner technological advancement. Furthermore, identifying the correlation between the strength of the applied magnetic field and the relaxation of nanostructures provides valuable information that can be extremely useful in developing contrast agent doses tailored to the field strength available in a given scanner.

Proof-of-concept *in vivo* studies were conducted with ^{89}Zr-DFO-SPION-Atezolizumab and ^{89}Zr-DFO-SPION as a non-targeted comparison. Mice were injected with radioconjugate and PET/CT and MRI were performed at various time points. Notably, leading bimodal probe did not show specific uptake in tumour after i.v., accumulating vastly in liver, spleen and bones. Consistent imaging data from MRI and PET studies after 10 minutes and 3 hours (respectively) show very rapid liver uptake and lack of radioconjugate in blood pool or tumour. Interestingly, such uptake was harnessed to enhance liver parenchyma while malignant lesions, which lack Kupffer cells, appear as signal voids, improving tumour-to-liver contrast [197]. This implies potential application of introduced nanostructure as PET/MRI probe for imaging of such lesions.

Biodistribution *ex vivo* confirms these results, showing higher uptake in liver or bone after 72 hours post injection than at 48 hours. This effect is most likely due to characteristic clearance of nanoparticles by mononuclear phagocyte system. Relatively high uptake of radioactivity in bones is consistent with known tendency of ^{89}Zr released from the nanostructure binding to hydroxyapatite in the bone matrix over time [193].

Future work on optimisation of this bimodal probe should involve modifications that would improve circulation times. This would reduce unspecific accumulation and enhance tumour exposure. Another possible optimisation, aimed at overcoming MPS effect, would be to modify the route of administration.

Available data show that SPION-based nanoparticles likely accumulate in liver, spleen and lymph nodes after intravenous administration [139]. Contrary, intratumoural injection of similar nanostructures showed long-term retention in the region of interest [198]. Similar nanostructures were also investigated after intraperitoneal administration, showing interesting biodistribution pattern and circulation in blood pool in time window in range 1-4 hours [199]. Non-targeted ^{89}Zr-DFO-SPION injected dermally on the forepaw was proposed for axillary lymph node group imaging. The same compound allowed for visualisation of lymphatic transport in transgenic model of prostate cancer after intraprostatic administration [161].

5.3 Implementation and technological aspect

This doctoral project had two main aims, both connected to worldwide trend in development of radiopharmaceuticals based on ^{89}Zr, with a very specific technological potential – to develop new technology for production of PET/MRI probes labelled with this isotope, and to design a new chelator characterised by improved complex stability compared to solutions available on the market.

In parallel to this research, production of ^{89}Zr has been implemented at the Radiopharmacy and Preclinical PET Imaging Unit (ZRO) at the Maria Skłodowska-Curie National Research Institute of Oncology (NRIO), Gliwice branch (data not yet published) and a new (February 2025) Laboratory of Preclinical Imaging equipped with PET/CT and MRI preclinical scanners has been opened. These innovations allow easier synthesis and more thorough analysis and implementation of novel bimodal PET/MRI probes.

In order to incorporate nanoparticle-based probes into the ZRO's portfolio it was necessary to develop and implement synthetic and analytical methods suitable for this type of compounds, which have not yet been used in the Unit. Analytical methods used in our laboratory for radiopharmaceuticals based on small molecules or proteins have not always been readily adaptable to structures with larger molecular weights, such as nanoparticles. An example is the MALDI technique, which has been successfully used to determine the degree of modification of mAbs, but is completely inadequate for SPIONs. The implementation and application of the isotopic dilution method for this application is particularly valuable and could be used with other compounds in the future. The effort put in the development of methods for functionalising nanoparticles will enable easy implementation of other similar compounds in ZRO, differing, for example, in their radioactive isotope or targeting vector. This offers hope for the advance in the field of personalised medicine, by expanding the library of radiopharmaceuticals e.i. to other targets or theranostic purposes. Of particular importance is the comparison of two methods for radiolabelling SPIONs, as well as the development of a two-step bioconjugation method characterised by higher efficiency compared to methods described in the literature.

Using an infrastructure available at NRIO, novel conjugates were prepared. They were successfully synthesised, analysed and administered to animal models. Obtained imaging data yielded interpretable results. Many issues at synthetic stages were caused by inconsistent starting nanomaterial (dextran-coated SPION), which differed between batches. In the case of implementation of these compounds in clinical practice, it would be advisable to implement an in-house production of these particles in order to increase

consistency, reduce costs and dependence on sub-suppliers. Many attempts were made to obtain the designed chelator, but it was not produced and isolated in its final form within the project's assumed duration. It is still anticipated that this structure has the potential to surpass other solutions available on the market (more stable, resulting in a lower nonspecific accumulation and improved image resolution), but hydrolysis conditions that would deprotect the chelator and obtain a form capable of forming eight coordination bonds still need to be developed.

The completion of this doctoral implementation project was made possible through cooperation between the National Research Institute of Oncology and the Silesian University of Technology, and the scientific research infrastructure of both institutions was used during the described research.

6. Figures

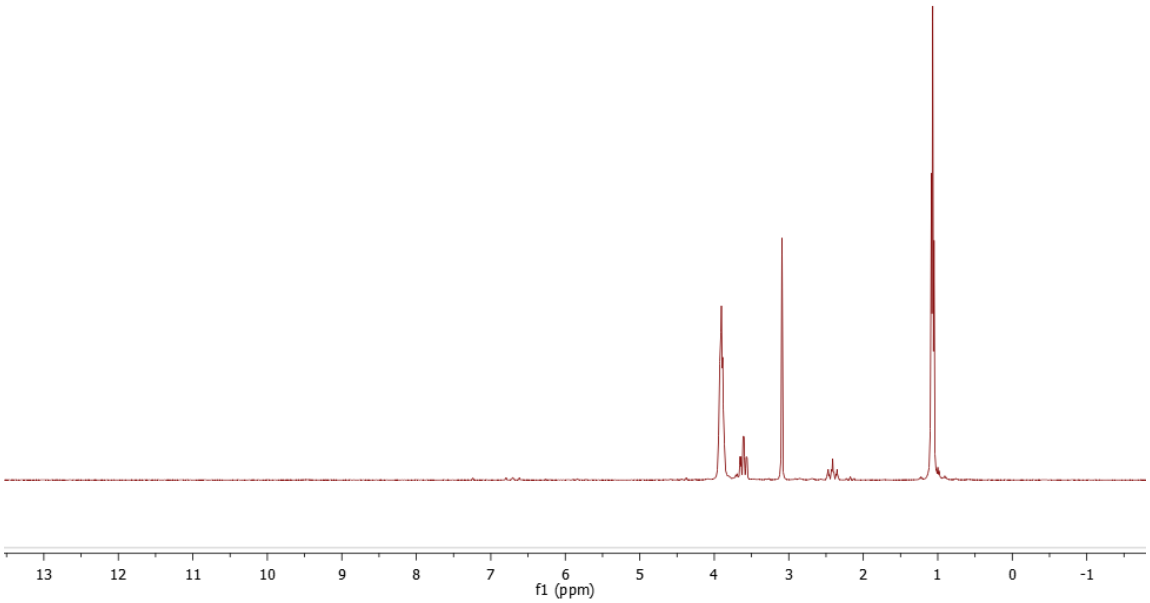

Figure 42– ^{1}H-NMR spectrum of intermediate (compound A)

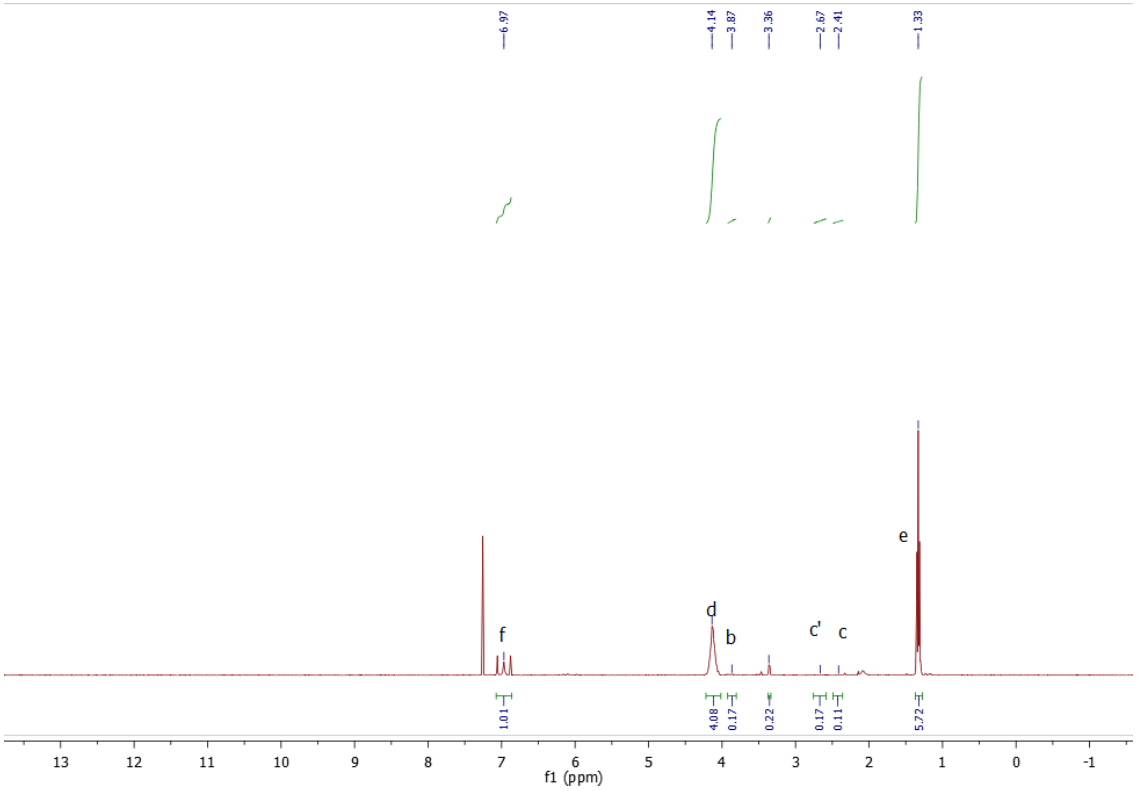

Figure 43- ^{1}H-NMR spectrum of fraction 1

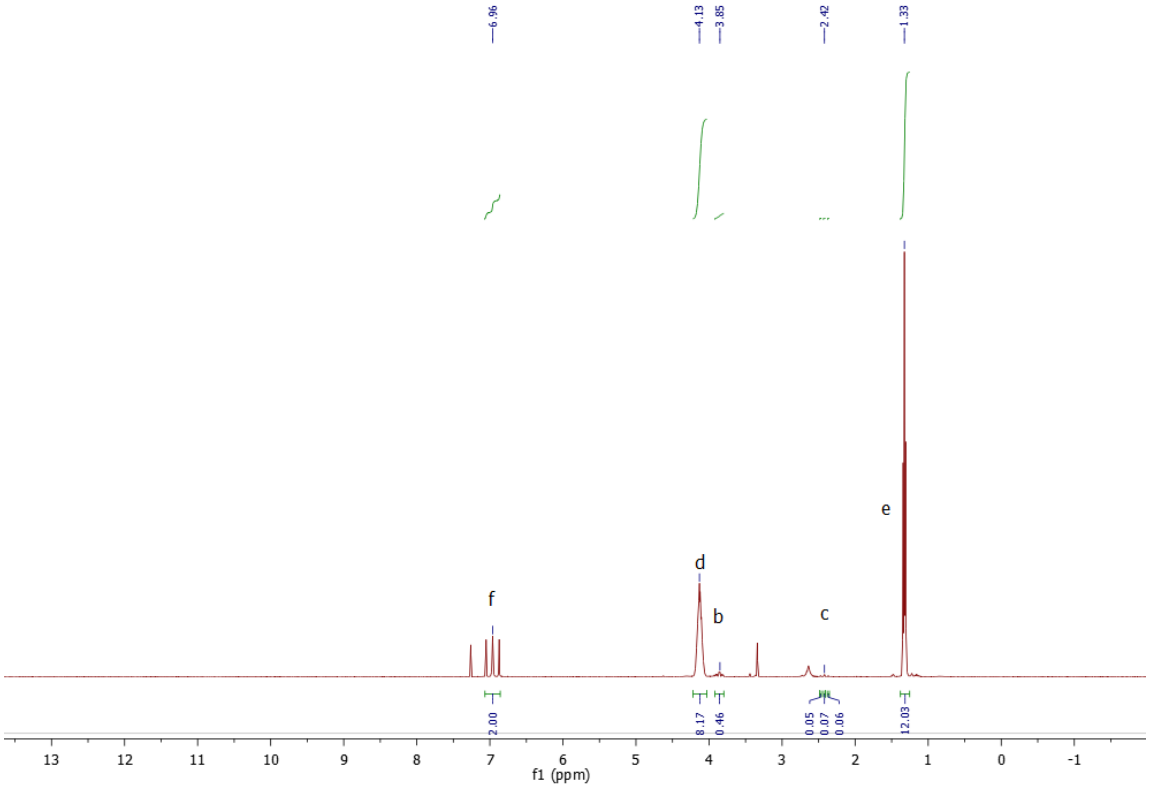

Figure 44- ^{1}H-NMR spectrum of fraction 2

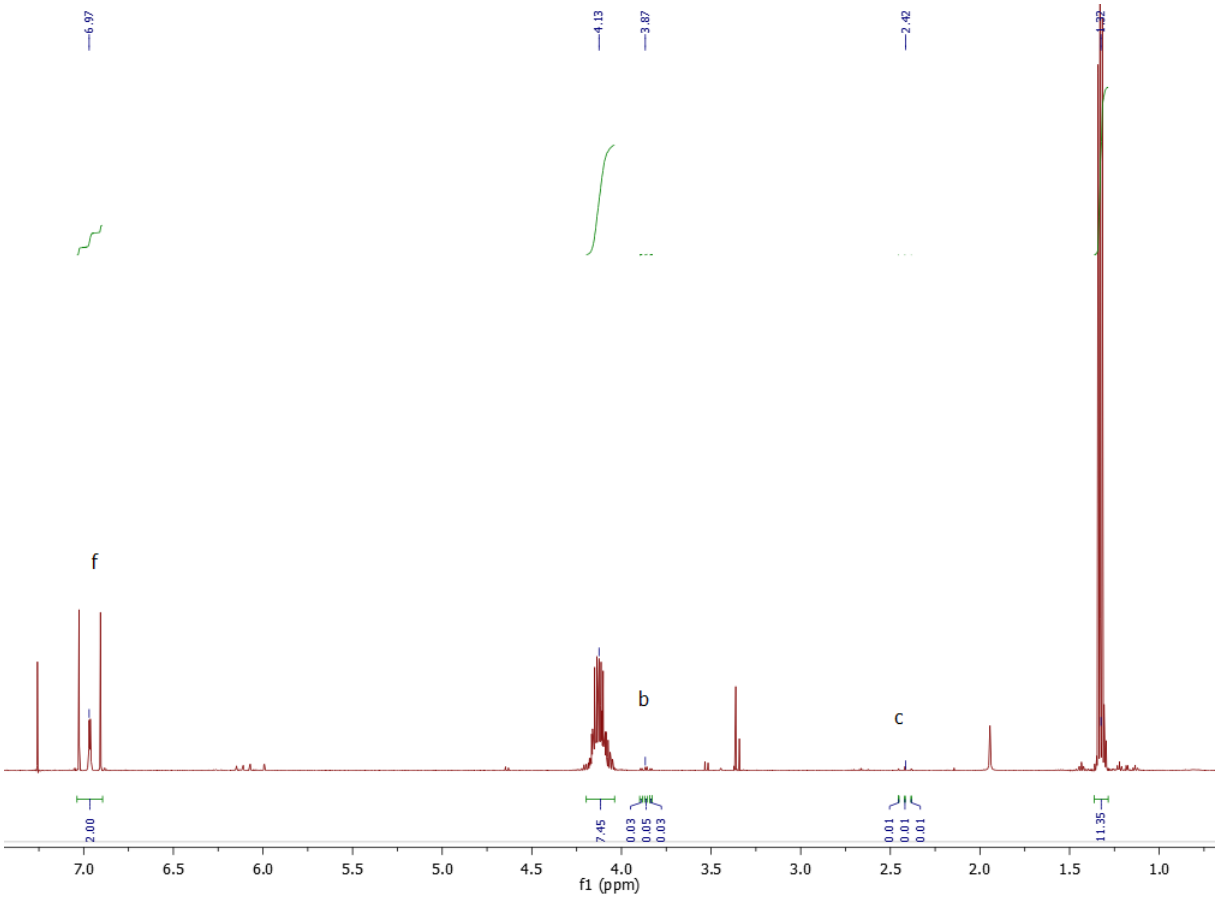

Figure 45- ^{1}H-NMR spectrum of fraction 6

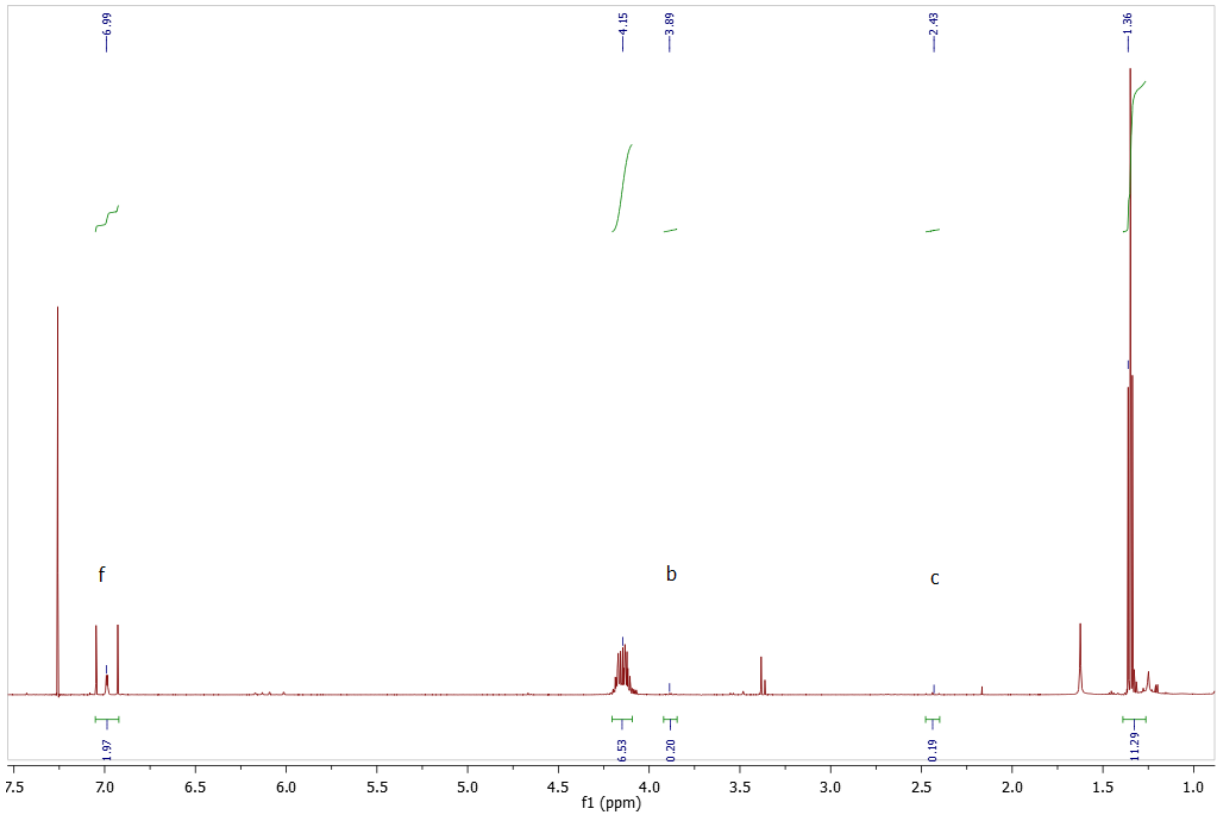

Figure 46- ^{1}H-NMR spectrum of fraction 13

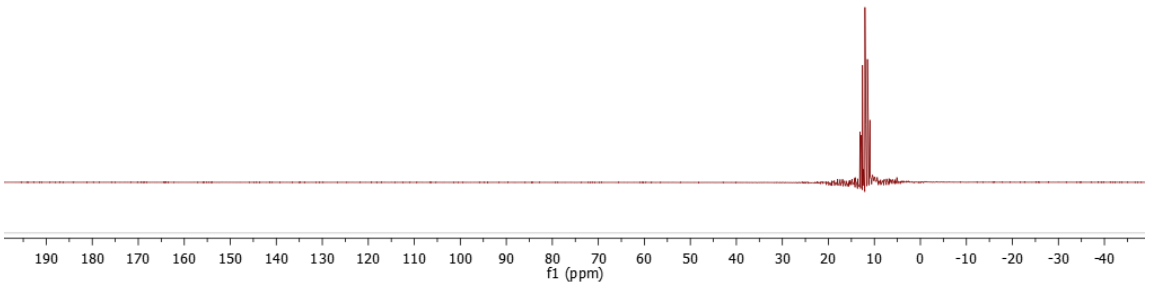

Figure 47- ^{31}P-NMR spectrum of H_3PO_2

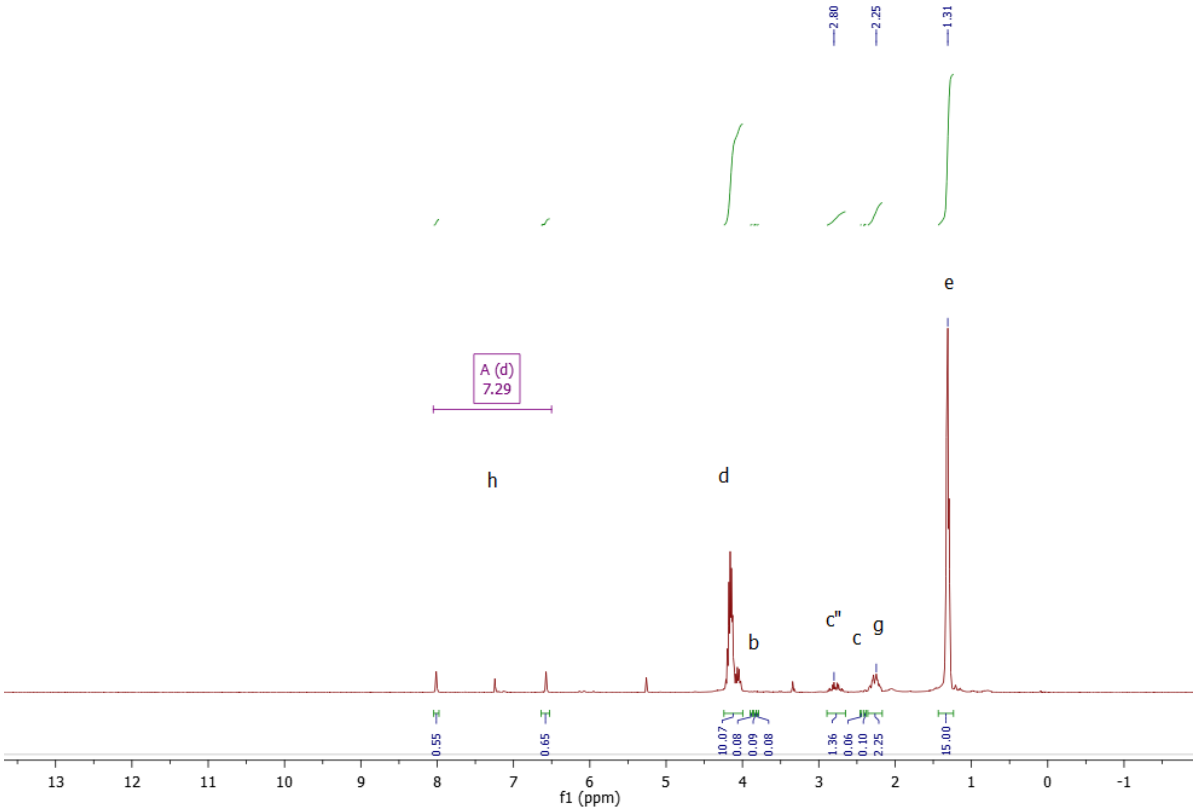

Figure 48- ^{1}H-NMR spectrum of compound G

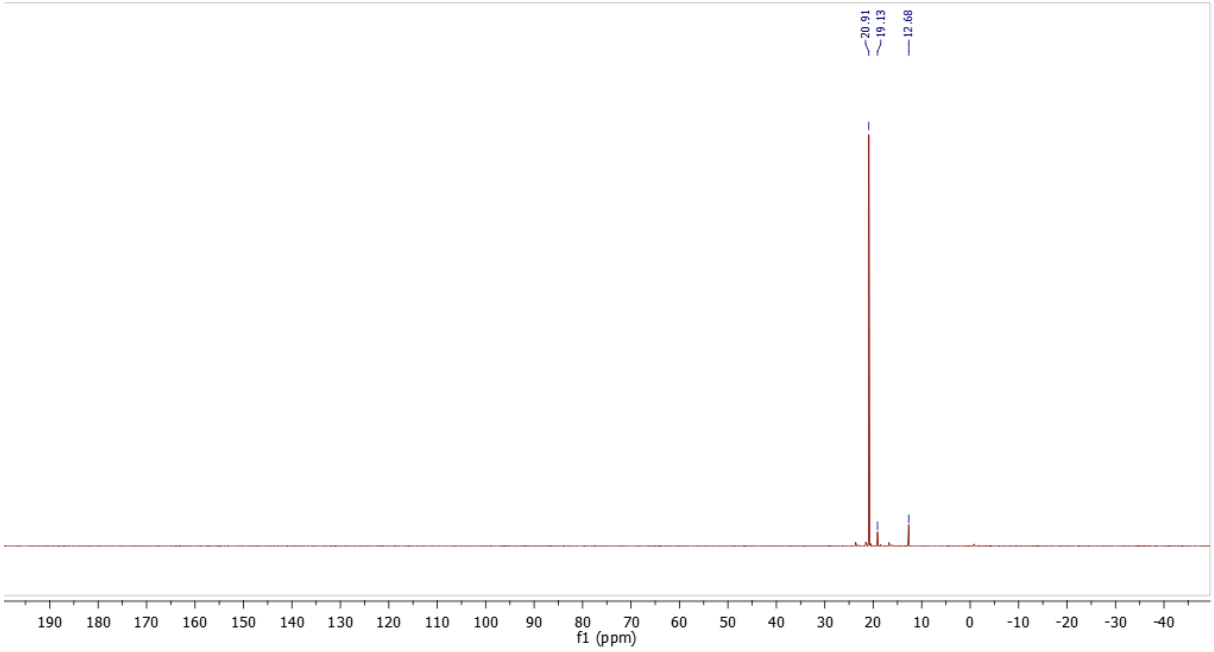

Figure 49 - ^{31}P-NMR spectrum of reaction mixture (substrate, A and B)

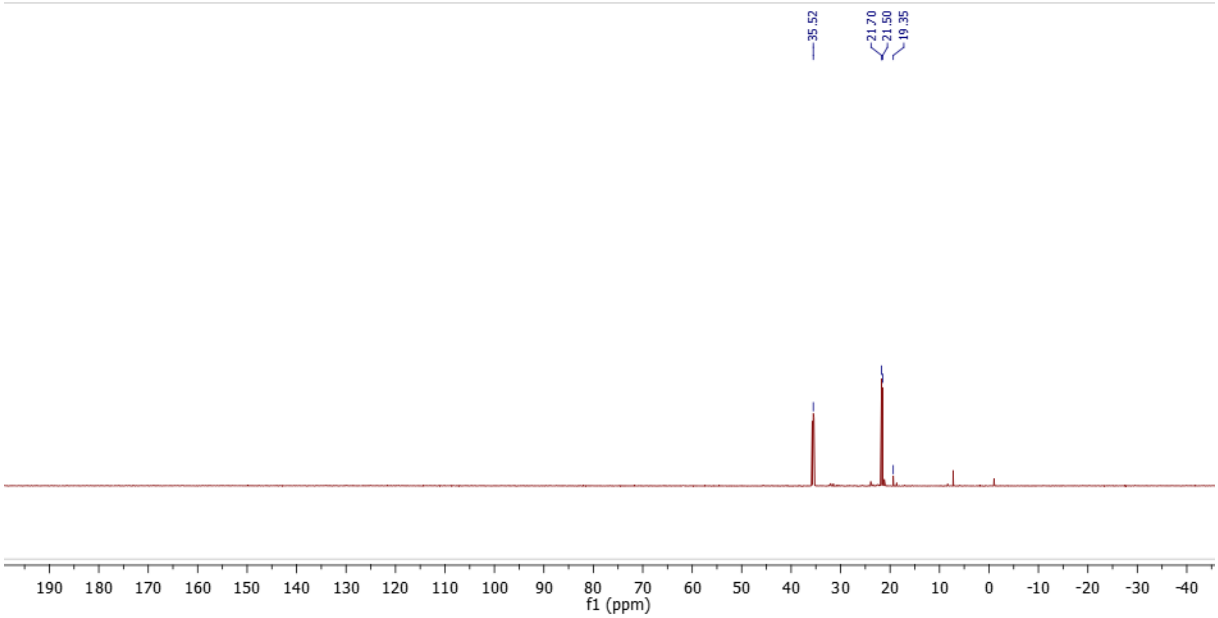

Figure 50- ^{31}P-NMR spectrum of compound D

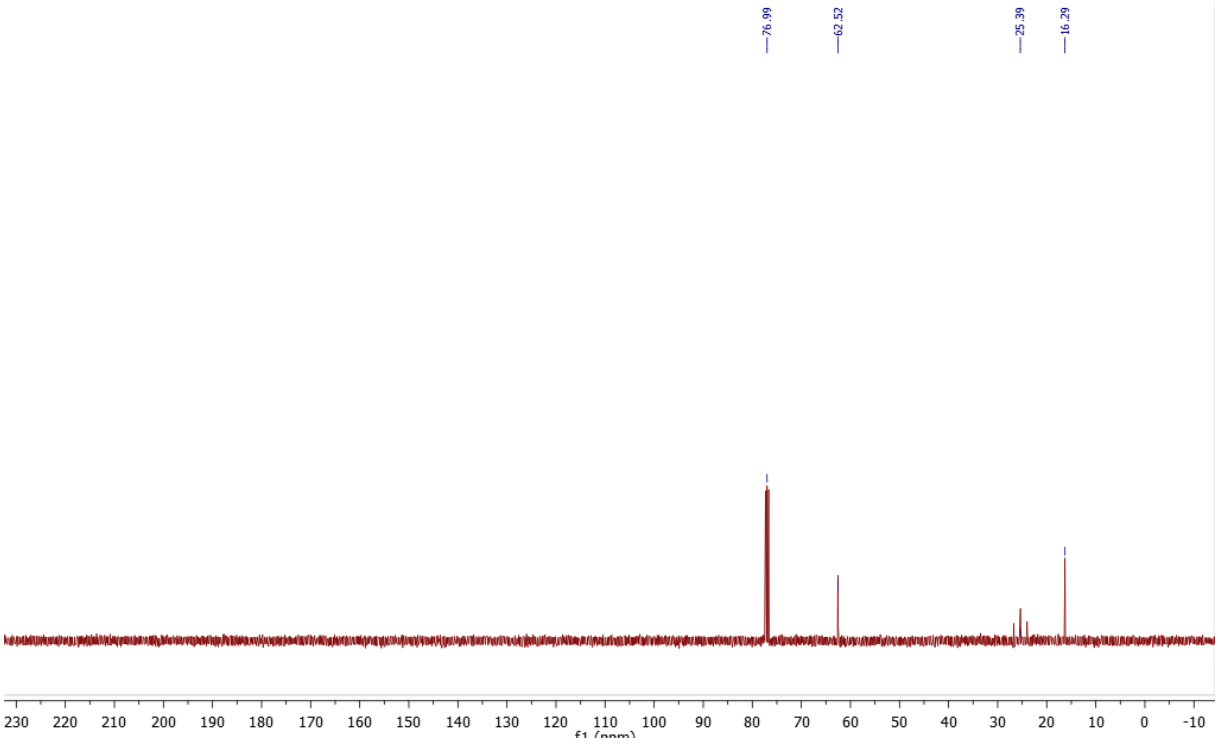

Figure 51– ^{13}C-NMR spectrum of compound A

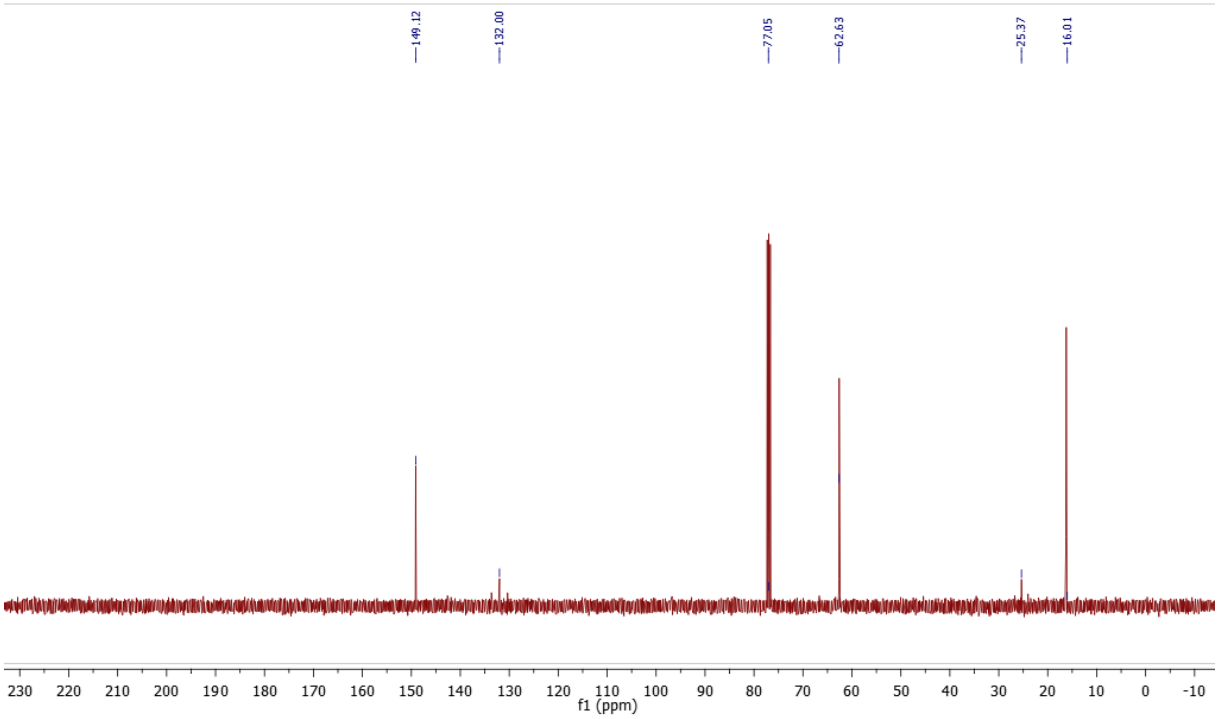

Figure 52 – ^{13}C-NMR spectrum of compound G.

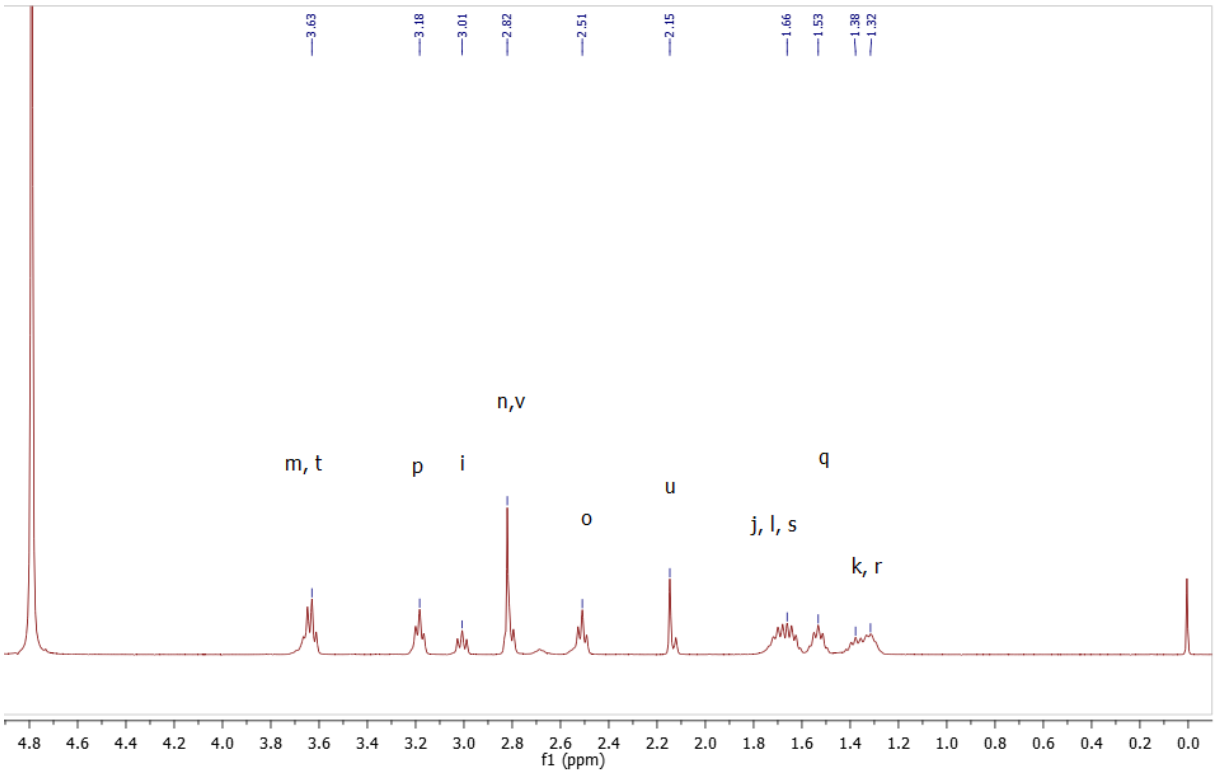

Figure 53- ^{1}H-NMR spectrum of DFO-Mes in D_2O

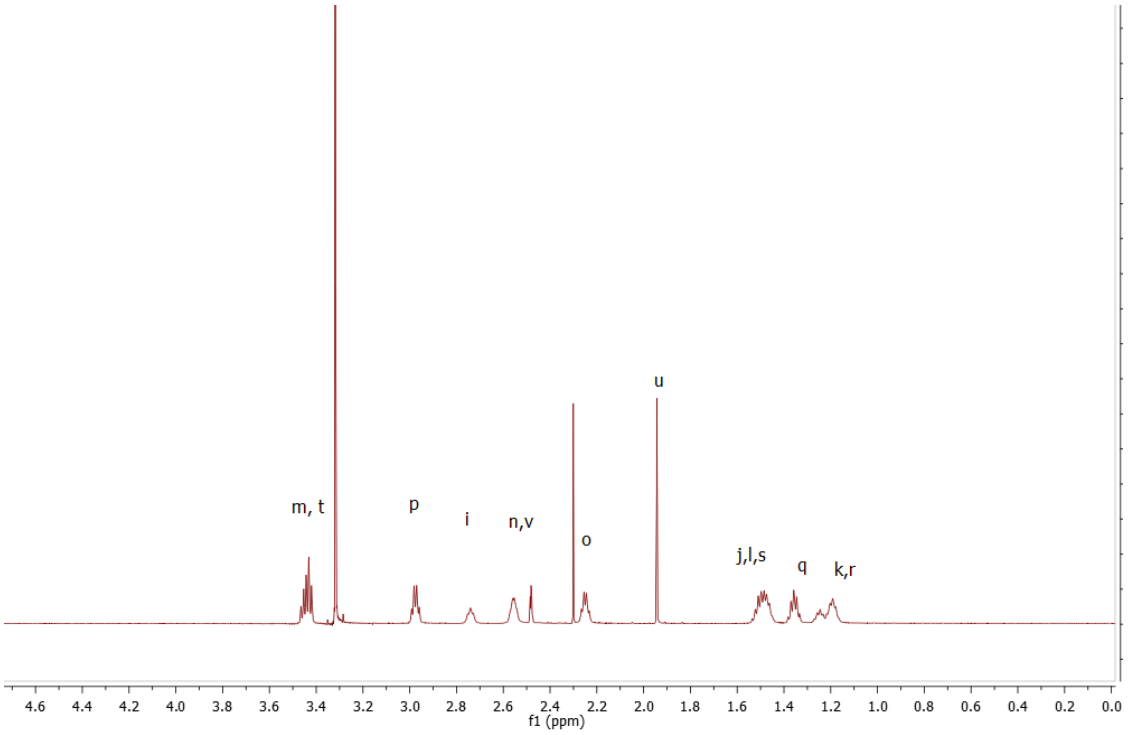

Figure 54- ^{1}H-NMR spectrum of DFO-Mes in DMSO-d_6

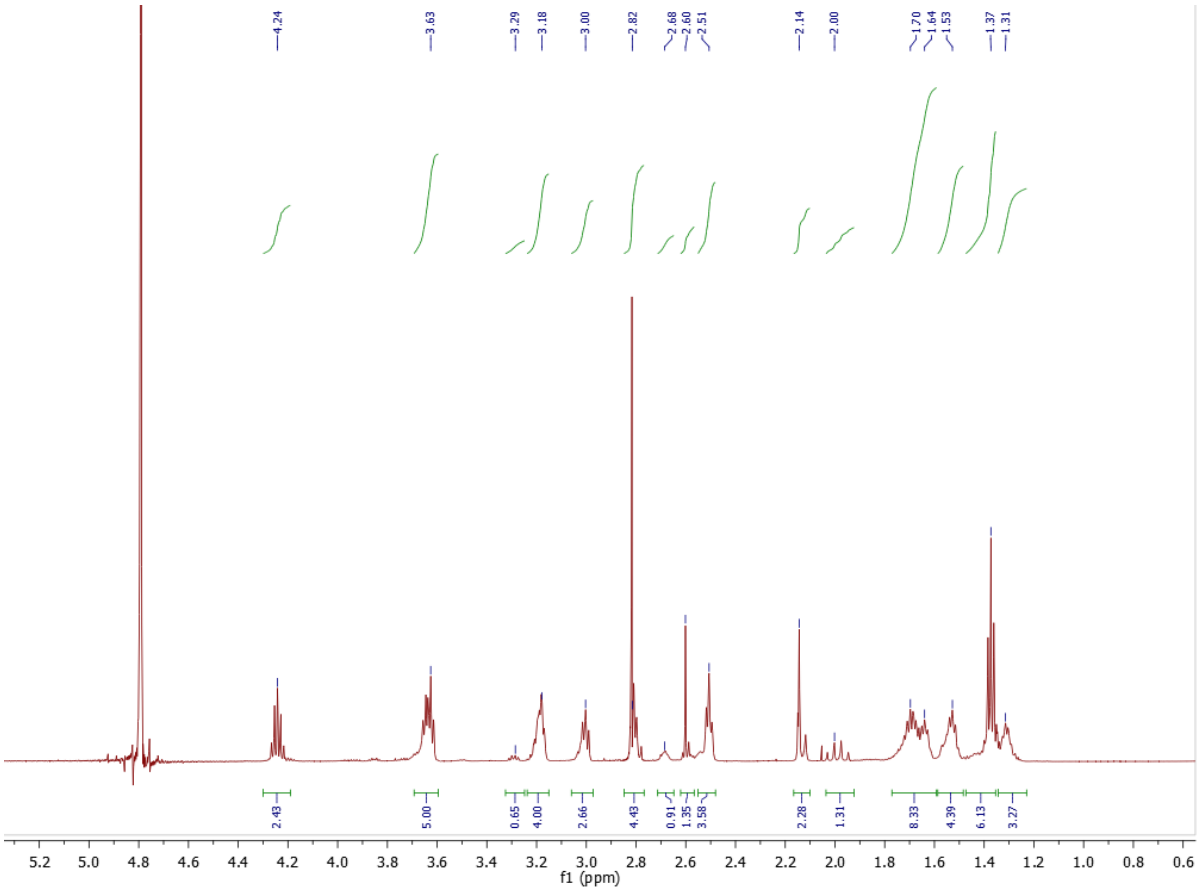

Figure 55- ^{1}H-NMR spectrum of reaction IV.

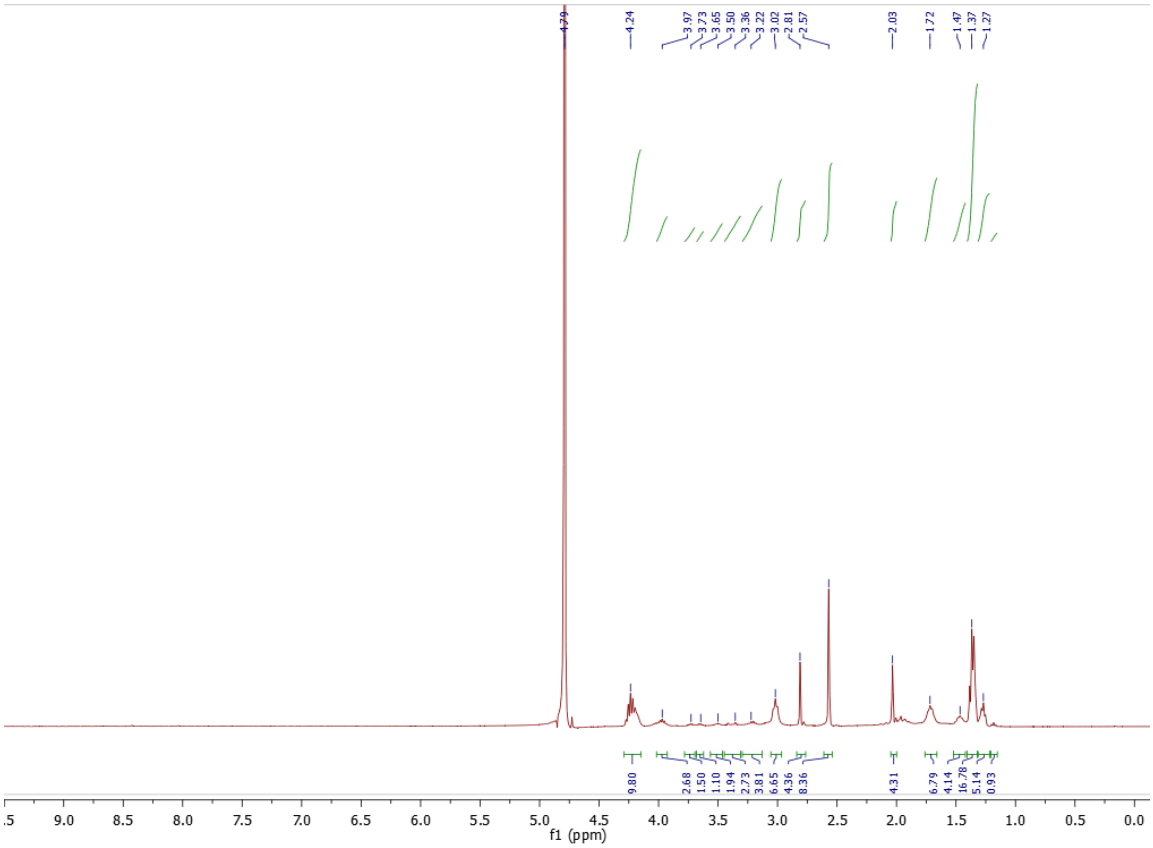

Figure 56- ^{1}H-NMR spectrum of reaction V.

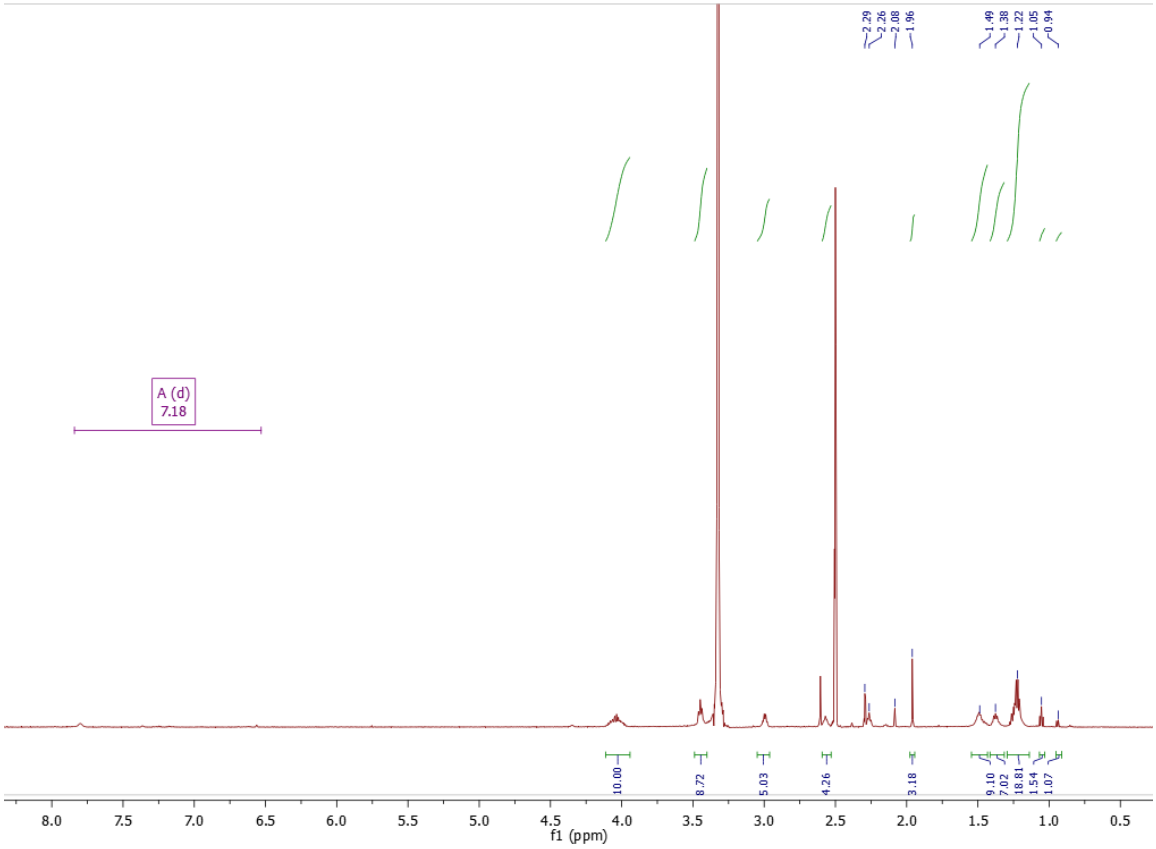

Figure 57- ^{1}H-NMR spectrum of reaction VI.

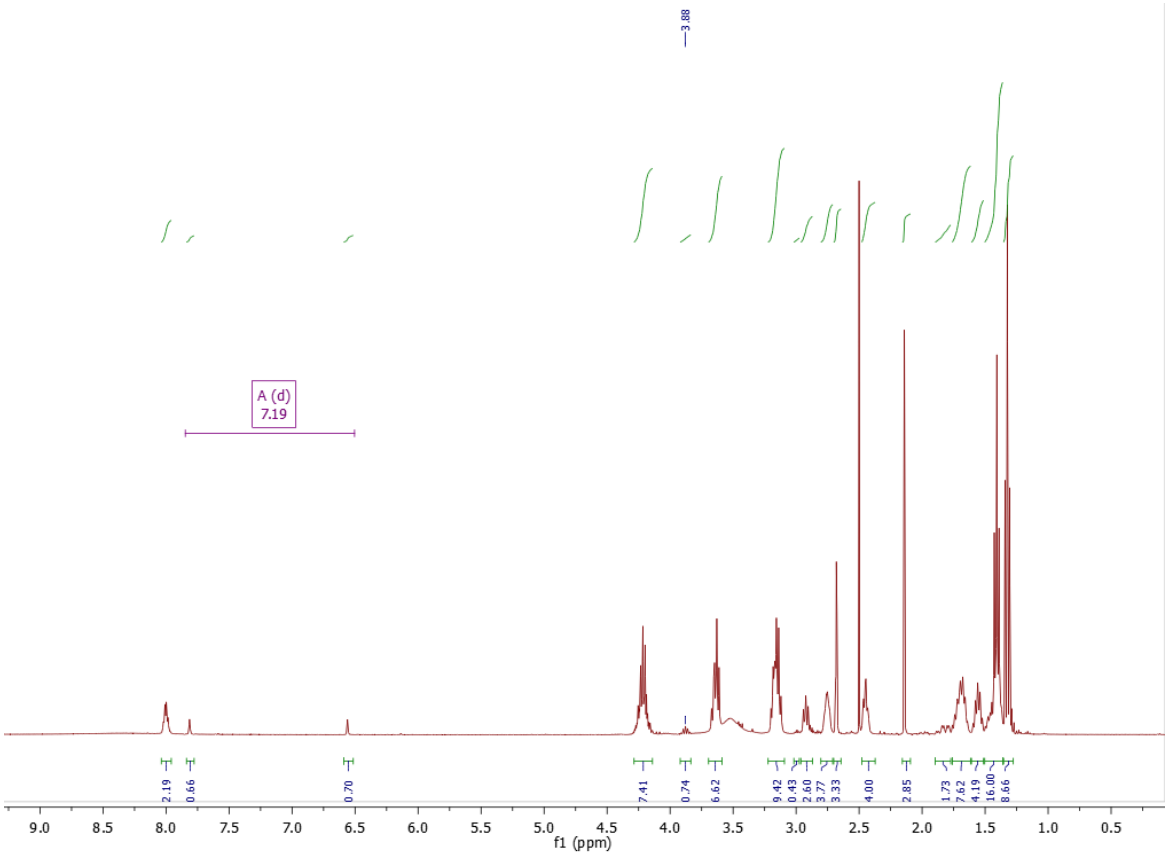

Figure 58- ^{1}H-NMR spectrum of reaction VII, 24 hours.

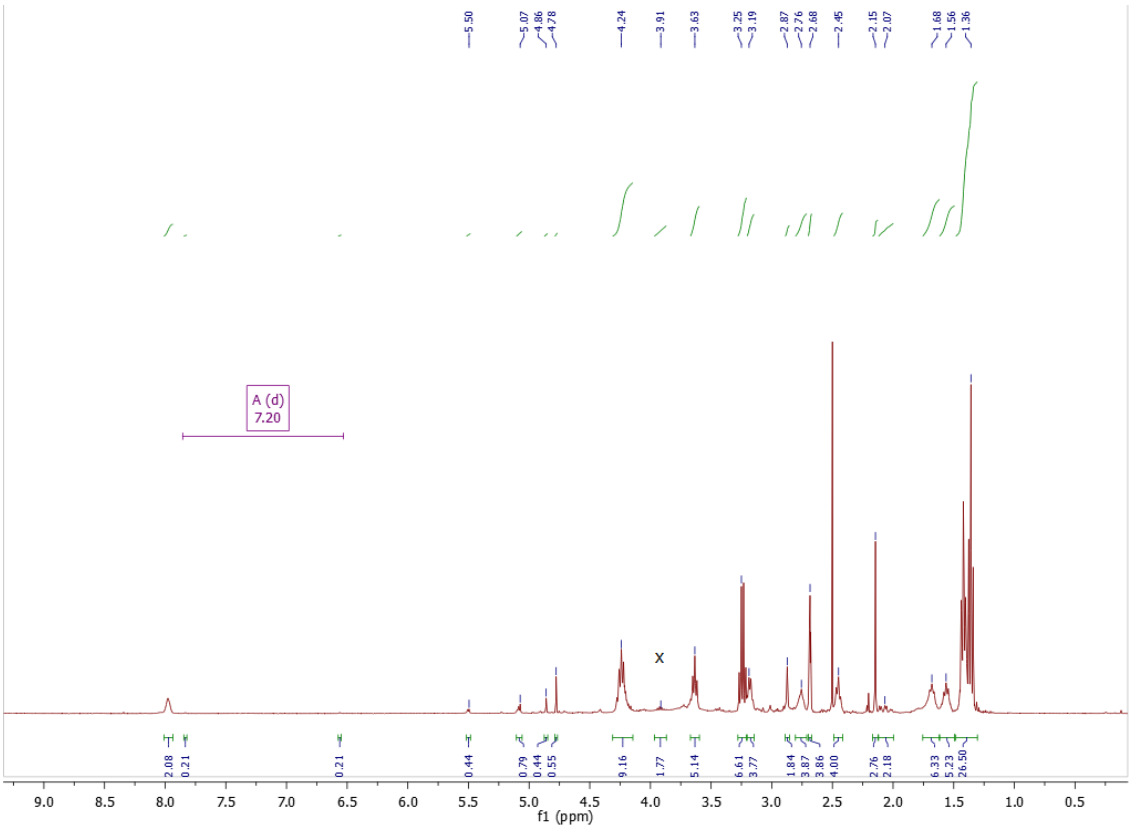

Figure 59- ^{1}H-NMR spectrum of reaction VII, 96 hours.

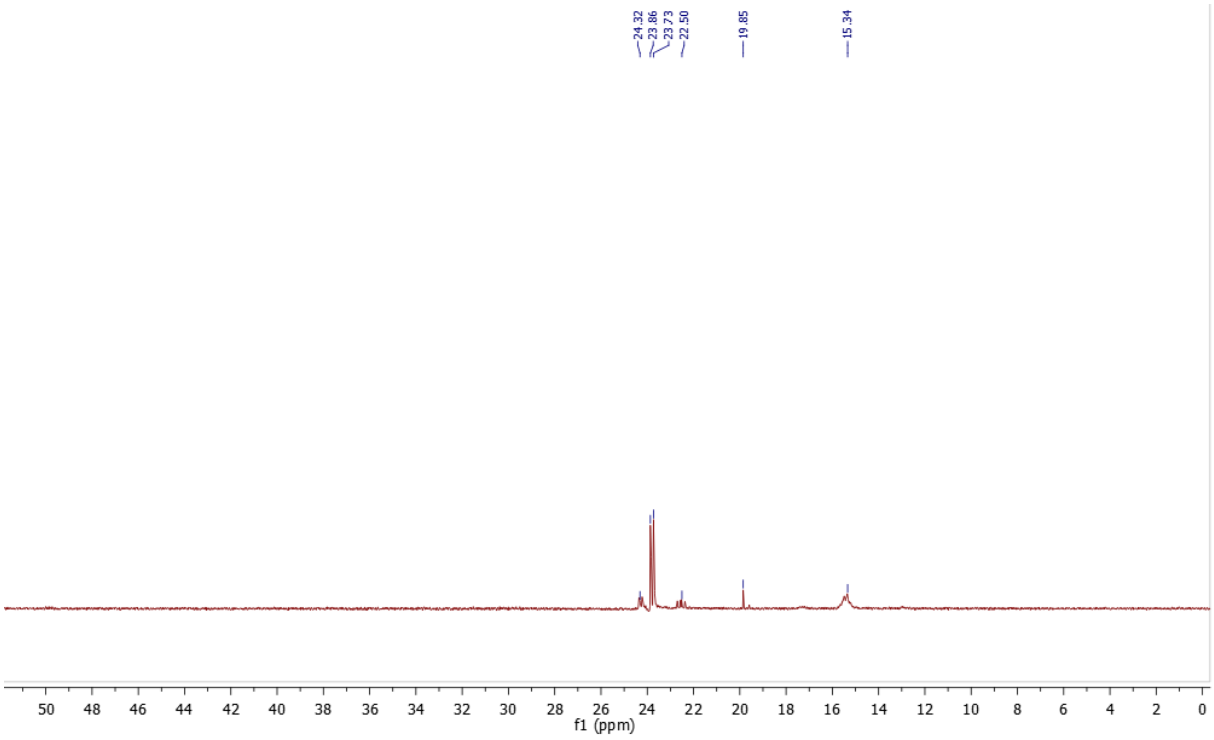

Figure 60– ^{31}P-NMR spectrum of reaction VII at 24 hours

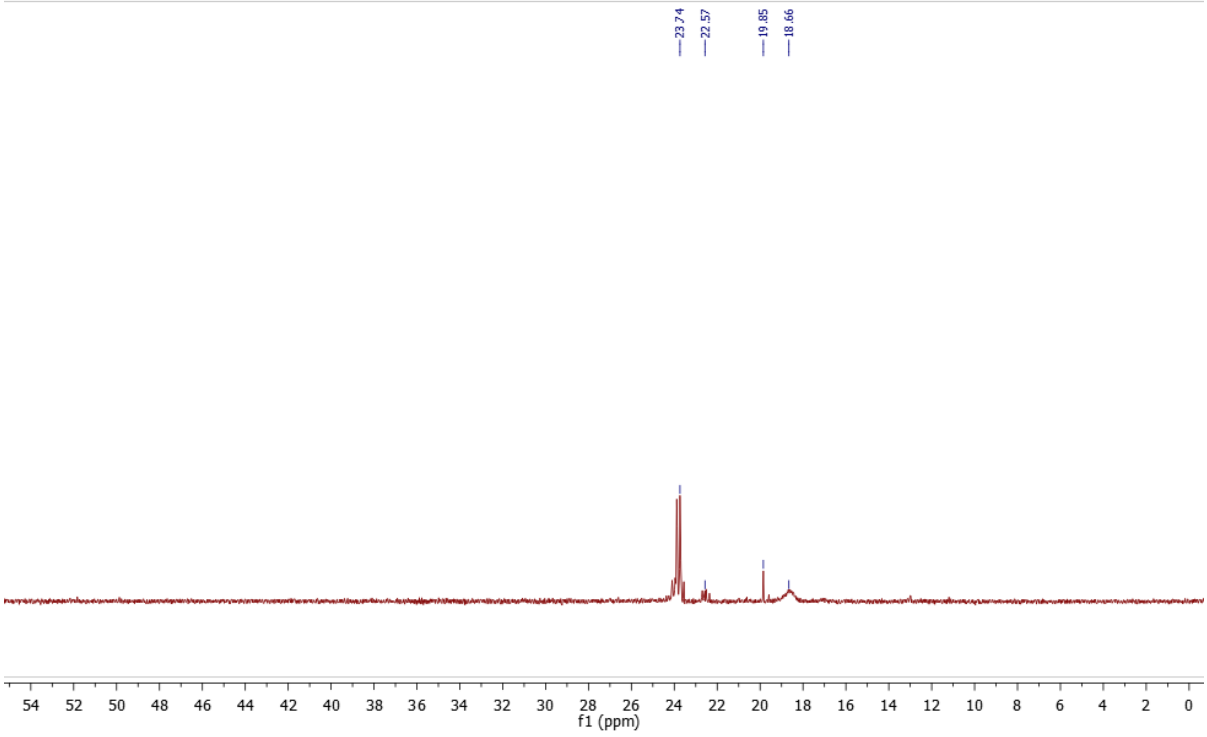

Figure 61- ^{31}P-NMR spectrum of reaction VII at 96 hours

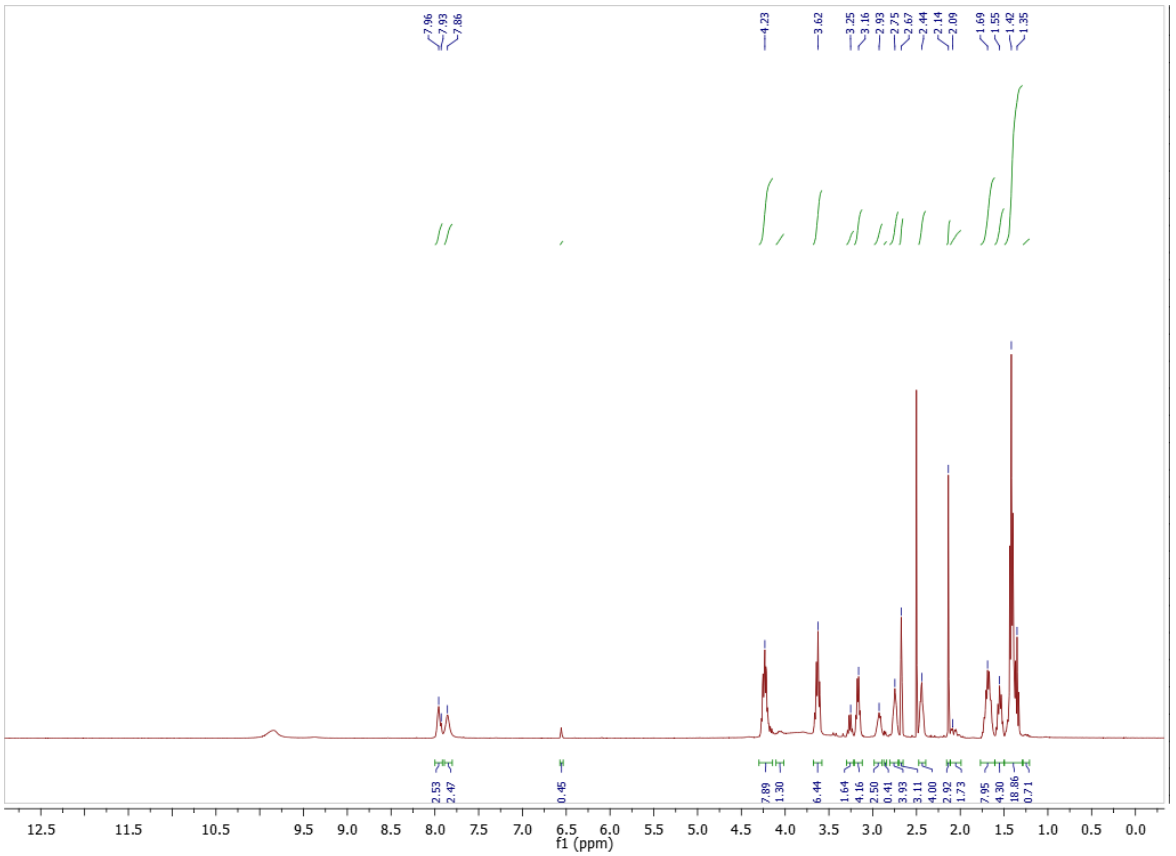

Figure 62- ^{1}H-NMR spectrum of reaction VIII, 24 hours.

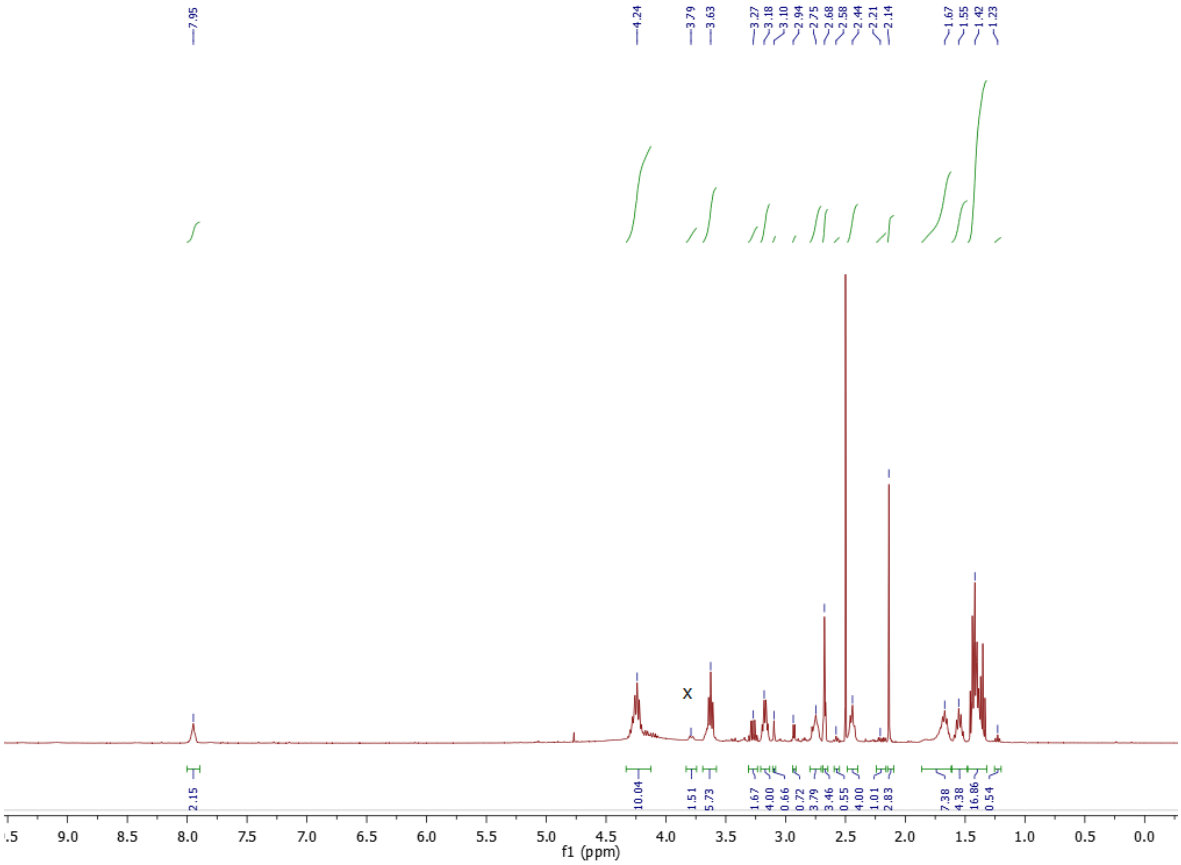

Figure 63- ^{1}H-NMR spectrum of reaction VIII, 96 hours.

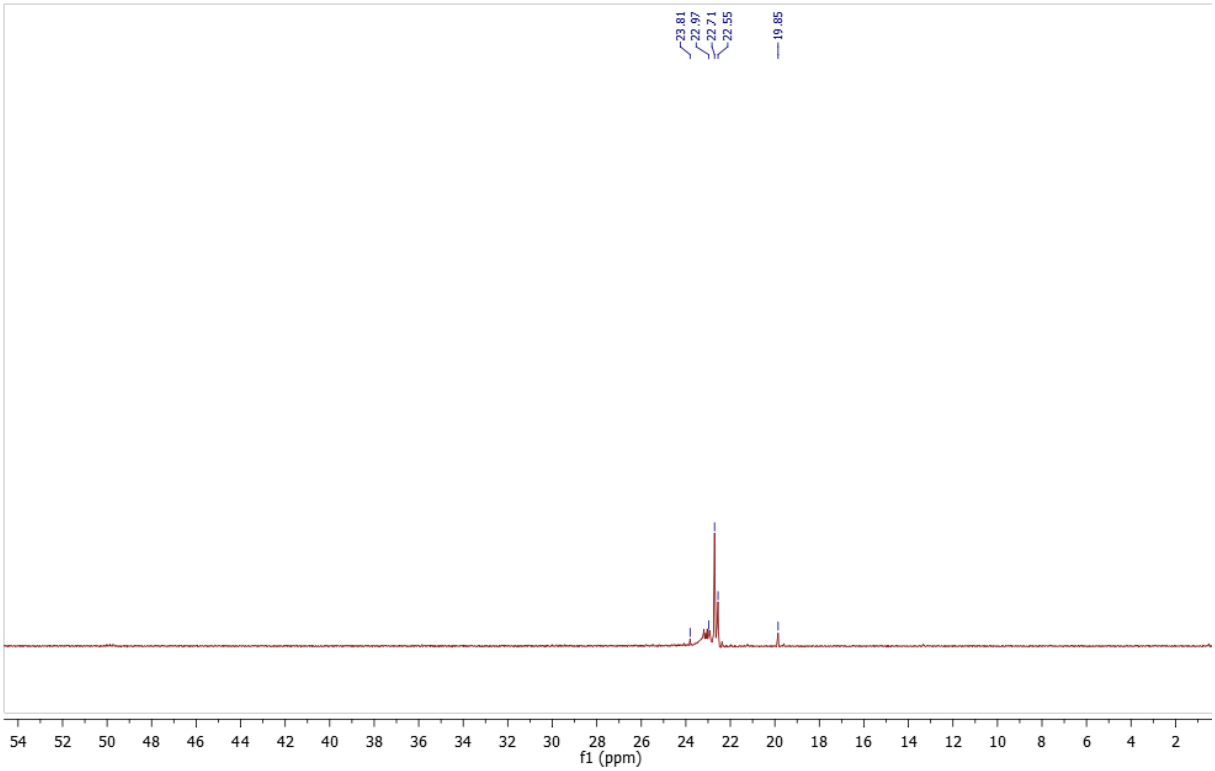

Figure 64 - ^{31}P-NMR spectrum of reaction VIII at 24 hours

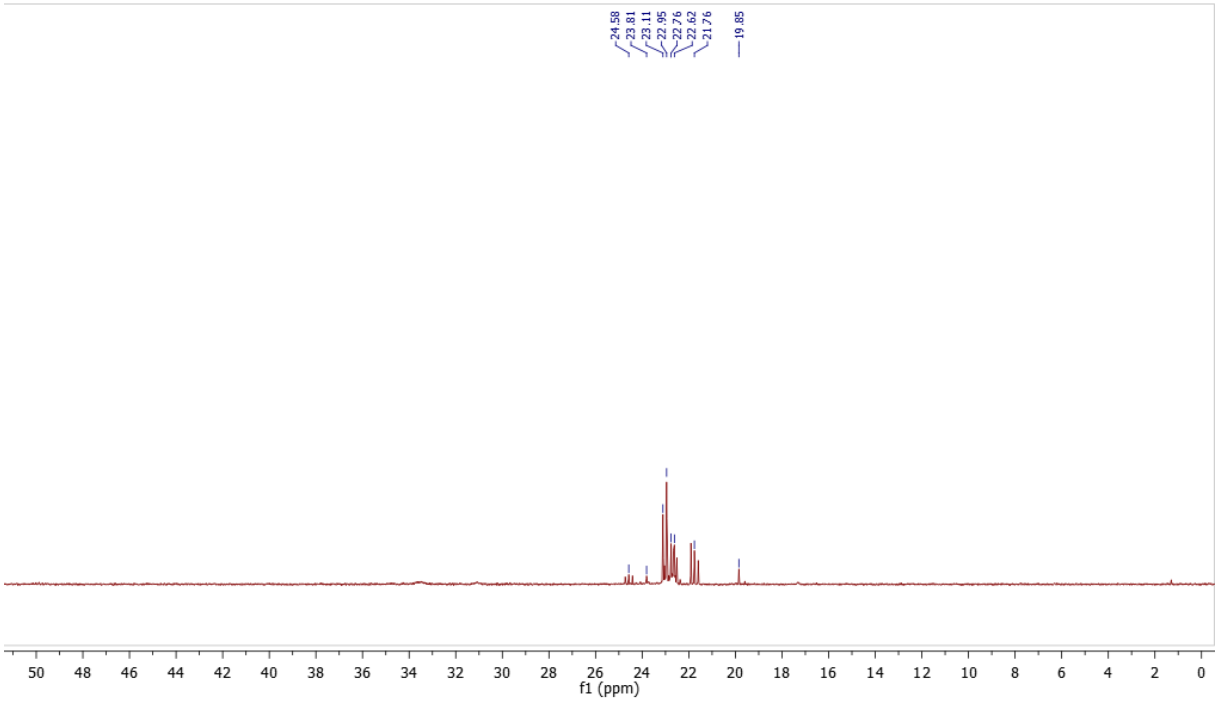

Figure 65- ^{31}P-NMR spectrum of reaction VIII at 96 hours

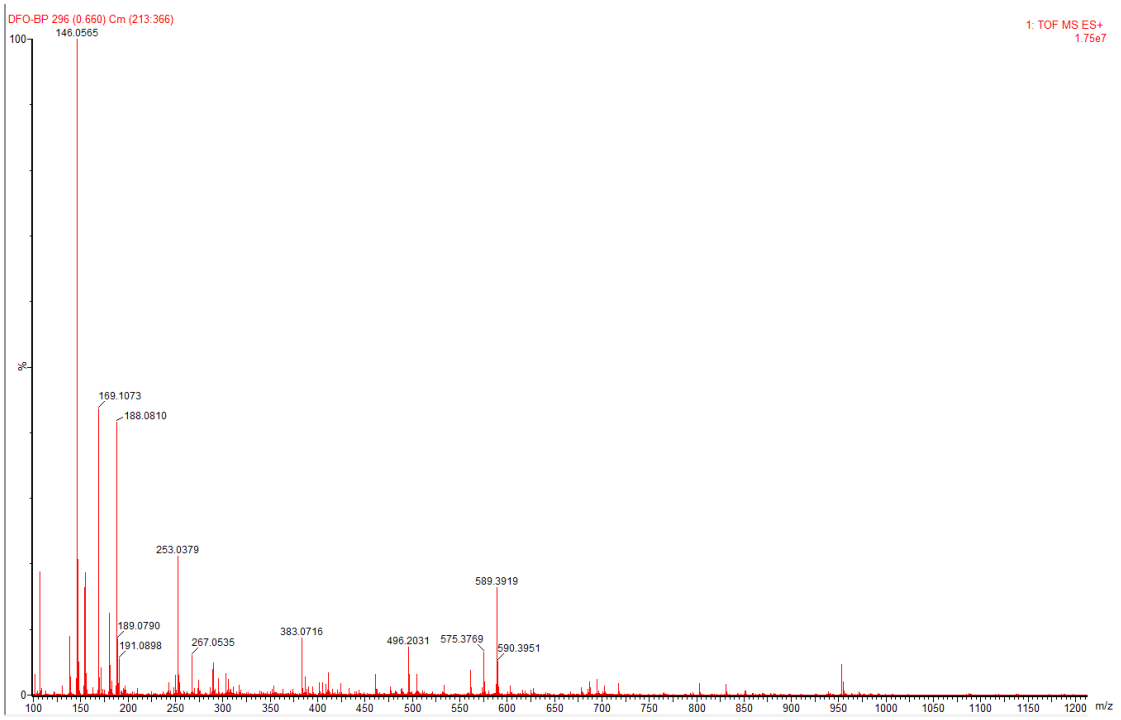

Figure 66 – ESI-MS positive field spectrum of reaction VIII products

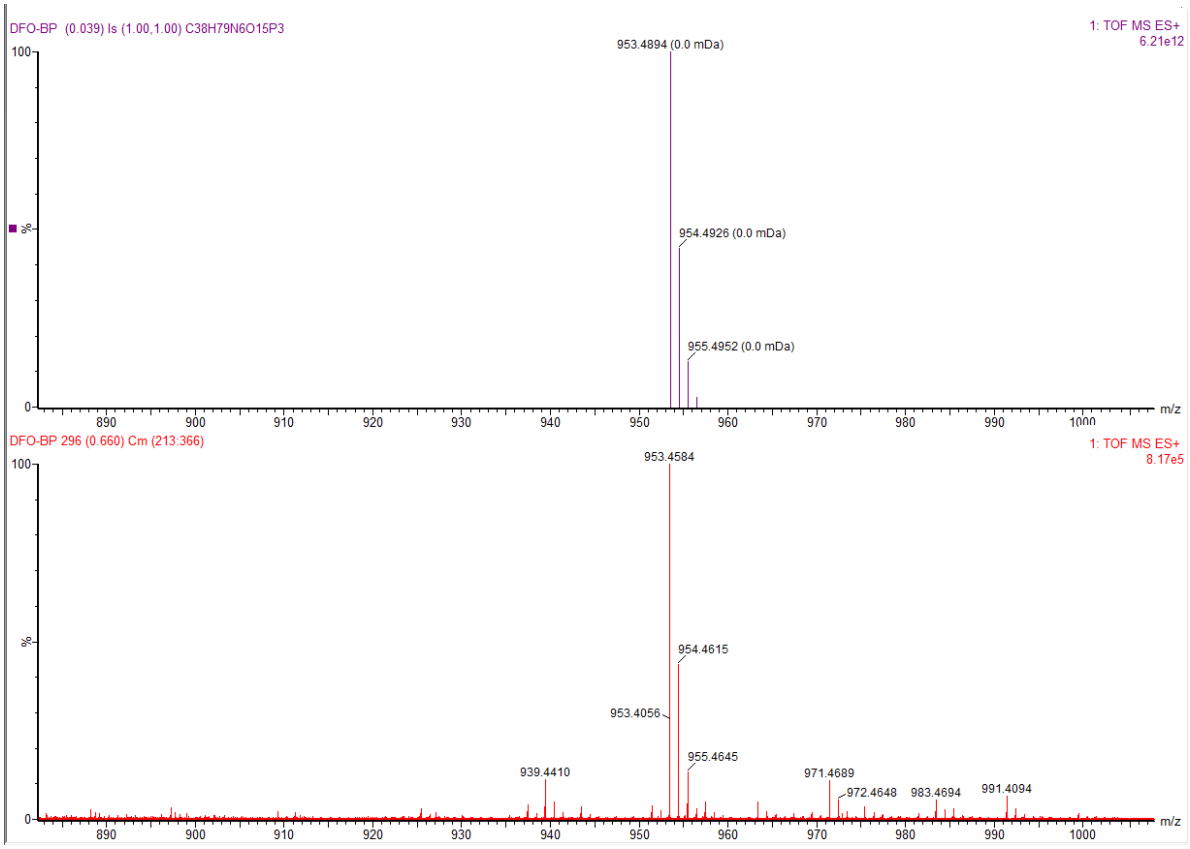

Figure 67– Excerpt of ESI-MS positive field spectrum. Simulation of m/z distribution of $C_{38}H_{79}N_6O_{15}P_3$ (top) and products of reaction VIII (bottom)

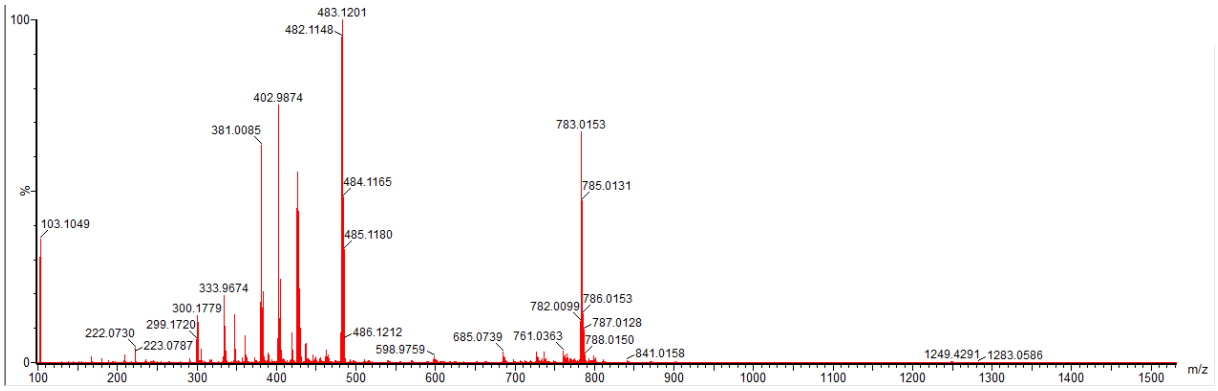

Figure 68 - Excerpt of ESI-MS positive field spectrum from reaction X mixture.

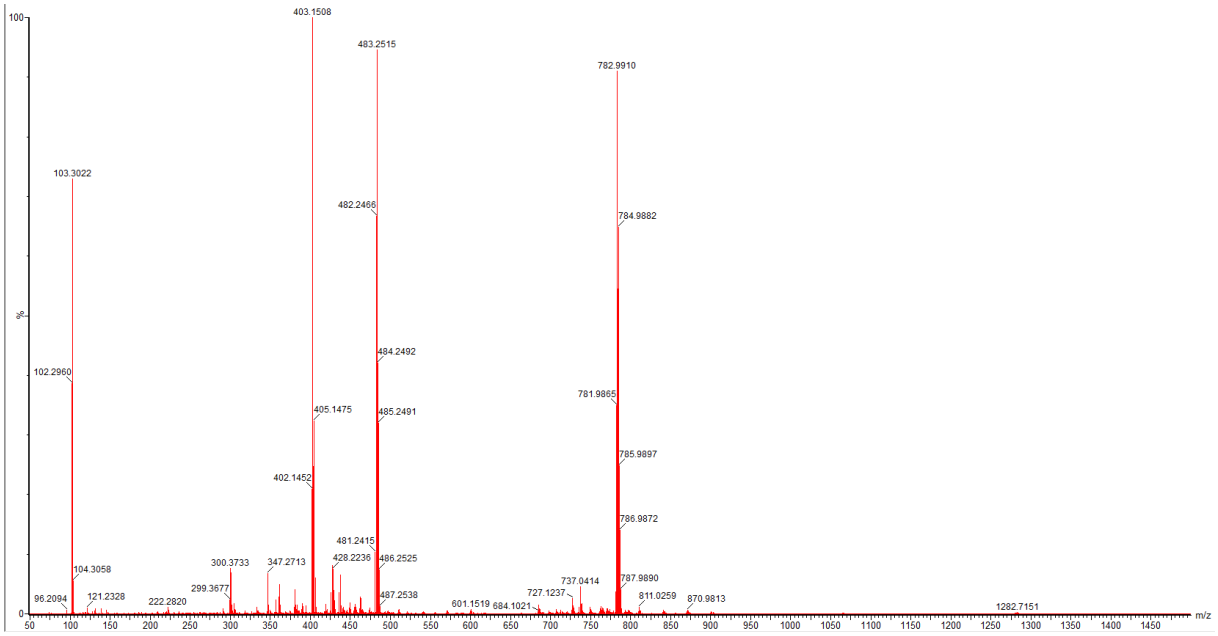

Figure 69 - Excerpt of ESI-MS positive field spectrum from reaction XI mixture

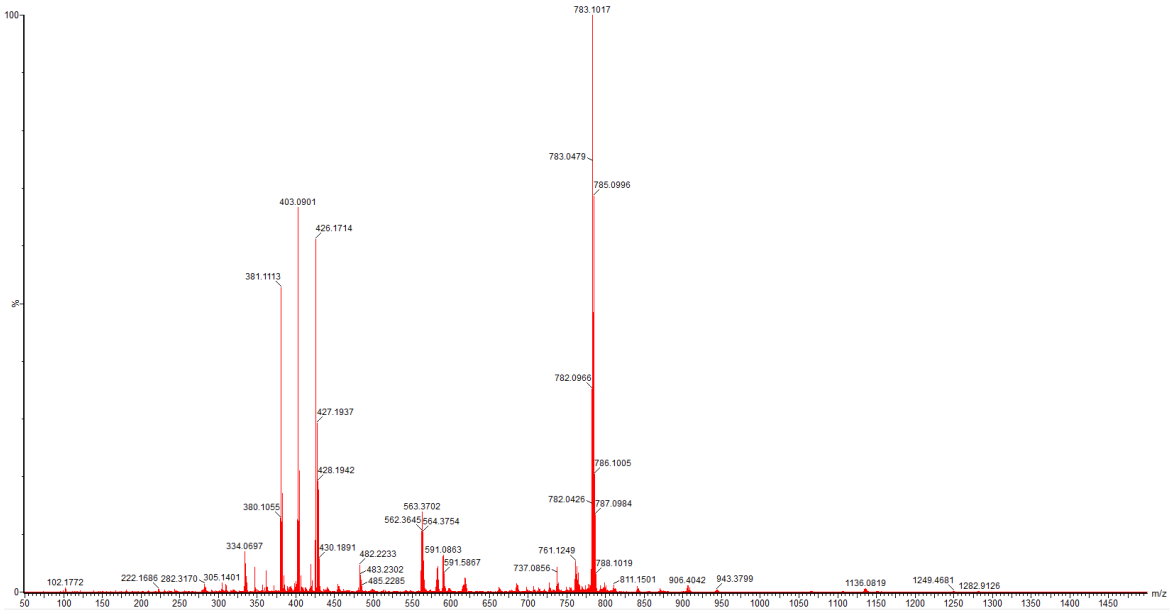

Figure 70 - Excerpt of ESI-MS positive field spectrum from reaction XII mixture.

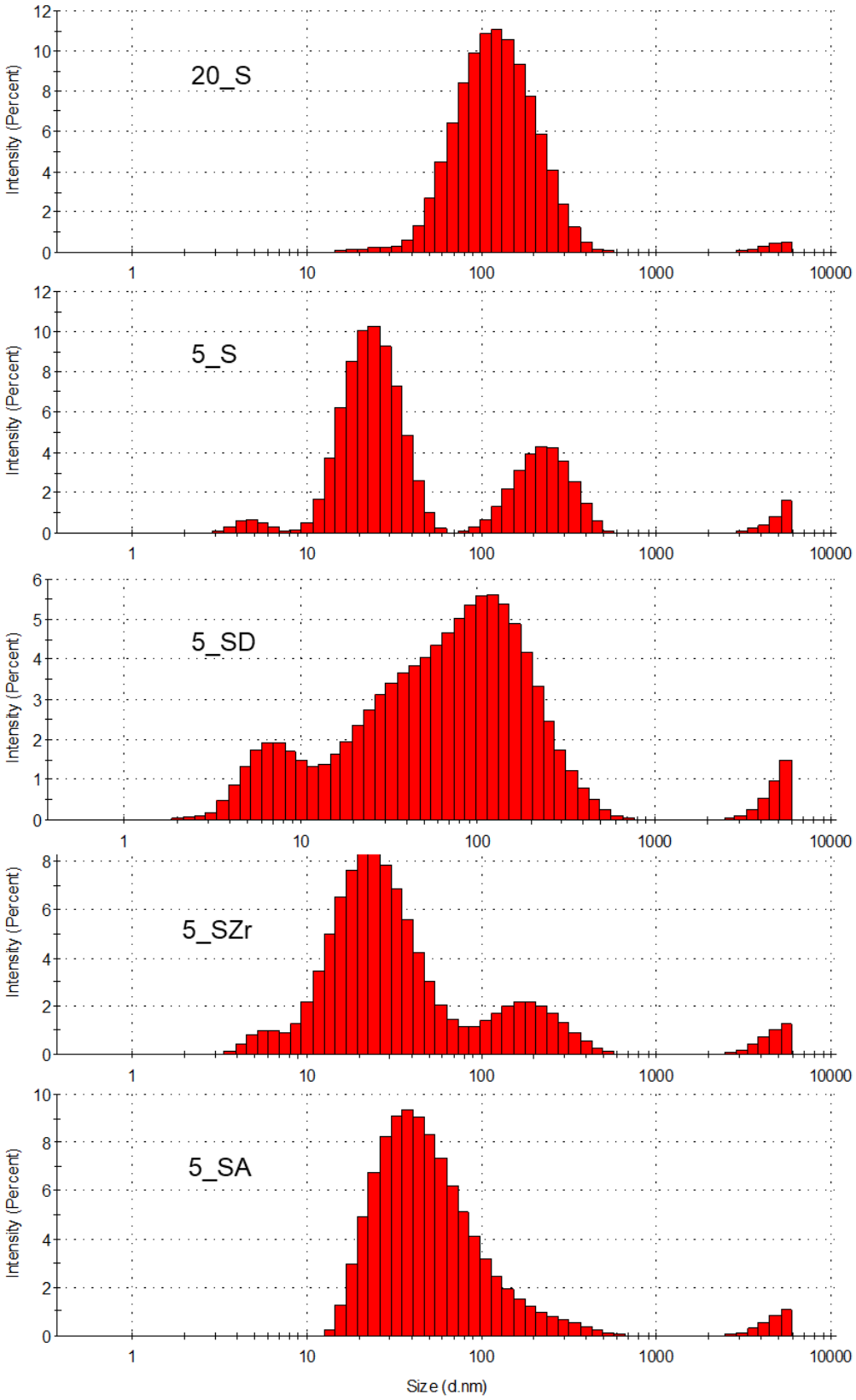

Figure 71– Size distribution by intensity, of samples 20_S, 5_S, 5_SD, 5_SZr, 5_SA, determined by dynamic light scattering

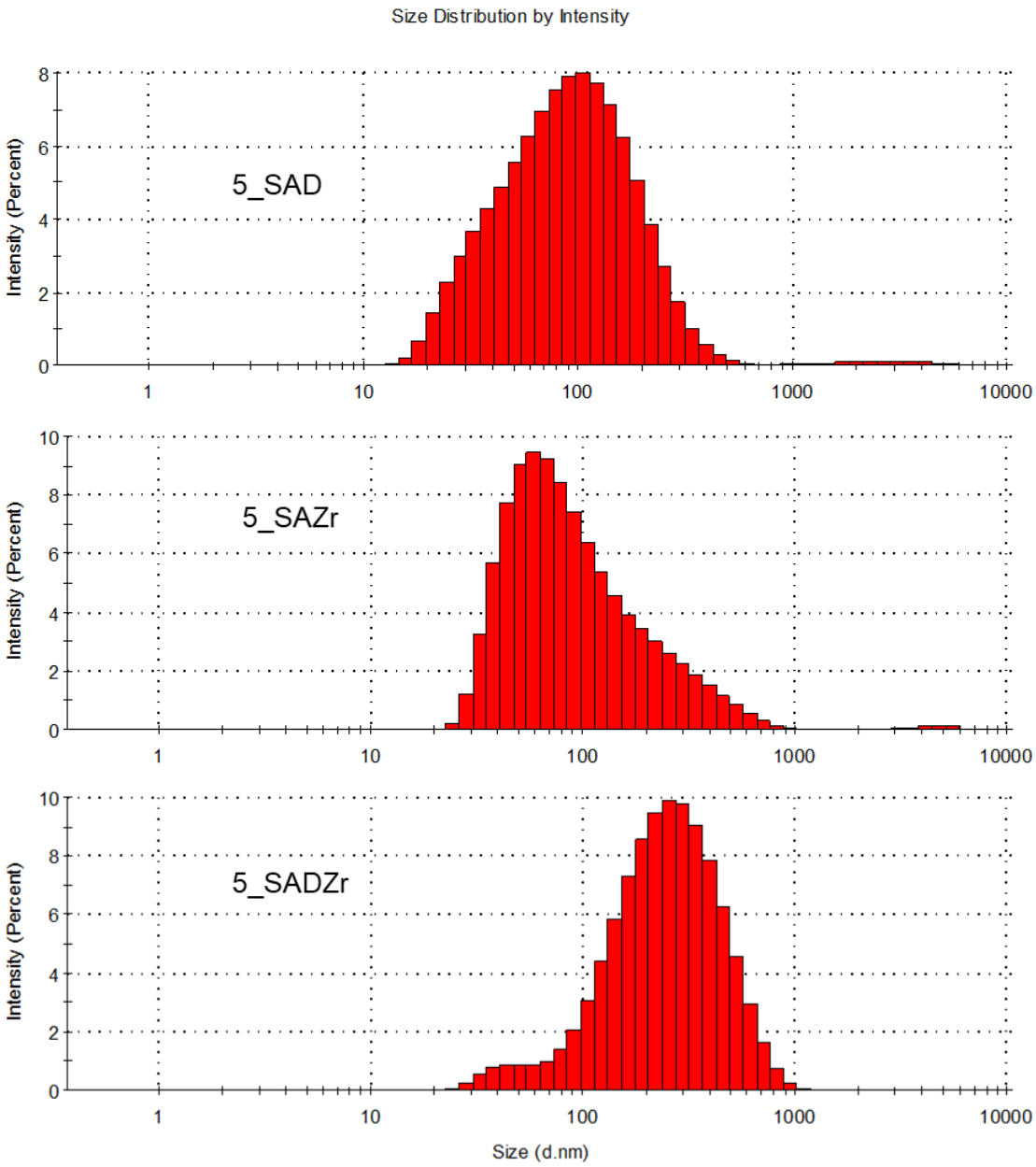

Figure 72– Size distribution by intensity, of samples 5_SAD, 5_SAZr, 5_SADZr determined by dynamic light scattering

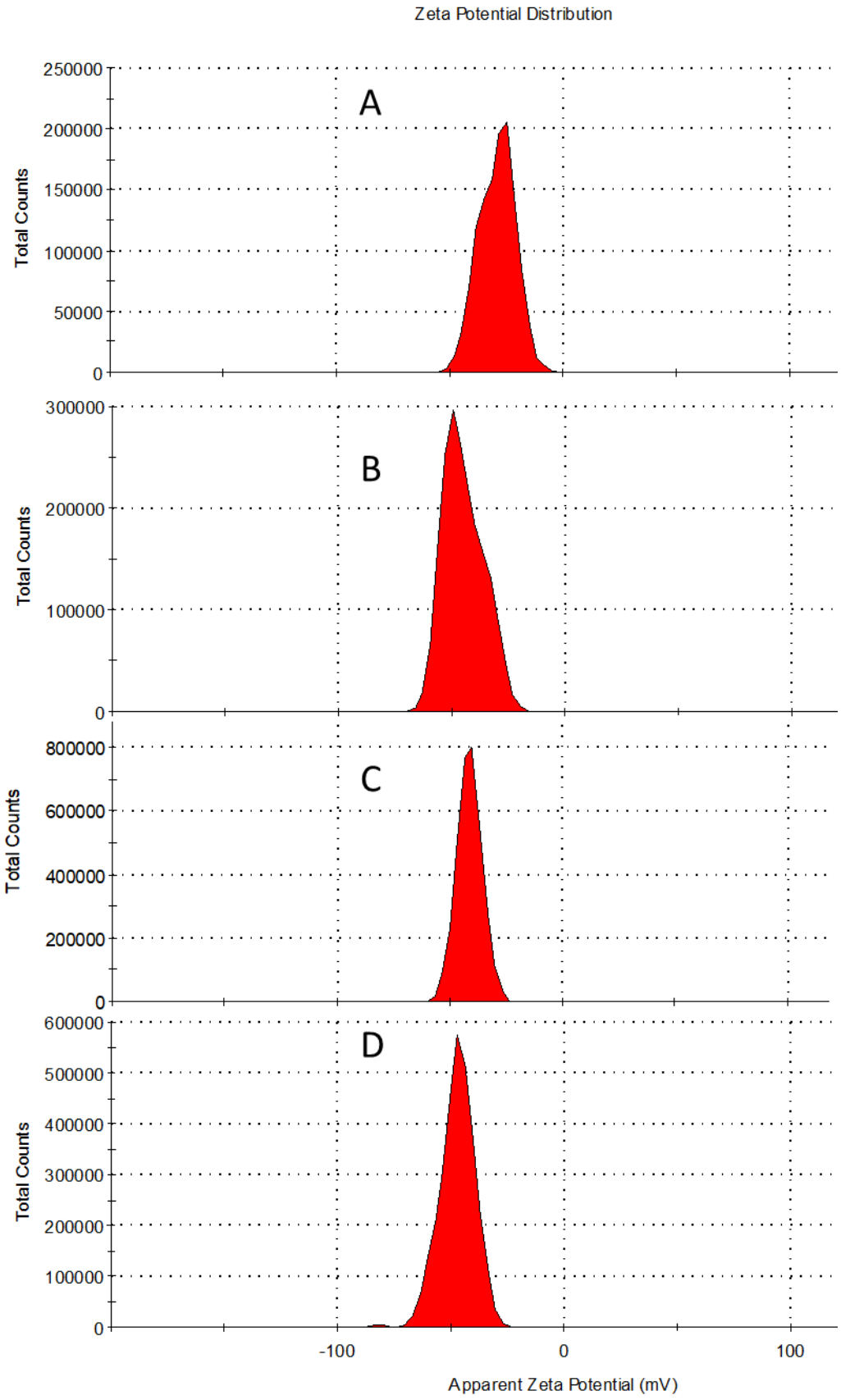

Figure 73- Zeta potential distribution of unmodified SPION of 20 nm diameter (A) and 5 nm diameter: unmodified (B); SPION-DFO (C) and ^{nat}Zr-SPION (D).

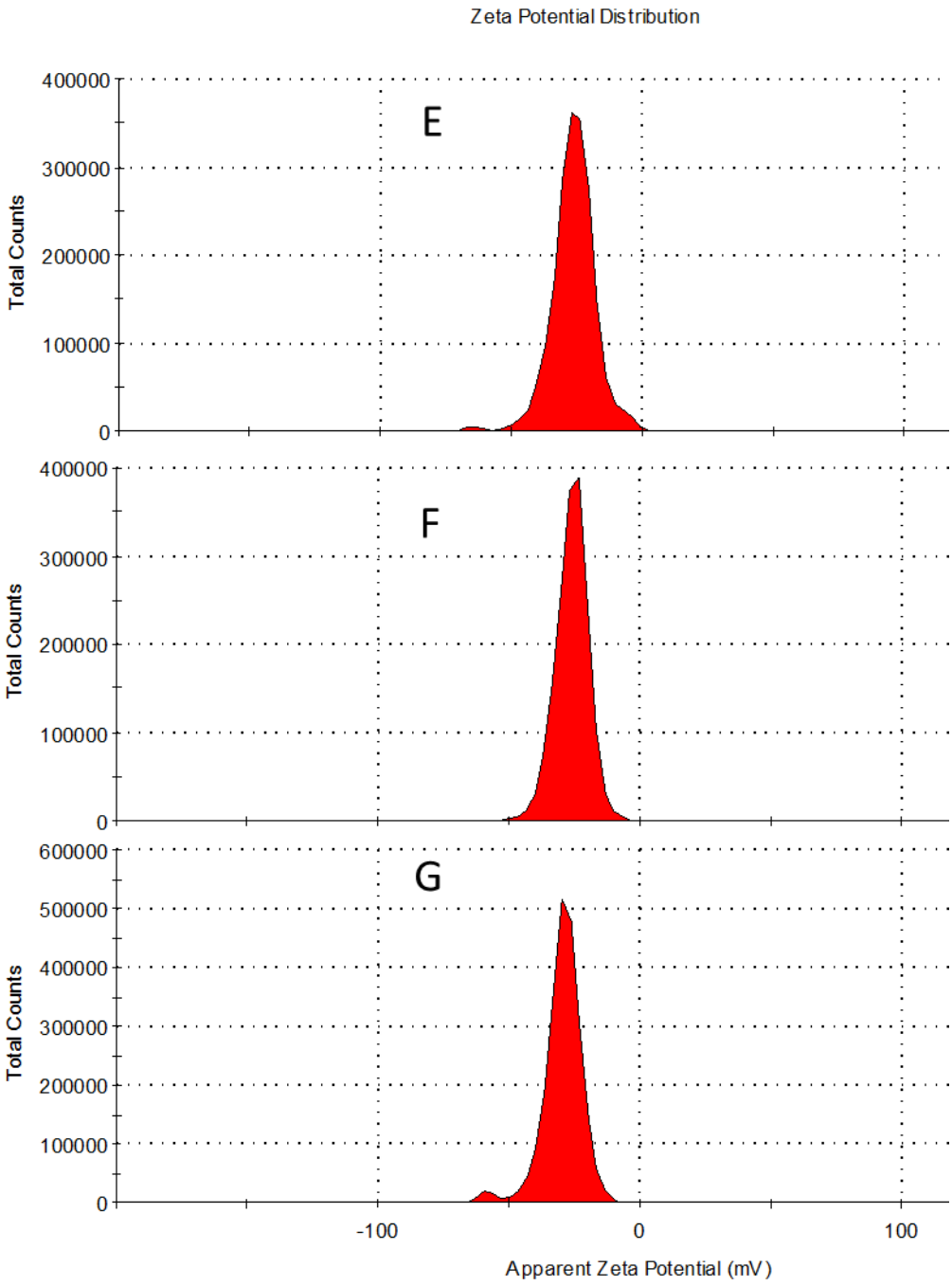

Figure 74- Zeta potential distribution of Atezolizumab-modified SPION of 5 nm diameter: SPION-Atezolizumab (E), SPION-DFO-Atezolizumab (F) and ^{nat}Zr-SPION-Atezolizumab (G).

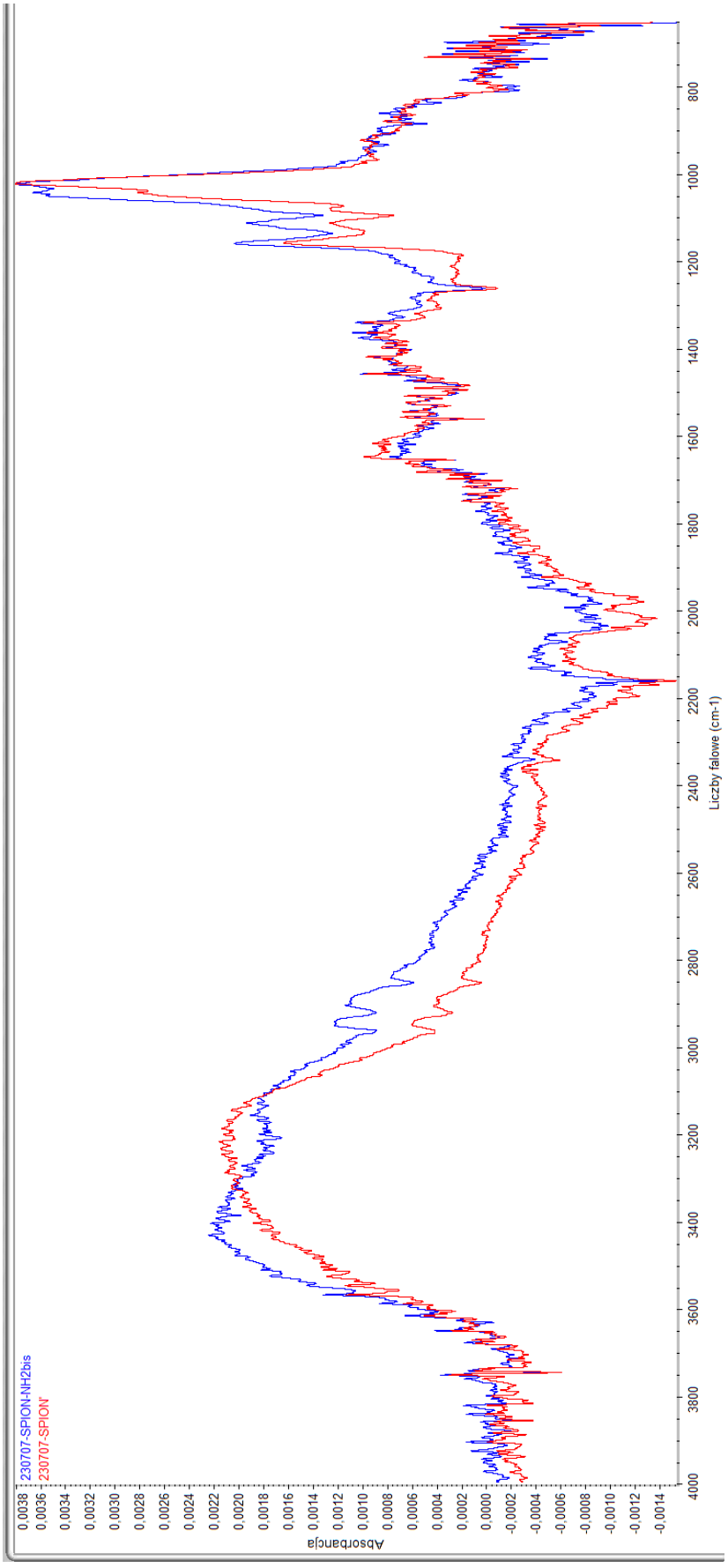

Figure 75 – FT-IR spectrum of SPION (red) and SPION-NH_2 (blue)

7. References

1. Wojciechowska, U., et al., *Cancer in Poland in 2022*. 2024, Polish National Cancer Registry: Warszawa. p. 93.
2. Hanahan, D. and R.A. Weinberg, *Hallmarks of cancer: the next generation.* Cell, 2011. **144**(5).
3. Kayyal-Tarabeia, I., et al., *Beyond lung cancer: air pollution and bladder, breast and prostate cancer incidence.* International Journal of Epidemiology, 2024. **53**(4).
4. Isaksen, I. and S. Dankel, *Ultra-processed food consumption and cancer risk: A systematic review and meta-analysis.* Clinical Nutrition, 2023. **42**(6).
5. Pulumati, A., et al., *Technological advancements in cancer diagnostics: Improvements and limitations.* Cancer Reports, 2023. **6**(2).
6. Parihar, A., et al., *Approaches to Imaging Immune Activation Using PET.* Journal of Nuclear Medicine, 2025. **66**(6).
7. Topalian, S.L., et al., *Safety, Activity, and Immune Correlates of Anti–PD-1 Antibody in Cancer.* New England Journal of Medicine, 2012. **366**(26).
8. Zhang, J., et al., *The role of CD8 PET imaging in guiding cancer immunotherapy.* Frontiers in immunology, 2024. **15**.
9. Li, J., et al., *Synergistic coordination in ^{89}Zr–DFO (deferoxamine) complexes: computational and experimental insights into auxiliary ligands.* Inorganic Chemistry Frontiers, 2025. **12**(13).
10. Wuensche, T.E., et al., *Good practices for 89Zr radiopharmaceutical production and quality control.* EJNMMI Radiopharmacy and Chemistry, 2024. **9**(1).
11. Verel, I., et al., *^{89}Zr immuno-PET: comprehensive procedures for the production of ^{89}Zr-labeled monoclonal antibodies.* Journal of Nuclear Medicine, 2003. **44**(8): p. 1271-81.
12. Affatigato, L., et al., *Magnetic and MRI Contrast Properties of HumAfFt-SPIONs: Investigating Superparamagnetic Behavior and Enhanced T2-Weighted Imaging Performance.* International Journal of Molecular Sciences, 2025. **26**(8).
13. Neuwelt, A., et al., *Iron-based superparamagnetic nanoparticle contrast agents for MRI of infection and inflammation.* American Journal of Roentgenology, 2015. **204**(3).
14. Królicki, L., *Medycyna nuklearna*. 1st ed. Vol. 1. 1996, Warszawa: Fundacja im. Ludwika Rydygiera. 391.
15. Saha, G.B., *Basics of PET imaging : physics, chemistry, and regulations*. 2nd ed. 2010, New York ; London: Springer. xiv, 241 p.
16. Gonzalez-Montoro, A., M.N. Ullah, and C.S. Levin, *Advances in Detector Instrumentation for PET.* Journal of Nuclear Medicine, 2022. **63**(8).
17. Zatcepin, A. and S.I. Ziegler, *Detectors in positron emission tomography.* Zeitschrift für Medizinische Physik, 2023. **33**(1).
18. Quinn, B., et al., *Radiation dosimetry of 18F-FDG PET/CT: incorporating exam-specific parameters in dose estimates.* BMC Medical Imaging, 2016. **16**(1).
19. Seibold, U., et al., *Bimodal imaging probes for combined PET and OI: recent developments and future directions for hybrid agent development.* BioMed Research International, 2014. **2014**.

20. Chen, Z., et al., *CT and CEST MRI bimodal imaging of the intratumoral distribution of iodinated liposomes.* Quantitative Imaging in Medicine and Surgery, 2019. **9**(9).
21. Xue, X., et al., *PET/NIR Fluorescence Bimodal Imaging for Targeted Tumor Detection.* Molecular Pharmaceutics, 2023. **20**(12).
22. Sharpe, A.H. and K.E. Pauken, *The diverse functions of the PD1 inhibitory pathway.* Nature Reviews Immunology, 2017. **18**(3).
23. Menke-van der Houven van Oordt, C., et al., *^{89}Zr-cetuximab PET imaging in patients with advanced colorectal cancer.* Oncotarget, 2015. **6**(30).
24. Ulaner, G.A., et al., *^{89}Zr-trastuzumab PET/CT for detection of HER2-positive metastases in patients with HER2-negative primary breast cancer.* Clinical Nuclear Medicine, 2017. **42**(12).
25. Sarrami, N., et al., *Immuno-PET Imaging of EGFR with ^{64}Cu-NOTA Panitumumab in Subcutaneous and Metastatic Nonsmall Cell Lung Cancer Xenografts.* Molecular Pharmaceutics, 2024. **21**(11).
26. Nirschl, C. and C. Drake, *Molecular pathways: coexpression of immune checkpoint molecules: signaling pathways and implications for cancer immunotherapy.* Clinical Cancer Research, 2013. **19**(18).
27. Hossain, A., *A comprehensive review of immune checkpoint inhibitors for cancer treatment.* International Immunopharmacology, 2024. **143**.
28. McCarthy, C.E., et al., *In vivo Imaging Technologies to Monitor the Immune System.* Frontiers in Immunology, 2020. **11**.
29. Yamane, H., et al., *Programmed cell death protein 1 and programmed death-ligand 1 are expressed on the surface of some small-cell lung cancer lines.* Am J Cancer Res, 2015. **5**(4): p. 1553-7.
30. Chi, Z., et al., *Transcriptional and epigenetic regulation of PD-1 expression.* Cellular and Molecular Life Sciences, 2021. **78**(7).
31. Gutic, B., et al., *Programmed cell death-1 and its ligands: Current knowledge and possibilities in immunotherapy.* Clinics, 2023. **78**.
32. Han, Y., D. Liu, and L. Li, *PD-1/PD-L1 pathway: current researches in cancer.* Am J Cancer Res, 2020. **10**(3): p. 727-742.
33. Lin, X., et al., *Regulatory mechanisms of PD-1/PD-L1 in cancers.* Molecular Cancer, 2024. **23**(1).
34. Tkachev, V., et al., *Programmed Death-1 Controls T Cell Survival by Regulating Oxidative Metabolism.* The Journal of Immunology, 2015. **194**(12).
35. Tjulandin, S., et al., *Novel PD-1 inhibitor prolgolimab: expanding non-resectable/metastatic melanoma therapy choice.* European Journal of Cancer, 2021. **149**.
36. Huang, M.-Y., et al., *Combination therapy with PD-1/PD-L1 blockade in non-small cell lung cancer: strategies and mechanisms.* Pharmacology & Therapeutics, 2021. **219**.
37. Au, L., et al., *Determinants of anti-PD-1 response and resistance in clear cell renal cell carcinoma.* Cancer Cell, 2021. **39**(11).
38. Uppaluri, R., et al., *Neoadjuvant and Adjuvant Pembrolizumab in Locally Advanced Head and Neck Cancer.* New England Journal of Medicine, 2025. **393**(1).
39. Zhang, Y., et al., *PD-1 Immune Checkpoint Inhibitor Therapy Malignant Tumor Based on Monotherapy and Combined Treatment Research.* Technology in Cancer Research & Treatment, 2021. **20**.

40. Khair, D.O., et al., *Combining Immune Checkpoint Inhibitors: Established and Emerging Targets and Strategies to Improve Outcomes in Melanoma.* Frontiers in Immunology, 2019. **10**.
41. Chae, Y., et al., *Current landscape and future of dual anti-CTLA4 and PD-1/PD-L1 blockade immunotherapy in cancer; lessons learned from clinical trials with melanoma and non-small cell lung cancer (NSCLC).* Journal for ImmunoTherapy of Cancer, 2018. **6**(1).
42. Dar, D., et al., *Imaging PD-L1 in the brain—Journey from the lab to the clinic.* Neuro-Oncology, 2025. **27**(2).
43. Verhoeff, S., et al., *^{89}Zr-durvalumab PD-L1 PET in recurrent or metastatic (R/M) squamous cell carcinoma of the head and neck.* Journal of Clinical Oncology, 2020. **38**(15).
44. Kok, I., et al., *^{89}Zr-pembrolizumab imaging as a non-invasive approach to assess clinical response to PD-1 blockade in cancer.* Annals of Oncology, 2022. **33**(1).
45. England, C., et al., *^{89}Zr-labeled nivolumab for imaging of T-cell infiltration in a humanized murine model of lung cancer.* European Journal of Nuclear Medicine and Molecular Imaging, 2018. **45**(1).
46. Dhoundiyal, S., et al., *Radiopharmaceuticals: navigating the frontier of precision medicine and therapeutic innovation.* European Journal of Medical Research, 2024. **29**(1).
47. Glazer, S.E., S. Kummar, and E. Mittra, *Illuminating immunotherapy response via precision T cell-targeted PET imaging.* Frontiers in Medicine, 2024. **11**.
48. Nerella, S.G., et al., *PET Molecular Imaging in Drug Development: The Imaging and Chemistry Perspective.* Frontiers in Medicine, 2022. **9**.
49. Ferris, T., et al., *Use of radioiodine in nuclear medicine—A brief overview.* Journal of Labelled Compounds and Radiopharmaceuticals, 2021. **64**(3).
50. Vitale, F., et al., *The pivotal role of endoplasmic reticulum in FDG uptake in cancer cells.* EJNMMI Research, 2024. **14**(1).
51. Zou, Y., et al., *Radiopharmaceuticals Targeting Gastrin-Releasing Peptide Receptor for Diagnosis and Therapy of Prostate Cancer.* Molecular Pharmaceutics, 2024. **21**(9).
52. Yip, C., et al., *Molecular imaging of hypoxia in non-small-cell lung cancer.* European Journal of Nuclear Medicine and Molecular Imaging, 2015. **42**(6).
53. Schrempf, A., A. Slyskova, and J.I. Loizou, *Targeting the DNA Repair Enzyme Polymerase θ in Cancer Therapy.* Trends in Cancer, 2021. **7**(2).
54. Chan, C.Y., et al., *[123-I]CC1: A PARP-Targeting, Auger Electron–Emitting Radiopharmaceutical for Radionuclide Therapy of Cancer.* Journal of Nuclear Medicine, 2023. **64**(12).
55. Suzuki, T., et al., *Imaging Gene Expression in Regional Brain Ischemia in Vivo with a Targeted [^{111}In]-Antisense Radiopharmaceutical.* Molecular Imaging, 2004. **3**(4).
56. Mukkamala, R., et al., *Design of a Fibroblast Activation Protein-Targeted Radiopharmaceutical Therapy with High Tumor-to-Healthy-Tissue Ratios.* Journal of Nuclear Medicine, 2024. **65**(8).
57. Aslanidis, I., et al., *18F-fluorodeoxyglucose PET/CT in the diagnosis of vascular graft infection.* Khirurgiia, 2021(2).
58. Lin, M., et al., *Monoclonal antibody based radiopharmaceuticals for imaging and therapy.* Current Problems in Cancer, 2021. **45**(5).

59. Williams, J.H., et al., *Implications of Immunogenicity Testing for Therapeutic Monoclonal Antibodies: A Quantitative Pharmacology Framework.* The AAPS Journal, 2024. **26**(2).
60. Hansel, T.T., et al., *The safety and side effects of monoclonal antibodies.* Nature Reviews Drug Discovery, 2010. **9**(4).
61. Vaisman-Mentesh, A., et al., *Molecular Landscape of Anti-Drug Antibodies Reveals the Mechanism of the Immune Response Following Treatment With TNFα Antagonists.* Frontiers in Immunology, 2019. **10**.
62. Johansson, M.U., et al., *Design of antibody variable fragments with reduced reactivity to preexisting anti-drug antibodies.* mAbs, 2023. **15**(1).
63. Schneider, D.W., et al., *In Vivo Biodistribution, PET Imaging, and Tumor Accumulation of ^{86}Y- and ^{111}In-Antimindin/RG-1, Engineered Antibody Fragments in LNCaP Tumor–Bearing Nude Mice.* Journal of Nuclear Medicine, 2009. **50**(3).
64. Zhao, Y., et al., *Two routes for production and purification of Fab fragments in biopharmaceutical discovery research: Papain digestion of mAb and transient expression in mammalian cells.* Protein Expression and Purification, 2009. **67**(2).
65. Monnier, P.P., R.J. Vigouroux, and N.G. Tassew, *In Vivo Applications of Single Chain Fv (Variable Domain) (scFv) Fragments.* Antibodies, 2013. **2**(2): p. 193-208.
66. Löfblom, J., et al., *Affibody molecules: engineered proteins for therapeutic, diagnostic and biotechnological applications.* FEBS Letters, 2010. **584**(12).
67. Muyldermans, S., *Nanobodies: Natural Single-Domain Antibodies.* Annual Review of Biochemistry, 2013. **82**.
68. Kostakoglu, L., H.J. Agress, and S.J. Goldsmith, *Clinical Role of FDG PET in Evaluation of Cancer Patients.* RadioGraphics, 2003. **23**(2).
69. Banerjee, S.R. and M.G. Pomper, *Clinical applications of Gallium-68.* Applied Radiation and Isotopes, 2013. **76**.
70. Zhang, Y., H. Hong, and W. Cai, *PET Tracers Based on Zirconium-89.* Current Radiopharmaceuticals, 2011. **4**(2).
71. Zhou, Y., et al., *^{64}Cu-based Radiopharmaceuticals in Molecular Imaging.* Technology in Cancer Research & Treatment, 2019. **18**.
72. Duatti, A., *Review on ^{99m}Tc radiopharmaceuticals with emphasis on new advancements.* Nuclear Medicine and Biology, 2021. **92**.
73. Wei, S., et al., *Radioactive Iodine-125 in Tumor Therapy: Advances and Future Directions.* Frontiers in Oncology, 2021. **11**.
74. Degueldre, C., et al., *Fission gas released from molten salt reactor fuel: the case of noble gas short life radioisotopes for radiopharmaceutical application.* Medicine in Novel Technology and Devices, 2021. **10**.
75. Poty, S., et al., *α-Emitters for Radiotherapy: From Basic Radiochemistry to Clinical Studies-Part 1.* Journal of Nuclear Medicine, 2018. **59**(6).
76. Jødal, L., *Beta emitters and radiation protection.* Acta Oncologica, 2009. **48**(2).
77. Ku, A., et al., *Auger electrons for cancer therapy – a review.* EJNMMI Radiopharmacy and Chemistry, 2019. **4**(1).
78. Terrien, J., *News from the Bureau International des Poids et Mesures.* Metrologia, 1975. **11**(4).
79. Council, N.R., *Evaluation of Guidelines for Exposures to Technologically Enhanced Naturally Occurring Radioactive Materials.* 1999.

80. Nagai, Y., *Production scheme for diagnostic-therapeutic radioisotopes by accelerator neutrons.* Proceedings of the Japan Academy. Series B, Physical and biological sciences, 2021. **97**(6).
81. (U.S.)., N.R.C., *Medical isotope production without highly enriched uranium*. Committee on Medical Isotope Production Without Highly Enriched Uranium.,. 2009, Washington, D.C.: National Academies Press. xviii, 202 p.
82. Kasbollah, A., et al., *Review on Production of ^{89}Zr in a Medical Cyclotron for PET Radiopharmaceuticals.* Journal of Nuclear Medicine Technology, 2013. **41**(1).
83. Dias, G., et al., *^{89}Zr for antibody labeling and in vivo studies - A comparison between liquid and solid target production.* Nuclear Medicine and Biology, 2018. **58**.
84. Zeng, D. and C.J. Anderson, *Rapid and sensitive LC-MS approach to quantify non-radioactive transition metal impurities in metal radionuclides.* Chemical Communications, 2013. **49**(26).
85. Feiner, I.V.J., et al., *The Race for Hydroxamate-Based Zirconium-89 Chelators.* Cancers, 2021. **13**(17).
86. Price, E.W. and C. Orvig, *Matching chelators to radiometals for radiopharmaceuticals.* Chemical Society Reviews, 2013. **43**(1).
87. Gourni, E., et al., *(R)-NODAGA-PSMA: A Versatile Precursor for Radiometal Labeling and Nuclear Imaging of PSMA-Positive Tumors.* PLOS ONE, 2015. **10**(12).
88. Sheikh, N., et al., *Tc-99m PSMA and Lu-177 PSMA Theranostic Pair in a Patient of Metastatic Castration Resistant Prostate Cancer.* J Pak Med Assoc, 2021. **71**(11): p. 2679-2682.
89. Fomenko, V.V., et al., *Crystal structure of copper (II) diethylenetriaminepentaacetate monohydrate.* Journal of Structural Chemistry, 1973. **14**(3).
90. Deri, M.A., et al., *Alternative Chelator for ^{89}Zr Radiopharmaceuticals: Radiolabeling and Evaluation of 3,4,3-(LI-1,2-HOPO).* Journal of Medicinal Chemistry, 2014. **57**(1 1).
91. Wang, Q., et al., *Folding Dynamics of 3,4,3-LI(1,2-HOPO) in Its Free and Bound State with U4+ Implicated by MD Simulations.* Molecules, 2022. **27**(23).
92. Wang, Q., et al., *Chelation Behaviors of 3,4,3-LI(1,2-HOPO) with Lanthanides and Actinides Implicated by Molecular Dynamics Simulations.* Inorganic Chemistry, 2023. **62**(10).
93. Basuli, F., et al., *Preparation of a Zirconium-89 Labeled Clickable DOTA Complex and Its Antibody Conjugate.* Pharmaceuticals, 2024. **17**(4).
94. Commission, U.S.N.R., *Multi-Agency Radiological Laboratory Analytical Protocols Manual*, in *NUREG-1576, Initial Report*. 2004, United States Nuclear Regulatory Commission. p. 91.
95. Vosjan, M.J.W.D., et al., *Conjugation and radiolabeling of monoclonal antibodies with zirconium-89 for PET imaging using the bifunctional chelate p-isothiocyanatobenzyl-desferrioxamine.* Nature Protocols, 2010. **5**(4).
96. Meijs, W.E., et al., *A facile method for the labeling of proteins with zirconium isotopes.* Nuclear Medicine and Biology, 1996. **23**(4).
97. Zeglis, B.M., et al., *Enzyme-Mediated Methodology for the Site-Specific Radiolabeling of Antibodies Based on Catalyst-Free Click Chemistry.* Bioconjugate Chemistry, 2013. **24**(6).
98. Bellotti, D. and M. Remelli, *Deferoxamine B: A Natural, Excellent and Versatile Metal Chelator.* Molecules, 2021. **26**(11).

99. Vugts, D.J., et al., *Comparison of the octadentate bifunctional chelator DFO*-pPhe-NCS and the clinically used hexadentate bifunctional chelator DFO-pPhe-NCS for ^{89}Zr-immuno-PET.* European Journal of Nuclear Medicine and Molecular Imaging, 2016. **44**(2).
100. Allott, L., et al., *Evaluation of DFO-HOPO as an octadentate chelator for zirconium-89.* Chemical Communications, 2017. **53**(61).
101. Raavé, R., et al., *Direct comparison of the in vitro and in vivo stability of DFO, DFO* and DFOcyclo* for ^{89}Zr-immunoPET.* European Journal of Nuclear Medicine and Molecular Imaging, 2019. **46**(9).
102. Chomet, M., et al., *Head-to-head comparison of DFO* and DFO chelators: selection of the best candidate for clinical ^{89}Zr-immuno-PET.* European Journal of Nuclear Medicine and Molecular Imaging, 2020. **48**(3).
103. Rousseau, J., et al., *Synthesis and evaluation of bifunctional tetrahydroxamate chelators for labeling antibodies with ^{89}Zr for imaging with positron emission tomography.* Bioorganic & Medicinal Chemistry Letters, 2018. **28**(5).
104. Seibold, U., B. Wängler, and C. Wängler, *Rational Design, Development, and Stability Assessment of a Macrocyclic Four-Hydroxamate-Bearing Bifunctional Chelating Agent for ^{89}Zr.* ChemMedChem, 2017. **12**(18).
105. Alnahwi, A., et al., *Promising Performance of 4HMS, a New Zirconium-89 Octadendate Chelator.* ACS omega, 2020. **5**(19).
106. Patra, M., et al., *An octadentate bifunctional chelating agent for the development of stable zirconium-89 based molecular imaging probes.* Chemical Communications, 2014. **50**(78).
107. Mitchell, M.J., et al., *Engineering precision nanoparticles for drug delivery.* Nature Reviews Drug Discovery, 2020. **20**(2).
108. Janib, S., A. Moses, and J. MacKay, *Imaging and drug delivery using theranostic nanoparticles.* Advanced Drug Delivery Reviews, 2010. **62**(11).
109. Das, K.P. and C. J, *Nanoparticles and convergence of artificial intelligence for targeted drug delivery for cancer therapy: Current progress and challenges.* Frontiers in Medical Technology, 2023. **4**.
110. Yusuf, A., et al., *Nanoparticles as Drug Delivery Systems: A Review of the Implication of Nanoparticles' Physicochemical Properties on Responses in Biological Systems.* Polymers, 2023. **15**(7).
111. Cai, Z., et al., *Assembly-Controlled Magnetic Nanoparticle Clusters as MRI Contrast Agents.* ACS Biomaterials Science & Engineering, 2020. **6**(5).
112. de Gouw, D., et al., *Controlled mechanical ventilation to detect regional lymph node metastases in esophageal cancer using USPIO-enhanced MRI; comparison of image quality.* Magnetic resonance imaging, 2020. **74**.
113. Pusta, A., et al., *Recent Advances in the Development of Drug Delivery Applications of Magnetic Nanomaterials.* Pharmaceutics, 2023. **15**(7).
114. Kianfar, E., *Magnetic Nanoparticles in Targeted Drug Delivery: a Review.* Journal of Superconductivity and Novel Magnetism, 2021. **34**(7).
115. Wu, M. and J. Shu, *Multimodal Molecular Imaging: Current Status and Future Directions.* Contrast media & molecular imaging, 2018. **2018**.
116. Murphy, A. and J. Yeung, *Spatial resolution (MRI) | Radiology Reference Article |.* Radiopaedia.org, 2011.

117. Stucht, D., et al., *Highest Resolution In Vivo Human Brain MRI Using Prospective Motion Correction.* PLOS ONE, 2015. **10**(7).
118. Crooks, L.E., et al., *High-resolution magnetic resonance imaging. Technical concepts and their implementation.* Radiology, 1984. **150**(1).
119. Benjamin, M.M., M. Shaker, and M.G. Rabbat, *Assessing coronary artery disease using coronary computed tomography angiography.* Cardiovascular and Coronary Artery Imaging, 2022. **1**.
120. Tang, J., et al., *Macromolecular MRI contrast agents: Structures, properties and applications.* Progress in Polymer Science, 2013. **38**(3-4).
121. Hao, D., et al., *MRI contrast agents: Basic chemistry and safety.* Journal of Magnetic Resonance Imaging, 2012. **36**(5).
122. Xiao, Y.-D., et al., *MRI contrast agents: Classification and application (Review).* International Journal of Molecular Medicine, 2016. **38**(5).
123. Harvey, H.B., V. Gowda, and G. Cheng, *Gadolinium Deposition Disease: A New Risk Management Threat.* Journal of the American College of Radiology, 2020. **17**(4).
124. Ersoy, H. and F.J. Rybicki, *Biochemical safety profiles of gadolinium-based extracellular contrast agents and nephrogenic systemic fibrosis.* Journal of Magnetic Resonance Imaging, 2007. **26**(5).
125. Kastelik-Hryniewiecka, A., et al., *Targeted PET/MRI Imaging Super Probes: A Critical Review of Opportunities and Challenges.* International Journal of Nanomedicine, 2022. **16**.
126. Debroye, E. and T.N. Parac-Vogt, *Towards polymetallic lanthanide complexes as dual contrast agents for magnetic resonance and optical imaging.* Chemical Society Reviews, 2014. **43**(23).
127. Wahsner, J., et al., *Chemistry of MRI Contrast Agents: Current Challenges and New Frontiers.* Chemical Reviews, 2018. **1 19**(2).
128. Hermanson, G.T., *Introduction to Bioconjugation.* Bioconjugate Techniques, 2013.
129. Hermanson, G.T., *Zero-Length Crosslinkers*, in *Bioconjugate Techniques*. 2013.
130. Peer, D., et al., *Nanocarriers as an emerging platform for cancer therapy.* Nature Nanotechnology, 2007. **2**(12).
131. Colombo, M., et al., *Biological applications of magnetic nanoparticles.* Chemical Society Reviews, 2012. **41**(11).
132. Ruiz, A., et al., *Short-chain PEG molecules strongly bound to magnetic nanoparticle for MRI long circulating agents.* Acta Biomaterialia, 2013. **9**(5).
133. Pellico, J., et al., *Fast synthesis and bioconjugation of (68) Ga core-doped extremely small iron oxide nanoparticles for PET/MR imaging.* Contrast media & molecular imaging, 2016. **11**(3).
134. Thomas, G., et al., *Innovative Magnetic Nanoparticles for PET/MRI Bimodal Imaging.* ACS Omega, 2019. **4**(2).
135. Yang, X., et al., *cRGD-functionalized, DOX-conjugated, and ^{64}Cu-labeled superparamagnetic iron oxide nanoparticles for targeted anticancer drug delivery and PET/MR imaging.* Biomaterials, 2011. **32**(17).
136. Shi, D., et al., *Optimizing superparamagnetic iron oxide nanoparticles as drug carriers using an in vitro blood–brain barrier model.* International Journal of Nanomedicine, 2016. **11**.
137. Yang, M., et al., *Dragon fruit-like biocage as an iron trapping nanoplatform for high efficiency targeted cancer multimodality imaging.* Biomaterials, 2015. **69**.

138. Gholami, Y., et al., *A Radio-Nano-Platform for T1/T2 Dual-Mode PET-MR Imaging.* International Journal of Nanomedicine, 2020. **15**.
139. Boros, E., et al., *Chelate-free metal ion binding and heat-induced radiolabeling of iron oxide nanoparticles.* Chemical Science, 2014. **6**(1).
140. Yuan, H., et al., *Heat-induced radiolabeling and fluorescence labeling of Feraheme nanoparticles for PET/SPECT imaging and flow cytometry.* Nature Protocols, 2018. **13**(2).
141. Chakravarty, R., et al., *Intrinsically germanium-69-labeled iron oxide nanoparticles: synthesis and in-vivo dual-modality PET/MR imaging.* Advanced Materials, 2014. **26**(30).
142. Jallinoja, V.I.J. and J.L. Houghton, *Current Landscape in Clinical Pretargeted Radioimmunoimaging and Therapy.* Journal of Nuclear Medicine, 2021. **62**(9).
143. Cheal, S.M., et al., *Pretargeting: A Path Forward for Radioimmunotherapy.* Journal of Nuclear Medicine, 2022. **63**(9).
144. Liu, G., *A Revisit to the Pretargeting Concept—A Target Conversion.* Frontiers in Pharmacology, 2018. **9**.
145. Locatelli, E., et al., *Biocompatible nanocomposite for PET/MRI hybrid imaging.* International Journal of Nanomedicine, 2012. **7**.
146. Desbois, N., et al., *Synthetic strategy for preparation of a folate corrole DOTA heterobimetallic Cu–Gd complex as a potential bimodal contrast agent in medical imaging.* Tetrahedron Letters, 2015. **56**(51).
147. Bourquin, J., et al., *Biodistribution, Clearance, and Long-Term Fate of Clinically Relevant Nanomaterials.* Advanced Materials, 2018. **30**(19).
148. Aryal, S., et al., *Positron Emitting Magnetic Nanoconstructs for PET/MR Imaging.* Small, 2014. **10**(13).
149. Kuźnik, A., et al., *Bisphosphonates—much more than only drugs for bone diseases.* European Journal of Pharmacology, 2020. **866**.
150. Oryan, A. and S. Sahvieh, *Effects of bisphosphonates on osteoporosis: Focus on zoledronate.* Life Sciences, 2021. **264**.
151. Czyżykowski, R., M. Krakowska, and P. Potemski, *Bisphosphonates for the treatment of patients with cancer.* Oncology in Clinical Practice, 2017. **13**(6).
152. Sandiford, L., et al., *Bisphosphonate-Anchored PEGylation and Radiolabeling of Superparamagnetic Iron Oxide: Long-Circulating Nanoparticles for in Vivo Multimodal (T1 MRI-SPECT) Imaging.* ACS Nano, 2012. **7**(1).
153. Gumienna-Kontecka, E., et al., *Bisphosphonate chelating agents: complexation of Fe(III) and Al(III) by 1-phenyl-1-hydroxymethylene bisphosphonate and its analogues.* Inorganica Chimica Acta, 2002. **339**.
154. Vitha, T., et al., *Gd(III) complex of a monophosphinate-bis(phosphonate) DOTA analogue with a high relaxivity; Lanthanide(III) complexes for imaging and radiotherapy of calcified tissues.* Dalton Transactions, 2009(17).
155. Abraham, S.J., et al., *Differences in Lysine pKa Values May Be Used to Improve NMR Signal Dispersion in Reductively Methylated Proteins.* Journal of Biomolecular NMR, 2009. **43**(4).
156. Degenhardt, C.R. and D.C. Burdsall, *Synthesis of ethenylidenebis(phosphonic acid) and its tetraalkyl esters.* Journal of Organic Chemistry, 1986. **5 1**: p. 3488-3490.

157. Golubev, N.S., et al., *Study of hydrogen bonds of hypophosphorous acid by ^{1}H, ^{2}H, ^{31}P, and ^{15}N NMR spectroscopy under slow exchange conditions.* Russian Journal of General Chemistry, 2006. **76**(6).
158. Řezanka, P., et al., *Synthesis of a Bifunctional Monophosphinate DOTA Derivative Having a Free Carboxylate Group in the Phosphorus Side Chain.* Synthesis, 2008. **2008**(09).
159. Kraszewski, A. and J. Stawinski, *H-Phosphonates: Versatile synthetic precursors to biologically active phosphorus compounds.* Pure and Applied Chemistry, 2007. **79**(12).
160. Harsági, N. and G. Keglevich, *The Hydrolysis of Phosphinates and Phosphonates: A Review.* Molecules, 2021. **26**(10).
161. Thorek, D.L.J., et al., *Non-invasive mapping of deep-tissue lymph nodes in live animals using a multimodal PET/MRI nanoparticle.* Nature Communications, 2014. **5**(1).
162. Sharma, R., et al., *Carbon-11 radiolabeling of iron-oxide nanoparticles for dual-modality PET/MR imaging.* Nanoscale, 2013. **5**(16).
163. de Rosales, R.T.M., et al., *Synthesis of 64CuII–Bis(dithiocarbamatebisphosphonate) and Its Conjugation with Superparamagnetic Iron Oxide Nanoparticles: In Vivo Evaluation as Dual-Modality PET–MRI Agent.* Angewandte Chemie International Edition, 2011. **50**(24).
164. Groult, H., et al., *Parallel Multifunctionalization of Nanoparticles: A One-Step Modular Approach for in Vivo Imaging.* Bioconjugate Chemistry, 2014. **26**(1).
165. Zeglis, B.M. and J.S. Lewis, *The Bioconjugation and Radiosynthesis of ^{89}Zr-DFO-labeled Antibodies.* Journal of Visualized Experiments, 2015(96).
166. Junutula, J.R., et al., *Site-specific conjugation of a cytotoxic drug to an antibody improves the therapeutic index.* Nature Biotechnology, 2008. **26**(8).
167. Silverstein, R.M., G.C. Bassler, and T.C. Morrill, *Spectrometric identification of organic compounds*. Fifth ed. Organic Mass Spectrometry. Vol. 26. 1991, New York: Wiley. 430.
168. Mu, K., et al., *Monoclonal antibody-conjugated superparamagnetic iron oxide nanoparticles for imaging of epidermal growth factor receptor-targeted cells and gliomas.* Molecular imaging, 2015. **14**(5).
169. Goyon, A., et al., *Determination of isoelectric points and relative charge variants of 23 therapeutic monoclonal antibodies.* Journal of Chromatography B, 2017. **1065-1066**.
170. Moroz, A., et al., *A Preclinical Assessment of ^{89}Zr-Atezolizumab Identifies a Requirement for Carrier Added Formulations Not Observed with ^{89}Zr-C4.* Bioconjugate Chemistry, 2018. **29**(10).
171. Gawęda, W., et al., *Trastuzumab Modified Barium Ferrite Magnetic Nanoparticles Labeled with Radium-223: A New Potential Radiobioconjugate for Alpha Radioimmunotherapy.* Nanomaterials, 2020. **10**(10).
172. Moaseri, E., et al., *A simple recoverable titration method for quantitative characterization of amine-functionalized carbon nanotubes.* Chemical Physics Letters, 2013. **555**.
173. Brandt, M., et al., *Radiolabelling of the octadentate chelators DFO* and oxoDFO* with zirconium-89 and gallium-68.* Journal of Biological Inorganic Chemistry, a publication of the Society of Biological Inorganic Chemistry, 2020. **25**(5).
174. Pharmacopoeia, E., *Deferoxamine mesilate*. 2018, Council of Europe: Strasbourg.

175. Deri, M.A., et al., *p-SCN-Bn-HOPO: A Superior Bifunctional Chelator for ^{89}Zr ImmunoPET.* Bioconjugate Chemistry, 2015. **26**(12).
176. Kramer-Marek, G. and J. Capala, *Can PET imaging facilitate optimization of cancer therapies?* Curr Pharm Des, 2012. **18**(18): p. 2657-69.
177. Maguire, C.M., et al., *Characterisation of particles in solution – a perspective on light scattering and comparative technologies.* Science and Technology of Advanced Materials, 2018. **19**(1).
178. Devi, K., et al., *Zeta potential: a key factor in drug delivery.* World Journal of Pharmaceutical Science and Research. **3**(6).
179. Clogston, J.D. and A.K. Patri, *Zeta Potential Measurement.* Methods in Molecular Biology, 2011.
180. Turrina, C., et al., *Superparamagnetic iron oxide nanoparticles for their application in the human body: Influence of the surface.* Heliyon, 2023. **9**(6).
181. Schermeyer, M.-T., et al., *Characterization of highly concentrated antibody solution - A toolbox for the description of protein long-term solution stability.* mAbs, 2017. **9**(7).
182. Pasieczna-Patkowska, S., M. Cichy, and J. Flieger, *Application of Fourier Transform Infrared (FTIR) Spectroscopy in Characterization of Green Synthesized Nanoparticles.* Molecules, 2025. **30**(3).
183. Mieloch, A.A., et al., *Bioevaluation of superparamagnetic iron oxide nanoparticles (SPIONs) functionalized with dihexadecyl phosphate (DHP).* Scientific Reports, 2020. **10**(1).
184. Saengruengrit, C., et al., *Iron oxide nanospheres and nanocubes modified with carboxyphenyl porphyrin and their magnetic, optical properties and photocatalytic activities in room temperature amide synthesis.* Journal of Magnetism and Magnetic Materials, 2021. **521**.
185. Balk, M., et al., *Cellular SPION Uptake and Toxicity in Various Head and Neck Cancer Cell Lines.* Nanomaterials, 2021. **11**(3).
186. Hanaoka, K., et al., *A Gd^{3+}-Based Magnetic Resonance Imaging Contrast Agent Sensitive to β-Galactosidase Activity Utilizing a Receptor-Induced Magnetization Enhancement (RIME) Phenomenon.* Chemistry – A European Journal, 2008. **14**(3).
187. Chen, S.-H., et al., *Development of a Gd(III)-Based Receptor-Induced Magnetization Enhancement (RIME) Contrast Agent for β-Glucuronidase Activity Profiling.* Inorganic Chemistry, 2012. **5 1**(22).
188. Zhou, Z., et al., *Artificial local magnetic field inhomogeneity enhances T2 relaxivity.* Nature Communications, 2017. **8**(1).
189. Zhang, Y., J. Cheng, and W. Liu, *Characterization and Relaxation Properties of a Series of Monodispersed Magnetic Nanoparticles.* Sensors, 2019. **19**(15).
190. Rohrer, M., et al., *Comparison of magnetic properties of MRI contrast media solutions at different magnetic field strengths.* Investigative Radiology, 2005. **40**(11).
191. Sharma, G., et al., *Immuno-PET Imaging of Tumour PD-L1 Expression in Glioblastoma.* Cancers, 2023. **15**(12).
192. Song, G., et al., *Nanoparticles and the mononuclear phagocyte system: pharmacokinetics and applications for inflammatory diseases.* Current rheumatology reviews, 2014. **10**(1).
193. Mostafa, A.M.A., et al., *Exploring the Potential of Zirconium-89 in Diagnostic Radiopharmaceutical Applications: An Analytical Investigation.* Biomedicines, 2023. **11**(4).

194. Toporivska, Y. and E. Gumienna-Kontecka, *The solution thermodynamic stability of desferrioxamine B (DFO) with Zr(IV).* Journal of Inorganic Biochemistry, 2019. **198**.
195. Dilworth, J. and S. Pascu, *The chemistry of PET imaging with zirconium-89.* Chemical Society reviews, 2018. **47**(8).
196. Tu, C., et al., *Multimodality PET/MRI agents targeted to activated macrophages.* JBIC Journal of Biological Inorganic Chemistry, 2013. **19**(2).
197. Shurin, M.R., et al., *Radiomodulating Properties of Superparamagnetic Iron Oxide Nanoparticle (SPION) Agent Ferumoxytol on Human Monocytes: Implications for MRI-Guided Liver Radiotherapy.* Cancers, 2024. **16**(7).
198. Vukadinović, A., et al., *^{90}Y-CA/SPIONs for dual magnetic hyperthermia-radionuclide nanobrachytherapy of solid tumours.* Nanotechnology, 2022. **33**(40).
199. Pham, B.T.T., et al., *Biodistribution and Clearance of Stable Superparamagnetic Maghemite Iron Oxide Nanoparticles in Mice Following Intraperitoneal Administration.* International Journal of Molecular Sciences, 2018. **19**(1).

8. Achievements

Achievements related to this doctoral project:

Publication:

- **Targeted PET/MRI Imaging Super Probes: A Critical Review of Opportunities and Challenges;** A. Kastelik-Hryniewiecka, P. Jewula, K. Bakalorz, G. Kramer-Marek, ✉ N. Kuźnik; International Journal of Nanomedicine 2022, 16:8465-8483. doi: 10.2147/IJN.S336299 ; Scholarship was received for this article published in collaboration with an author representing a foreign research centre or non-academic partner, 2022, IDUB program, Silesian University of Technology

Scientific grant:

- **PRELUDIUM 21** grant on *Development of novel bimodal PET/MRI probes targeting PD-L1*; Principal Investigator: Anna Kastelik-Hryniewiecka; Scientific Supervisor: prof. Gabriela Kramer-Marek

Conference presentation:

- **Targeted and bioresponsive molecular probes for MRI and PET tomography based on new iron-zirconium-89 chelates**; A. Kastelik-Hryniewiecka, N. Kuźnik; COPM2024; online

Scientific apprenticeship

- Internship at the **Institute of Cancer Research in London (UK),** at **Preclinical Molecular Imaging team** (Division of Radiotherapy and Imaging). Apprenticeship was focused on cellular research methodology and molecular imaging techniques for small animals. The acquired expertise and additional funding enabled the development of in vitro and in vivo components and in-depth validation of the prepared conjugates.

Other scientific achievements, non-related to this doctoral thesis:

Publications:

- **Efficiency of ^{124}I radioisotope production from natural and enriched tellurium dioxide using ^{124}Te(p,xn)^{124}I reaction**, P. Bzowski, D. Borys, K. Gorczewski, A.Chmura, K. Daszewska, I. Gorczewska, A. Kastelik-Hryniewiecka, M. Szydło, A. d'Amico, ✉ M. Sokół: European Journal of Nuclear Medicine and Molecular Imaging; EJNMMI Physics, 9, (2022)
- **Green Dynamic Kinetic Resolution—Stereoselective Acylation of Secondary Alcohols by Enzyme-Assisted Ruthenium Complexes**, M. Heba, A. Wolny, A. Kastelik-Hryniewiecka, D. Stradomska, S. Jurczyk, A. Chrobok, ✉ N. Kuźnik; Catalysts; 11, (2022)

Grants

- **Ocena odpowiedzi immunologicznej u chorych leczonych pembrolizumabem z nowo zdiagnozowanym glejakiem wielopostaciowym mózgu (PIRG)** founded by Medical Research Agency (grant no: 2019/ABM/01/00062. Principal investigator: prof. dr hab. n. med. Gabriela Kramer-Marek. Project duration: 2022-2026); role in grant: radiochemist
- **Ocena heterogenności statusu HER2 u pacjentek z zaawansowanym rakiem piersi z wykorzystaniem obrazowania [68Ga]-DOTA-ABY025 oraz molekularnej oceny materiału histopatologicznego** – pilot study; role in grant: radiochemist

Posters and conference presentations:

- *Liquid target production of zirconium-89 for antibody labelling*; A. Chmura, A., A. Tomasik, A. Kastelik-Hryniewiecka, K. Miszczyszyn, Ł. Sochaczewski, M. Żółtowska, R. Mikołajczak, F. Y Frejd, M. Nestor, G. Kramer-Marek; COPM2024; online;
- *^{89}Zr-DFO-Atezolizumab for Imaging of PD-L1 in Glioblastoma: First Clinical Experience*; A. Kastelik-Hryniewiecka, I. Gorczewska, M. Niedbala, E. Chmielik, A. d'Amico, B. Bobek-Bilewicz, E. Nowicka, R. Tarnawski, W. Kaspera, G. Kramer-Marek; XVIII Sympozium PTMN; Poznań, Poland 6-8.06.2024
- *Translating immuno-PET imaging of PD-L1 in glioblastoma: journey from the laboratory to clinical practice*. D. Dar, A. Kastelik-Hryniewiecka, Ch. Da Pieve, I. Gorczewska, G. Sharma, M. Niedbala, P. Bzowski, E. Chmielik, A. d'Amico, B. Bobek-Bilewicz, E. Nowicka, R.Tarnawski, W. Kaspera, G. Kramer-Marek; Nuclear Medicine and Neurooncology (NMN) Symposium; Vienna, Austria 26-27.04.2024
- *^{89}Zr-DFO-Atezolizumab for PD-L1 Imaging of Glioblastoma: Clinical Experience*; A. Kastelik-Hryniewiecka, I. Gorczewska, M. Niedbała, C. Da Pieve, G. Sharma, P. Bzowski, M. Rodak, E. Chmielik, A. d'Amico, B. Bobek-Bilewicz, W. Kaspera, G. Kramer-Marek; European Symposium of Radiopharmacy and Radiopharmaceuticals, Coimbra, Portugal, 18-22.04.2024 - nomination for best poster award
- *Obrazowanie PD-L1 w glejaku wielopostaciowym z zastosowaniem immuno-PET*; I. Gorczewska, A. Kastelik-Hryniewiecka, M. Niedbała, A. d'Amico, B. Bobek-Billewicz, E. Chmielik, E. Nowicka, R. Tarnawski, W. Kaspera, G. Kramer-Marek;20-te Śląskie Seminarium Fizyki Medycznej organizowane przez Polskie Towarzystwo Fizyki Medycznej; opublikowano w: Inżynier i Fizyk Medyczny, 2/2024, vol.13
- *^{18}F-PSMA-1007 – specific imaging of prostate cancer (and more)*; A. Kastelik-Hryniewiecka; IV Seminarium Ogólnoakademickie, Wydział Nauk Farmaceutycznych Śląskiego Uniwersytetu Medycznego, April 2023 – best poster award
- *PSMA theranosthics - opportunities and challenges;* A. Kastelik-Hryniewiecka; XXVI Gliwice Scientific Meetings, November 2022